University of Brighton
School of Architecture, Technology and Engineering
Advanced Engineering Centre

University of Brighton

Advanced Engineering Centre

Development and Characterisation of an Innovative Battery Thermal Management System for Electric Vehicles with Loop Heat Pipes and Graphite Sheets

A thesis submitted in partial fulfilment of the
requirements of the University of Brighton
for the degree of Doctor of Philosophy

PhD Candidate:
Marco Bernagozzi

Supervisors:
Prof. Marco Marengo
Dr. Nicolas Miché
Dr. Anastasios Georgoulas

External Supervisor
from Ricardo plc:
Dr. Cedric Rouaud

January, 2022

Abstract

A new era for passenger transportation is beginning, where Electric Vehicles have emerged as an immediate solution to reduce emissions from passenger cars, when charged from renewable electric energy sources. However, their distribution is currently limited to only the 1% of the global fleet, due to key issues such as long charging time, limited all-electric range and elevated cost. A properly designed Thermal Management System (TMS) can improve on these points by reducing both the maximum temperature of the battery pack during fast charge and parasitic power consumed. The present thesis utilises a combination of numerical and experimental investigations to propose an innovative TMS concept using Loop Heat Pipes (LHPs) and graphite sheets. In the proposed concept the LHP acts as the main thermal vector, transferring heat from the bottom of a battery module to a remote heat exchanger, connected to the HVAC system already present in the vehicle. LHPs are reliable, low-maintenance, safe and not expensive systems, already used in electronics, space and aeronautical applications. Since LHPs do not need electrical power to operate, they reduce the parasitic power consumption compared to forced air or liquid based TMS. Graphite sheets have the twofold function of promoting heat transfer along the cell plane direction, whilst hindering it in the transverse direction. The feasibility of the presented innovative design was first verified thanks to a Lumped Parameter Model, which was validated against in-house experimental data, using a copper flat plate LHP applied to a module of dummy prismatic cells and two different working fluids, ethanol and water. Results showed that this design complies with the requirements of maximum cell temperature and temperature difference across the cell and, when compared against an equivalent liquid cold plate design, its achieved maximum temperature after fast charge was lower by 3.6°C. Furthermore, following automotive industry demands for environmentally friendly systems, Novec™ 649 is, for the first time, experimentally investigated as the LHP working fluid, due to its exceptional environmental and safety properties. The results showed that with this fluid the proposed design provides

excellent cooling at fast charge conditions. Moreover, compared to ethanol, maximum temperatures were only 0.7°C higher, proving that the adoption of Novec™ 649 improves on safety and environmental impact with no detriment to the thermal performance. Additionally, aiming at practical implementations of the proposed TMS concept, the developed numerical model was used to study the effect of active heating zone and thickness of the evaporator and the number of LHPs applied to a 12-cell module. Moreover, an extensive parametric analysis on various combinations of LHP materials and working fluids, with particular attention to their safety and environmental properties, was performed. Finally, after a comparison against the use of passive free convection and an active liquid cold plate, the LHP-based TMS resulted in the lowest temperature after fast charging.

List of Contents

List of Figures

List of Tables

Nomenclature

Acronyms and Abbreviations			
AEC	Advanced Engineering Centre	LHP	Loop Heat Pipe
BEV	Battery Electric Vehicle	LPM	Lumped Parameter Model
BIC	Boiling Immersion Cooling	NCG	Non-Condensable Gases
CC	Compensation Chamber	NEDC	New European Driving Cycle
CPL	Capillary Pumped Loop	Num	Numerical
C-rate	Charging Rate	ODE	Ordinary Differential Equation
DOD	Depth Of Discharge	ODP	Ozone Depletion Potential
EREV	Extended Range Electric Vehicle	PCM	Phase Change Materials
EV	Electric Vehicle	PHEV	Plug-in Hybrid Electric Vehicle
Exp	Experimental	PHP	Pulsating Heat Pipe
FCEV	Fuel Cells Electric Vehicle	PMBLDC	Permanent Magnet Brushless Direct Current
FVM	Finite Volume Method	SEI	Solid Electrolyte Interphase
GHG	GreenHouse Gases	SOC	State of Charge
GWP	Global Warming Potential	SS	Stainless Steel
HEX	Heat Exchanger	TC	Thermocouple
HEV	Hybrid Electric Vehicle	TEG	Thermoelectric Generators
HFCH	Highway—Fast Charging—Highway	TMS	Thermal Management System
HP	Heat Pipe	VC	Vapour Chamber
HVAC	Heating Ventilation Air Conditioning	WLTP	Worldwide Harmonised Light Vehicle Test Procedure
ICE	Internal Combustion Engine		
LCA	Life Cycle Assessment		
Physical Quantities			
A	Surface [m^2]	$\dot{Q}_{conv}$	Heat Absorbed Cold Plate
C	Thermal Capacity [J/K]	R	Thermal Resistance [K/W]
C_0	Capacity [Ah]	$\bar{r}$	Pore Size Medium Radius
c_p	Mass Heat Capacity [J/g K]	Ra	Rayleigh Number
D	Diameter [m]	Re	Reynolds Number
F	Faraday number [Coulomb/mol]	R_{ieq}	Internal Equivalent Resistance [Ω m^3]
g	Gravity [m/s^2]	$R_{fouling}$	Fouling Thermal Resistance [K/W]
H	Height [m]	S	Entropy [J/mol K]
h_c	Convection Heat Transfer Coefficient [W/m^2K]	SOC	State Of Charge
h_{LV}	Latent heat of Vaporisation [J/g]	t	Time [s]/Thickness [m]
h'_{fg}	Modified Latent heat of Vaporisation [J/g]	T	Temperature [°C]
I	Current [A]	$\dot{T}_{cool}$	Variation Temperature cold plate [°C]

i	Discharge current per unit volume [A m^3]	$T_{c,eff}$	Effective Coolant Temperature
k	Thermal Conductivity [W/m K]	u	Internal energy [J/kg]
k_g	Adiabatic index	U	Open Circuit Voltage [V]
k_w	permeability coefficient [m^2]	v	Velocity [m/s]/kinematic viscosity [St]
L	Length [m]	V	Voltage [V]
m	Mass [kg]	x	Vapour Quality
$\dot{m}$	Mass and volumetric Flow Rate [kg/s]	Z	Elevation [m]
$\dot{m}_v$	Volmetric flow rate [m^3/s]		
n_{module}	Number of Cells Composing a Module		
NTU	number of transfer unit	*Greek letters*	
Nu	Nusselt Number	α	Thermal Diffusivity [m^2/s]
P	Pressure	α_f	Dittus Boelter Heat transfer Coefficient [W/m^{2}K]
P^*	Reduced Pressure	β	expansion coefficient
Pr	Prandtl Number	θ	Meniscus Contact Angle
q	Heat Generation Rate Cell [W]	μ	Viscosity [Pa s]
$\dot{q}$	Rate of internal heat generation per unit volume [W/m^3]	ρ	Mass Density [kg/m^3]
$\dot{Q}$	Heat [W]	σ	Surface Tension [Nm]
Subscripts			
amb	Ambient	$leak$	Leakage
C	Cell, concentrated	ll	Liquid Line
cap	capillary	ndb	Dittus-Boelter coefficient
cc	Compensation Chamber	P	Pipe
$cond$	Condenser	$plate$	Cold Plate
cw	containment wall	pw	Primary Wick
d	distributed	sat	Saturation
$eLHP$	LHP evaporator	v	Vapour
$evap$	evaporator	vo,vg	Vapour Grooves/Outlet
ext	External	$wall$	Evaporator wall
fg	Latent heat of Vaporisation	$\parallel$	Inplane
g	Graphite	$1,2,3$	LPM Nodes
HEX	Heat Exchanger	$\perp$	Normal
l	Liquid		

Acknowledgements

The work this PhD thesis is based on has been carried out at the Advanced Engineering Centre, at the University of Brighton, UK, in collaboration with the industrial partner Ricardo plc. I would like to thank the Centre, the University and Ricardo plc for the financial support.

I would like to express my thanks to my supervisory team for their support throughout these three years: Prof. Marco Marengo, for the guidance, for testing me and ultimately making me understand that he never had a doubt about my abilities; Dr. Nicolas Miché, for coming out to teach me how to work with vacuum, when staying at home was the preferred options; Dr. Anastasios Georgoulas, for the overall guidance and support showed many times in every little aspect, that eventually helped me be the researcher I am.

I would like also to thank Dr. Cedric Rouaud, from Ricardo plc, for his constant support, high standards and for always setting the intensity and the bar high. Being able to finish this work in time, despite the COVID-related university closures, was also thanks to him.

I also would like to thank all the teaching and research staff, technicians, fellow PhD students at the University of Brighton for the small breaks, pearls of wisdom and encouraging words shared amongst the years. Every little moment of being a nice person counts. I would also like to thank the ones who did not help me during the last years, for making this even sweeter.

I want to thank my family, my mum Livia, my dad Luigi, for their unwavering support and motivation during my studies and all my life, for teaching me manners, respect and integrity. My sister Ilaria, for challenging me to be a better researcher than her, which is impossible. I am incredibly lucky to have you all and I feel very proud of the family we have become. Vi voglio bene.

I want also to thank all my friends for the all the memories shared together and their support. One day you guys will understand what I do for a living, hopefully.

Finally, I want to thank my girlfriend, Emma, who has been sensational throughout. You believed so much in me that I started to believe in myself as well and I cannot thank you enough for that. I can’t wait to see what life has in store for us.

Author's Declaration

I declare that the research contained in this thesis, unless otherwise formally indicated within the text, is the original work of the author. The thesis has not been previously submitted to this or any other university for a degree, and does not incorporate any material already submitted for a degree.

Signed

Dated

05/06/2022

Chapter 1 - Introduction

To assess and contain the deteriorating of Earth conditions has been one of the main research interests of the last decades. It is now understood that the Global Warming phenomenon is attributed to the increasing concentration of GreenHouse Gases (GHG) in our atmosphere and governments worldwide are under pressure to take action. The electrification of the transportation sector is a major movement in the direction of a green Earth, since it accounts for the 28% and 34% of the 2018 overall CO_2 emissions (predominant GHG) in the UK [1] and US [2], respectively. It was reported that Electric Vehicles (EVs) can provide a reduction of 20% in GHG emissions compared to Internal Combustion Engine (ICE) vehicles [3]. For these reasons, governments have set in the near future the end of the sale of new conventional fossil fuel cars and vans (e.g., 2030 for UK, 2035 for China and EU). However, despite the steep growth in numbers of the recent years (43% increase in 2020 with respect to the previous year, despite the Covid-19 pandemic), EVs are still representing about 1% share of the global stock of passenger cars [4]. In fact, the spreading of EVs is hindered by customers having reservations on mainly three issues: limited all-electric range, elevated purchase cost, long recharging times. Hence, significant improvements are still needed to help EVs take over the market and contribute to a significant reduction of the CO_2 emissions from the passenger vehicles sector.

The most suitable energy storage technology for EVs, so far, is represented by Li-ion batteries, which are components that are greatly influenced by temperature. Both high and low temperatures affect the power output and operational life of these batteries, e.g., cycling a cell at 55°C and -40 °C can lose 70% [5] and 95% [6] of its capacity, respectively. Therefore, an EV needs an efficient Thermal Management System (TMS) to control the temperature of the battery pack and its subcomponents in order to guarantee maximum performance.

A TMS is also needed to dissipate the excess heat during charge time. This is a pressing matter as the long charging time is one of the major issues regarding EVs. The current state-of-the-art is approximately 20 minutes for a partial charge (from 20% to 80% of the total capacity). In order to achieve even shorter charge times, the power delivered to the battery cells needs to be even higher, resulting in higher current and hence greater amount of generated heat. A cooling system that can contain the cell temperature below the selected temperature thresholds and allows ultra-fast charge would therefore be desirable. The typical temperature thresholds are set so that the cell should not overcome 40°C for optimum performance [7], 50°C for good acceptable performance [8] and 60°C for safety limit [9]. In fact, another crucial consideration regarding temperature control for Li-ion batteries is safety, as a potentially disruptive condition called thermal runaway onsets when the separator melts and a strongly exothermic reaction takes place leading to smoke, fire and potential explosions.

Up until now, EV manufacturers have relied on two methods of thermal management, air and liquid convection:

- Forced air convection is the simplest, lightest and cheapest of the two methods, thanks to a series of fans and intakes that are used to direct the airstream into the battery pack. However, due to the poor thermal properties of the thermal medium, air convection cannot cope with high thermal loads usually connected with the high Charing-Rates (C-rates) typical of fast charging (C-rate > 2-3, temperature > 40°C [10]). Due to the inadequate thermal properties of the thermal medium (air), this method cannot maintain a homogeneous temperature distribution along the battery module. Finally, due to the power required for the operation of the fans, it can consume up to 10 times more parasitic power than forced liquid convection [11].
- Forced indirect liquid convection based TMSs can employ different enclosures for the working fluid circulation, such as tubing, minichannels, cold plates or jackets, providing excellent heat transfer coefficients and, after optimizing mass flow rates and pressure drops, they can consume 10 times less power than air convection [11]. However, since they usually include several components (pumps, valves, reservoirs), their cost, weight and maintenance requirements are higher [12,13].

Extensively researched but not yet employed is the use of other TMS technologies that utilise Phase Change Materials (PCM) [14], Heat Pipes and Boiling Immersion Cooling (BIC) [15]:

- PCMs have been extensively studied, thanks to their appealing working principle whereby during discharge, heat is removed firstly due to sensible heat in the solid, then is removed

thanks to latent heat during the phase transition from solid to liquid. The heat stored can be reversed to the cell for heating purposes, preventing the cell to reach low temperatures. However, the most common PCMs have low values of thermal conductivity, which makes them not able to adapt to high-demand applications, without prohibitively increasing the weight of the battery pack.

- BIC relies on the transfer of the latent heat during the phase transition from liquid to vapour when the cell is submerged in a pool of liquid, allowing for substantially higher cooling capacities than conventional methods [15,16]. However, performance is strongly dependent on the boiling mode and as such, to finely control the pressure of the system to reach the desired boiling mode is a challenging design task, which increases the complexity of the system. Furthermore, strict fluid requirements in terms of safety and environmental, on top of obvious dielectric properties, limit the working fluid selection to expensive solutions.
- Heat Pipes are a reliable passive technology, already widely used in space and aeronautical applications, laptops and smartphones, where the fluid motion is maintained by a combination of pressure gradients and capillarity actions arising in a porous structure and/or gravity, where heat is removed utilising the phase-change (evaporation/condensation of the contained working fluid). Despite being very promising for their exceptional heat transfer capabilities, they still present design challenges in terms of selecting the best cooling solutions for the condenser, minimising weight and optimizing interfacing with the modules.

The motivations behind this work are therefore to find a TMS that:

a) consumes less power, to increase the all-electric range of the vehicle;

b) needs low maintenance and has low number of parts and complexity level, keeping the overall vehicle cost low;

c) provides sufficient cooling during fast charging.

The final TMS design proposed in the present PhD thesis consists of a Loop Heat Pipe (LHP) placed at the bottom of a battery module, which cells are sandwiched between thin graphite sheets. The LHP acts as the main thermal vector, carrying the excess heat from the module to a remote chiller. The graphite sheets, thanks to their anisotropic thermal conductivity, maximise heat transfer in the vertical direction from the cell to the LHP, while minimising at the same time the heat transfer from one cell to the other. The LHP is a member of the Heat Pipe family, distinguishing itself for having a porous wick structure, responsible

for the capillarity, inside the evaporator only, allowing to transfer heat through long distances without the use of additional energy or moving parts. Moreover, thermal solutions with multi-evaporators can integrate other heating sources, helping to create a thermal network system in the car.

The feasibility of this design idea was studied both numerically and experimentally in the present PhD thesis. First, a Lumped Parameter Model (LPM) was developed and then implemented into the open-source software GNU Octave to describe the thermal behaviour of both the cell-graphite assembly and the LHP. To validate the numerical code, an experimental demonstrator was built comprising of a flat-plate copper LHP and a 3-cell battery module mock-up. The validation procedure was carried out over two different working fluids, water and ethanol, and over a range of driving cycles, including a bespoke driving cycle reproducing a real-life event of a motorway driving phase, followed by a 10-minute fast charging phase. Temperature differences between the experimental measurements and numerical prediction were minimal, indicating the validity of the numerical code predictions. The optimized and validated version of the code was then used to simulate the effect of the variation of several parameters of interest to the industrial supporter of the project, further illustrating the suitability of the code as an actual design tool for the automotive industry.

Finally, an additional gap in the knowledge was identified. The Author's research found out that given the recent surge in interest on the TMS for EV, research is focussed on achieving the best possible performances, perhaps disregarding other important limitations posed by the automotive industry, especially regarding safety (intended as added risk in case of failure) and environmental impact. One important example are investigations employing flammable thermal medium, such as paraffin wax for PCM, ethanol, acetone and similar working fluids for Heat Pipes, ethylene glycol-water mixtures for liquid TMSs. The use of water adds some complications as well, such as being an electrical conductor and having a high freezing point, both features that would add further risks in case of failure. The environmental impact often is overlooked when it comes to choosing a refrigerant for the battery cooling medium, as many works in literature suggest the use of R134a, which has a Global Warming Potential (GWP) value of 1300, which is significantly higher than the threshold of 150, set by the European Union. From the analysis of the current research on EV TMS conducted in the first part of the present PhD thesis, what emerges is a lack of an efficient cooling method for TMS that considers not only the thermal performance but also the safety and environmental impact of the cooling medium. With this in mind, at the last part of this work, the heat transfer fluid Novec™ 649, developed by 3M™, is used as a working fluid in a LHP for the first time. This

selected fluid possesses the desired physical properties, in conjunction with favourable features such as non-flammability, a low freezing point and a GWP value of 1. Additionally, according to the Author's best knowledge, this work presents the first time that a fluid with these properties (non-flammable and non-toxic, ultra-low GWP, inert, low freezing point) is used as a working fluid in a member of the Heat Pipe family. The last part of this thesis is focussed on comparing experimentally the performance of the Novec™ 649 fluid against the performance of an already well-established working fluid in the sector of passive two-phase devices i.e., ethanol. Finally, the performances of the proposed TMS are evaluated over a series of fast charge cycles, to address its applicability to the EV market.

The present PhD thesis is structured as follows:

- Chapter 2 – Literature Review: an overview of the needs, technology and market status of the EV sector is given, together with an extensive bibliographic review on the TMSs used and studied so far. This review is used to generate a decision matrix that was used to identify the LHP as the most suitable heat transfer vector for the targeted application.
- Chapter 3 – Loop Heat Pipes: a description of the LHP fundamentals and characteristics of operation is provided.
- Chapter 4 - Modelling of Battery Cooling with Loop Heat Pipes: this chapter describes in detail the modelling of the LHP and of the cell-graphite assembly and finally of the whole system (cell-graphite + LHP); for the two separated parts of the code, two separate validation procedures were carried out by means of literature available data and FVM simulations; finally, a comparison with a standard liquid cold plate cooling system is performed.
- Chapter 5 - Experimental Validation and Investigation: the experimental demonstrator is described in depth, from the design to the tests of the LHP only as well as the tests of the entire system; the results of the validation procedure are included together with a comparison with an existing liquid cold plate cooling system.
- Chapter 6 - Automotive-Tailored Investigations: this chapter includes all the investigations performed after the successful results of the feasibility study; these include simulations on the effects of the number of evaporators applied to the considered battery module, the thickness of the flat-plate LHP evaporator, the effect of reducing the number of graphite sheets and a comprehensive parametric analysis on working fluid – solid material combinations. Moreover, an additional comparison with free convection is also conducted,

over different driving cycles. Finally, the experimental investigation on Novec™ 649 is presented.

- Chapter 7 – Conclusions

1.1. Research Question and Research Objectives

The research question at the base of this PhD thesis is the following:

- How to develop a novel Battery Thermal Management System that can tackle the limitations of the existing adopted technologies, in order to improve the customer's perception of EVs, ultimately to expand EV presence in the global fleet of passengers' cars.

The research objectives are divided as follows:

- To understand the current challenges and state of the art of thermal management solutions applied to EVs and to identify an innovative design for an efficient thermal management system.
- To develop a numerical model of the chosen design using the lumped parameter methodology.
- To build and characterize an experimental demonstrator, used to validate the numerical model and allowing it to study the feasibility of the proposed innovative TMS design with confidence.
- To evaluate different scenarios and parameters, to enhance the appeal of this novel proposed TMS design to the automotive sector.

1.2. List of Publications

Following, the publications emerged from the PhD work presented in this thesis are listed:

[1] M. Bernagozzi, A. Georgoulas, N. Miché, C. Rouaud, and M. Marengo, "A Novel Loop Heat Pipe Based Cooling System for Battery Packs in Electric Vehicles," in *2020 IEEE Transportation Electrification Conference & Expo (ITEC)*, **2020**, pp. 251–256.

[2] M. Bernagozzi, A. Georgoulas, N. Miché, C. Rouaud, and M. Marengo, "Critical Review and Ranking of Novel Solutions for Thermal Management in Electric Vehicles," *Advances in Heat Transfer and Thermal Engineering*, pp. 543–548, **2021**.

[3] M. Bernagozzi, A. Georgoulas, N. Miché, C. Rouaud, and M. Marengo, "Novel battery

thermal management system for electric vehicles with a loop heat pipe and graphite sheet inserts," *Applied Thermal Engineering*, vol. 194, no. May, **2021**.

[4] M. Bernagozzi, A. Georgoulas, N. Miché, C. Rouaud, and M. Marengo, "Numerical investigation on a combined loop heat pipe and graphite sheets cooling system for automotive applications," in *Joint 20th IHPC and 14th IHPS*, **2021**.

[5] M. Bernagozzi, N. Miché, A. Georgoulas, C. Rouaud, and M. Marengo, "Performance of an Environmentally Friendly Alternative Fluid in a Loop Heat Pipe-Based Battery Thermal Management System," *Energies*, vol. 14, no. 22, p. 7738, **2021**.

[6] M. Bernagozzi, A. Georgoulas, N. Miché, C. Rouaud, and M. Marengo "Comparison Between Different Battery Thermal Management Systems During Fast Charge Cycles" in *17th UK Heat Transfer Conference* (UKHTC2021), **2022**

Chapter 2 - Literature Review

2.1. Need for Electric Vehicles

The evident deteriorating of the Earth health conditions during the last 40 years has pushed governments worldwide to take actions, in particular to reduce the emissions of GreenHouse Gases (GHG). In Fig. 1, Earth's surface temperature evolution is presented at three successive instances since 1950, where blue and red regions represent temperatures below and above the average of the previous years, respectively. This provides undeniable evidence of the global warming phenomena which is taking place in the last century.

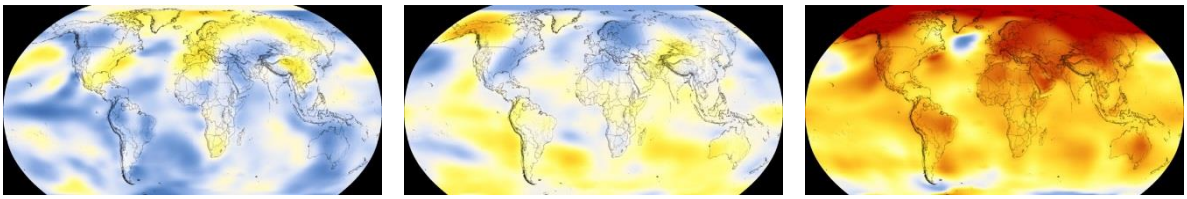

1950 1980 2018

Fig. 1. Earth's average surface temperature evolution during 3 instants since 1950 [17]; the blue spots represent below average temperature and the red spots represent above average (compared to the previous years) temperature in a scale from -4 to 4°F difference.

This phenomenon is attributed to the increased concentration of GreenHouse Gases in the atmosphere. These long-life gases trap radiating heat that would otherwise be released to outer space, and eventually emit this heat back to the atmosphere, in the so-called "greenhouse effect". Gases that contribute to the greenhouse effect are [18]:

- Water vapour: it increases with the increase of the Earth's atmosphere temperature, but it also increases the possibility of clouds and precipitation, making these some of the most important feedback mechanisms to the greenhouse effect.

- Carbon dioxide (CO_2): it is released through natural processes such as respiration, volcano eruptions and through human activities such as deforestation, land use changes and burning fossil fuels. Humans have increased atmospheric CO_2 concentration by more than a third since the Industrial Revolution began. This is the most important long-lived "forcing"[1] of climate change.
- Methane (CH_4): it is a hydrocarbon gas produced both through natural sources and human activities, including the decomposition of wastes in landfills, agriculture, and especially rice cultivation, as well as ruminant digestion and manure management associated with domestic livestock. On a molecular level, methane is a far more active greenhouse gas than CO_2, but also one which is much less abundant in the atmosphere. However, the melting of the icepack and the iced lands in Siberia and Canada can emit in a very short time an amount of methane, which is far more dangerous than CO_2 [19].
- Nitrous oxide (N_2O): it is a powerful greenhouse gas produced by soil cultivation practices, especially by the use of commercial and organic fertilizers, fossil fuel combustion, nitric acid production, and biomass burning.
- Chlorofluorocarbons: they are synthetic compounds entirely of industrial origin used in a number of applications, but now largely regulated in production and released to the atmosphere by international agreement due to their ability to contribute to the destruction of the ozone layer.

The transportation sector is one of the predominant sources of harmful emissions, accounting for 28% of the 2018 overall UK CO_2 emissions (being this the predominant of the GHGs) [1], and for the 34% of all CO_2 emissions in the US [2]. The need of quick action is motivated by the fact that CO_2 emission from road transport within the EU increased by 23% between 1990 and 2010 [20]. Hence amongst the several strategies sought to reduce the GHG emissions, the electrification of passengers' transportation seems one of the most promising. In fact, it has been reported how switching from vehicles powered by Internal Combustion Engine (ICE) to Electric Vehicles (EVs) could drastically reduce GHG emissions. Several studies in the past years have reported different figures and also contradictory theories, fuelling a fierce debate between experts worldwide. Looking at in-use operation only, EVs provide a clear reduction of 20% in GHG emissions compared to ICE vehicles [3]. Many studies have focused on the

[1] Long-lived gases that remain semi-permanently in the atmosphere and do not respond physically or chemically to changes in temperature are described as "forcing" climate change.

total life implication of the EVs adoption, by means of a technique known as Life Cycle Assessment (LCA), which assess the environmental impacts associated with all the stages of a product's life, from raw material extraction through materials processing, manufacture, distribution, use, repair and maintenance, concluding with disposal or recycling. Boureima et al. [21] stated that the GHG effect of hybrid and battery EVs is respectively 27.44% and 78.27% lower than for the gasoline vehicles; Hawkins et al. [22] proposed a very interesting LCA considering vehicle production, use, and end of life together with all relevant supply chains. They compared two baseline commercial vehicles, Mercedes Class A representing all ICE vehicles and Nissan Leaf representing all EVs, on a lifetime of 150,000 km. They investigated the influence of the electricity production method, and it was found that EVs powered by the present European electricity mix decrease the Global Warming Potential (GWP) by 10% to 24% with respect to conventional ICE vehicles. However, they show potential for significant increases in human toxicity, freshwater eco-toxicity, freshwater eutrophication, and metal depletion impacts, largely deriving from the vehicle supply chain. Because production impacts are more significant for EVs than conventional vehicles, increasing the assumed lifetime improves the GWP benefits whereas decreasing the lifetime reduces them. Obviously, these types of results are sensitive to assumptions regarding electricity sources, use-phase energy consumption, vehicle lifetime, and battery replacement schedules.

The impact of new technology on the planet environmental situation is assessed through two indexes: the GWP and the Ozone Depletion Potential (ODP). The GWP is the heat absorbed by a substance in the gas form in the atmosphere, as a multiple of the heat that would be absorbed by the same mass of CO_2. The ODP of a substance is the relative amount of degradation to the ozone layer it can cause, defined as the ratio of global loss of ozone due to the given substance and the loss CFC-11 (Trichlorofluoromethane) of the same mass (which has a fixed ODP of 1).

To tackle global warming, many governments around the world have decided to implement measures. For example, the UK government has set the end of the sale of new conventional petrol and diesel cars and vans by 2040, as part of the 2017 UK Air Quality Plan [23] and then anticipated it to 2030 [24].

Nonetheless, the electrification of the transportation sector is not the magic formula solving the problem of global warming, as this must be faced throughout a global phenomenon starting from sustainable energy production and concluding to commercial transportation. In fact, EVs cannot solve the problem of heavy-duty transportation due to the prohibitive requirements of

energy and power density of this application, hence ultra-low emission ICE engines still need to be developed [25]. Furthermore, other alternatives such as fuel cell and biofuels are worth studying.

2.2. Electric Vehicles Background and Present Situation

EVs were firstly introduced by Scotsman Robert Davidson in 1873. Contrarily to the general opinion, at the end of the nineteenth century electric cars were more developed than ICE cars. In fact the first car to break the 100km/h barrier was the Belgian EV "La Jamais Contente" in 1899 [26]. Later, the automotive market has turned to ICEs for their higher power density. The next advent of the electric cars was made possible by the increased availability of the permanent magnets for the brushless DC motor in 1980, followed by the appearance of the Li-ion battery, made commercially available by Sony in 1991 [27].

Nowadays, 5 types of electric vehicles are available depending on their powertrain architecture [20]:

- Battery Electric Vehicle (BEV): they rely solely on the electric motor powered by batteries only, without the presence of an ICE.
- Hybrid Electric Vehicle (HEV): they both possess an ICE and an electric motor, while batteries are recharged during motion.
- Plug-in Hybrid Electric Vehicle (PHEV): they both possess an ICE and an electric motor, while batteries are recharged externally.
- Extended Range Electric Vehicle (EREV): they have an additional ICE used as generator to power the electric motor in order to extend the range.
- Fuel Cells Electric Vehicle (FCEV): they exploit the fuel cell technology, hence obtaining power from the exothermic reaction between hydrogen and oxygen.

Electric cars sales were more than 2.1 million worldwide in 2019, with a 40% increase from 2018. Despite this great growth, EVs were still accounting for only 2.6% of global car sales and 1% of the global car stock globally in 2019 [28]. In 2020, despite the Covid-19 pandemic, the yearly increment was of 43% and 4.6% of global car sales; still remaining at 1% of the stock share [4]. A 2019 survey [29] explains the barriers perceived by the customers against purchasing an EV (listed in Fig. 2), hence explaining EV limited diffusion.

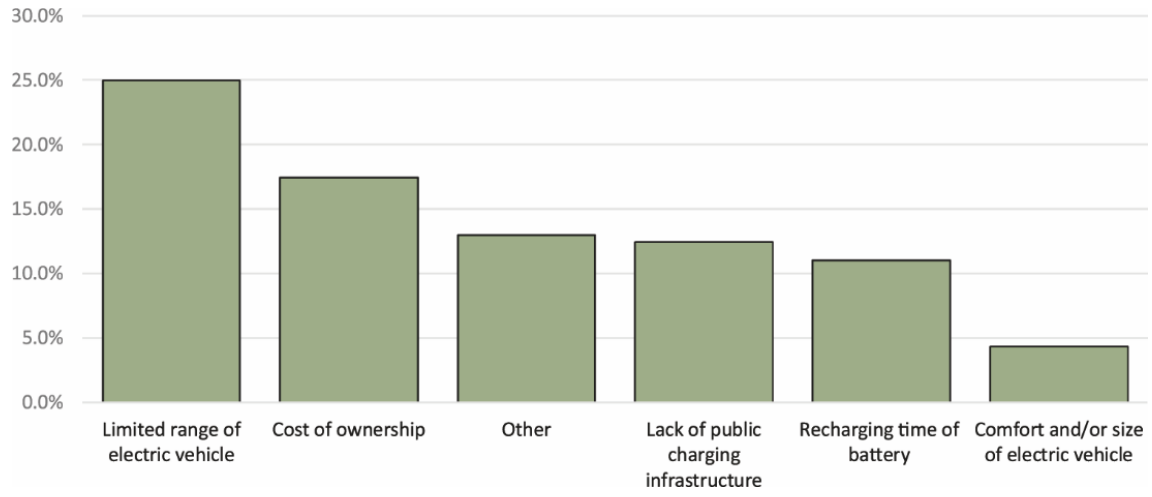

Fig. 2. Barriers against EV spreading deriving from 2019 costumer survey [29].

A quarter of the people interviewed stated that the limited *all-electric range* of the EV (which is defined as the maximum distance that the vehicle can travel relying only on a single charge) is the main reason blocking them to purchase an EV. Currently, average all-electric range stands around 250-300 km, with exceptions such as Tesla Model S setting the state-of-the-art with 660 km. This barrier is fostered by the range anxiety phenomenon, which is a psychological response to the stressful situation of the battery running low [29]. However, studies show that the average trip is below 100 km [30], hence the current range of most vehicles would be enough for most trips. The second biggest cause of scepticism on EVs is their cost, which ranges between £22,000 and £30,000 for small size cars to £70,000 for the Tesla Y, for example. However, it has been shown that a cost reduction from 9 up to 27% could greatly enhance the price competitiveness [31]. The third most critical barrier is the lack of public charging points. For instance, only 42,000 connectors were available in the UK in 2020 [32] (however this presents an increase of 7000 in that year alone), against the almost 280,000 UK registered BEV. But the government has launched a £400 million investment specifically to increase the number of charging stations. Generally, the issues presented in Fig. 2 could be ascribed to a fear of changing habits, augmented from the lack of knowledge on the functioning of EVs.

In Table 1 a summary of characteristics for the main EVs available on the 2021 market is presented, where there is a recognizable trend between high range and high cost of ownership.

Table 1 - Breakdown of the main EVs available in the market in 2019 [33]. Only the ones of which it was possible to have information on their Thermal Management System (TMS) are reported. Liquid means that a liquid medium is the main heat removal vector, while Air refers to when free or forced air convection removes the excess heat from the battery pack.

Vehicle	Battery Capacity [kWh]	Range [km]	Fast Charge [min]	TMS	Price
Lucid Air Pure	85	540	16	Liquid	£70,000
Tesla Model 3 Long Range	75	485	30	Liquid	£54,990
Porsche Taycan Plus	83.7	475	19	Liquid	£76,899
Ford Mustang Mach-E ER AWD	75.7	420	43	Liquid	£58,230
Kia EV6 Long Range	77.4	400	16	Liquid	£40,945
Hyundai Kona Electric	64	395	44	Liquid	£35,050
Hyundai IONIQ 5 Long Range 2WD	70	380	17	Liquid	£43,090
Jaguar I-Pace EV400	90	380	44	Liquid	£65,620
Kia e-Niro	64	370	44	Liquid	£34,995
Audi e-tron 55 quattro	86	365	26	Liquid	£72,175
Mercedes EQA 250	66.5	355	29	Liquid	£47,510
Volkswagen ID.3 Pro	58	350	30	Liquid	£30,700
Renault Zoe ZE50 R110	52	315	56	Air	£27,595
Opel Corsa-e	50	285	26	Liquid	£25,805
Peugeot e-208	50	285	30	Liquid	£28,260
BMW i3 120 Ah	42	235	18	Liquid	£33,805
Fiat 500e	42	235	25	Liquid	£27,335
Nissan Leaf	40	220	43	Air	£26,995
Volkswagen e-Up!	32.3	205	48	Air	£22,585
Mini Cooper SE	28.9	185	29	Liquid	£27,000
Mazda MX-30	30	170	39	Liquid	£27,650
Honda e	28.5	170	36	Liquid	£34,365
Fiat 500e	24	135	24	Liquid	£22,335
Smart EQ forfour	16.7	95	-	Liquid	£20,795

It should be mentioned that EVs can bring other benefits that are not based on sustainability, such as fuel cost savings up to 75% compared to petrol cars [34], better performance and street noise reduction. Other perks are higher motor efficiency with respect to ICE, high torque at low rpm and regenerative breaking.

2.3. Li-ion Battery Working Characteristics

2.3.1. Li-ion Battery Working Principle

In the present PhD thesis, the focus is on Li-ion batteries only, as they currently provide the highest specific energy and specific density with respect to the other battery chemical compositions utilized so far in commercially available EVs, as presented in Fig. 3.

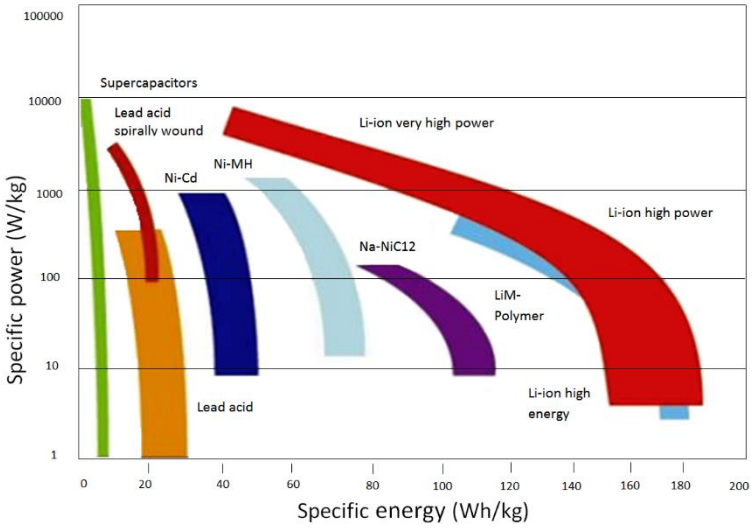

Fig. 3. Specific power vs specific energy for different types of batteries [35].

The Li-ion battery is formed by two electrodes: the positive pole, called *cathode*, which is usually a lithium containing compound, such as lithium cobalt oxide or lithium manganese oxide; the negative pole, called *anode*, which is usually graphite. In between the two electrodes there is the electrolyte, an organic solution containing a lithium salt, allowing for the Li-ions movements from one electrode to the other. Physically separating the two electrodes and thus preventing short-circuit, is a very thin sheet of micro-perforated plastic called *separator*. The current collectors, placed at the edge of the electrodes, are usually copper for the anode and aluminium for the cathode, as the first one is more stable at lower potential and the latter more stable at higher potential. A schematic of the Li-ion battery components and working principle is given in Fig. 4.

A fundamental element is the Solid Electrolyte Interphase (SEI), which is a surface film generating when a battery is charged for the first time. The SEI originates when part of the electrolyte reacts with free Li-ions at the interface of the anode, thus creating a surface film thick enough to block all the electrons from entry. This protects the anode from corrosion by chemical reduction, with little effect on the Li-ion transportation rate [36].

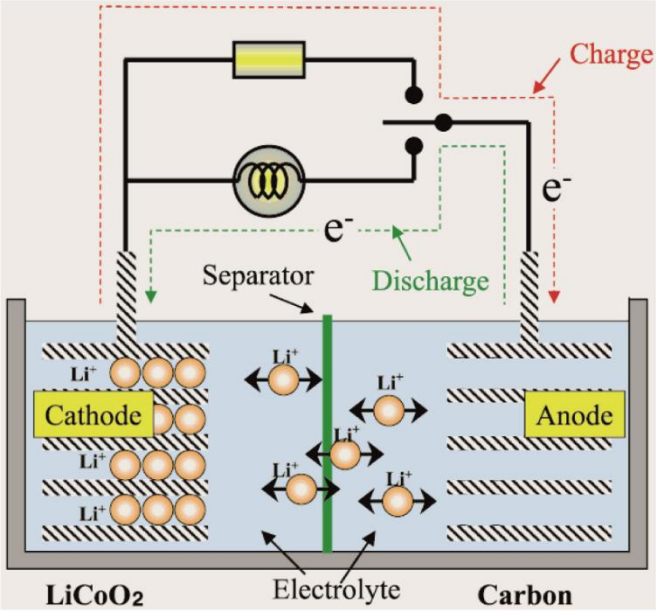

Fig. 4. Schematic of Li-ion battery and its working principle (adapted from [27]).

The working principle is divided in discharging and charging operations. During discharge, the negative charged anode sees the Li-ion leaving and moving to the cathode through the electrolyte, causing an electrical imbalance as the anode becomes positively charged. Thus, the electrons flow towards the cathode, through an external circuit connected to the load, generating in this way the required current. On the other hand, during the charging operation, the external current supply makes the Li-ion to move back towards the anode, followed by the compensation electrons, in similar fashion to the discharge process. This completely reversible process ("*rocking chair*") of the Li-ions entering and exiting the crystal structure of metals is known as *intercalation*.

The above explains the functioning of a single cell, which can come in three different shapes: cylindrical, prismatic and pouch, to which different heat generation rates are applied. The energy storage apparatus in an EV is represented by the battery pack, which is an array of battery modules, which in turn are an array of cells.

2.3.2. Temperature Effect on Li-ion Batteries

Thermal management of Li-ion batteries is a challenging task because of the dynamic nature of the battery cells usage and the wide range of environments under which they need to operate.

Temperature is one of the most influential parameters affecting the operation of Li-ion batteries, as it changes their chemical behaviour. In fact, according to the Arrhenius law, the reaction rate increases exponentially with the rising of the temperature, leading to a faster rate of ageing. Moreover, the utilisation patterns of the cell affect its temperature, especially in

terms of discharge cycles, as presented in Fig. 5, where it is evident how more demanding C-rates correspond to higher temperatures. Both low and high temperatures have strong effects, which will be explained below.

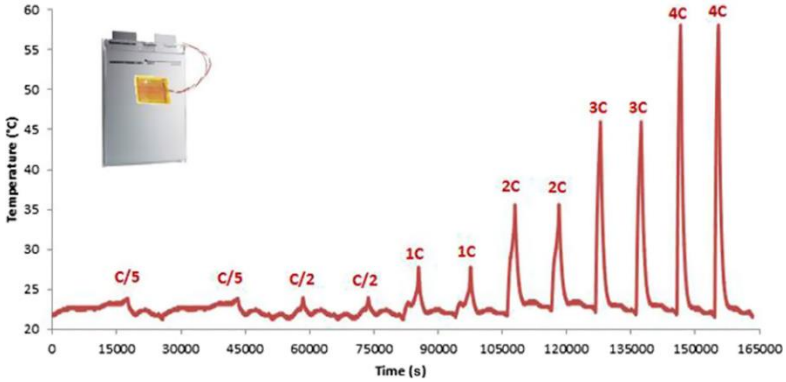

Fig. 5. Surface temperature of a Li-ion pouch cell subjected to C/5, C/2, 1C, 2C, 3C and 4C discharge cycles (C-rate: current-rate, defined as the charge or discharge current divided by the nominal capacity of battery) [10].

Considering extremely severe low temperature test conditions such as -40°C, 18650[2] Li-ion battery can only deliver 5% and 1.25% of the initial energy capacity and power capacity, respectively [6]. At -20°C, the available energy of the cell is only 60% of the original normal ambient temperature value [37]. This happens because at low temperature, the conductivity of the electrolyte decreases limiting the Li-ion transportation and increasing its internal resistance. Similarly, the diffusivity within the electrode is hindered, as well as the intercalation process. Lithium plating takes place as well, where there is a high polarization of the graphite anode, and the anode potential gets close to the lithium potential. This not only reduces performance but degrades the battery itself. Some researchers [38] stated instead that the primary cause of poor Li-ion cell performance at low temperatures lies in the Li-ion diffusion in the carbon anode, not in the electrolyte. This is linked to the fact that charging a cold discharged cell is more onerous than discharging a charged cold one, because of the rise of the charge-transfer resistance, which is the Ohmic resistance associated to the process of transferring electrons from the electrode to the electrolyte.

A real life example is the 2012 Nissan Leaf battery pack, which at -10°C can only deliver less than half of its advertised capacity (110 km instead of 225) [39]. Trying to solve this issue without turning to thermal management systems, research has been investigating low freezing

[2] Battery sizes are defined with a numerical system, where typically the first two digits are the diameter in millimetres and the last three are the length in tens of millimetres.

electrolytes with high ionic conductivities, such as carbonate or beryllium based electrolytes [40].

At high temperature, negative effects are reported as well. Again looking at the example of the 18650 cell, research showed capacity loss of 36% after being cycled 800 times at 45 °C and loss of more than 70% at 55 °C after 490 cycles [5]. This happens because the SEI dissolves, leaving the anode surface free and subjected to corrosion by the electrolyte. At the same time, the SEI permeability to Li-ion is reduced, limiting the intercalation process and therefore reducing the capacity and power output. Nissan Leaf customers in Arizona, when driving in environment characterized by temperature in the order of 50°C, complained about the range of their vehicles being half of the advertised one.

Ageing is another deteriorating phenomenon influenced by temperature, where the battery sees either its impedance rising or its capacity fading. Ageing can occur while the cell is in storage and not in use, in which case is called "*calendar ageing*", and it is influenced by storage temperature and the State Of Charge (SOC). Higher storing temperature increase the rate of chemical reactions leading to a faster capacity depletion [41]. The SOC instead is the quantity of Li-ions present on the electrodes, and it has been reported that an elevated SOC results in higher battery calendar ageing [42]. When ageing happens during the use of the battery, is called "*cycle ageing*", and it is influenced mainly by temperature (for the reasons described above) and by the utilization mode of the cell. One parameter to interpret this last phenomenon is the Depth Of Discharge (DOD), which is a complementary parameter to SOC as it expresses how much energy is being drawn out of the battery on a given cycle, stated as a percentage of the total capacity of the battery. According to [43], deep DOD accelerates the cycle ageing phenomena. Moreover, premature ageing of Li-ion batteries is influenced by high temperature as their lifespan is reduced by two months for every degree rise between 30°C and 40°C [44].

At high temperature there is a dangerous disruptive condition called *thermal runaway*, whereby a self-sustained exothermic reaction takes place when the separator melts (~130°C), increasing uncontrollably the temperature, eventually leading to fire and explosions [45]. Thermal runaway can be the result of different fault scenarios, such as mechanical abuse, electrical abuse or thermal abuse [46]:

- Mechanical abuse: it can be caused by nail penetration, when a conductive material pierces the battery and triggers a short circuit phenomenon, like in the 2013 Tesla S case where it caught fire running over some sharp debris that pierced the battery pack [47]. It could also be caused by crush or battery deformation, which in the first case will tear the separator and the two electrodes will come into contact, leading to short-circuit,

or in the second case where the liquid coolant will leak and, if conductive, will create short-circuit (2012 GM Volt accident [48]).

- Electrical abuse: it can be caused from overcharging (2015 Bus in China [49]), where excessive lithium intercalation originated a lithium dendrite at the surface of the anode, that can eventually create a bridge to the two electrodes. On the other hand, excessive de-intercalation leads to a collapse of the cathode with heat generation and oxygen release, accelerating the decomposition of the electrolyte. Another source of electrical abuse can be internal short circuit, usually derived from a failure in the separator that makes the two electrodes collide (this was most likely the case of the fire on the 2013 Boeing 787 [50]).
- Thermal abuse: all the above-mentioned abuse scenarios lead to thermal abuse, where overheating leads to failure; in addition, there could be maintenance problems such as expired warranty (fire on 2015 hybrid bus [51]) and faulting connection (fire on 2008 Prius [52]).

All these issues concerning Li-ion batteries temperature dependence raise the need of an efficient dedicated battery TMS that must guarantee high performances on three levels [7]. In fact, overall at pack level, the cells temperature needs to be maintained withing the interval 25°C-40°C, in order to provide the best operational life and performance; at module level, temperature homogeneity needs to be ensured, meaning that the temperature difference between adjacent cells needs to be below 5°C, as otherwise it will create an electrochemical imbalance that deteriorates the performance of the whole pack; similarly, at cell level, the temperature gradient across a single cell should not exceed 3-5°C, to guarantee optimum performance. A more relaxed threshold for acceptable performance and operational life is set at 50°C [8], together with a safety limit to not exceed 60°C under normal operating conditions [9].

On top of these fundamental requests that the battery TMS has to fulfil, a good thermal management system needs to satisfy several requirements, such as being able to safely operate in both hot and cold environments, under high C-rates (current-rate, defined as the charge or discharge current divided by the nominal capacity of battery [53]), and with lower operating power consumption in order not to reduce the range while also keeping low complexity and costs.

2.4. Thermal Management Systems Technologies

Research on this topic has flourished in the past few years, and many different technical solutions have been investigated. Fig. 6 presents a chart displaying the variety of the studied options, which will be discussed in this section.

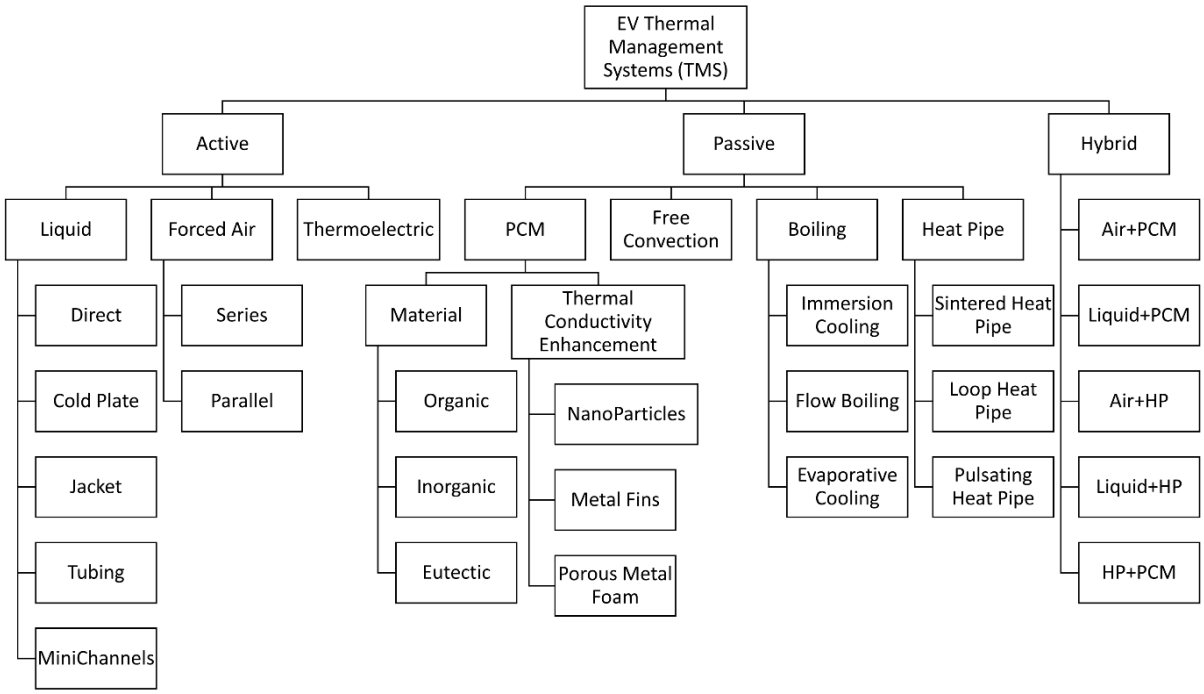

Fig. 6. Breakdown of technological solutions (employed or only investigated) applied as Battery Thermal Management Systems.

2.4.1. Air

The most common TMS solution at the beginning of the EV era was air cooling, chosen for its simplicity and low cost. The working principle can be explained considering a single line of cells, as in Fig. 7a. Generally, air is coming from the environment and thanks to a combination of intakes and fans, it is directed to the battery pack. In other cases, air arrives from the cabin air conditioning (Toyota Prius).

Looking at the single line case, due to heat transfer deterioration of the coolant (air) along the streamline, the last cells will be at higher temperature than the first cells. This happens as air will heat up from the first cell, hence it will be less able to remove heat from the last cells. In order to try to remedy to this issue, wedged channels to increase air speed near the last cells (Fig. 7b) and reciprocating fans at the ends of the channel (Fig. 7c) have been used. However, these strategies increase the amount of parasitic power consumed.

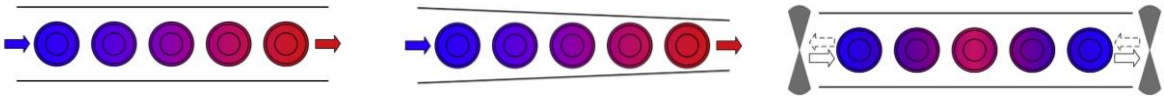

(a) (b) (c)

Fig. 7. Single battery line air cooling; a) simple channel; b) wedged channel; c) reciprocating fans [54].

Extending the same design to a 2D array of cells, as presented in Fig. 8, similar homogeneity problems occur, even with analogous mitigating strategies, such as using a staggered configuration (Fig. 8b) or a trapezoidal duct shape (Fig. 8c).

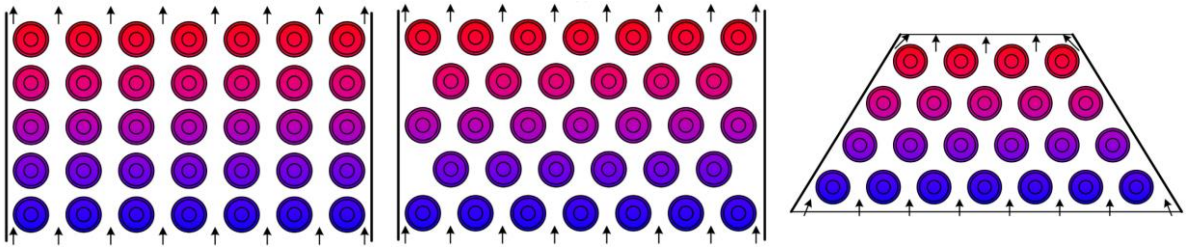

(a) (b) (c)

Fig. 8. Parallel batteries air cooling configurations: a) series-parallel; b) staggered configurations; c) trapezoidal duct [54].

However, the best performance in terms of maximum temperature reduction and temperature homogeneity are presented by the Z or U type flow, employed on Toyota Prius and presented in Fig. 9, where the coolant first goes into a distributor, gets split into equal branches and then exits in a collector.

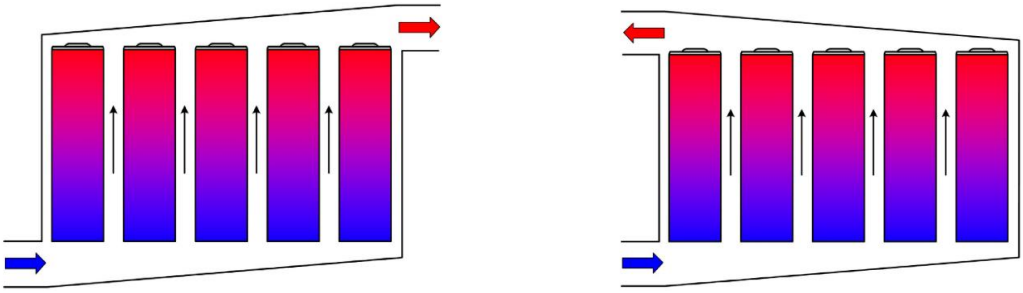

(a) (b)

Fig. 9. Z-type (a) and U-type (b) air parallel cooling [54].

Air TMS can be active or passive, in the sense that the air stream approaching the battery cells could be either heated or cooled beforehand (active air cooling), or it could be used at ambient temperature (passive air cooling) and in this way relaying on environmental conditions. Alternatively, active or passive air cooling can mean forced or free convection, respectively, depending on the presence of fans. Keeping this in mind, active air cooling will

consume parasitic power as fans will be needed to direct the air to the battery pack, especially when the car is not moving, as in the case of charging operations.

The critical point against achieving satisfactory performances with air cooling is the fact that, to provide enough cooling at high discharge or charge rates, either the mass flow rate needs to be increased or the initial airstream temperature needs to be lowered. Both these solutions not only increase the parasitic power, but they also increase the cells temperature difference across the module. On the other hand, if one wants to privilege temperature homogeneity, this will penalise cooling in high demand situations. In other words, this system requires a large amount of air to remove the battery excess heat, which results in bulky ducts and manifolds where the energy consumption and noise produced by the fans is high. Chen er al. [11] compared performance of forced fluid convection with three different medium/configurations: air cooling, mineral oil direct cooling and cold plate with water-ethylene glycol mixture. Comparing results when all cooling methods rejected the same power shows that, at the same temperature rise, ideal power consumption for air is 116mW, for mineral oil is 0.15mW and for the liquid cold plate it is 0.051mW [11]. Hence, due to the presence of fans, air cooling consumes even 10 times more parasitic power, reducing thus the available range.

Despite its poorer performance with respect to liquid, a simple air cooling configuration can be very effective, doubling the lifetime of a battery pack [55]. In fact, research worldwide still considers air cooling as a viable solution, and the investigation is focussing now on the optimisation of the air flow path inside the battery pack, which resulted in the best way to improve the performance [56].

In Table 2, a comprehensive summary of research papers investigating the properties of air cooling applied to the battery TMS for EVs is reported, highlighting year of publication, methods and/or key findings.

Table 2 - Summary of investigation on battery TMS employing air (from the Author's research).

Author	Year	Investigation	Comments/Results
Pesaran [57]	2002	Numerical	Pioneer work on battery cooling for EVs – first time parallel air cooling is considered.
Zolot et al. [58]	2002	Experimental	Work done on the Prius thermal management, feeding air from the HVAC system to the battery pack.
Nelson et al. [59]	2002	Numerical	Air and liquid cooling were compared – liquid resulted in better performances both during heating and cooling.
Jung et al. [60]	2002	Numerical	Overall battery thermal management developed – air cooling considered through CFD simulations
Sabbah et al. [61]	2008	Both	Air only compared with air cooling + PCM-graphite composite – max temp 55°C under 6.6C discharge.
Mousavi et al. [62]	2011	Numerical	Genetic algorithm used for optimization of the smooth tubes design.
Teng et al. [63]	2011	Numerical	Pouch cells; air cooling channels design starting from compact heat exchangers.
Mahamud et al. [64]	2011	Numerical	2D CFD model compared with and a lumped-capacitance model - period of 120s reduces max temp by 72%.
Kruger et al. [65]	2012	Numerical	Co-dependence of air battery cooling and air conditioning – 1 K increase in the cabin when battery cooling is on
Giuliano et al. [66]	2012	Experimental	10°C temperature rise above ambient under 200 A charge-discharge cycles.
Hu et al. [67]	2012	Numerical	Linear parameter-varying model proposed to investigate both cell and small module with U-type air cooling.
Karimi et al. [68]	2013	Numerical	Comparison between air and liquid with a transient 2D model with heterogeneous thermal properties – free convection leads to unacceptably high temperatures
Xu et al. [69]	2013	Both	Battery pack of 48 batteries made by 4 modules - horizontal orientation better depending on environmental temperatures
Park [70]	2013	Numerical	Pressure relief ventilation introduced in a HEV TMS, decreasing the power consumed by the fan
Li et al. [71]	2013	Both	Direct measurement of the internal temperature at multiple locations inside a pouch cell – ΔT over a 7mm thick cell was 1.1°C, hence, to consider when measuring only outside temperature; over the plane variations were of 10°C under moderate charge/discharge.
Li et al. [72]	2013	Both	CFD model validated with wind tunnel feeding into a reduced order model
Fan et al. [73]	2013	Numerical	Parametric analysis on gap spacing between cells and flow velocity – increasing gap increases temperature uniformity
Zhu et al. [74]	2013	Both	Theoretically based thermal model, to predict heat generation, heat dissipation and temperature rise of the single cells within lithium-ion battery pack in Z-type cooling.
Choi et al. [75]	2014	Both	Lumped thermal model for predicting air-cooled Li-Ion battery system for HEV. Homogeneity identified as critical issue.
Kritzer et al. [76]	2014	Experimental	CO_2 from mobile air conditioning used to extinguish thermal runaway through a J-T valve.
Wang et al. [77]	2014	Both	Found an optimum compromise between the cell spacing, their heat generation and the mass flow rate.
Sun et al. [78]	2014	Both	Parallel configuration U and Z types tested. Geometries of inlet and outlet flow ducts play a major role in the uniformity of flow rates of cooling channels.
Severino et al. [79]	2014	Numerical	Optimization process for the battery layout design and thermal management with evolutionary algorithms.
He et al. [80]	2014	Both	2D CFD model coupled with non-intrusive thermometry to replace thermocouples.
Liu et al. [81]	2014	Numerical	Compared to liquid and PCM, air is better in pre-heating at sub-zero temperature.

Yang et al. [82]	2015	Numerical	Increasing the transverse interval leads to the increase of the battery temperature, while it improves the temperature uniformity and reduces the power requirement for both aligned and staggered arrangements.
Wang et al. [83]	2015	Numerical	When ambient temperature is higher than 35°C, flow speed above 1 m/s is required.
He et al. [84]	2015	Both	Actively controlled reciprocating air flow can improve temperature uniformity, reduce the temperature fluctuation of the cells over time, and reduce the total amount of cooling required.
Zhao et al. [85]	2015	Numerical	There is a trade-off between spacing distance between cells and inlet air flow. In warm weather conditions, ambient air is not effective.
Mohammadian et al. [86]	2015	Numerical	New pin fin heat sink to decrease both temperature and standard deviation of the temperature field inside the battery – the height of the pin fin increase linearly in the direction of the air-cooling flow.
He et al. [87]	2015	Both	Combined use of active control and reciprocating flow led to 84% reduced parasitic energy and cooling flow consumption at the cost of a slightly increased temperature rise.
Ling et al. [88]	2015	Both	Hybrid system combining forced air convection and PCM successfully controlled the maximum temperature of the battery pack below 50 °C in cycles at any rates lower than 2 C, even with a 7 °C increase in ambient temperature.
Wang et al. [89]	2016	Both	Controller-based scheme composed of forced convection with monitored battery temperature and regulated by on-board controller - parasitic power reduction by 30% while maintaining almost identical temperature rise.
Tong et al. [90]	2016	Numerical	Faster inlet air and smaller cells distance lowers maximum temperature but increases parasitic power.
Saw et al. [91]	2016	Numerical	Correlation between Nu and Re developed assessing that more air increases heat transfer coefficient and pressure drop.
Chen et al. [11]	2016	Numerical	Compared with other technologies, air cooling does not increase the parasitic power.
Chen et al. [92]	2017	Numerical	Optimization of spacing between cells – larger space between high temperature cells.
De Vita et al. [93]	2017	Both	CFD simulations for both free and forced air cooling and liquid cooling.
Chen et al. [94]	2017	Numerical	Optimization on the size of the inlet and outlet plenum.
Yuksel et al. [55]	2017	Numerical	Impact of regional and drive cycle degradation of a Prius - A simple air-cooling system can double the life estimate of the battery.
Xie et al. [95]	2017	Both	Multi parameter optimization leading to a reduction of 12.82% in maximum temperature reduction and 29.72% in temperature difference.
Situ et al. [96]	2017	Experimental	Air coupled with PCM - 6 m/s of air for optimal cooling.
Hong et al. [97]	2018	Numerical	Secondary vent addition - Maximum temperature reduced by 5K.
Jilte et al. [98]	2019	Numerical	Use of confined passages exhibits lower surface temperature around 3.42–6.19 °C as compared to open flow.
Zhou et al. [99]	2019	Both	Increasing inlet pressure at 3C discharge, reduces max temperature but with a rise in the power consumption.
Han et al. [100]	2019	Both	Delta winglets used as fins for forced air cooling, resulting in increasing turbulence and an inlet temperature difference of 150W/K.
Cheng et al. [101]	2020	Numerical	Multi-objective genetic algorithm applied to a new type of finned forced air TMS, to optimize the thermodynamic, fluid-dynamic and mechanical structure problems.
Chen et al. [102]	2021	Both	Investigation on effect of symmetry and uneven spaces to improve temperature uniformity in the module.

Wang et al. [103]	2021	Numerical	Forced air cooling with aluminium metal foam between cells resulted in temperature reduction compared to only air cooling; however, higher flow resistance and pressure loss thus uneven temperature distribution.
Zhang et al. [104]	2021	Numerical	Spoilers in the airflow distribution plenum of a parallel air-cooling model was proposed. The maximum temperature and maximum temperature difference were reduced by 1.86 K and 2.51 K compared to no spoilers.
Kirad et al. [105]	2021	Numerical	The effect of variation in longitudinal and transverse spacing between batteries on forced air convection performance is evaluated. It resulted that the transverse spacing greatly affects the cooling efficiency.
Zhang et al. [106]	2021	Both	Experimentally validated thermal network used to improve an I-type air cooling, optimising the width of parallel channels and divergent/convergent ducts.

2.4.2. Liquid

Liquid Cooling is currently the most common technology employed in modern EVs. It is the most powerful solution in terms of temperature reduction and homogeneity, given the much higher thermal conductivity and mass heat capacity of liquid coolants with respect to air. Liquid TMS design allows for a more compact battery pack, thus increasing the energy density.

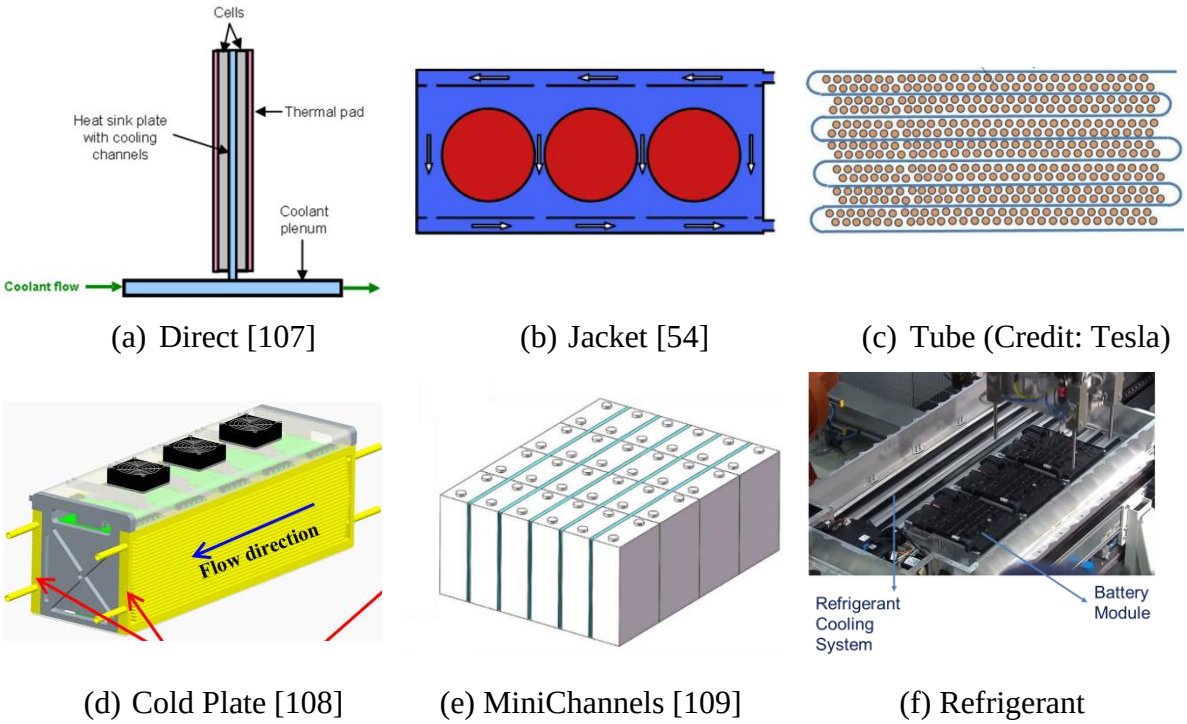

(a) Direct [107] (b) Jacket [54] (c) Tube (Credit: Tesla)

(d) Cold Plate [108] (e) MiniChannels [109] (f) Refrigerant

Fig. 10. Liquid TMS different architectures; (in case a) the heat sink plate replaces the battery cell.

Liquid TMS can be divided into two main categories: direct cooling (Fig. 10a), where the coolant is in actual contact with the battery pack (hence posing important limitations on the dielectric nature of the working fluid), and indirect cooling. A design example for direct cooling is when a plenum duct is placed underneath the battery module and from here the liquid flows in some open ducts (dug into a heat sink plate) while still being in contact with the cell.

Indirect cooling can happen through a variety of configurations, as depicted in Fig. 10, listed below:

- Jacket: it is a coolant filled casing surrounding the module (Fig. 10b).
- Tube: where the coolant is controlled in a bent tube travelling through the cells (Fig. 10c).
- Cold plate: it is a thin-walled metal plate with inbuilt channels for the coolant passage (Fig. 10d).

- Minichannels: where several small diameter channels are dug into metallic plates sandwiched in between the cells (Fig. 10e).
- Refrigerant: when a refrigeration cycle is used (Fig. 10f).

The main design choices are the channel geometry/cross-section, type of configuration, and the working fluid selection. Not only standard thermal properties, such as specific heat and thermal conductivity, need to be maximised to obtain the best efficiency, but also safety aspects such as flammability and sustainability of the working fluid are of paramount importance. Specifically, the working fluid for a liquid TMS for EVs needs to be dielectric, such as dielectric water, silicon-based oil, mineral oil and the recent NOVEC™ 7000, which was developed by 3M™ and has a favourable boiling point of 34°C. Mineral oil has better thermal properties but poorer fluid properties, hence requiring higher pumping power which compromises the range due to the corresponding increase in the parasitic power consumption.

The drawbacks of this technology are in the added complexity given by moving and additional parts such as expansion tanks, valves, pumps, compressors and so on. This reflects in cost increase and weight addition, which hinders the car performance and competitiveness.

The choice between air and liquid TMS (being the two only solutions used in the EV market) can be translated into the choice of either investing in an expensive, heavy but relatively compact liquid system, or a cheap, light but bulky air cooling, due to the requirements of cells spacing to allow proper cooling. This reflects in a choice between energy density and specific power.

Latest research trends on liquid cooling are focused on nanofluids and liquid metals to reduce the cost of liquid cooling systems. At the same time, in order to reduce its energy consumption, combination of refrigeration cycles with an automated control system are foreseen [12].

In Table 3, a comprehensive summary of research papers investigating the properties of liquid cooling applied to the battery TMS for EVs is reported, highlighting year of publication, methods and/or key findings.

Table 3 - Summary of investigation on battery TMS employing liquid (from the Author's research).

Author	Year	Investigation	Comments/Results
Nelson et al. [59]	2002	Numerical	One of the first works on liquid/air comparison stating that liquid works better in both heating and cooling.
Pendergast et al. [110]	2011	Experimental	Panasonic cell developed to work underwater.
Jarret et al. [111]	2011	Numerical	Optimization of a single cold plate - optimum design for lowest temperature is almost identical to that for lowest pressure drop.
Parrish et al. [112]	2011	Experimental	Cooling loop for Chevy Volt, made by water and glycol with fins addition.
Teng et al. [107]	2012	Numerical	Direct liquid cooling has advantages over indirect liquid cooling regarding the battery thermal management. However, there is a trade-off between packaging and so on.
Karimi et al. [68]	2013	Numerical	Comparison between air and liquid with a transient 2D model with heterogeneous thermal properties – free convection leads to unacceptably high temperatures.
Xun et al. [113]	2013	Numerical	Multi-dimensional model to investigate the effect of the cooling channel design on the discharge processes.
Jin et al. [114]	2014	Experimental	Oblique minichannels liquid cold plate - heater surface temperature below 50 °C with low flow rates of 0.1 l/min and 0.9 l/min for heat loads of 220W and 1240W respectively.
Hamut et al. [115]	2014	Numerical	Exergoeconomic analysis for optimizing a hybrid liquid (for the battery) and air (for the cabin) TMS.
Chen et al. [116]	2014	Experimental	Water glycol bath used to control a prismatic cells pack temperature
Mohammadian et al. [117]	2015	Numerical	Internal cooling using electrolyte as coolant inside rectangular microchannels in the electrodes – it decreases the standard deviation of the temperature field inside the battery more than 5 times compare to external cooling at the pumping power of 0.024 W.
Huo et al. [118]	2015	Numerical	Lattice Boltzmann method to estimate the effect of Al2O3 water nanofluids – thermal efficiency improved.
Huo et al. [119]	2015	Numerical	Minichannels cold plate - higher number of channels leads to lower temperature; best performances happened when flow is directed close to the electrode.
Panchal et al. [120]	2016	Experimental	Liquid cold plates tested for different discharge rates – max T (42.3 °C) was for 4C at 35 °C and the lowest maximum average temperature (13.3 °C) was for 2C at 5 °C.
Basu et al. [121]	2016	Both	In addition to liquid channels, aluminium metal barriers used between liquid and cells in order to reduce the temperature non-uniformity.
Panchal et al. [122]	2016	Both	Heat generation increases with the discharge rate; for high discharge rate and low temperature boundary condition there is the highest heat generation rate.
Smith et al. [123]	2016	Experimental	Different cold plates tested and it was found that the best compromise between thermal performance, energy consumption, and vehicle integration is a simple U-flow.
Lan et al. [124]	2016	Numerical	Aluminum minichannels - the more minichannels are used, the better cooling performance can be achieved, though the inlet flow speed is reduced accordingly; alternating inlets and outlets is not beneficial.
Yang et al. [109]	2016	Numerical	Jacket cooling with liquid metal – needs to use heavier materials for the channels and higher density (6x).
Qian et al. [125]	2016	Numerical	Minichannels - more channels in the cold plate increase the performance, but after 5 the increase in negligible.

Chen et al. [11]	2016	Numerical	Compared with other technologies, mineral oil liquid cooling provides the minimum temperature but the maximum temperature uniformity.
Rao et al. [126]	2016	Numerical	Minichannels liquid cooling coupled with PCM – temperature kept 15°C lower than with PCM only.
De Vita et al. [93]	2017	Both	CFD simulations for both free and forced air cooling and liquid cooling.
Zhang et al. [127]	2017	Experimental	Aluminum flat tube and flexible graphite surrounding cells - flat tube minimizes flow rate with respect to cold plate; flexible graphite helps to improve the temperature uniformity.
Rao et al. [128]	2017	Numerical	Channels dug into aluminium blocks sandwiched between cells – changing the block volumes changes the contact surface but it depends on the mass flow rate.
Xu et al. [129]	2017	Numerical	Water and ethylene glycol in minichannels in aluminium plates to prevent thermal runaway due to nail penetration spreading - even with 10L/min of flow rate, it is not enough to prevent thermal runaway.
Bahiraei et al. [130]	2017	Experimental	Two Liquid water cooling methods tested - smaller Re number better for low temperature distribution.
Mondal et al. [131]	2017	Numerical	Six different coolants investigated, H20 and EthylenGlycol-H2O with 1% and 4% of Al_2O_3 nanoparticles. Pure Water was always better, since it has higher thermal conductivity.
Ramotar et al. [132]	2017	Both	Thermal equivalent circuit model for the entire battery system including dynamically varying environment, cells, engine compartment at the front of the box, underbody of the vehicle and the radiative properties of the road surface.
Tian et al. [133]	2018	Experimental	Comprehensive TMS model of motor/battery pack/cabin for an EV with waste heat recovery cycles – extended driving range by 32%.
Cen et al. [53]	2018	Experimental	Battery pack cooled via the AC cooling system – temperature always below 35°C.
Zhao et al. [134]	2018	Numerical	Mathematical model divided in 3 sub models: Li-ion battery, aluminium wavy channel, coolant. Maximum temperature is 35°C and 1°C spreading even at 5C rate of discharge.
Jiaqiang et al [135]	2018	Both	Rectangular channels in cold plate with water as working fluid.
Saw et al. [136]	2018	Both	Mist cooling - 5g/s of mass flow rate with 3% mist keeps temperature below 40°C for 3C discharge rate. Power savings up to 45%.
Chowdhury et al. [137]	2018	Both	Three thermal loops in a fiat 500 EV: cabin air conditioning loop, battery heating/cooling loop, motor cooling loop. R134a is used as refrigerant. Range improvement of 18%.
Park et al. [138]	2019	Both	Refrigerant-cooled active TMS developed and it showed excellent cooling performance within the wide ambient temperature range of 20–40 °C because of its low dependency on ambient temperature.
Zhao et al. [139]	2019	Numerical	Aim to reduce non-uniformity - Two approaches: multiple short channels and orderly magnified contact areas leading to maximum temperature differences 5C discharge of 2.2 K and 0.7 K, respectively.
Panchal et al. [140]	2019	Experimental	Experimentally investigated constant current release rates of 1 C and 2 C and ambient temperatures of 35 °C, 25 °C, 15 °C, and 5 °C using water.
Chung and Kim [141]	2019	Numerical	A new structural design for the large-scale battery pack is suggested to enhance temperature uniformity of the battery pack minimizing the increase in system volume, weight, and pressure drop.
Hong et al. [142]	2020	Experimental	Comparison refrigerant cycle vs liquid as working fluid in cold plate. Refrigerant cooling kept temperature below 45 °C even under harsh environmental conditions. Refrigerant cooling provides 16.1% higher battery capacity and 15.0% lower internal resistance compared with the liquid cooling under harsh environmental conditions

Shen and Gao [143]	2020	Both	Liquid cold plate with refrigerant. Performance is limited by the evaporation temperature of the refrigerant.
Wiriyasart et al. [144]	2020	Numerical	CFD work on nanofluids flowing in minichannels. Cooling performance is improved by 28% compared to not having nanofluids. However, pressure drops are increased.
Monika et al. [145]	2021	Numerical	Mini-channel cold plate investigate via COMSOL. Found that 5 minichannels 4mm wide running water with $\dot{m}$ of 0.003 kg/s at 25°C is the ideal trade off for heat transfer and pressure drop.
Akbarzadeh et al. [146]	2021	Both	Hybrid TMS with liquid cold plate embedded in PCM, giving 30% less power consumption compared to aluminium cold plate. Moreover, it can delay the temperature drop during cold parking, hence reducing the energy needed for the active heating.
Tang et al. [147]	2021	Both	Support regression model to improve implementation of liquid B TMS and heat pumps for the HVAC system.

2.4.3. Phase Change Materials

The technical solution that was investigated the most but not yet employed in EVs, is the use of Phase Change Materials (PCM). PCM is a general term referring to a material that accumulates or release energy by undergoing a phase change, taking advantage of the steadiness of temperature during this process. For EV thermal management applications, PCM usually refers to solid materials undergoing liquefaction and vice versa.

Applied to battery TMS, the working principle is as follows. During discharge, heat is removed firstly due to sensible heat in the solid, then is removed thanks to latent heat during the phase transition from solid to liquid. The same heat can be reversed to the cell for heating purposes, preventing the cell to reach low temperatures. The main benefit is that it is a passive technology, where no moving parts or additional electrical power is required, hence no need of maintenance and low parasitic power consumption. An example of application of PCM to a battery module is presented in Fig. 11, where the PCM bricks are sandwiched between the cells.

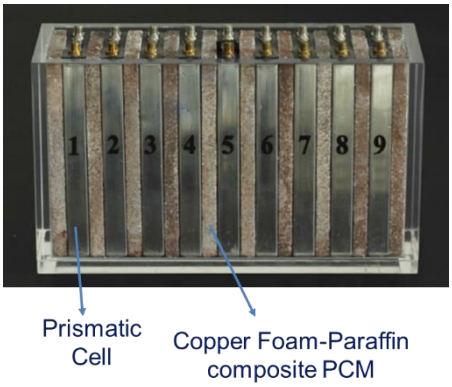

Fig. 11. Example of PCM application on a battery module, where prismatic cells are sandwiched between copper foam/paraffin composite PCM bricks (modified by [148]).

There are three types of PCM materials: organic, inorganic and eutectic [149]. Organic PCM are usually stable, possess good heat of fusion (greater than 180 kJ/kg) and suitable operative temperature range (15-45°C). However, they can be toxic and flammable and usually characterized by low thermal conductivity (0.1-0.35W/m K). Examples of organic PCM are fatty acids and paraffin, with the latter being the most investigated for EV thermal management as its melting point is between 26-28°C. Inorganic salts comprehend hydrated salts and metals; they provide safe operation and high latent heat (above 220kJ/kg) and wide temperature range (5-130°C). On the other hand, they are unstable in the long term and in the case of metallic PCMs present good thermal conductivity (15 W/m K), but they are costly and heavier. Eutectic

mixtures contain of organic and inorganic compounds at specific atomic ratio of products at which the mixture melts as a whole. For further information on the application of PCMs on thermal management for automotive, please refer to the comprehensive review paper by Jaguemont et al. [149].

From [149] it emerges that in order to design an efficient TMS, the most important parameters to select are the materials, specifically looking at latent heat of liquefaction and melting temperature, with the latter targeted to be in the desired operative range of the battery. When creating the PCM material, the length of the fibres, need to be considered as well, as shorter fibres are better as longer cannot reject heat in a uniform way. Another important design parameter is the element thickness, as increasing the mass of the PCM will delay the phase change completion, hence allowing for more heat storage but it also increases weight and cost, de facto reducing EV performance. In fact, once the phase change is completed and the PCM is fully liquid, its thermal performances are seriously deteriorated leading to an ill-performing TMS. Therefore, even though this is categorized as a passive solution, there is still the need for an additional cooling solution to remove the excess heat from the PCM, in order to keep the TMS operational.

Unfortunately, PCM present some intrinsic drawbacks such as the fact that the mechanical design needs to consider the volume changes associated to the phase change (which degrade the mechanical properties of the battery pack), low heat transfer surface available to the ambient and safety aspect (e.g., paraffin flammability) [9]. Moreover, as mentioned, it is not fully independent, in the sense that a way to remove the excess stored heat is needed.

But the biggest drawback lies in the low values of thermal conductivity, which slows the adaptation to high-demand applications. In fact, low thermal conductivity causes PCM to have slower regeneration times and therefore are not effective in applications characterized by quick discharge and charge. A mitigating strategy could be to initially design the TMS to have suitable performance in severe operations, but hence resulting in a waste of materials and inefficient weight increase, through most part of the vehicle operational life. However, techniques for improving the thermal conductivity have been sought, such as the addition of conductive nanoparticles, metal fins or the use of porous materials [150], [151]. These methods can increase the thermal conductivity by two orders of magnitude with respect to their original values, at the cost of a latent heat reduction.

In Table 4, a comprehensive summary of research papers investigating the properties of PCM applications to the battery TMS for EVs is reported, highlighting year of publication, methods and/or key findings.

Table 4 - Summary of investigation on battery TMS employing PCM (from the Author's research).

Author	Year	Investigation	Comments
Al-Hallaj and Selman [152]	2002	Numerical	First work done on PCM application for EV thermal management.
Khateeb et al. [153]	2004	Numerical	PCM employed on electric scooter.
Khateeb et al. [154]	2005	Experimental	Validation of PCM employed on electric scooter.
Kizilel et al. [155]	2008	Experimental	PCM embedded in graphite for power application thermal management – showed potential for weight and parasitic power consumption reduction
Sabbah et al. [61]	2008	Experimental	PCM+graphite used in demanding applications – cell temperature kept below 55°C under 6.6C discharge
Kizilel et al. [156]	2009	Numerical	PCM showed potential for good temperature homogeneity and to contain the spreading of thermal runaway
Duan et al. [157]	2010	Experimental	Two designs investigated for PCM TMS – PCM cylinder and PCM jacket
Rao et al. [158]	2011	Both	3D numerical model coupled with heat generation rate deriving from in-house experiments to characterize the efficiency of a PCM based TMS when either thermal conductivity or latent heat is privileged
Li et al. [81]	2014	Numerical	Comparison between different TMS solutions – PCM resulted best for temperature homogeneity
Ling et al. [159]	2014	Both	PCM with too low or too high melting temperature are not suitable for EV TMS – melting point should be between 40°C and 45°C
Javani et al. [160]	2014	Numerical	PCM surrounding the cell changing the thickness - the thicker the PCM, the lower the maximum temperature but the higher the temperature distribution.
Qu et al. [161]	2014	Both	2D transient model for PCM thermal management and validated via experiments
Javani et al. [162]	2014	Both	PCM with nanoparticles and nanotubes – obtained correlations for heat exchanger design
Li et al. [148]	2014	Experimental	Comparison between free convection, pure PCM and copper foam-PCM composite – the latter resulted in the lowest battery temperature and most uniform temperature distribution in the cell pack.
Wang et al. [163]	2015	Experimental	Paraffin embedded in aluminium foam - thermal conductivity of the composite PCM 218 times larger than pure paraffin
Schweitzer et al. [164]	2015	Both	Simple 0-D model that worked fine till 2C discharge rates, then diverged from the experimental data.
Ling et al. [88]	2015	Both	Hybrid system combining forced air convection and PCM controlled the maximum temperature of the battery pack below 50 °C in cycles at rates lower than 2 C, even with a 7 °C increase in ambient temperature.
Greco et al. [165]	2015	Numerical	PCM+graphite composite was able to reduce the maximum temperature and skin temperature from respectively 75°C to 45.9°C and 61°Cto 31.1°C compared to forced convection
Rao et al. [166]	2015	Experimental	PCM paraffin/copper - when ambient temperature was 29°C and 33°C, maximum temperature was 41°C and 42°C, and the local temperature difference was 3°C and 4°C.
Lin et al. [167]	2015	Both	In addition to paraffin PCM, they used graphite sheets in the middle of the cells - Maximum temperature differences within the module less than 5°C during 1C and 2C-rate discharges
Zhao et al. [168]	2016	Experimental	PHP and expanded graphite paraffin tested for charge and discharge different levels, inclinations and heating powers.

Wang et al. [169]	2016	Experimental	Copper and acetone PHP coupled with paraffin PCM - Start-up temperature of PHP should be lower than melting point of PCM.
Hussain et al. [170]	2016	Experimental	Nickel foam-paraffin composite - surface temperature is reduced by 31% and 24% as compared to natural air and pure paraffin under a 2C discharge rate;
Wu et al. [171]	2016	Experimental	Ternary PA/EG/copper mesh PCM plate with fins - at discharge rate of 5C, 4°C reduction using the ternary PCM instead of normal PCM
Rao et al. [126]	2016	Numerical	Hybrid minichannels liquid PCM - PCM only is 15°C higher temperature than PCM and liquid
Moraga et al. [172]	2016	Numerical	The use of a three layers PCM set can contribute to enhance the thermal management system because the battery cooling can be implemented in a progressive way, layer by layer
Jiang et al. [173]	2016	Both	Composite PCM with expanded graphite, with varying graphite composition - EG gives better performances with respect to air and liquid cooling
Yan et al. [174]	2016	Numerical	A composite board made of three parts (heat conducting shell, an insulation panel and PCM) is proposed, aiming to enhance temperature uniformity and heat insulation. Four cases tested: no space; heat sink only; composite board; enhance PCM.
Wu et al. [175]	2017	Numerical	Investigation on graphite mass fraction to improve performance in EV - higher mass fraction o can increase the thermal conductivity and lower the phase change enthalpy and the use of a graphite sheet can help contain thermal runaway.
Situ et al. [96]	2017	Experimental	Quaternary PCM and coupled with air cooling - thermal conductivity enhanced; 6 m/s optimal $\dot{m}$ air.
Wang et al. [176]	2017	Both	Cylindrical battery cell with paraffin PCM. The battery had fins submerged in the PCM.
Mortazavi et al. [177]	2017	Numerical	Multiscale numerical simulations to investigate the influence of paraffin composite on TMS for Li-ion batteries - the fabrication of the paraffin nanocomposites does not yield significant improvement
Zhao et al. [178]	2017	Experimental	Heat Pipes embedded in PCM - the HP can extend the time of phase transition process for PCM in dynamic process of heat storage and release
Huang et al. [179]	2018	Experimental	PCM to remove and store heat from the battery; evaporator of a HP inside the PCM to remove heat from it; forced convection to the condenser of the HP – improvement with respect to PCM only but worsening of the temperature homogeneity
Arora et al. [180]	2018	Experimental	Investigation on battery orientation with PCM cooling, plus a coupled TEC system to generate electricity by recovering waste heat - inverting the battery orientation along the pack increases the performance of the PCM during extremely demanding operations
Ling et al. [181]	2018	Experimental	Two PCMs, one with high thermal conductivity and one with low thermal conductivity. Cold testing conditions - the lower thermal conductivity allow for slower cooling down period, but it is not suitable for the thermal management of the pack as it does not maintain homogeneity.
Hussain et al. [151]	2018	Experimental	Investigation on the performance of graphene coated nickel foam saturated with paraffin wax - it improved the thermal conductivity of the pure paraffin by 23 times
Zhang et al. [150]	2018	Experimental	The kaolin/EG/paraffin ternary composite prepared can enhance the thermal conductivity of paraffin by more than 20 times. The maximum temperature of the battery at different discharge rates was reduced by about 13.4% (2C), 20.76% (3C) and 27.74% (4C).
Qin et al. [8]	2019	Both	Hybrid TMS with PCM and air cooling. Temperatures are maintained between acceptable ranges even at 4C.

Lv et al.[182]	2020	Experimental	PCM is serpentine shape rather than blocks. Coupled with forced air cooling, achieved 2.3°C temperature reduction from block configuration and increase in energy density by 13.8Whkg-1.
Landini et al. [183]	2020	Experimental	PCMs integrated with Direct-Metal-Laser-Sintered aluminium heat exchangers (HEX) as a passive TMS, employed to enhance the equivalent thermal conductivity and thermally connect the cells to PCM.
Wu et al. [184]	2020	Numerical	Hybrid TMS with bottom minichannels cold plate, side heat spreading plates and PCM sandwiched between cells. Comparing to liquid cooling without PCM, the max temperature and temperature difference are reduced by about 43% and 38 %.
Chen et al. [185]	2020	Numerical	Comparison between air and PCM cooling on battery cycle life. Air cooling has a lower cyclical cost (newly proposed index) than PCM cooling.
Heyhat et al. [186]	2020	Numerical	Comparison between enhancement methods for PCM: nanoparticles, fins and porous metal foam. Results showed that the best performances are with porous metal foam.
Safdari et al.[187]	2020	Numerical	Three PCM shapes investigated, coupled with forced air flow, hexagonal, circular and rectangular. Last one best for high rate of charging.
Joshy et al.	2020	Experimental	Study on effect of vibration on a PCM TMS, using frequency of 20-30 Hz, typical of PHEV. Results showed increasing temperature trend with increasing vibration frequency.
Patil et al. [188]	2021	Experimental	Pouch cell immersed in flowing dielectric fluid assisted with tab cooling showed gave 46.8% lower maximum temperature compared to natural convection at 3C discharge rate.
Liu et al. [189]	2021	Numerical	Hybrid system coupling PCM/copper foam with helical liquid channels is proposed and results shows it can reduce temperature compared to free convection by 30K.
Landini et al. [190]	2021	Experimental	Effect of mass and geometry studied on a Direct-Metal-Laser-Sintered filled with PCM. Compared to free convection at 3C, proposed TMS reduces the max temperature by 5°C.

2.4.4. Boiling

In this section, the term “boiling” is used to refer to different technologies found in literature, sometimes referred to as boiling: direct two-phase liquid cooling, liquid to vapour PCM, evaporative cooling, immersion cooling, pool boiling and flow boiling. In general, it exploits the latent heat during the phase transition from liquid to vapour allowing for cooling capacities substantially beyond that of conventional methods. Furthermore, it provides excellent thermal homogenisation, as it happens irrespective of heat fluxes but at a fixed temperature for a given pressure. As with PCM, it does not need moving parts or additional electrical power, hence in this review it is considered as a passive technology (exception made for the flow boiling case, which needs a pump for flow circulation). Evaporative cooling happens when a thin liquid film evaporates since it is in direct contact with the surface to be cooled down; Boiling Immersion Cooling (BIC) is another term to describe pool boiling, where the cell is entirely or partially submerged in a stagnant liquid pool. Flow boiling instead happens when boiling conditions arise in a moving stream inside a duct or pipe [191].

From the example schematic presented in Fig. 12, the battery cell/module is represented by the heater placed in an enclosed control volume where the liquid partially or entirely covers the cells surface, absorbing heat from it and starting to boil. The vapour originated from this process is then cooled down in an external condenser and then fed back to the control volume. Therefore, in a similar fashion to PCM, boiling TMS might need an external source of cooling in case free convection is not enough for the complete condensation of the vapour.

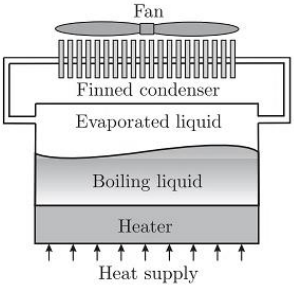

Fig. 12. Boiling working principle and design schematic [192].

The most used fluid is NOVEC™ 7000 developed by 3M™, thanks to its suitable thermal properties such as melting point of 34°C and high latent heat (142 kJ/kg) and more importantly for its dielectric nature [16]. In the graph of Fig. 13, the boiling curve is described, in which the slope of the curve represents the heat transfer coefficient. Thus, the steeper the curve, the higher the heat transfer coefficient. It is therefore evident that the operating condition to be sought is nucleate boiling, which is characterized by a series of bubbles detaching from the

heated surface. Here, heat is removed not only by the bubble formation and growth (hence through latent heat), but also because when the bubble leaves the surface it leaves a gap that the liquid fills, thus creating a convective motion that greatly enhances the heat transfer.

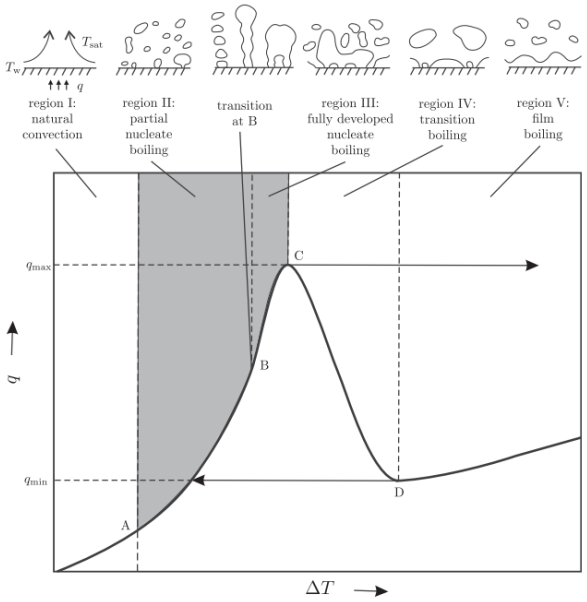

Fig. 13. Typical boiling curve, showing qualitatively the dependence of the interface heat flux (q) on the surface superheat (ΔT), defined as the difference between the solid surface temperature and the saturation temperature of the liquid [193].

In order to achieve this operating condition, the system pressure must be controlled, since a pressure increase or decrease induces an increase or decrease of the saturation temperature, hence a change to the entire boiling process.

The most important design parameters are the fluid selection, in terms of latent heat, boiling point and other physical properties. The immersion percentage needs to be considered as it influences the boiling performance but also the weight and the cost of the system. Finally, the system pressure needs to be controlled, as the variation of the pressure will change the boiling point of the fluid.

The drawbacks of this technology are that it is difficult to control; the working fluid increasing the costs and weight and that, as the PCM, it is not independent as it needs an additional source of cooling for the condenser.

Latest research on this type of cooling considers the use of nanofluids [194], new configuration such as hydrogel [195] and flow boiling in minichannels [196]. In Table 5, a comprehensive summary of research papers investigating the properties of boiling applied to the battery TMS for EVs is reported, highlighting year of publication, methods and/or key findings.

Table 5 - Summary of investigation on battery TMS employing boiling or evaporation solutions (from the Author's research).

Author	Year	Investigation	Comments
Van Gils et al. [192]	2011	Numerical	Numerical model in which they made a control law based on the system pressure to suppress/stimulate boiling.
Hirano et al. [16]	2014	Experimental	Battery module with porous materials in between cells – NOVEC™ 7000 used as working fluid gave great results compared to air cooling.
Zhao et al. [197]	2014	Experimental	Sodium polyacrylate hydrogel used on normal discharge tests and also penetration tests. Performances compared with standard cooling technologies such as free and forced cooling air cooling and PCM
Van Gils et al. [15]	2014	Experimental	Boiling setup with NOVEC™ 7000 - Temperature differences between positive and negative pole of the battery of approximately 0.7°C are observed in the non-boiling regime, while these temperature differences are eliminated when the liquid around the battery starts boiling.
Zhang et al. [198]	2014	Both	Sodium polyacrylate hydrogel - Battery pack equipped with the hydrogel TMS exhibits a lower capacity fading rate (2.07 mAh/cy) compared to the high fading rate (6.08 mAh/cy) of the battery pack in ambient condition
Zhao et al. [199]	2016	Both	A hydrogel based TMS used to successfully prevent thermal runaway.
Ren et al. [195]	2017	Experimental	TMS based on sodium alginate hydrogel – temperature increase with the proposed TMS is 3.8°C lower.
An et al. [196]	2017	Experimental	Flow boiling in minichannels dug into metallic plates between cells – temperature always kept below 40°C
Al-Zareer et al [200]	2017	Numerical	Propane has been used both as coolant both as fuel to power the ICE for the hybrid vehicle - Covering 30% of the battery length by saturated liquid propane keeps the temperature below 34°C
Al-Zareer et al. [201]	2018	Numerical	Same layout as above - Tested discharge rates of 6C and 4C, discovering that it is possible to keep it below 49°C and 35°C when the battery is covered by 15% and 5% respectively.
Al-Zareer et al. [202]	2019	Numerical	Stationary boiling in aluminium tubes – improved temperature homogeneity compared to direct contact boiling.
Wang et al. [203]	2020	Both	NOVEC™ 7000 flowing and surrounding the module. Max temperature was 35.1°C with 0.3 m/s inlet velocity and 5C discharge. Re uniformity, temperature difference of 3.71 °C found at 5C discharge rate and 0.1m/s.
Zhao et al. [204]	2021	Both	Air-based BTMS is modified by integrating a direct evaporative cooling (DEC) system. Investigation on the effect of the relative humidity in the cooling performance.
Devahdhanush et al. [205]	2021	Numerical	Dielectric fluid Novec7100 used in a subcooled flow boiling TMS targeted to fast charge cables.
Fang et al. [206]	2021	Experimental	R1233zd(e) flow boiling in minichannels heat sink. Studied effect of mass flux – dependency becomes important after 30kW/m^2. Also verified predictive method reported in literature.

2.4.5. Heat Pipes

As for the PCM, heat pipes have been investigated but not yet employed for EV thermal management, even if they have been widely implemented in electronics and space applications. Originally introduced by R.S. Gaugler in 1942, heat pipes are a passive technology where the fluid motion is ensured by a combination of pressure gradients, capillarity and/or gravity. Heat is removed by a combination of liquid to vapour (evaporation) and vapour to liquid (condensation) phase change as well as by conduction from the bulk liquid movement.

The term heat pipe is a general term referring to a family of devices, which comprises of, for example, standard sintered Heat Pipes, Loop Heat Pipes and Pulsating Heat Pipes.

Standard sintered Heat Pipes (HP) are sealed evacuated devices encapsulating a porous structure (called *wick*) that runs along the whole length of the device in the vicinity of the walls of the solid enclosure. The working principle is as follows (Fig. 14): heat is applied to one end of the HP, called evaporator, and the working fluid turns into vapour. This then flows (thanks to the pressure gradient generated by the boiling process) to the other end, called condenser, which is in contact with a cold source, hence condensation occurs and heat is rejected. Finally, the newly generated liquid from the condensation process flows into the wicked walls by capillary action, all the way back to the evaporator, and thus the cycle is closed and repeated. Standard sintered heat pipes are an established technology (TRL 9).

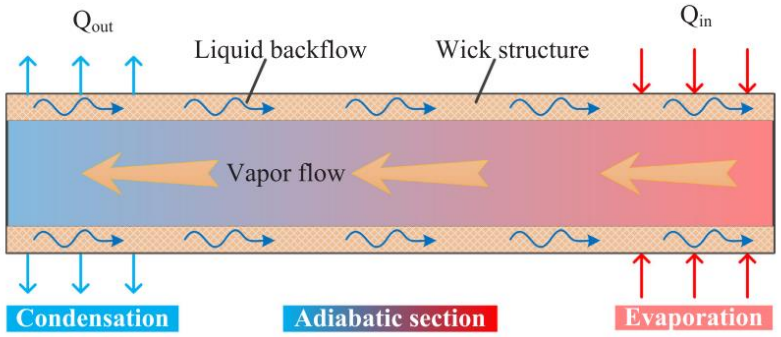

Fig. 14. Heat pipe structure and working principle schematic [207].

The Loop Heat Pipe (LHP) is characterized by having the wicked structure in the evaporator only, allowing for heat transfer over longer distances at reduced costs of a same dimension HP (as the wick is the most expensive part). As described in Fig. 15, a LHP consists of five main components:

- the evaporator, where the wick is situated, providing the pressure gradient necessary for the evaporated working fluid to travel through the entire device;

- the vapour and liquid lines, responsible for the transportation of the working fluid in its corresponding two states;
- the condenser, which can come in different shapes and designs, as long as it releases the heat that the evaporator absorbs;
- the compensation chamber, that has the twofold function to supply the evaporator with working fluid in case of dry-out and to balance the pressure differences throughout the operations.

The LHP, thanks to its evaporator structure, can operate regardless of the gravity orientation and also it behaves as thermal diode.

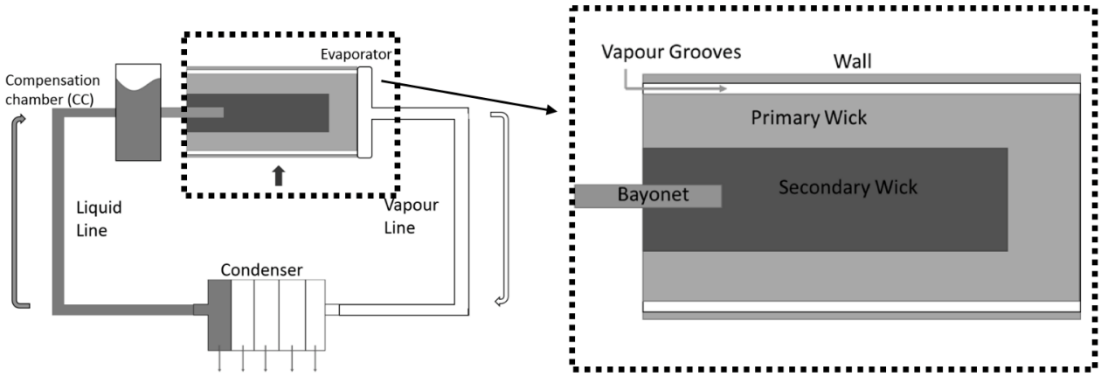

Fig. 15. LHP schematic and magnified evaporator with highlighted components [208].

The Pulsating Heat Pipe (PHP) is an evacuated and sealed meandered tube partially filled with a working fluid (Fig. 16), where the pipe inner diameter is under the critical capillary threshold, that allows surface tension to be dominant with respect to gravity [209]. This causes the fluid to settle in an alternation of liquid and vapour elements, called liquid slug and vapour plug (following the terminology used by [210]). When heat is applied to the evaporator, vapour plugs expand thanks to the evaporation of the liquid film surrounding them, consequently pushing liquid slugs in the direction of the condenser. There, in contact with the cold source, heat is rejected and the vapour bubble shrinks, thus creating the characteristic spring-like pulsating motion responsible for the heat transfer in such devices. As the previous discussed passive technologies, they are not independent, in the sense that they need a way of removing heat at the condenser.

The most important design parameters are the working fluids and piping materials combinations. The design of the evaporator and the condenser also needs to be tailored to satisfy the requirements of the different applications.

The drawbacks for heat pipes are given by the lack of technological maturity regarding both LHP and PHP, in fact they have not been widely employed nor produced in large scale. Moreover, their design still needs an additional cooling source at the condenser, similarly to the other two passive cases. However, their heat transfer capability of these two technologies for long distances, allows for more flexibility in the design phase of a TMS.

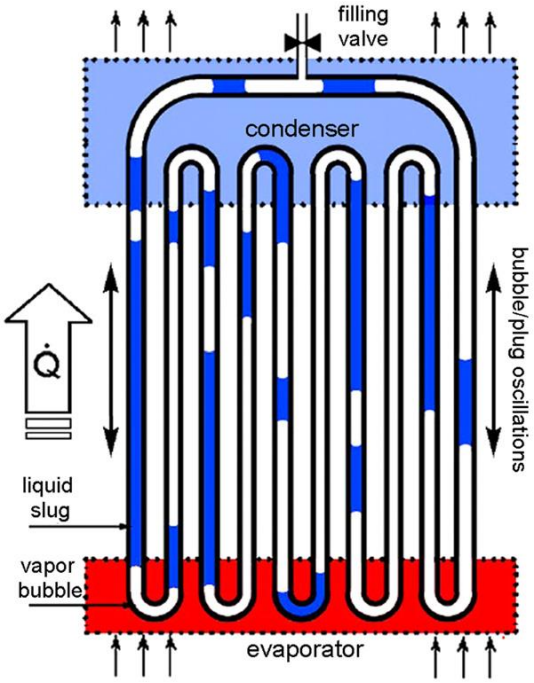

Fig. 16. Schematic of a PHP [211].

Lastly, a new member of the heat pipe has emerged, the Vapour Chamber (VC), which schematic is presented in Fig. 17. A vapour chamber is a thin-flat heat pipe, mostly used to transfer heat from a localized heat source and to spread it to a much larger area. In these devices, heat is applied at the bottom and the wick structure is placed at both bottom and top inner surfaces, connected by vertical columns, which allow passage to the condensed liquid [212].

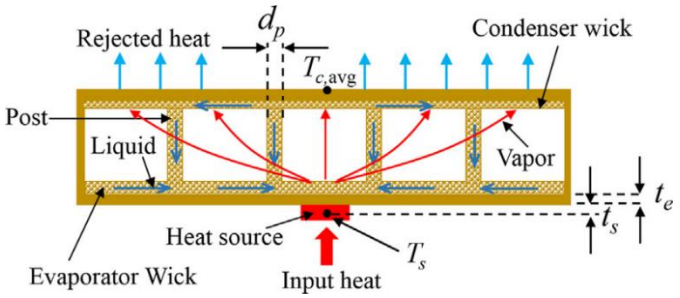

Fig. 17. Vapour chamber schematic [213].

In Table 6, a comprehensive summary of research papers investigating the properties of different types of heat pipes applied to the battery TMS for EVs is reported, highlighting year of publication, methods and/or key findings.

Table 6 - Summary of investigation on battery TMS employing heat pipes of different types: HP – standard Heat Pipes; TS – thermosiphons; PHP – Pulsating Heat Pipe; LHP – Loop Heat Pipe; VC – Vacuum Chamber (from the Author's research).

Author	Year	Investigation	Type	Comments
Wu et al. [214]	2002	Both	HP	HPs used to cool down a large battery - at discharge current 10 A, the temperature increases and reach 65°C; difference between maximum and minimum temperatures at the end of discharge is around 20°C.
Jang et al. [215]	2010	Experimental	TS	TS used to transfer heat from space in between the cells to a common radiator cooled down by forced convection.
Rao et al. [216]	2013	Experimental	HP	Condenser of the HP is cooled down via liquid – cell maximum temperature kept below 50°C if the heat generation rate is not above 50W.
Burban et al. [217]	2013	Experimental	PHP	Copper PHP tested with different fluids and with different forced convection conditions at the condenser representing the air velocity relative to the driving cycles.
Greco et al. [218]	2014	Numerical	HP	1D lumped numerical model to analyse the performance of an HP embedded in the TMS for EVs
Wang et al. [219]	2014	Experimental	HP	L-shaped HP sandwiched between cells and partially submerged in a liquid pool - if the cell does not generate more than 10W/cell, temperature can be kept below 40°C.
Tran et al. [220]	2014	Experimental	HP	Different types of condenser cooling applied to the HP at different orientations – amongst free convection, forced convection and chimney cooling where the best was forced convection.
Tran et al. [221]	2014	Experimental	HP	HP cooling compared to heat sink cooling. HP reduced thermal resistance of a common heat sink by 30% under free convection and 20% under low forced convection.
Rao et al. [222]	2014	Experimental	PHP	Copper –acetone PHP directly sandwiched between two adjacent cells. PHP needs to be close to the battery terminal and not horizontal.
Zhao et al. [223]	2015	Experimental	HP	Flat HP for pouch cells cooling. Investigation on the best way of cooling the condenser of the HP – water spray wet cooling was the best.
Ye et al. [224]	2015	Both	HP	HP based cooling targeting 8C fast charging - If air cooled, the HP will be effective at unit level but not at the pack level.
Manno et al. [225]	2015	Experimental	PHP	PHP aimed at automotive/battery cooling however not tested on a battery configuration. Effect of road driving was investigated and, despite good thermal performance, dynamic pitch and roll tests discourage the application to automotive.
Hong et al. [226]	2015	Experimental	LHP	Ultra-thin LHP with big flat evaporator in the middle of the cell. Achieved start-up at 47°C, with minimum thermal resistance was just 0.097 W/K while heat loads ranged from 20 W to 120 W.
Putra et al. [227]	2016	Experimental	LHP	Copper and SS LHP applied to a battery dummy model, working fluids are alcohol, ethanol and water. Very long start-up period due to large thermal mass – it was achieved a thermal resistance of 0.2 k/W.
Ye et al. [228]	2016	Numerical	HP	HP with finned condenser submerged into a flowing liquid channel is used to cool down during 8C fast charging. The best strategy was to delay the cooling of 100s after the charging.
Shah et al. [229]	2016	Both	HP	They inserted a HP in the cell and found that that a 2% decrease in energy density of the cell, given by the encumbrance of the HP, brings a significant cooling benefit.

Liu et al. [230]	2016	Both	HP	Ultra-micro thin HP in between cells –mathematical model implemented in CFD simulations validated through IR imaging.
Zou et al. [231]	2016	Experimental	HP	Integrated system of thermal management comprising cooling and heating by means of a heat pump and HPs L-shaped indies the cell. Different ambient condition -20°C and 20°C. Thermal resistance of the HP is 0.87K/W in cooling and 1.11K/W in preheating.
Zhao et al. [168]	2016	Experimental	PHP	PHP coupled with PCM (graphite/paraffin) for both cell heating and cooling. Adiabatic section of the PHP embedded on the storage PCM tank.
Wang et al. [169]	2016	Experimental	PHP	Copper acetone PHP coupled with paraffin PCM - Start-up temperature of should be PHP lower than melting point of PCM.
Yuan et al.[232]	2016	Both	HP	Heat pipe with fins applied to a single cell. An Aluminum collector plate was employed at the evaporator.
Worwood et al. [233]	2017	Both	HP	HP to minimize the spreading in the radial direction with HP and spreader disk used inside the cell. Good thermal performances but reduction in energy density: for the 18650 cell, the addition of the 3 mm HP and 2 mm spreader discs reduces the cell energy density by 5.8% and increases the cell mass by 11.7%.
Zhao et al. [178]	2017	Experimental	HP	HP embedded in PCM - HP can extend the time of phase transition process for PCM in dynamic process of heat storage and release, and the function of HP can increase the temperature uniformity before the phase transition of PCM is completed.
Huang et al. [179]	2018	Experimental	HP	HP embedded in PCM and cooled down from forced convection – works better for maximum temp reduction but worse for temperature homogeneity
Liang et al. [234]	2018	Experimental	HP	4 copper-water HPs, whose evaporator is submersed into a liquid coolant flow. Start operations at the early working stage of battery increases the non-uniformity of battery temperature. They implemented intermittent cooling, to save power.
Qu et al. [235]	2016	Experimental	PHP	Investigation on flexible PHP reported that bending of adiabatic section had a negative impact due to increase in two-phase flow resistance. Heating wire used instead of battery application, despite the title.
Ye et al. [236]	2018	Experimental	HP	Micro HP array to minimize the temperature variation along the cell - it stays around 1°C.
Huang et al. [179]	2018	Experimental	HP	Tested 3 different TMS: PCM pure; PCM + HP w/air; PCM + HP w/ ethyl alcohol. - after transient cycle tests results were that PCM + HP works better
Chi et al. [237]	2018	Experimental	PHP	PHP sandwiched between cells, bottom liquid cold plate as condenser. A heater used as a simulated battery was sustained under 60°C under 10 W and 14 W heating conditions.
Smith et al. [238]	2018	Experimental	HP	Copper water HP in between cells to minimize temperature distribution. Longer HP to transfer heat to a cold plate cooled down by liquid - dissipate 400 W with maximum temperature of 55°C and +- 5°C across, thermal resistance 0.075 C/W.
Zhou et al. [239]	2018	Experimental	HP	HPs at the centre of battery pack - At 1C-rate discharge, compared to cooling in ambient, the maximum temperature of pack decreases 15°C when a fan is embedded in the centre of pack.
Gou et al. [240]	2019	Both	VC	Novel 3D vapour chamber coupled with water loop – 120% filling ratio is the optimum for this configuration
Wang et al. [241]	2019	Both	HP	HP for cylindrical cells, with some conduction element to improve heat transfer surface – thickness of the conduction elements more important than conduction.

Dan et al. [242]	2019	Both	HP	Investigated effect of air (from free convection to forced convection) on a microarray of HP. Maximum temperature different between the cells < 2°C.
Liang et al. [243]	2019	Both	HP	HPs sandwiched between cells and liquid cooled. The voltage of the battery module decreases and the available capacity decreases by about 0.88%-1.17% with reducing coolant temperature by 10 °C at 5C discharge.
Liu et al. [244]	2019	Numerical	HP	Heat pipes applied to a battery module with air cooling. They found that increasing the air inlet velocity can improve the thermal uniformity of the battery pack, while changing the air inlet temperature doesn't.
Chi et al. [245]	2019	Experimental	PHP	PHP sandwiched inside cells, and condenser inside liquid flow. Average temperature of the heater's surface was maintained at 56.4°C using 14 W with 25°C coolant water
Gou et al. [246]	2019	Experimental	HP	Heat pipe embedded in PCM embedded in the mandrel of battery. 6mm mandrel was found to be best.
Wei et al. [247]	2019	Experimental	PHP	PHP with flat evaporator tested with water, ethanol and their mixtures and applied to a battery pack. Mixtures gave better start-up, and average battery pack temperature was kept below 46.5 °C @ 56 W.
Deng et al. [248]	2019	Experimental	HP	L-shape HP with massive fins compared to free convection. Aluminum plate sandwiched between cell and heat pipe. Improvement of 4.8°C found compared to free convection.
Putra et al. [249]	2020	Experimental	HP	HP sandwiched between PCM and cells; HP decrease the battery temperature by 26.62°C under a 60 W heat load compared to no cooling.
Zhou et al. [250]	2020	Experimental	HP	Combination of immersion cooling (in porous mats filled with flame retardant liquid), HP and air cooling to hinder the spread of thermal runaway. During non-TR operations, maximum temperature was limited to 47°C.
Gan et al. [251]	2020	Both	HP	Feasibility studied with a validated thermal network model. Compared with natural cooling, HP battery temperature reduced by 14 °C in the 5 C discharge rate
Zhang et al. [252]	2020	Experimental	HP	Combination of HP, PCM and forced convection. The highest temperatures under 1C, 3C, and 4C discharge rates are all under 45 °C.
Behi et al. [253]	2020	Both	HP	Experimental comparison of liquid and flat plate HP, which reduced the temperature by 29.9% and 32.6%, respectively, compared to air cooling.
Bernagozzi et al. [254]	2020	Numerical	LHP	TMS Proposed using LHPs and graphite sheet to enhance vertical heat transfer. Numerical results showed potential to reduce parasitic power by one order of magnitude compared to liquid cold plate.
Yuan et al. [255]	2020	Experimental	HP	HP and cold plate coupled. Investigation on effect of effect of how much HP was submersed in liquid.
Jouhara et al. [256]	2020	Experimental	HP	Flat HP (heat mat) applied to a 16cell module. Approximately 60% of the heat generated by the cells was removed by the heat mat.
Lei et al. [257]	2020	Experimental	HP	HP cooled by water spray; At 24 A, maximum temperature and maximum temperature difference drop by 29.2°C and 8.0 °C in comparison to no cooling
Chen et al. [258]	2020	Experimental	PHP	Experimental study on PHP with TiO2 Nanofluids. At ambient temperature of 35 ºC and discharge rate of 1C, the maximum temperature stays below 43ºC
Behi et al. [259]	2020	Numerical	HP	Comparison between free convection, forced convection and HP. Maximum module temperature for forced-air cooling, HP, and HPCS reaches 42.4°C, 37.5°C, and 37.1°C.
Yao et al. [260]	2020	Experimental	HP	Micro heat pipe array used. Managed to contain ΔT of 3.44°C @ 50W. A mild vehicle vibration condition improved temperature uniformity by 3.3 °C at a heat generation rate of 10 W.

Wei et al. [261]	2020	Numerical	HP	Heat pipe sandwiched in cells. Wanting to reduce the uniformity of the battery module, a reciprocating cooling strategy for the liquid water flow at the condenser was introduced and gave reduction of 13.5%.
Zhang et al. [262]	2020	Numerical	HP	Heat and TEG were applied to cell. It was found that for midlevel C-Rates, heat pipe alone was sufficient. For more stringent cases, TEG addition was investigated.
Huang et al. [263]	2020	Numerical	HP	Heat pipe and air cooling. Nonlinear controller for the temperature and to evaluate power consumption.
Kleiner et al. [264]	2021	Both	HP	HPs used for terminal cooling in addition to conventional bottom cooling. Jelly roll temperature decreases by a maximum of 4.3°C.
Liang et al. [265]	2021	Numerical	HP	Numerical investigation of a 168-cell battery pack cooled by a flat-heat-pipe under 5C discharging rate. Maximum temperature and temperature difference are under 50°C and 5°C respectively.
Yao et al. [266]	2021	Numerical	HP	Energy and exergy evaluation of the effect of pre-set temperature on air and HP coupled cooling.
Chen et al. [267]	2021	Numerical	HP	HP coupled with PCM, after an optimization cycle on the thickness of the PCM, numerical results showed a temperature reduction of 30%.
Alihosseini and Shafaee [268]	2021	Both	HP	Using forced convection in the condenser section of the heap pipe, keeps temperature below 40°C, and it also improves temperature distribution.
Abbas et al. [269]	2021	Experimental	HP	Experimental Investigation on combined use of HP and PCM
E et al. [270]	2021	Both	HP	Experimental and numerical investigation on HP and air cooling. Parametric investigation on the spacing.
Bernagozzi et al. [271]	2021	Both	LHP	Experimental investigation on LHP and graphite sheets applied to a module. Compared to liquid cold plate, temperature after 4C max fast charging is 3.6°C lower.
Yue et al. [272]	2021	Experimental	HP	Hybrid cooling with HPs applied to battery module, cooled with forced air and sporadic water sprays. Max temperature with sprays reduced by 21% compared with no sprays.
Behi et al. [273]	2021	Both	HP	With 8C discharge, a forced air-HP sandwich system reduces the temperature from 58°C to 38°C.
Li et al. [274]	2021	Both	HP	Hybrid TMS with liquid cold plate cooling HPs embedded in the battery module. Compared to cold plate only, HPs drop the max temp and the temperature difference by 7% and 11% respectively.
Jiaqiang et al. [270]	2021	Both	HP	HP TMS targeted on central China climate. Optimization on fins layout and forced airflow at the condenser was performed, achieving an average heat transfer coefficient of ~10W/m·K
Mbulu et al. [275]	2021	Experimental	HP	Battery surrogate sandwiched with heat pipes L and I shaped. Maximum temperature kept below 55°C @ 60W, and temperature difference $\Delta T < 5°C$. Liquid flowrate at condenser was varied.
Liang et al. [276]	2021	Experimental	HP	U shaped flat micro heat pipe applied to battery module. It reduced temperature by 16% and ΔT by 60%.
Panahi et al. [277]	2021	Experimental	HP	Micro heat pipe arrays. Results highlighted the importance of the evaporator inclination. Best thermal performance was found to be at an angle of inclination of −15° where in bottom heated mode.
Jouhara et al. [278]	2021	Experimental	HP	16cell module. Tmax was kept below 30°C and 28°C @6C. Temp uniformity across the module stays in a +/-1°C range. Temperature difference across the cells was 6°C and 2°C for horizontal and vertical configurations.
Behi et al. [279]	2021	Both	HP	Multiple heat pipes applied to a single cell and encased in PCM. Max temperatures for natural convection, heat pipe, and PCM assisted heat pipe reaches 56°C, 46.3°C, and 33.2°C, respectively
Karimi et al. [280]	2021	Experimental	HP	PCM and six flat plate HP. Compared to natural convection, 35% temperature reduction, while 15% reduction only using heat pipes.

Chen et al. [281]	2021	Experimental	PHP	Nanofluid PHP used for low temperature heating under continuous heat preservation, obtaining capacity enhancement ratio reached up to 56.6%.
Wafirulhadi et al. [282]	2021	Experimental	HP	Heat pipe coupled with soy wax PCM placed in the heat sink box surrounding the single cell. Maximum temperature reached was 58.3°C, which is quite high considering that the TMS is applied to a single cell.
Zhang et al. [283]	2021	Numerical	HP	Combined liquid, PCM and heat pipe cooling system. Thermal conductivity and thickness of PCM, heat pipe length and the velocity of inlet water have most significant influence.
Zhou et al. [284]	2021	Experimental	PHP	Copper flat plate evaporator PHP. Aimed to fast charging processes. Working fluid is ethanol aqueous solutions of carbon nanotubes. Nanotubes improve the start-up and performances.
Bernagozzi et al. [285]	2021	Experimental	LHP	LHP and graphite based TMS. NOVEC™ 649 used in LHP. Compared to using ethanol, no detriment in thermal performance found. Also, TMS able to keep temperature below 50°C at 3C.

2.4.6. Thermoelectric Generators (TEG)

On top of the technologies analysed above, there is a niche of a small cooling technology that has been studied in a handful of research works, which is the Thermoelectric Generators (TEG), also commercially known as Peltier cells. In TEGs a heat flux is created at the junction of two different types of metals thanks to an electric current flowing between them (the so-called Peltier effect). TEGs are made by doped semiconductor elements, comprising of a series of p-type and n-type elements, sandwiched in thermally-conductive substrates (but not electrically conductive) to transfer heat across a junction made by different materials [36]. As voltage is applied to a TEG, electrons jump from a lower energy level of the p-type thermo-element to a higher energy state in the n-type thermo-element by absorbing thermal energy from one side of the module, in effect cooling it. Some of the advantages of TEGs are that the same module can function both as heater or cooler depending on the direction of the current flow and they are also compact, lightweight and precise components. Li et al. [286] developed a TEG coupled with forced convection and compared it with natural convection cooling and forced convection cooling, applied to batteries. The results showed that the TEG system could decrease the temperature by 16.44% at the discharge rate of 3C. Alaoui and Salameh [287] also applied TEG to the TMS of an EV and found out that, to have acceptable performances, there was the need of increasing the weight of the battery pack by 64.4%, and its volume by 152.88%, due to the presence of fins. Luy et al. [288] used a combination of thermoelectric cooling, forced air cooling, and liquid cooling, obtaining promising results on the cooling effect but quite high power utilised by the TEG. Following a different approach, Suh et al. [289] used a TEG as waste heat storage device, absorbing energy and converting during summer and as a pre-heating device during winter.

However, their coefficient of performance (10%) is too low for employment in the EV TMS, and also it leaves the technical challenge of cooling down the hot side of the Peltier cell.

2.5. Thermal Management Requirements in other Vehicle Areas

Batteries are not the only area where thermal management is needed, in fact also the cabin and the electric motor as well as the fast charging process require ad-hoc thermal control.

Cabin thermal management, in terms as Heating Ventilation Air Conditioning (HVAC), serves a twofold purpose: firstly, it ensures passenger comfort by controlling air temperature, relative humidity and air velocity; secondly, it provides safety, in terms of visibility (defogging and de-icing). This comes at a compelling power cost, as the energy required to drive increases

by 10% on cooling and 50% on heating [290] using standard methods such as Positive Temperature Coefficient coil. A promising solution employed in the most recent EVs is the adoption of a Heat Pump, which has a very high COP (namely, 3 for cooling and 4 for heating). Heat Pumps work thanks to compression and expansion of a working fluid (Fig. 18): heat is absorbed from the air surrounding the vehicle, thus heating the fluid; this high temperature fluid is then compressed and goes to heat up the air destined to the cabin; then the low temperature high pressure fluid is expanded in a valve and returns to the first heat exchanger to close the loop.

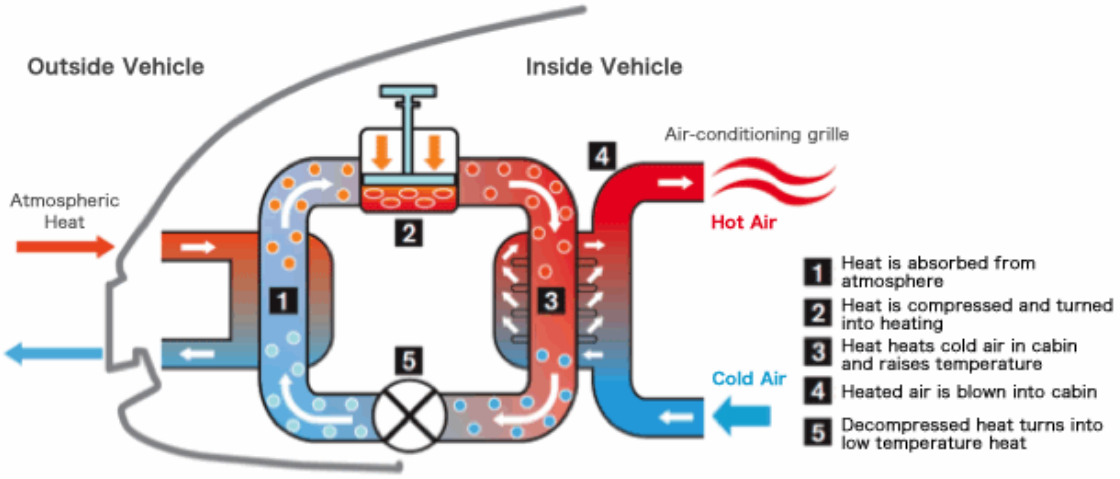

Fig. 18. Heat Pump operations schematic [291].

A very pressing matter lately is fast charging, which poses serious thermal management challenges to maintain favourable temperature during the entire processes. The target for fast charging has been set at 8C charging rate [228]. The C-Rate is the current rate, defined as the charge or discharge current divided by the battery capacity; this means that a 1C charge will completely charge the battery in 1 hour, 2C means full charge in half an hour and so on. Hence, 8C means a full charge in less than 10 minutes, which if achieved will drastically reduce the customer restraints from purchasing EVs (Fig. 2). However, charging at high rates was proven to accelerate degradation, decreasing both capacity and power output. The heat generated during fast charging due to resistive heating is often difficult to remove in a uniform and efficient manner. Moreover, fast charging is usually only achievable up to 80% SOC level, due to safety limitations. In fact, at high SOCs, the charging current needs to be gradually decreased to avoid exceeding the maximum cell voltage limits, so the charge is slowed for the final 20% of the SOC, creating the so-called CC-CV charging curve (Constant Current – Constant Voltage).

Presently, the state of the art is represented by the Porsche Taycan [292], which is able to perform fast charge at 3C in 19 minutes, thanks to newly introduced 350kW charging capability. Other luxury EV manufacturer like Tesla uses 120 kW charging, while standard medium price range EVs like Nissan Leaf and BMW i3 use 50kW charging.

Another part of the EV requiring thermal management is the electric motor. In current EVs, the most adopted type of electric motor is the Permanent Magnet Brushless Direct Current (PMBLDC) motor, selected for its high efficiency, high-quality Torque vs speed characteristics, high output power to size ratio, fast dynamic response and noise free operations. All EVs are employing this technology, thanks to the increased availability in the 21st century of high quality rare earth permanent magnet materials, such as samarium cobalt (Sm-Co) and Neodymium-Iron-Boron (Nd-Fe-B) [293]. The PMBLDC has 4 different heat generation sources [294]: Joule Losses, deriving from the Ohm's Law; Iron Losses, deriving from the conversion of electric energy into thermal energy in the iron, such as hysteresis and eddy losses (currents inducted into a conductor); friction losses, between rotor and stator; stray losses, which are minor losses like skin effect and high frequencies.

The temperature threshold for the PMBLDC motor is set at 150°C as above it, demagnetization of neodymium will take place. The most common cooling methods are either totally enclosed fan cooling, where fan, air path and motor are under the same case or liquid cooling with oil. In Fig. 19, two innovative strategies of motor cooling via heat pipe are presented; heat pipes are embedded in the stator and rotor, respectively, removing heat from the solid part and releasing it to a cooling chamber where a coolant flows.

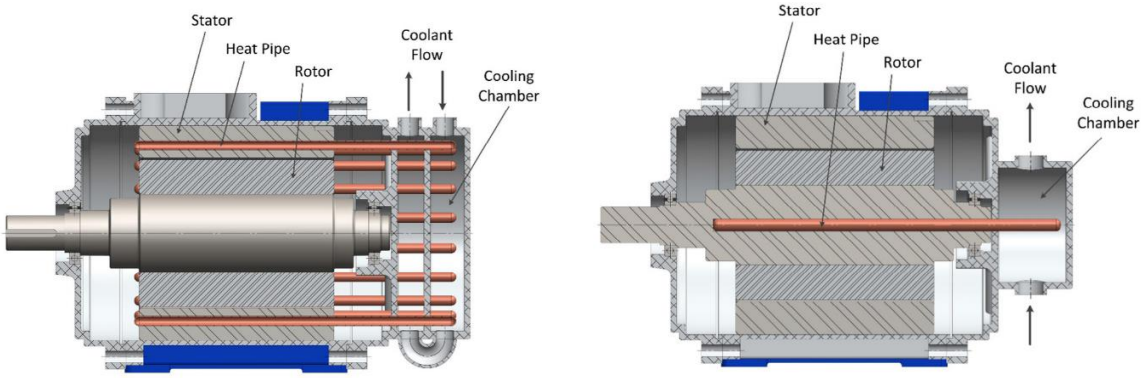

(a) Heat Pipe stator cooling (b) Heat Pipe rotor cooling

Fig. 19. Different strategies of electric motor cooling by means of heat pipes [294], case (a) the heat pipe removes heat from the stator and in case (b) it removes heat from the rotor. In both cases the heat pipes condensers are submerged in a flowing liquid chamber.

2.6. Decision Matrix

From the conducted literature review, it is evident that at the moment there is not a unique technology that can satisfy all the requirements at once. However, for the purposes of the present PhD thesis it was deemed appropriate to compose a matrix ranking these different technologies on several identified key factors:

- *Independency*, from other technologies (e.g., source of cooling at the condenser) or from environmental conditions.
- Possibility to be used for *heating* as well.
- The *Cooling Performance* in terms of maximum temperature reduction.
- Ability to maintain *temperature homogeneity*.
- *Weight.*
- Lower *Cost.*
- Reducing the required power and hence extending the *range.*
- *Adaptability* of the design, in terms of flexibility of the configurations, complexity and number of parts.

For each of these factors, a mark of 1 if negative, 2 if neutral, 3 if positive was assigned for all the considered technologies in order to form the matrix presented in Table 7.

Table 7 - Simplified decision matrix

List of Key Factors	Air	Liquid	PCM	Boiling	Heat Pipe	LHP	PHP
Independency	2	3	1	1	1	1	1
Heating	2	3	2	2	2	1	2
Cooling Performance	1	3	2	3	3	3	2
Temp homogeneity	1	3	3	3	3	3	2
Weight	3	1	1	2	3	3	3
Lower Cost	3	1	3	2	2	2	3
Power Required	1	2	3	3	3	3	3
Design Adaptability	3	2	1	1	2	3	2
Total	19	20	17	20	22	22	21

The scores for independency come from the fact that liquid and air are the only self-sufficient solutions, with air being penalised due to its lack of capacity to cope with fast charging (all the other technologies, being passive, will need an external heat sink to dissipate the heat to).

The scores for heating have been assigned considering that LHP, for example, cannot be used for heating (hence the minimum score); liquid TMS is the only technology that does not

change performance whether used for heating or cooling; in fact, two-phase passive devices, even when are able to provide heating, will have opposite performance between cooling and heating. Since in the zones of the devices where boiling is expected in cooling mode, nucleation is favoured with treatments that will increase the number nucleation points. This is detrimental for the heating mode, as condensation will be hindered by these treatments [295].

The cooling performance and temperature homogeneity scores were assigned considering that standard ranges for heat transfer coefficient for air forced convection is 25-250 W/m^2K, for liquid is 100-20,000 W/m^2K, for boiling or condensation is 2,500-100,000 W/m^2K [296].

The scores for weight, cost and design adaptability have been assigned integrating the literature review presented herein with the table produced by [36], [14], [297], [298].

In Table 7, the heat pipes family seems to represent the best possible alternative, giving the highest sums of scores. However, no importance has been given to the different factors, as surely some are more sought after than others. Therefore, weighting factors have been introduced to mimic different applications scenarios, characterized by different requirements. In order to present the results on a percentile-based scale, the baseline weight applied to the different key factors was 12.5, as presented in Table 8 .

Table 8 - Baseline weighting factor scenario.

List of Key Factors	Weighting Factor	Air	Liquid	PCM	Boiling	Heat Pipe	LHP	PHP
Independency	12.5	25	37.5	12.5	12.5	12.5	12.5	12.5
Heating	12.5	25	37.5	25	25	25	12.5	25
Cooling Performance	12.5	12.5	37.5	25	37.5	37.5	37.5	25
Temp homogeneity	12.5	12.5	37.5	37.5	37.5	37.5	37.5	25
Weight	12.5	37.5	12.5	12.5	25	37.5	37.5	37.5
Lower Cost	12.5	37.5	12.5	37.5	25	25	25	37.5
Power Required	12.5	12.5	25	37.5	37.5	37.5	37.5	37.5
Design Adaptability	12.5	37.5	25	12.5	12.5	25	37.5	25
Total out of 100		66.7	75	66.7	70.8	79.2	79.2	75

Following the same thinking that led to Table 8, other tables were created representing 5 different scenarios. The differences are in the system requirements and boundary conditions: firstly, a starting scenario #0 is considered as the best compromise amongst the different requirements and system conditions; in scenario #1, a hot environment is considered, with temperature between 30°C and 50°C, without aid from the heat pump (which stresses the necessity for heating) and wanting to privilege cost reduction; in scenario #2, again a hot environment is considered, with temperature between 30°C and 50°C, with heat pumps and aiming for range increase and weight reduction; in scenario #3 instead, cold climate is

considered, with temperature between -20°C and 0°C, no heat pumps and aiming to reduce costs; in scenario #4, temperate weather is considered, between 10°C and 30°C, without heat pumps and privileging independency and design simplicity; in the last scenario #5, cold environment between -20°C and 0°C with heat pump, privileging range and independency is considered. In Table 9 the breakdown of the different weighting factors is presented and in Table 10 the results for the different technologies are shown.

Table 9 - Weighting Factors for the considered scenarios.

	Scenarios					
	#0	#1	#2	#3	#4	#5
Independency	10	9.5	9.5	11.5	15.5	15.5
Heating	9	15.5	9.5	15.5	14	9.5
Cooling Performance	15	15.5	15.5	9.5	14	15.5
Temp homogeneity	15	12.5	12.5	12.5	12.5	12.5
Weight	12	9.5	15.5	11.5	9.5	10.5
Lower Cost	15	15.5	12.5	15.5	9.5	10.5
Power Required	15	12.5	15.5	12.5	9.5	15.5
Design Adaptability	9	9.5	9.5	11.5	15.5	10.5

Table 10 - Decision Matrix for the different considered scenarios (green represent the most favourable solution).

	Air	Liquid	PCM	Boiling	Heat Pipe	LHP	PHP
#0	63.7	74	71.3	75.3	82.3	82.3	77.3
#1	64.7	76	70.7	73.8	80.2	78.2	76
#2	64.7	73	68.7	74.8	83.2	83.2	78
#3	68	74	68.7	70.5	78.2	76.8	76
#4	66.2	79	63.7	68.3	76.7	77.2	71
#5	62.7	77.3	67.3	72.5	79.5	79.8	73.7

From the numbers emerging from Table 10, HP and LHP looks promising amongst the two-phase passive technologies, whereas liquid ranks always better than air cooling. Scenario #4 is the only scenario where liquid has higher score than either HPs or LHPs, being in fact the one that had the less favourable requirements and conditions for their technology.

Finally, considering that none of the presented technologies can satisfy the necessary requirements alone, a combination of these might be the correct strategy. A *hybrid* TMS composed by more than one solution, exploiting the different benefits brought by the different technologies, would be the optimum option, as suggested in literature [36]. Looking again at the results from Table 10, combining HPs and/or LHPs with either air or liquid looks an encouraging solution to achieve a reliable TMS under a variety of conditions. Especially considering that the limitations for air and liquid are linked to their direct application to the battery pack, e.g., spacing for air cooling and dielectric fluid for liquid. It is therefore possible,

with a smart of combination of TMS technologies, to use air or liquid TMS in a different area of the vehicle (e.g., to cool down the heat pipe condenser) and thus maximizing their performance and reducing their cost.

In the next chapters, the hybrid design proposed in the present PhD thesis will be introduced. It foresees the employment of two of the discussed TMS: Loop Heat Pipes as main thermal vector from the battery pack; Liquid cooling at the remote condenser of the LHPs, employing the liquid loop already present for the HVAC system of the vehicle. The design thus creates a perfect example of the hybridization of two technologies, as the LHP will save the parasitic power and extra components needed for an equivalent pumped liquid loop, while still achieving excellent thermal performance.

Chapter 3 - Loop Heat Pipes

3.1. Introduction

Loop Heat Pipes (LHPs) are a variation of the standard sintered Heat Pipe (HP) heat exchanger. Developed by Maydanik and Gerasimov in the Soviet Union in the early 70s [299], the LHP is a two-phase passive heat transfer device, originally developed for space applications due to its independence from gravity in operation. They differ from the standard sintered Heat Pipe (HP) because the characteristic porous structure is present in the evaporator only, while the rest of the device is made by smooth tubing, allowing for a considerable price difference between standard HPs of the same length.

Looking at practical implementation, LHPs offer the advantages of allowing small diameter transport tubes, thus reducing encumbrance and weight and allowing complex tube layouts. Furthermore, they open the possibility to incorporate flexible sections in the liquid and vapour transport lines [300]. LHPs can be used to thermally connect together heat sources and sinks several meters apart (e.g., a 21 meters LHP was successfully tested [299]).

The miniaturizing trend that has been characterizing electronics in the recent years has pushed the need of efficient cooling devices, due to the resulting high values of heat flux needing to be dissipated. In their first application, the aerospace sector used LHPs as it was in need of high operational reliability and robustness, but LHPs nowadays are studied for applications such as solar and nuclear energy waste heat recovery, laptop cooling and aircraft thermal management for instance.

In Fig. 20, a schematic of the LHP is presented, as well as a magnification of the evaporator section. The LHP is composed by 5 main parts: the *evaporator*, which is the part receiving heat

from the component to cool down and where evaporation takes place; the *vapour line*, which transfers the newly generated vapour from the area of heat removal to the area of heat release; the *condenser*, which is a part of the tube that is embedded in any kind of heat exchanger to aid the condensation process of the working fluid; the *liquid line*, which returns the condensate to the evaporator; and finally, the *Compensation Chamber* (CC), which is a two-phase reservoir which saturation pressure sets the operative temperature of the loop.

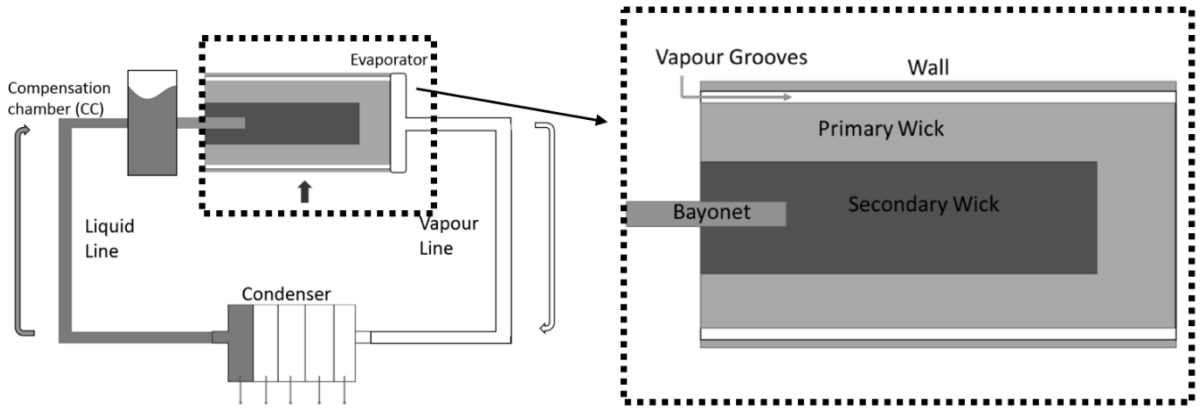

Fig. 20. LHP schematic in case of a cylindrical evaporator [208].

LHPs are evacuated devices, partially filled with a working fluid. The vacuum level inside the device is of paramount importance to ensure both high performance and long operational life. Having suitable vacuum levels inside the device (10^{-5} mbar) ensures that, after filling it with working fluid, only one chemical species lives inside the device. Thus, filling only partially (i.e. 40-60% of the available volume) with liquid, forces the fluid to assume a saturated state, filling the remaining volume with its own vapour. In other words, thanks to the vacuum, inside the LHP there will be only liquid and vapour of the same substance. Not having the same substance inside the LHP causes operational issues in the evaporation and condensation processes, and additionally it makes it impossible to perform any analytical simulation of the fluid behaviour and hence to predict the thermal performance of the device.

A few years before the advent of the LHP, in the United States, a similar device was developed, called Capillary Pumped Loop (CPL), with the compensation chamber position being the main difference between the two devices. Compared to a CPL, LHPs have more robust operational characteristics and are self-starting. In fact, despite the fact that CPL offer finer temperature control, they need pre-conditioning before start-up, which nullify the advantages of having a passive device (i.e., a device that does not consumes any power to function). For the LHP, the fact that the two-phase reservoir is close to the evaporator simplifies the start-up and makes the LHP vapour-tolerant.

This Chapter will detail the fundamental thermo-fluid operations of the LHP, with particular emphasis on operational characteristics such as filling ratio, start-up and temperature hysteresis, influence of mass, materials and fluids and Non-Condensable Gases. The Chapter will conclude with a brief overview of past and current LHP applications.

3.2. LHP Operations

The evaporator is the most crucial part of the LHP, being the only part containing the porous structure, called *wick*, which capillarity properties provide the fluid with the adequate pressure gradient necessary to travel the entire loop. This is the main difference distinguishing the LHP from the classic sintered HP. The pressure gradient is generated thanks to the capillarity originating in the small pores of the wick, following the Laplace-Young equation [301].

$$\Delta P_{cap} = \frac{2\sigma}{\bar{r}} \cos\theta \tag{1}$$

where σ is the surface tension, $\bar{r}$ is the medium pore size radius and θ is the equilibrium contact angle of the menisci in the wick pores. For the LHP to properly function, this pressure gradient needs to be greater or equal to the sum of all the pressure drops present in the loop. In other words, the evaporator, thanks to its wick, acts as a "passive pump", where no moving parts or external electric power are required to ensure the fluid motion. One of the advantages of a capillary loop is that the meniscus in the evaporator wick will automatically adjust its radius of curvature such that the resulting capillary pressure is equal to the total system pressure drop.

In order to better explain the fundamental operation of the LHP, Fig. 21 shows the working cycle with respect to the saturation line on a P-T diagram [299].

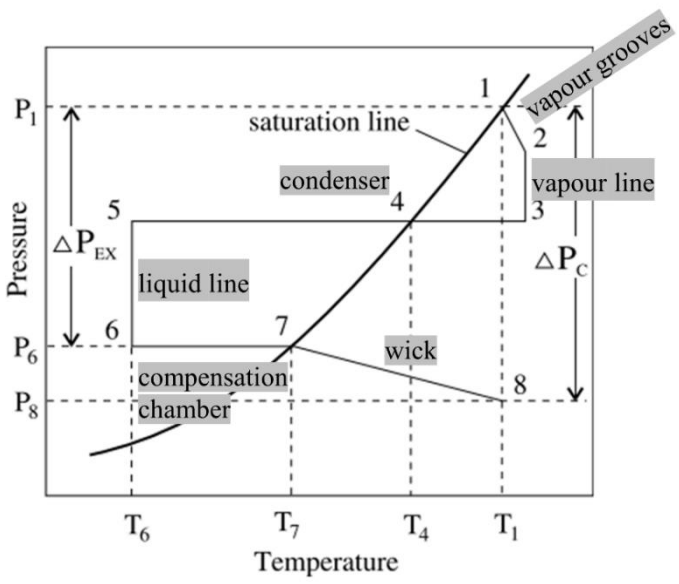

Fig. 21. P-T graph of an ideal LHP working cycle (modified from [299]).

When heat is applied to the evaporator, the liquid entrapped inside the primary wick evaporates, thanks to conduction through the evaporator envelope (wall). Point 1 in Fig. 21 represents the saturation pressure and temperature (P1, T1) at the edge of the wick in the evaporator, coincident with the vapour bubble generating at the meniscus of the capillary pore. This newly generated vapour flows inside the vapour grooves, which are small size channels dug into the outer surface of the primary wick, and it is directed towards a preferential direction due to the adverse pressure gradient happening in the wick (given by capillarity), which effectively prevents the vapour from travelling back inside the wick. The section 1-2 corresponds to the vapour groove section, where the vapour temperature increases due to the contact with the evaporator wall and the pressure decreases due to the motion of the vapour, hence a slight superheat arises. From 2 to 3, the vapour travels on the vapour line, which can usually be considered as isothermal. The 3-5 section represent the condenser section, where 3-4 is the condensation process while 4-5 is the (optional) subcooling phase. Please note that in the graph of Fig. 21, the pressure drop due to load losses in the condenser is neglected, for clarity purposes. The liquid line is represented by section 5-6, showed as isothermal, although this section is often subjected to heat transfer with the ambient. At this point there is liquid, determined by T6 and P6, that enters the compensation chamber, which in turn is receiving a bit of the heat from the evaporator. Thus, the working fluid is heated to the temperature T7 on the saturation line, as the compensation chamber is a two-phase reservoir and hence it is saturated. It is important to point out that the presence of a certain number of vapour bubbles in the liquid line, which can freely penetrate the compensation chamber, do not interfere with the normal operation of the device, but only lead to an increase in the operating temperature. The boiling of a working fluid in the compensation chamber is not critical for LHPs, contrarily to the CPL case. The section 7–8 corresponds to the pressure drop due to permeability, given by the liquid filtration through the wick into the evaporation zone. On this way the liquid may prove to be superheated, but its boiling-up does not take place owing to the short duration of such state. Point 8 determines the state of the working fluid in the vicinity of the evaporating menisci, and pressure drop ΔP_c corresponds to the value of total pressure losses in all the sections of the LHP, that needs to be at least matched by the pressure given by capillarity in equation 1.

In case of a cylindrically shaped wick, evaporation will take place not only on the outer surface of the wick, but also from the internal one. Hence some of the heat provided to the evaporator ends up wasted, as only the heat “stored” in the vapour directed to the condenser will then be rejected, whereas the heat utilized to vapourize the working fluid in the inner side

of the wick will only increase the temperature of the evaporator and compensation chamber, thus reducing the performance of the LHP itself. This heat is called *heat leakage* or *parasitic heat*, and it usually accounts for the 10% of the total heat applied [302]. In order to mitigate the heat leakage generation, dual-wick structures have been introduced, with the distinction of primary and secondary wick (Fig. 22). Fluid in the primary wick evaporates and travels towards the condenser; the secondary wick is in between the primary wick and the bayonet (portion of the liquid line protruding inside the evaporator) and it has a particular geometry characterized by channels dug into its inner surface, allowing for the vapour generated by the heat leakage to flow back to the CC. There, thanks to the subcooled condensed liquid coming back from the condenser, the temperature increase provided by the heat leakage is balanced.

The secondary wick provides a liquid link between the compensation chamber and the evaporator so that the evaporator will always be replenished with liquid. Summarising, the CC has a twofold role in the device, firstly to act as an emergency source of fluid to prevent dry out phenomena at the evaporator and secondly to accommodate the parasitic vapour from the secondary wick. This leads to two major advantages of the LHPs: a) the LHP starts directly when heat is applied to the evaporator, without the need of pre-conditioning (as in case of the CPL) and b) the evaporator is vapour tolerant (the CPL evaporator is not). In fact, vapour bubbles in the liquid line can freely penetrate the CC, without interfering with the operation of the device but only increasing the operating temperature.

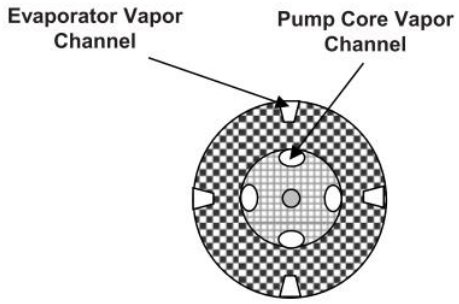

Fig. 22. Detailed view of primary and secondary wick with annexed vapour removal channels [303].

The significance of minimizing the heat leakage emerging from the last discussion leads to the understanding that only the evaporator surface corresponding to the wicked area should be in contact with the component to cool down. This part of the evaporator is thus called active zone. If heat is applied directly to the compensation chamber as well, it can generate a series of adverse events, culminating in the stoppage of the LHP functioning due to dry-out, as the working fluid would travel the loop in the opposite direction (as, due to the presence of the wick, the loop is one way only).

The characteristic of the LHP of allowing only one direction for the working fluid to travel within, makes this device a perfect example of a thermal diode, characteristic that is much appreciated in the aerospace sector, as additional safety barrier to prevent certain components to overheat.

Many operational and design parameters can influence the LHP performance and functioning. Following, a small paragraph is dedicated to each of these design parameters for clarity.

3.2.1. Compensation Chamber Design

The compensation chamber is a critical component of the LHP and it necessitates a carefully thought design. The size of the CC will affect the overall thermal resistance, the start-up at low power and the overall performance of the LHP. Moreover, the filling ratio, i.e., the percentage of available volume filled by the working fluid, is another determining parameter to consider carefully. From the Archimedes' principle, the fluid charge of the CC will coincide with the fluid charge of the whole loop.

There is not any upper limit to the size of the CC from the thermo-fluid dynamics point of view, however there are limits dictated by common sense and cost, volume and weight constraints. On the other hand, there is a lower limit of a minimum volume requirement, as the CC needs to be able to accommodate the liquid volume swing due to the density changes between the hottest case and coldest case. The hottest case happens when a maximum heat load is applied to the evaporator and the condenser is at the maximum temperature. The coldest case sees no heat load to the evaporator and the condenser temperature is at the minimum. The reader is referred to [304] for more information on the CC sizing formulas.

From a thermodynamic point of view, the filling ratio has no effect on the steady state performance, however it does affect the loop operation. There is no golden rule when it comes to the filling ratio, as it is a very case dependent parameter, however studies have reported optimum values between 40-60% [305,306].

The filling ratio also strongly influences the start-up, as it will be discussed in the next section.

3.2.2. Start-Up

The start-up is an extremely complex transient phenomenon. It is defined as the time it takes to the LHP to become operational. In other words, when a LHP is properly functioning, due to the return of the cold condensate, the liquid line temperature should decrease. The time from

the application of the heat load to the initiation of the fluid circulation is called start-up time [300]. A good start-up is characterised by having a small time and low increase in temperature due to the sensible heat, before the boiling starts (this ΔT is called overshoot). A good start-up is reported to be around 3 minutes' duration and a good overshoot ΔT to be lower than 5 K. On the other hand, bad start-ups take longer than half an hour and have large overshoots (>40 K) [307].

In a cylindrical evaporator, the secondary wick ensures that the primary wick is always wet hence the LHP can start as soon as power is applied to the evaporator, without the need of pre-conditioning process, making up much of the LHP appeal. However, self-start does not necessarily imply instant or quick start [304].

Start-up is a function of many factors:

1. the arrangement of the fluid over the loop, in terms of its distribution and its temperature (i.e., where the saturated state lies);
2. the thermal conductivity of the wick, as it affects the heat leakage;
3. the heat applied to the evaporator at start-up, as it needs to be enough to provide the right amount of superheat to the working fluid to initiate boiling during particular adverse conditions (which will be discussed next);
4. the heater mass attached to the evaporator, as it will influence the thermal inertia of the system and therefore the quantity of heat absorbed by the evaporator;
5. the design of the coupling of CC and evaporator wick;
6. the respective position of evaporator and CC (which will be discussed in section 2.7);

There are four possible arrangements of the working fluid inside the evaporator (wicks and CC) before the start-up [303], as shown in Fig. 23. These arrangements are described under the assumptions that the entire LHP is at the same temperature as with the ambient. Considering that liquid fills up the evaporator, a superheat is needed to activate boiling and instead if vapour is present in the vapour grooves, as soon as power is applied there will be an activation, four situations can be identified:

1. Situation 1 – vapour present in the vapour grooves, wicks completely filled with liquid: this is the most favourable condition for start-up. As soon as the heat load is applied to the evaporator, the LHP will activate as no amount of superheat is required. As such, in the graph shown in Fig. 23a, T_{wall} and T_{cc} rapidly increase at the beginning, as the cool condensate returning from the liquid line will take some time before reaching the CC. Since

liquid is present in the evaporator core, the heat leakage is small. Eventually, temperatures decrease as the system reaches equilibrium.

2. Situation 2 – vapour present in both the vapour grooves and the evaporator core: similarly to the previous case, start-up onsets as soon as heat is applied to the evaporator. However, due to the presence of vapour in the evaporator core, the heat leakage is greater, therefore the graph of Fig. 23b shows a much higher temperature overshoot.
3. Situation 3 - vapour grooves and evaporator core completely filled with liquid: this means that the working fluid in the evaporator is not in saturated state. Thus, when heat is applied, the liquid in the vapour grooves needs to be heated up from the subcooled to the saturated state, hence the sharp increase in T_{wall} in Fig. 23c. On the other hand, the heat leakage is small, because of the liquid presence, therefore the T_{cc} remains almost constant. At the onset of boiling, a small overshoot is observed in T_{cc} as some boiling is observed in the inner side of the wick, directing some hot vapour to the CC. Eventually, once start-up is reached, saturation temperature and equilibrium are reached.

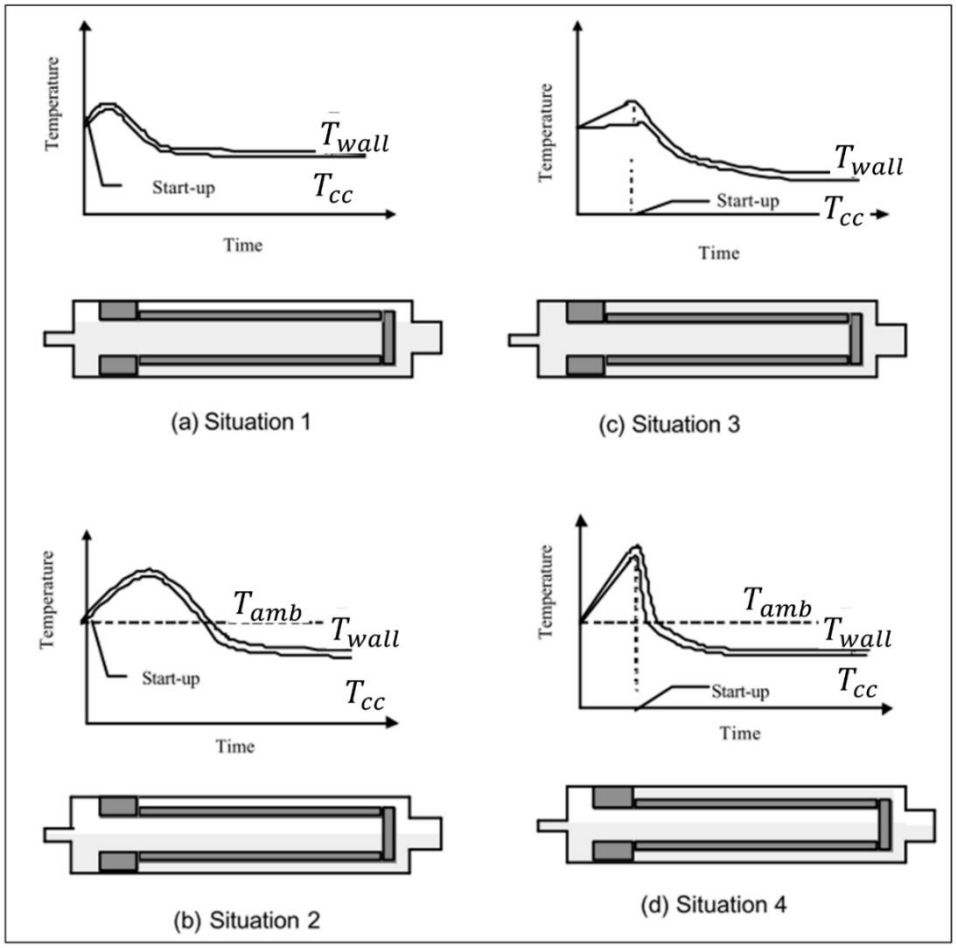

Fig. 23. Four start-up modes characteristics to four starting conditions arising in the evaporator of a LHP [303].

4. Situation 4 – vapour present in the evaporator core and liquid present in the vapour grooves: this is the most unfavourable condition to achieve start-up. Heat is needed at the vapour grooves to bring the liquid inside them to saturated state, before having a possibility to start the nucleate boiling. Meanwhile, due to the vapour in the core, heat leakage remains high until the CC refills the wick with liquid. This results in serious temperature increase for both T_{wall} and T_{cc}.

The last condition can generate adverse scenarios. If the temperature increase in the liquid present the vapour grooves is fast enough, the boiling can start, otherwise if the CC temperature increase is quicker than the one in the liquid, the loop will not start. On another scenario, the time to reach boiling can be so long that the temperatures are high enough that the applied heat is dissipated to the surrounding by natural convection and/or radiation. Moreover, the LHP could even work in a reverse mode, where the vapour starts to circulate from the CC in the opposite direction, leading to a disruptive condition called *dry-out*, where the evaporator is deprimed of working fluid and the LHP becomes inoperative.

It is evident therefore, how the start-up is a delicate phenomenon, extremely complicated to account for in the design phase, mostly due to the unpredictability of the liquid/vapour arrangement around the evaporator and the rest of the loop. However, few strategies have been devised to mitigate the start-up problems [300]: high heat flux bottom heaters, to locally heat up a part of the evaporator in order to bring the liquid inside the vapour grooves to the required saturated conditions; Thermoelectric Coolers, connecting their cold end to the CC and the hot end to the evaporator, they can create the required superheat for initiate boiling; dual CC (valid only on 1-g conditions), to increment the chances to have saturated vapour near the evaporator.

3.2.3. Temperature Hysteresis

Empirical observations on the behaviour of the LHP revealed another interesting yet challenging phenomenon, known as temperature hysteresis. This term indicates the phenomenon whereby the LHP operates at different temperatures over repeated tests when the test conditions (i.e., external power, ambient and condenser sink temperatures) are all kept the same.

Different hypothesis were made to explain these phenomena [308]. It was postulated that temperature hysteresis might happen more evidently at lower powers and during great jumps in the applied power. In [309], after a 50W/400W/50W cycle, the temperature at 50W was 4°C higher. A step down from 400W to 50W in the applied power will cause the amount of subcooled liquid returning to the evaporator to be greater than the amount of superheat of the

vapour exiting the evaporator. Hence, to balance the evaporator energy and mass, the temperature of the CC will rise, to compensate the returning subcooled liquid, hence raising the temperature of the entire loop.

A different explanation to the temperature hysteresis was given in the case reported in Fig. 24. Two tests were performed in two consecutive days, resulting in the operating temperature of the second day being considerably higher, with a temperature increase of approximately 10°C. It was postulated that there was an influence from the deprime procedure of the previous day. In fact, it may have happened that some vapour bubbles were still entrapped in the evaporator wick as they have not entirely collapsed. This would have caused a higher heat leakage and hence a higher operating temperature.

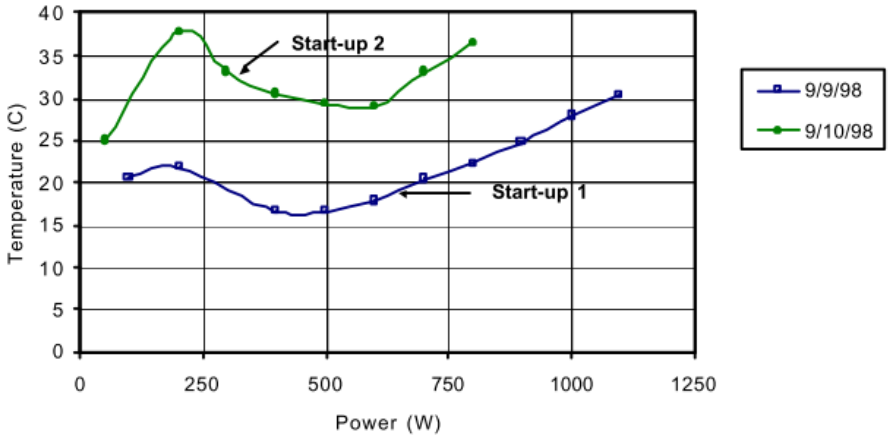

Fig. 24. Example of temperature hysteresis: difference in operating temperatures of two consecutive days in the Switch Box LHP (ammonia as working fluid) [304].

3.2.4. Influence of Evaporator Mass

In most of the literature studies, the LHP is heated by heaters directly connected to the evaporator active zone. In the few applications actually tested, LHP have been used mostly for cooling down electronics components, which are characterised by a high heat flux and a small mass. Having a small mass means having a low thermal inertia, hence the LHP response will be quick even at low heat loads.

In space applications, the instrument attached to the evaporator normally has a larger mass, which helps to dampen transient phenomena due to heat load changes. Hence, it may help to eliminate temperature hysteresis.

A larger evaporator mass, or larger heater mass, means that the thermal inertia is significant. Thus, the loop will almost always work through low power operation, because a large part of the heat goes into the thermal inertia component, rather than transmitted to the evaporator. In

low power operation, temperature is more difficult to control and the start-up may be hindered by increasing its time and the temperature overshoot or even preventing the event from being successful.

This analysis will renew its importance in a later stage of this work, where the thermal mass of the heater (in this case, the battery cells) will play in important role in the start-up and steady state operation of the TMS.

3.2.5. Materials and Fluids

Wicks are usually made from sintered nickel, titanium, copper and stainless steel powders with an effective pore radius between 0.7 and 15 μm and porosity between 55% and 75%. The sintering process is the process of compacting and forming clean metal particles by heating up to about 80% of their melting temperature when they start to sinter together, but without reaching liquefaction. Sintering is driven by a reduction in surface energy, which is high for small metallic particles. The atoms from adjacent particles bonds together creating small bridges between particles (Fig. 25).

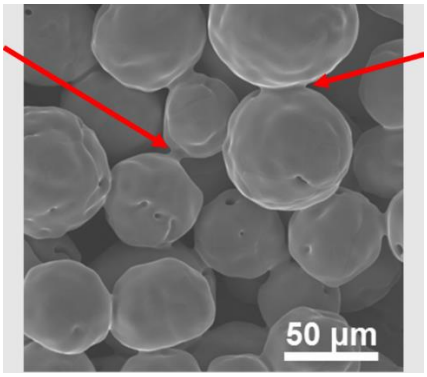

Fig. 25. SEM photo of sintered copper powder. The two red arrows show some of the connections between particles [310].

The sintering process of the metallic wick is the most expensive process in the creation of the LHP, hence why alternative wick materials have been researched in the recent years: ceramic wicks [311], carbon fibre [312], polytetrafluoroethylene (PTFE) and other synthetic materials [313,314].

LHPs bodies are usually made from copper, to maximise the thermal performance, or stainless steel, due to its adaptability to be processed to different kinds of vacuum-hermetic welding procedures and its high strength. A LHP material should have a sufficiently high strength mostly to withstand the internal pressure of the working fluid in case of out of design

operations. The characteristic nature of the LHP of having the wick in the evaporator only, allows for having flexible tubes connecting evaporator and condenser.

Regarding the working fluid, from the thermal point of view, ammonia is reported to be the best performing one in the -20°C to 80°C range [299], with allowance made for its toxicity, flammability and soaring vapour pressure. Water becomes the better choice at higher temperature ranges (i.e., 100°C-150°C). However, due to the peculiar freezing behaviour of water, it poses serious complications to the device integrity and leak tightness. Neon, oxygen, methanol, ethanol, nitrogen, ethane, propane, propylene, freon 152A, freon 11, freon 21, n-pentane, acetone, toluene and other synthetic working fluids were also successfully used [299,301,315]. The choice of the working fluid ultimately is a trade-off between key performance physical parameters such as latent heat of vaporisation, surface tension, vapour pressure and boiling temperature, together with applications-specific requirement such as safety parameters (toxicity, flammability, electrical conductivity) and compatibility with the manufacturing materials.

3.2.6. Effect of Non-Condensable Gases (NCGs)

In two-phase heat transfer devices, Non-Condensable Gases (NCG) are the gases that cannot be condensed to liquid during the operation and always remain in the gas state. Generally, NCG consists of nitrogen, light hydrocarbons, carbon dioxide and other gaseous materials [316]. They can be originating from poor cleaning of the envelope, wicks and pipes, from the impurity of the working fluid and, if there are incompatibilities between the working fluid and the manufacturing materials, chemical reactions may arise that could generate NCG. Specific to space applications only, NCG can arise by ionizing radiation causing the working fluid to breakdown [300]. The amount of NCG generated is a function of the amount of the working fluid, the surface area of the materials in contact, the operating conditions, and the length of the exposure period.

NCGs can collect in numerous locations. Usually, they collect at the CC, as they are carried by the working fluid motion from all over the loop to this stagnant region. Here, the static nature of the fluid and the proximity with the wick that blocks the NCG passage makes it that they collect here. Alternatively, NCGs can collect in the condenser, due to the temperature being lower. In the more benign cases, the NCG can be absorbed by the working fluid or by the manufacturing materials.

If NCGs remain in the form of gas bubbles, they will spoil the LHP performance. In the condenser, they will block part of it and reduce the system overall thermal conductance. The

ones that accumulate in the CC will increase the subcooling requirement for the liquid returning from the condenser, since the liquid within the CC itself must be slightly subcooled in order to coexist with a mixture of working fluid vapour and NCG at the same temperature and pressure. Another study [317] mentioned that NCG generates mostly at the start of the LHP life (after vacuuming, filling and sealing), so good practice would indicate to run the LHP for a few cycles, without permanently sealing the device, then flushing out the newly generated NCGs.

In order to prevent the NCGs generation, special care must be taken to degas the working fluid, to evacuate the device prior to filling to suitable level of vacuum (e.g., 10^{-5} mbar) and to clean the materials used in the LHP. Otherwise, the outcome will be an increase of the loop operating temperature and hence a decrease of the overall thermal conductance.

3.2.7. Effect of Tilt and Elevation

Elevation and tilt are the two parameters that accounts for the influence of gravity on the performance of the LHP [305].

Elevation is the height of the evaporator with respect to the condenser, and it is considered as positive elevation if the evaporator is above the condenser (top heated mode) and adverse elevation is when the condenser is above the evaporator (bottom heated mode). The LHP capability to function on adverse elevation is managed by the primary wick, and this working mode tends to increase the operating temperature at lower heat loads, as the influence of the gravitational heads becomes smaller than the pressure load losses due to friction (when the LHP is in nominal operation mode). This is due to the fact that adverse elevation increases pressure drop across the wick, thus the temperature difference across it also increases (due to the Clausius–Clapeyron relationship). This increases the heat leakage, resulting in a higher operating temperature.

Tilt is defined as the height difference between the evaporator and the CC. When the CC is below the evaporator is called adverse tilt, whereas when the CC is above the evaporator it is referred as favourable tilt. The adverse tilt capacity is dictated by the secondary wick (in case of a cylindrical evaporator). During this condition, the secondary wick provides working fluid to the primary wick, since the bayonet will be containing vapour only (being the CC below the evaporator and not hard filled, the vapour will be at the top of the volume, in conjunction with the bayonet inlet). The liquid supply to the primary wick is thus dictated by the secondary wick (which hydraulically connects it to the CC). To solve the start-up problems associated with this situation, dual CC LHPs are used under 1-g conditions [300].

3.3. LHP Applications

LHPs have been investigated in different forms, devised for different applications. The classic LHP evaporator shape is cylindrical, with the double wick structure. However, since most often the object to cool down have a flat surface, to improve the thermal contact a saddle or flat interface is needed around the cylindrical evaporator, which despite being made by a good thermal conductor, will inherently increase the thermal resistance of the device. For this reason, flat-plate LHP evaporators were developed. This was a considerable challenge as the evaporator is one single body combining the wick and the CC, and it has been discussed how the CC volume has a lower limit. Hence, the possibilities for decreasing an evaporator thickness are very limited, also considering that the evaporator walls must be thick enough to resist the working fluid vapour internal pressure.

Historically, LHPs have been originated and dedicated mostly in the aerospace field. The first flight experiment in microgravity conditions was aboard of the Russian Spacecraft Gorizont in 1989. During this flight, albeit successful, it was found that the selected fluid (Freon-11) had a too high boiling point to ensure start-up even when the spacecraft was in the shade of the Earth. For the following flight, in the same year, on the spacecraft Granat, the fluid was switched to propylene and that lead to normal operation for 7 years, from 1989 to 1996.

The first real application for a space LHP was on the Russian satellite “Obzor” in 1994, where two ammonia and one propylene LHPs were employed. Nowadays LHPs are of wide use in space applications [299], e.g. they are employed in the Russian Spacecraft Mars-96, the Chinese meteorological satellite FY-IC and the US satellite Hughes-702. American made LHPs flew twice on the Space Shuttle STS-83 and STS-94 in 1997 and STS-87 in 1997. In 2003, two LHPs were used to cool the Geoscience Laser Altimetry System aboard of the US ICESar. Moreover, an LHP was the baseline design for thermal control of several others spacecrafts, including NASA’s EOS-Chemistry and GOES spacecraft, ESA’s (European Space Agency) ATLID, CNES’ (French space agency) STENTOR, and several commercial satellites [304]. LHPs are part of the baseline design for instrument thermal control for the Netlander spacecraft [318] and the long-term robotic Mars Pathfinder mission [319].

Moving towards lower altitudes, LHPs have been also studied as thermal vectors in aircrafts [301], for thermal management of the nacelle compartment and anti-icing for the wings [320].

LHPs have been investigated as ways to cool down electronics and computers. They have been used to cool down transistors (first instance dated back into the seventies) and quantum-electronic converters in notebooks. The market now is pushing towards ultra-slim, quiet and

long-lasting charge laptops while in the recent years, laptops power consumptions almost halved, whereas the CPU heat power output has remained almost unchanged [321]. If the available space for cooling inside the laptop chassis is limited by the device thickness, a more powerful fan is required to dispose of the excess heat, even with the conventional flattened sintered HP configuration, resulting in extra power consumption and more noise. In this situation, novel miniature two-phase heat transfer devices with higher heat transport capacity such as LHPs are gaining more appeal.

The increase of the heat flux needing dissipation and the multi-point distribution of heat sources caused by the spatial arrangement of high-power components (e.g., in laptops), has pushed LHP research into looking at multi-source cooling. Two avenues are pursued at the moment: multi-evaporator LHPs [322] and large evaporator LHPs [323].

Finally, LHPs have been investigated as thermal vectors in solar water heating of buildings. Amongst the solar thermal system worldwide, solar water heating in buildings accounts for 80% of the applications, despite the poor efficiency of the technology [324]. LHPs are investigated as a mean of reducing the heat loss happening during the transfer of the heat collected by the solar panel to the water tank and hence increase the efficiency. Moreover, LHP can at the same time allow for a simple implementation, that detracts less from the aesthetics of the buildings.

3.4. Conclusions

This Chapter has highlighted how the LHP is an excellent heat transfer device, despite the underpinned complexity of its governing thermo-fluid dynamics behaviour. The benefits of exceptional heat transfer capabilities, no parasitic power consumption, reliability, no noise and long transportation length makes the further study of this device a worthwhile option. In the next Chapter, the modelling of the LHP thermo-fluid dynamics will be detailed. Moreover, the modelling of the battery cells and graphite sheets assembly will be explained in detail, together with the numerical validation procedure for the two codes.

Chapter 4 - Modelling of Battery Cooling with Loop Heat Pipes

4.1. Introduction

The decision matrix that ended Chapter 2, showed the potential benefits that can be obtained when selecting a hybrid TMS comprising of two or more of the listed TMS technologies. This would allow to progress in answering favourably to the request of the EV market, such as to minimize parasitic power, complexity, weight and cost.

As already discussed, liquid cooling is the most effective cooling technology amongst the ones already employed commercially; amongst the emerging cooling technologies, two-phase vapour/liquid passive devices show the biggest potential. Therefore, this work proposes to investigate a TMS based on LHPs transferring heat from a battery module to a remote liquid chiller.

Having a compact chiller, instead of a liquid loop travelling across the whole battery pack, can aid to reduce the system complexity, weight and cost. The reduced length of the tubing will reduce the load losses that the chiller pump has to balance, effectively allowing for a smaller and/or less powerful pump, thus leading to a decrease in the parasitic power consumption. Furthermore, the choice of the chiller working fluid can be made disregarding the dielectric requirement, as it will not enter in contact with the battery pack, reducing the safety concerns.

Regarding the choice of a LHP over the other members of the Heat Pipe family, this is due to the benefit they provide in terms of long length heat transportation. In addition, LHPs have been preferred to PHPs as the latter still present uncertainties on their sensitivity to external accelerations, which makes their applicability to a moving vehicle troublesome. Even if PHPs

can be made of considerable distances, their thermal behaviour is strongly affected by the working fluid flow pattern, which in turn is affected by the external acceleration of the vehicles.

This Chapter will explain the proposed TMS and the related feasibility study. Firstly, the Lumped Parameter Model (LPM) describing the thermo-fluidic behaviour of the LHP is described in detail, with proof of its validation through literature available data. Secondly, the LPM of the cell-graphite assembly is described, followed by a verification with CFD results. Finally, the general numerical model is presented and, thanks to the confidence given by the two separated validation processes, a first feasibility study and comparison with a standard liquid cold plate TMS is performed and presented.

4.2. Proposed Thermal Management Design

At this point, the Author deems appropriate to refresh what are the three levels of requirements that a successful EV TMS needs to fulfil, to ensure both maximum performance and operational life:

1. Cell level: temperature gradient across the cell should not exceed 5°C.
2. Module level: temperature between cells should be maintained within a 5°C difference.
3. Pack level: overall temperature of the cells belonging to the pack needs to be kept between 25°C and 40°C for optimum performance, 50°C for acceptable performance and an ultimate overall limit of 60°C, for safety purposes.

To conform to the third requirement, the use of one or more LHPs per module is envisaged for the design proposed in this work. To respect the requirement on the first and second level, the design should consider also to maximise is the energy density of the battery pack. The higher this value, the more performing the car will be in terms of speed, acceleration and all electric range. High energy density is reached by keeping the encumbrance of the battery pack and its weight as low as possible. Since the number and/or type of cells cannot be changed, the thermal engineer needs to work on reducing as much as possible the gaps between the cells (one of the problems of using air cooling) and to use light and efficient materials. Hence, the proposed design places the LHP at the bottom of a battery module, with graphite sheets sandwiched between the cells, as depicted in Fig. 26.

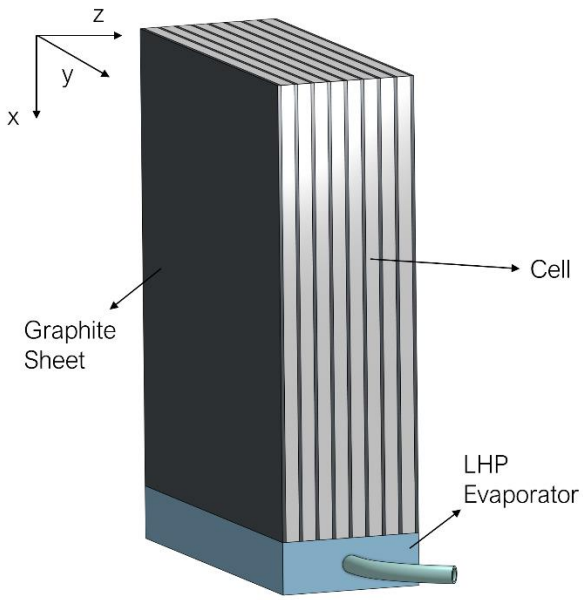

Fig. 26. Schematic of the proposed cooling design at the battery module. Size and proportion of the LHP, cells and graphite sheets are for representation purposes only and do not necessary conform with the components used in this investigation.

In the design presented in Fig. 26, the LHP acts as the main thermal vector to transfer the excess heat from the battery cells to a remote heat sink, which will then be linked to a compact chiller connected to the pre-existing cooling circuit of the HVAC system of the vehicle. Graphite sheets were chosen due to their favourable bi-directional properties in terms of thermal conductivity. Due to the woven structure of graphite, it presents very high values of thermal conductivity (e.g., 300-800 W/m·K depending on manufacturer and thickness) in the x-y plane (sometimes herein referred to as *parallel* plane or with the symbol ∥), whereas in the perpendicular z direction (sometimes herein referred to as *perpendicular or normal* plane or with the symbol ⊥) the thermal conductivity is two orders of magnitude lower (e.g., 3-20 W/m·K). As such, graphite allows for good heat transfer in the vertical direction, from the cell to the LHP, and it acts as good thermal barrier to and from the adjacent cells.

4.3. Loop Heat Pipe Lumped Parameter Model

4.3.1. Lumped Parameter Modelling

To describe the thermo-fluidic dynamics and performance of LHPs, a one-dimensional LPM was developed. Lumper Parameter Modelling is a technique enabling to represent a complex continuous domain into a discrete domain, formed by a topology of discrete quantities, called *nodes* or *lumps*, where the variables of interest are calculated under simplified assumptions. In

this way, the complexity of integrating the mass, momentum and energy balance equations along actual geometries are avoided, and this is particularly useful when the system is large compared with the scale of the phenomena, such as encountered in the presence of phase-change.

In fact, a CFD analysis of flows in porous structures with phase change in a system several meters long may become unfeasible, and only a hybrid approach [325] may be a good alternative with respect to the method used in the present work. For LPMs, the thermal electrical [326] and hydraulic electrical [327] analogies are typically used. Their principal features are listed in Table 11, where R_t is the thermal resistance, R_d is the pressure resistance associated to the distributed losses (e.g., load losses due to pipe inner rugosity) and R_c is the pressure resistance associated to the concentrated losses (e.g., a bend or a change in pipe size).

Table 11. Electric analogies. R_t is the thermal resistance, R_d is the pressure resistance associated to the distributed losses and R_c is the pressure resistance associated to the concentrated losses.

Value	Electrical	Thermal	Hydraulic
Potential	V	T	P
(value on the nodes)	Voltage	Temperature	Pressure
Flux	I	$\dot{Q}$	$\dot{m}_v$
(value travelling the network)	Current	Heat Transfer Rate	Volumetric flow rate
Resistance	R	R_t	R_d, R_c
Fundamental Law	$\Delta V = RI$	$\Delta T = \dot{Q} R_t$	$\Delta P = \dot{m}_v (R_{d,c})$
(for Lumped Parameter Model)	Ohm's Law	Newton's Law	Poiseville's Law

The final mathematical form of this approach is a simplified ordinary differential equation system (ODE) for transient conditions. Hence, an approximate, but still accurate solution is achieved, significantly reducing the computational time.

The assumptions considered for the present model are:

- the model is one dimensional;
- the liquid is incompressible;
- the vapour is compressible and it is treated as an ideal gas;
- the vapour line is adiabatic while the liquid line can exchange heat with the ambient;
- the working fluid physical properties are calculated as function of temperature and/or pressure, employing polynomial fits obtained by empirical data (from Aspen Properties v10);
- given the usual small size of the LHP pipes, the hydraulic inertia of the fluid is not considered.

The proposed LPM code consists of a section for the start-up and four additional sections (evaporator, liquid and vapour line, and condenser) in accordance with the actual components division of the simplified system (Fig. 27). Following, the mathematical modelling of each section will be presented in detail in dedicated sections.

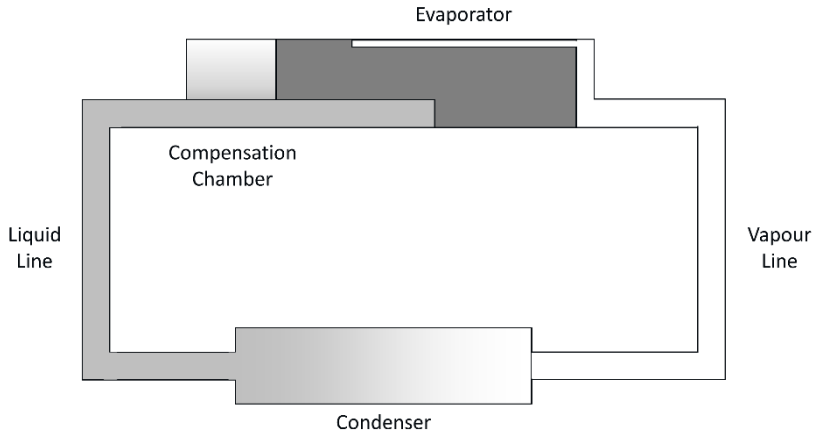

Fig. 27. Loop Heat Pipe schematic with flat evaporator, to represent the one utilized in this thesis.

4.3.2. Start-Up

Since the aim is to reproduce numerically realistic, transient applications, in the proposed numerical model initially all the LHP parts (starting conditions) are at the same ambient temperature T_{amb}. This chosen start-up scenario is when the liquid fills completely both the wick and the bayonet, with saturated vapour being only present in the vapour grooves (scenario 1 presented in Chapter 3). Due to the vacuum conditions ensured in the device, the fluid assumes the corresponding saturation pressure at the initial ambient temperature and consequently, the vapour expands immediately as soon as the external heat load is applied [304]. Since the LHP is a closed system with known, constant total specific volume v_{fr}, the start-up transient condition was treated as an isochoric heating process, and pressure needs to be incremented accordingly until the corresponding temperature at the condenser is high enough to be able to dissipate the total heat input. To do so in the LPM code, the procedure is to seek the pressure corresponding to the new value of internal energy of the liquid-vapour mixture, given by the following equation, which considers $\dot{q}$, which is the resultant of the heat rate balance introduced in equation (2), Δt, the time step and m_{evap} which is the solid mass of the evaporator:

$$u(t_{i+1}) = u(t_i) + \frac{\dot{q}\Delta t}{m_{evap}} \tag{2}$$

where the internal energy of the mixture is obtained by the following equation $u = xu_v + (1-x)u_l$ in which the initial vapour quality is estimated by the initial specific volume, i.e. filling ratio, $x = (v_{fr} - v_l)/(v_v - v_l)$. This operation is then repeated for every time step according to the classical heat rate balance equation:

$$\dot{Q}_{ext} = \dot{Q}_{cond} + \dot{Q}_{ll} + m_{evap} c_p \frac{dT_{evap}}{dt} \tag{3}$$

where c_p in this case is the average specific heat capacity associated to the evaporator, $\dot{Q}_{ext}$ is the external heat rate applied to the LHP evaporator, $\dot{Q}_{cond}$ and $\dot{Q}_{ll}$ are the heat rates dissipated at the condenser and at the liquid line, respectively (the vapour line is adiabatic). From equation (3), the parameter $\dot{q}$ in equation (2) can be easily derived:

$$\dot{q} = \dot{Q}_{ext} - \dot{Q}_{cond} - \dot{Q}_{ll} - \frac{m_{evap} c_p (dT_{evap})}{dt} = \dot{Q}_{ext} - \dot{Q}_{cond} - \dot{Q}_{ll} - \frac{m_{evap} c_p \Delta T_{evap}}{\Delta t} \tag{4}$$

To conclude the start-up calculations, the mass flow rate is obtained as:

$$\dot{m} = \frac{\dot{Q}_{ext}}{h_{LV}} \tag{5}$$

where h_{LV} is the heat of vaporisation.

4.3.3. Evaporator

A previous version of this model developed by the Author [208] utilised a cylindrical geometry for the evaporator, which comprised of a double wick system to minimize heat leakage. In the present model, only flat plate LHP evaporators are considered.

The thermal network associated to the flat plate evaporator is presented in Fig. 28. T_{wall} is the node associated to the evaporator wall, which transfers the external heat applied to the LHP, $\dot{Q}_{ext}$, through conduction and convection to both the vapour grooves (T_{vg}) and the primary wick (T_{pw}), hence explained the parallel configuration. The primary wick then is in thermal contact with the compensation chamber (T_{cc}), which in turn receives the heat and mass transfer back from the liquid line. Since the compensation chamber always contains both liquid and vapour, T_{cc} is considered as the saturation temperature for that node. It is important to point out how the vapour grooves node is not connected with the compensation chamber node, since the vapour grooves are not running the entire length of the wick. In fact, if that were the case, it would create a pressure short-circuit that would nullify the capillarity pressure gradient, de facto nullifying the characteristic one directional fluid flow of the LHP. Following, the ODE system solving the thermal network is presented in Fig. 28.

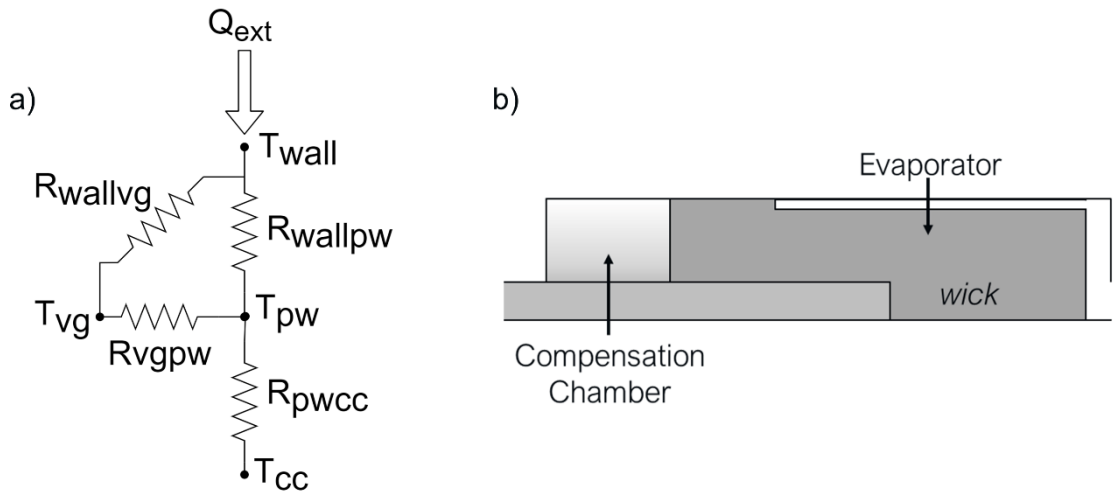

Fig. 28. Flat Plate LHP evaporator a) thermal network and b) schematic for reference.

Vapour Grooves Node

$$m_{vg}c_{p,v}\frac{dT_{vg}}{dt} = \frac{T_{pw}-T_{vg}}{R_{vgpw}} + \frac{T_{wall}-T_{vg}}{R_{wallvg}} + \dot{m}c_{p,v}\left(T_{sat}-T_{vg}\right) \quad (6)$$

Primary Wick Node

$$m_{pw}c_{pw}\frac{dT_{pw}}{dt} = \frac{T_{vg}-T_{pw}}{R_{vgpw}} + \frac{T_{wall}-T_{pw}}{R_{wallpw}} + \frac{T_{cc}-T_{\mathrm{pw}}}{R_{pwcc}} - \dot{Q}_{leak} \quad (7)$$

Evaporator Wall Node

$$m_{wall}c_{pwall}\frac{dT_{wall}}{dt} = \frac{T_{vg}-T_{wall}}{R_{wallvg}} + \frac{T_{pw}-T_{wall}}{R_{wallpw}} + \dot{Q}_{ext} \quad (8)$$

Compensation Chamber Node

$$m_{cc}c_{p,cc}\frac{dT_{cc}}{dt} = \dot{m}c_p(T_{\mathrm{cc}}-T_1) + \dot{Q}_{leak} + \frac{T_{amb}-T_{cc}}{R_{amb,cc}} + \frac{T_{pw}-T_{cc}}{R_{pwcc}} \quad (9)$$

where the terms on the left-hand side are the transient heat capacity terms, and on the right-hand side there are the heat transfer rate components. The last term on eq (6) is considering the amount of superheat given to the vapour exiting the evaporator; eq (7) assumes the heat leakage as 10% of the external heat, as suggested by literature [302]; eq (9) received the heat leakage as well as the heat and mass transfer from the liquid line, where T_1 represents the temperature of the last node of the liquid line. The index vg refers to the vapour grooves (considering the temperature at the Outlet of the vapour grooves); pw stands for primary wick (or only wick in case of flat evaporator); $wall$ stands for the evaporator wall; sat indicates the saturation conditions; cc stands for the compensation chamber; amb stands for ambient (used in the thermal resistance for free convection); $\dot{Q}$ is heat power [W] and ext and $leak$ are respectively the heat applied to the evaporator and leakage to the compensation chamber; m, c_p and T are

respectively mass [kg], specific mass heat capacity [J/kg K] and temperature [K]. Heat exchanged between the nodes due to their temperature difference is regulated by their thermal resistances, listed below, where h_c is the convection heat transfer coefficient [W/m K], t is thickness [m], k is thermal conductivity and A is cross surface [m^2].

$$R_{vgpw} = \frac{\frac{1}{h_{cvg}A_{vg}} \cdot \frac{t_{pw}}{k_{pw}A_{vg}}}{\frac{1}{h_{cvg}A_{vg}} + \frac{t_{pw}}{k_{pw}A_{vg}}} \tag{10}$$

$$R_{wallvg} = \frac{1}{h_{cvg}A_{vg}} + \frac{t_{ev}}{k_{wall}A_{vg}} \tag{11}$$

$$R_{wallpw} = \frac{t_{ev}/2}{k_{wall}A_{pw}} + \frac{\frac{1}{h_{cvg}A_{vg}} \cdot \frac{t_{pw}}{k_{pw}A_{pw}}}{\frac{1}{h_{cvg}A_{vg}} + \frac{t_{pw}}{k_{pw}A_{pw}}} \tag{12}$$

$$R_{pwcc} = \frac{L_{pw}}{k_{pw}A_{pwcc}} + \frac{L_{cc}}{k_l A_{pwcc}} \tag{13}$$

$$R_{ambcc} = \frac{1}{h_{c,cc}A_{cc}} \tag{14}$$

where $h_{c,vg} = 3.66\frac{k_l}{2r_{vg}}$ [302] is the convection coefficient inside the vapour grooves. R_{vgpw} and R_{wallpw} are expressed as parallel resistances as it is considered that the edge of the wick is interspersed by vapour grooves, instead of being a uniform contour. For this reason, the evaporator wall will be in parallel contact with both vapour grooves and wick.

Looking at the pressure values, starting from pressure P_1 at the end of the liquid line and using the electric-hydraulic analogy the pressure inside the bayonet or at the end of the compensation chamber (P_2) can be calculated, following a readaptation of the Poiseville's law equation [328], expressing the velocity as function of the mass flow rate:

$$P_2 = P_1 - \dot{m}R_{d12} \qquad R_{d12} = \frac{8\mu_l L_{cc}}{\rho_l \pi r_{cc,i}^4} + \frac{8\mu_l L_{bay}}{\rho_l \pi r_{bay,i}^4} \tag{15}$$

In order for the fluid to circulate inside the device, a positive ΔP_{cap} due to capillarity needs to be applied by the wicks, governed by the Laplace-Young equation [304]:

$$\Delta P_{cap} = \frac{2\sigma}{\bar{r}} cos\theta \tag{16}$$

where $\overline{r}$ is the medium pore radius and θ is the equilibrium contact angle of the menisci in the wick pores. The curvature of the menisci changes naturally in order for the capillary pressure to balance the total pressure in pressure drop in the loop [329], hence the numerical model controls that the total drop does not exceed the maximum pumping power of the wick:

$$\Delta P_{cap,max} \geq \Delta P_{vg} + \Delta P_{vl} + \Delta P_{cond} + \Delta P_{ll} \tag{17}$$

To conclude the pressure side analysis for the evaporator, the pressure drop inside the vapour grooves is calculated:

$$P_{vg} = P_{pw} - \dot{m} R_{dvg} \qquad R_{dvg} = \frac{8\mu_v L_{vg}}{\rho_v \pi r_{vg,i}^4} \tag{18}$$

4.3.4. Vapour Line model

Vapour is assumed to be an ideal and compressible gas, and the vapour line is assumed to be adiabatic. Therefore, standard polytropic relations with exponent k_g are used [330]:

$$TP^{\frac{1-k_g}{k_g}} = cost \tag{19}$$

where $k_g = \frac{c_p}{c_v}$ is the adiabatic index.

From the evaporator values, temperature and pressure at the start of the vapour line are known, hence:

$$P_{i+1} = P_i - \dot{m}(R_{d,i} + R_{c,i}) + g\rho_v \Delta z_{vl} \tag{20}$$

where $R_c = \frac{k_c v}{2\pi r_i^2}$ and k_c is a parameter that takes into account the additional pressure loss given by a turn [328].

In eq. (20), the *i* subscript is the node number and the last term is the pressure drop due to gravity, which depends from the position of the condenser with respect to the evaporator, i.e., if the latter is at a higher elevation Δz_{vl}, will have a negative sign. Using the polytropic relations the iterative procedure is continued for every vapour line node:

$$T_{i+1} = T_i \left(\frac{P_i}{P_{i+1}}\right)^{\frac{1-k_g}{k_g}} \tag{21}$$

$$\rho_{i+1} = \rho_i \left(\frac{P_{i+1}}{P_i}\right)^{\frac{1}{k_g}} \tag{22}$$

$$v_{i+1} = \frac{\dot{m}}{\rho_{i+1}\,\pi r_i^2} \tag{23}$$

This sequence will be executed for every node resulting in the calculation of the values for temperature and pressure at the inlet of the condenser.

4.3.5. Condenser model

The first node of the condenser is considered to have a vapour quality of one, assuming that no early condensation happens inside the vapour line. The vapour superheat is not common and desirable, so this has been disregarded. Condenser is assumed to be horizontal, in order to use empirical correlation for the internal convection heat transfer coefficient.

The way the fluid condenses inside the tube is strongly dependent upon its velocity. In fact, for low velocity vapour streams, condensation occurs with the condensate moving from the upper portion of the tube to the bottom and then carry on longitudinally alongside the vapour, creating a complete, constant and uninterrupted interface between the phases. This is called stratified flow (Fig. 29a). Instead, when the vapour velocity is high, shear forces dominate over gravity forces and the liquid takes an annular shape (hence annular flow – Fig. 29b) creating a film around the vapour, with a negative thickness gradient going from the bottom to the top of the tube. For more information on the flow patterns on horizontal tubes, please refer to the works of Coleman and Garimella [331].

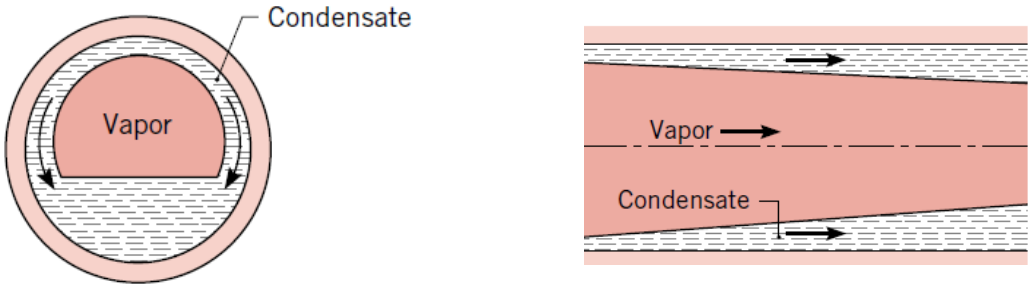

(a) (b)

Fig. 29. Condensation in horizontal tubes: (a) stratified flow, due to low vapour velocities; (b) annular flow, due to large vapour velocities [296].

The type of flow pattern influences the empirical model that can be used to calculate the internal convection heat transfer coefficient. In the produced LPM, two different models have been used, in accordance with the two flow patterns considered depending upon the Reynolds vapour number at the inlet of the pipe. Following the two correlations are introduced.

Stratified Flow	$Re_v = \frac{\rho_v v_v D}{\mu_v} < 35000$	Chato Correlation [332]	(24)
Annular Flow	$Re_v = \frac{\rho_v v_v D}{\mu_v} > 35000$	Shah Correlation [333]	(25)

4.3.5.1. Stratified Flow

In the case of stratified flow, the Chato correlation is used, where an equivalent internal convection heat transfer coefficient is calculated, presented in equation (25).

$$\bar{h}_c = 0.555 \left[\frac{g \rho_l (\rho_l - \rho_v) k_l^3 h'_{fg}}{\mu_l (T_{sat} - T_s) D} \right]^{1/4} \tag{26}$$

where h'_{fg} is the modified latent heat defined as $h'_{fg} = h_{fg} + \frac{3}{8} c_{p,l}(T_{sat} - T_s)$. In this case, T_{sat} and T_s are the temperatures of the saturated fluid and the external body which is exchanging heat with, respectively. It can be appreciated as equation (26) does not depend on the vapour quality of the working fluid, but only on the physical properties at the inlet and the inner diameter D of the pipe. The liquid physical properties are evaluated at the film temperature defined as $T_f = (T_{sat} + T_s)/2$ whereas vapour density and the modified latent heat are evaluated at saturation temperature.

This allows for a simpler solution approach where the heat power dissipated by the condenser $\dot{Q}_{cond}$ is calculated as in equation (27), introducing the external heat transfer coefficient inside the condenser thermal resistance.

$$\dot{Q}_{cond} = \frac{T_{c,in} - T_{sat}}{R_t} \tag{27}$$

The calculation of the external heat transfer coefficient will be presented in the next chapter, where the overall system will be introduced.

4.3.5.2. Annular Flow

The annular flow is characterized by the vapour occupying the core of the annulus, diminishing in diameter as the thickness of the outer condensate layer increases in the flow direction. As such, the formulation of the heat transfer coefficient depends on the liquid film thickness which will vary in time and space depending on the heat transfer condition. In order to describe this condensation mechanism, the Shah correlation is chosen [333]:

$$h_{c,i} = \alpha_f \left[(1 - x)^{0.8} + \frac{3.8 x^{0.76} (1 - x)^{0.04}}{P^{*0.38}} \right] \tag{28}$$

where $\alpha_f = 0.023 Re_l^{0.8} Pr_l^{0.3} \frac{k_l}{2r_i}$ is the liquid convection coefficient from Dittus-Boelter [334], where $Pr = {c_p \mu}/{k}$ is the Prandtl number and P^* is the reduced pressure of the fluid defined as the actual pressure divided by the critical pressure.

It is evident that equation (28) depends on the vapour quality x of the working fluid, which will vary along the axis of the condenser. Hence, to fully characterize the condenser when the flow pattern is annular, the vapour quality in every point has to be known. This changes the way the condenser is analysed. A nodes discretization needs to be applied to the condenser geometry, considering that the total mass inside the total number of condenser nodes n_c needs to maintain the mass of working fluid passing through the node during the integration time step:

$$m_i = \rho_l \pi r_i^2 L_x = \rho_l \pi r_i^2 \frac{L_{cond}}{n_c} \tag{29}$$

$$n_c = \frac{\rho_l \pi r_i^2 L_{cond}}{m_i} = \frac{\rho_l \pi r_i^2 L_{cond}}{\dot{m} h_{step}} \tag{30}$$

Since the mass flow rate is a function of the external heat rate (equation (5)), the number of nodes is also function of the external heat. Hence, the lower the heat input, the higher the necessary number of nodes and thus the computational time.

The physical properties in two-phase conditions are calculated as equivalent properties with the homogeneous formulation for density and a novel viscosity [335] formulation that works best for annular and bubble flow:

$$\rho_{2p} = x\rho_v + (1-x)\rho_l \tag{31}$$

$$\mu_{2p} = \mu_l - 2.5\mu_l \left(\frac{x\rho_l}{x\rho_l + (1-x)\rho_v} \right)^2 + \left(\frac{x\rho_l (1.5\mu_l + \mu_v)}{x\rho_l + (1-x)\rho_v} \right) \tag{32}$$

The iterative procedure to calculate the vapour quality at every node starts from the pressure evaluation at every node:

$$P_i = P_{i-1} - \dot{m}(R_d + R_c) \tag{33}$$

where Rd and Rc are respectively the load losses due to distributed $R_d = \frac{8\mu_{2p} L_x}{\rho_{2p} \pi r_i^4}$ and concentrated losses $R_c = \frac{k_c v}{2\pi r_i^2}$, with k_c being an empirical parameter accounting for change of pipe size and/or turns [328]. In order to calculate the physical properties at every node, the vapour quality is needed.

In this model, to reduce the required computational time, a more traditional approach than the one used in [208] is taken. Since the fluid is condensing, it is in saturated state, thus by

solving the pressure problem and knowing the saturation pressure, it is possible to find the saturation temperature at the same node. From there, the heat rate lost at the node $\dot{Q}_{c,i}$ is computed, which equals the enthalpy lost while travelling to the following node, h_{i+1}. Hence also the two-phase enthalpy at the following node is computed. Knowing the saturation temperature, the vapour and liquid enthalpy are calculated and finally used to calculate the vapour quality as a function of the enthalpy loss.

Finally, the vapour quality is calculated as function of the enthalpy loss. Since a tube in tube Heat Exchanger (HEX) is used in the experimental investigation presented in the next Chapter, the same type is modelled in this work (Fig. 30).

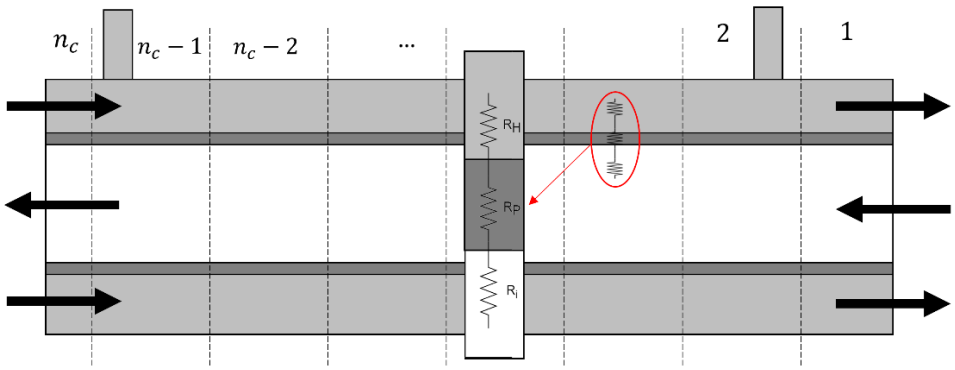

Fig. 30. Schematic model for tube in tube heat exchanger in the condenser section of the LPM concerning the LHP part; R_H,R_P,R_i are the thermal resistances for the heat exchanger, pipe and internal working fluid, respectively.

$$T_{cond,i} = f_{sat}\left(P_{cond,i}\right) \tag{34}$$

$$\dot{Q}_{cond,i} = \frac{T_{HEX} - T_{cond,i}\left(P_{cond,i}\right)_{sat}}{R_{HEX} + R_P + R_{cond}} = \dot{m}(h_{i+1} - h_i) \tag{35}$$

$$h_{i+1} = \frac{\dot{Q}_{cond,i}}{\dot{m}} + h_i \tag{36}$$

$$h_{v,l} = f_{sat}(T_{cond,i}) \tag{37}$$

$$x_{i+1} = f_{sat}(h_{i+1}) = \frac{h_{i+1} - h_l}{h_v - h_l} \tag{38}$$

with the thermal resistances being:

$$R_{HEX} = \frac{1}{\alpha_l A_{HEX}} \quad R_{cond} = \frac{1}{h_{c,i} A_{HEX}} \quad R_p = \frac{ln\left(\frac{r_{cond,e}}{r_{cond,i}}\right)}{2\pi k_c L_x}$$

In order to gauge the benefit of using a passive two-phase device on the power consumption, the mass flow rate at the HEX side was calculated. In the LPM, a section

modelling a shell and tube HEX by means of the ε-NTU method is added and provided in Appendix.

First, there is the need to calculate the heat rate that needs to be removed from the condenser at every time step, which is equal to the difference in enthalpy of the working fluid:

$$\dot{Q}_{cond} = \dot{m}(h_l - h_v) \tag{39}$$

This is the heat rate that will need to be matched by the HEX in order to obtain full condensation at the end of the condenser. Hence the assumption made here is that the mass flow rate for the HEX gets updated at every time step to achieve full condensation and no subcooling.

Second, the HEX internal convection heat transfer coefficient needs to be calculated. Assuming that the HEX working fluid (ethylene glycol, in this case) stays always in liquid state, allows to use the Dittus-Boelter correlation:

$$\begin{gathered} Re_{HEX} > 10000 \\ 0.7 < Pr_{HEX} < 160 \\ L_{HEX} > 20 r_{HEX} \\ h_{c,e} = 0.023 \left(Re_{HEX}^{4/5}\right)\left(Pr_{HEX}^{1/3}\right)\left(\frac{k_{l,HEX}}{2r_{HEX}}\right) \end{gathered} \tag{40}$$

For the condenser internal convection heat transfer coefficient $h_{c,i}$, the correlation for annular and stratified flow detailed in the previous sections are used. At this point, knowing both heat transfer coefficient, the overall heat transfer coefficient UA is calculated:

$$\frac{1}{UA} = \frac{1}{h_{c,i}A_{c,i}} + \frac{R_{fouling}}{A_{c,i}} + \frac{log\left(\frac{r_{c,e}}{r_{c,i}}\right)}{2\pi k_{c,i} L_{c,i}} + \frac{R_{fouling}}{A_{HEX}} + \frac{1}{h_{c,e}A_{HEX}} \tag{41}$$

where $R_{fouling}$ is a fouling (i.e., accumulation of working fluid residuals on the inner surface of heat exchanger that ruins the performance) coefficient for refrigerants; on the right term of eq. (42) are considered both the internal and external heat transfer phenomena for convection as well as the fouling effect and the conduction thought the condenser pipe wall.

The last thing required for the number of transfer unit (NTU) is to calculate the minimum thermal capacity C_{min}. Remembering that the specific heat during phase change is infinite:

$$\begin{cases} C_{HEX} = \dot{m}_{HEX}\, c_{p,HEX} \\ C_{cond} = \dot{m}\, c_{p,cond} = \infty \end{cases} \xrightarrow{yields} C_{min} = C_{HEX} \tag{42}$$

hence, following the method it leads to:

$$NTU = \frac{UA}{C_{min}}$$

$$\begin{aligned} \varepsilon &= 1 - e^{-NTU} \\ \dot{Q}_{max} &= C_{min}\left(T_{c,in} - T_{HEX,in}\right) \\ \dot{Q}_{HEX} &= \varepsilon \dot{Q}_{max} \\ T_{HEX,out} &= T_{HEX,in} + \frac{\dot{Q}_{HEX}}{C_{cold}} \end{aligned} \tag{43}$$

If $\dot{Q}_{HEX} \neq \dot{Q}_{cond}$, that means that full condensation has not been reached or subcooling conditions have arisen. Thus, in order to avoid that, a subroutine changes the m_{HEX} until the absolute difference between the heat exchanged from the HEX (eq. 44) and the condenser (eq. 40) is less than 0.1W.

4.3.6. Liquid Line model

The liquid is incompressible and subcooled, and the temperature of the surroundings T_{amb} is known from the boundary conditions. The heat exchange at the node is equal to:

$$Q_{ll,i} = \frac{T_{amb} - T_i}{R_{t,i}} \tag{44}$$

where:

- $R_{t,i} = \frac{1}{h_{ce,i}A_{e,i}} + \frac{1}{h_{ci,i}A_{i,i}}$;
- $h_{ci,i} = 0.023Re^{0.8}Pr^{ndb}\frac{k_l}{2r_i}$ with *ndb* being Dittus-Boelter coefficient which is 0.4 for heating and 0.3 for cooling [296] and $h_{ce,i}$ depending on the application;

For the pressure problem:

$$P_{i+1} - P_i = \dot{m}(R_{d,i} + R_{c,i})) - g\rho_l \Delta z_{ll} \tag{45}$$

where $g\rho_v \Delta z_{ll}$ is the pressure drop due to gravity, which in this case assists the fluid motion.

To close the solution cycle:

$$Q_{amb,i} = \dot{m}(h_{i+1} - h_i) \tag{46}$$

$$\Delta h = \frac{Q_{amb,i}}{\dot{m}} = c_p \Delta T \tag{47}$$

$$T_{i+1} = T_i - \frac{Q_{amb,i}}{\dot{m}c_p} \tag{48}$$

The temperature of the last node of the liquid line is the new T_1 for the evaporator at the following time step, and thus the loop is closed and repeated.

4.4. Validation of the Loop Heat Pipe Lumped Parameter Model

In a previous work by the Author [208], the LPM for the LHP has been validated for three different working fluids and different geometries, availing by experimental data available in literature. Satisfactory results were obtained reproducing the results by Pouzet et al. [336], Tharayil et al.[337] and Chen et al. [338].

In the first paper [336] the aim of the authors was to investigate the instability of the cyclic behaviour of the device, with particular attention to the liquid-vapour interface in the compensation chamber. The procedure was to examine the response to both upward and downward swings of the externally applied heat, comparing experimental results with their simulations. The externally applied heat power was varied from 200 W to 400 W and then back to 200 W. The working fluid is R134a and the chosen materials are Fortal® Aluminium Alloy for the evaporator, copper for the condenser, vapour line and liquid line tubes and steel for the compensation chamber.

A comparison between the numerical and experimental results with the numerical results of the present LPM is displayed in Fig. 31, which shows the comparisons between the temperatures of the evaporator wall and of the compensation chamber, and temperatures of the vapour grooves and the primary wick (that in [336] are described as the temperatures above and below the meniscus). From Fig. 31(a) the comparison indicates that the model is able to capture the trend of the evaporator wall temperature and of the compensation chamber with small absolute error of 0.9°C and 2.7 °C, respectively. It also predicts the overshoot in the upward variation of external heat, something that was not captured by the corresponding numerical model in [336]. The comparison in Fig. 31(b) shows that the model is able to predict the opposite trends of the vapour grooves and primary wick nodes. In this case the errors are 2.3°C for the for the vapour grooves temperature and 5.5°C for the primary wick temperature. In the analysed work [336], it is suggested that this inverse pattern between the wick and the vapour grooves allows the evaporator to be thermally stable.

In the second paper [337], the aim was to study the effect of different filling ratios on the heat transfer performance of a miniature LHP. A finned geometry was used for the evaporator to increase the allowable heat flux. The LHP was made of copper and the working fluid was water. In the present work the response of the temperatures to varying heat load conditions is numerically reproduced. In Fig. 32 is the comparison between the evaporator wall temperatures, with the LHP subjected to a stepwise increment of the external heat rate of 40 W each step, from 40 W up to 380 W.

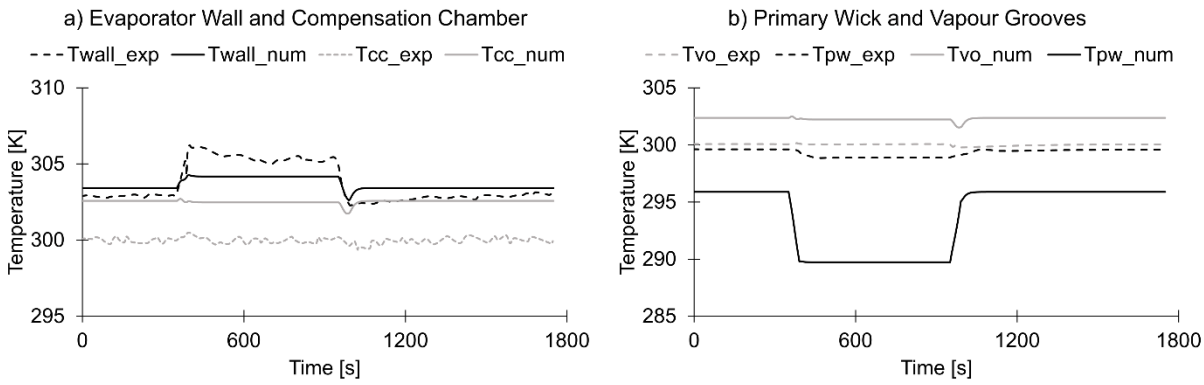

Fig. 31. Validation of the LHP code from [336] with the r134a fluid, showing the comparison of the temperature results after a heat loads swing from 200W to 400W and back to 200W: a) evaporator wall and compensation chamber temperatures; b) primary wick and vapour grooves. In these graphs, the temperature of the vapour grooves is indicated by T_{vo}, as in vapour origin, to respect the position of the measurement described in the referenced paper.

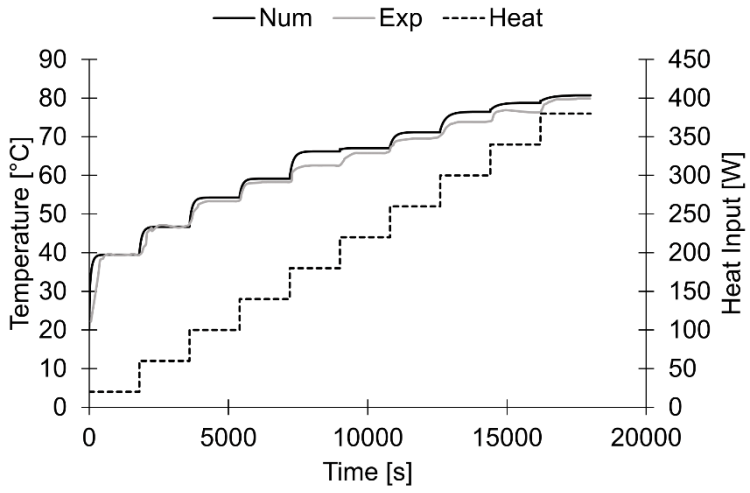

Fig. 32. Validation of the LHP code from [337] with water as working fluid, showing the comparison of the evaporator wall temperatures.

Fig. 32 reveals an excellent agreement between the experimental measurements and the numerical predictions, leading to an average absolute error of 1.5°C. In the third paper considered for the validation of the present model ([338]), a disk shaped evaporator LHP was considered and the maximum heat load was investigated. The tube material is stainless steel and the working fluid is ammonia. Following is the proof of the validation with two different cycles of heat load variations, considering two nodes in the evaporator, the wall and the primary wick:

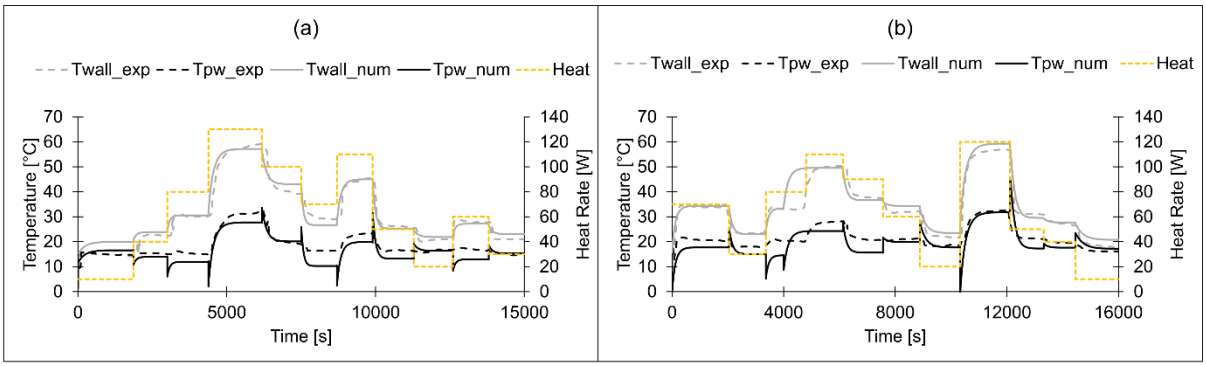

Fig. 33. Validation of the LHP from [338] with ammonia as working fluid: comparison of evaporator wall and primary wick temperatures for (a) power cycle of 10 40-80-130-100-70-110-50-20-60-30 W and (b) 70-30-80-110-90-60-20-120-50-40-10 W.

Fig. 33 shows again a good prediction of the experimental results. The average absolute errors are 1.6 °C on T_{wall} and 2.5°C for T_{pw} for case (a) and 1.3°C and 2.8°C for case (b), respectively. The two cases present similar errors for the two nodes, nevertheless there is a slightly bigger error in the prediction of the primary wick, and this is due to the fact that in the lumped parameter model this node considers also the solid properties of the wick, not only the working fluid.

Concluding, the presented validation campaign proved the reliability of the developed LPM to predict the transient temperature evolution of a LHP, considering different heat fluxes, geometries, working fluids and manufacturing materials. This gives enough confidence in moving forward to move to the second part of the modelling activities, involving the modelling of the battery cell module, which will be coupled with the LPM detailed in this chapter.

4.5. Battery Cell Modelling

In order to evaluate the feasibility of the proposed TMS design, a new LPM was created to simulate the temperature increments and the heat distribution during different driving cycles of the cell and graphite assembly.

4.5.1. Heat Generation Rate Modelling

As introduced in Chapter 2, a battery cell generates heat depending on their utilization, thus different driving cycles give different heat generation rates profile. The heat generation rate of a battery can be described from the equation proposed by Bernardi et al. [339]:

$$\dot{Q} = I\left(U - V - T\frac{dU}{dT}\right) \tag{49}$$

with I being the current, T the temperature [K], U the open circuit voltage (which is the potential difference existing when no load is connected to the circuit) and V is the working voltage of the cell. The first term on the right side of equation (49) is the irreversible over-potential heat due to Ohmic losses in the cell, charge-transfer over potentials at the interface, and mass transfer limitations. The second term is reversible entropic heat from electrochemical reactions. Since it is assumed that there is only one electrochemical reaction occurring in these batteries [340], equation (49) can be reformulated as :

$$\dot{q} = R_i i^2 - i \cdot T \frac{\Delta S}{F} \tag{50}$$

where $\dot{q}$ is the rate of internal heat generation per unit volume, R_i is the internal equivalent resistance of the unit cell, i is the discharge current of the cell per unit volume, ΔS is the entropy change and F is the Faraday number (96485 C/mol). The second term on the right is the reversible heat, which is usually neglected in thermal problems. The internal resistance of the cell can be expressed as a function of the SOC, which is a relative quantity that denotes the capacity that is currently available as a function of the rated capacity and the utilization patterns, and it is defined as [341]:

$$SOC(t) = SOC(t_0) - \frac{\int_0^t I(t)dt}{C_0(t_0)} \tag{51}$$

where $SOC(t_0)$ is the initial state of charge, $I(t)$ is the instantaneous discharge current, t is the discharge duration and C_0 is the initial electric capacity of the battery (amount of the electric charge that can be delivered from the cell at a specific voltage). Seldom a factor η, called Coulomb efficiency, is used inside the integral, which reflects the ratio between the discharge and charge capacity of a same cycle, as function of the current and the temperature [342]. The SOC is the quantity influenced by the driving cycle to which the vehicle is subjected. Therefore, expressing the driving cycle as a function of SOC allows to re-create the connected heat generation profile of the cells.

The physical properties of the cell and its heat generation rate were provided by Ricardo, the industrial collaborator of the present PhD project.

4.5.2. Cell and Graphite Assembly Thermal Network

Considering the repetitive nature of the design schematised in Fig. 26 (cell-graphite, cell-graphite, and so on), the developed thermal network describes the behaviour of one cell only. In order to simulate whole modules or packs, their cells are assumed to be at the same

temperature, hence allowing to calculate the heat rate applied to the LHP by multiplying the heat rate generated by the single cell by the number of cells.

Other assumptions of this model are:

- Perfect thermal contact between the surfaces.
- Electrolytic convection inside the battery is neglected.
- Inside the coupled cell-graphite control volume only heat transfer by conduction is considered.
- The open sides of the cells are in contact with ambient air at room temperature and hence a free convection heat transfer boundary condition is applied.
- In accordance with the industrial collaborator and being between the most commonly used cells type in commercially available vehicles, prismatic cells are chosen as cell type.

In Fig. 34a, the thermal network associated to a single cell and graphite assembly is presented.

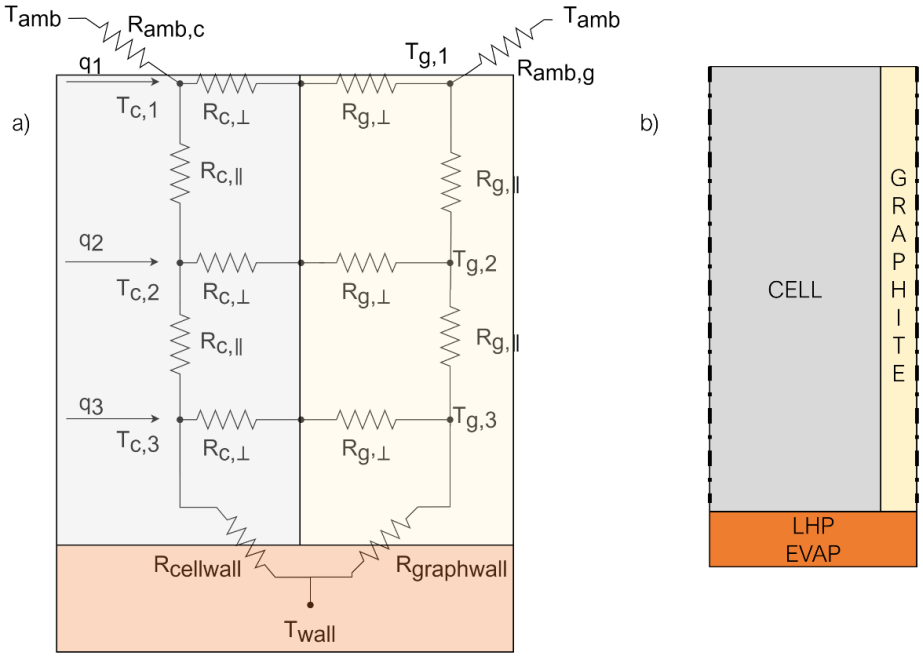

Fig. 34. a) Thermal network of a cell-graphite assembly and b) cell-graphite schematic for reference. The subscripts *c* and *g* refer to cell and graphite respectively. The chosen colours and boundary positions are only for display purposes and not representative of the actual geometry.

The battery cell is subdivided in three equidistant nodes with three corresponding nodes on the graphite side. The system of Ordinary Differential Equations (ODEs) that needs to be solved for the proposed thermal network is presented below:

$$m_c c_{p,c} \frac{dT_{c,1}}{dt} = q_1 + \frac{T_{amb} - T_{c,1}}{R_{amb,c} + R_{c,\parallel}} + \frac{T_{g,1} - T_{c,1}}{R_{g,\perp} + R_{c,\perp}} + \frac{T_{c,2} - T_{c,1}}{R_{c,\parallel}} \quad (52)$$

$$m_c c_{p,c} \frac{dT_{c,2}}{dt} = q_2 + \frac{T_{c,1} - T_{c,2}}{R_{c,\parallel}} + \frac{T_{g,2} - T_{c,2}}{R_{g,\perp} + R_{c,\perp}} + \frac{T_{c,3} - T_{c,2}}{R_{c,\parallel}} \quad (53)$$

$$m_c c_{p,c} \frac{dT_{c,3}}{dt} = q_3 + \frac{T_{c2} - T_{c,3}}{R_{c,\parallel}} + \frac{T_{g\,3} - T_{c,3}}{R_{g,\perp} + R_{c,\perp}} + \frac{T_{wall} - T_{c,3}}{R_{cellwall}} \quad (54)$$

$$m_g c_{p,g} \frac{dT_{g,1}}{dt} = \frac{T_{amb} - T_{g,1}}{R_{amb,g} + R_{g,\parallel}} + \frac{T_{c,1} - T_{g,1}}{R_{g,\perp} + R_{c,\perp}} + \frac{T_{g,2} - T_{g,1}}{R_{g,\parallel}} \quad (55)$$

$$m_g c_{p,g} \frac{dT_{g,2}}{dt} = \frac{T_{g,1} - T_{g,2}}{R_{g,\parallel}} + \frac{T_{c,2} - T_{g,2}}{R_{g,\perp} + R_{c,\perp}} + \frac{T_{g,3} - T_{g,2}}{R_{g,\parallel}} \quad (56)$$

$$m_g c_{p,g} \frac{dT_{g,3}}{dt} = \frac{T_{g,2} - T_{g,3}}{R_{g,\parallel}} + \frac{T_{c,3} - T_{g,3}}{R_{g,\perp} + R_{c,\perp}} + \frac{T_{wall} - T_{g,3}}{R_{graphwall}} \quad (57)$$

where:

- m_c and m_g are the total mass of the battery cell and graphite sheet, respectively, divided by three, as three are the nodes;
- $c_{p,c}$ and $c_{p,g}$ is the equivalent specific heat of the cell and graphite, respectively;
- $T_{c,i}$ and $T_{g,i}$ are the temperature of the 3 nodes inside the cell and graphite, respectively;
- q_i is the heat rate generated by the cell divided by three, which is applied to the cell nodes; this is considered as a variable boundary condition that increases the cell internal temperature and it derives from equations (49) and (50);
- T_{wall} is the temperature of the LHP evaporator wall.

Following in Table 12 the formulas used to calculate the thermal resistances by conduction are reported:

Table 12. Thermal Resistance and heat exchange areas employed the cell-graphite assembly LPM.

Thermal Resistances	Heat Transfer Areas	
$R_{amb,\,c} = \frac{1}{h_c A_{c,\parallel}} + R_{c,\parallel}$	$A_{c,\parallel} = t_c l_c$	(58)
$R_{amb,g} = \frac{1}{h_c A_{g,\parallel}} + R_{g,\parallel}$	$A_{g,\parallel} = t_g l_g$	(59)
$R_{c,\perp} = \frac{t_c}{k_{\perp,c} A_{c,\perp}}$	$A_{c,\perp} = \frac{h_c l_c}{3}$	(60)

$$R_{c,\parallel} = \frac{H_c/4}{k_{\parallel,c} A_{c,\parallel}} \tag{61}$$

$$R_{g,\perp} = \frac{t_g}{k_{\perp,g} A_{g,\perp}} \qquad A_{g,\perp} = \frac{H_g l_g}{3} \tag{62}$$

$$R_{g,\parallel} = \frac{H_g/4}{k_{\parallel,c} A_{g,\parallel}} \tag{63}$$

$$R_{cellwall} = \frac{t_{ev}}{k_{wall}(t_{cell} + t_g) l_g} + \frac{t_{ev}/2}{k_{wall} A_{cellwall}} + R_{c,\parallel} \qquad A_{cellwall} = w_{wall} t_c \tag{64}$$

$$R_{graphwall} = \frac{t_{ev}}{k_{wall}(t_c + t_g) l_g} + \frac{t_{ev}}{k_{wall} A_{graphwall}} + R_{g,\parallel} \qquad A_{graphwall} = w_{wall} t_g \tag{65}$$

where h_c is the convection heat transfer coefficient, which for free convection is usually set at 10 W/m^{2}K; the symbols ∥ and ⊥ are referring to the parallel and perpendicular direction to the plane identified by the graphite sheet; t,H,l are thickness, height and length respectively; k_i is the thermal conductivity in the different plane directions; finally, t_{ev} is the thickness of the evaporator wall. Finally, in the resistances $R_{cellwall}$ and $R_{graphwall}$ an empirical term accounting for the contact resistances with the LHP is considered.

4.5.3. Verification of Cell-Graphite Thermal Network

In order to verify the reliability of the new proposed thermal network, a verification procedure has been carried out by means of Thermal Analysis via Finite Volume Method (FVM) simulations on ANSYS Fluent 20.2®. Comparison is made between the cell temperature results from the proposed thermal network and the FVM model under the same boundary conditions.

The material physical properties are reported in Table 13. The chosen material for the LHP evaporator wall for the validation processes was Stainless Steel (SS). The modelled geometry and the associated mesh are presented in Fig. 35.

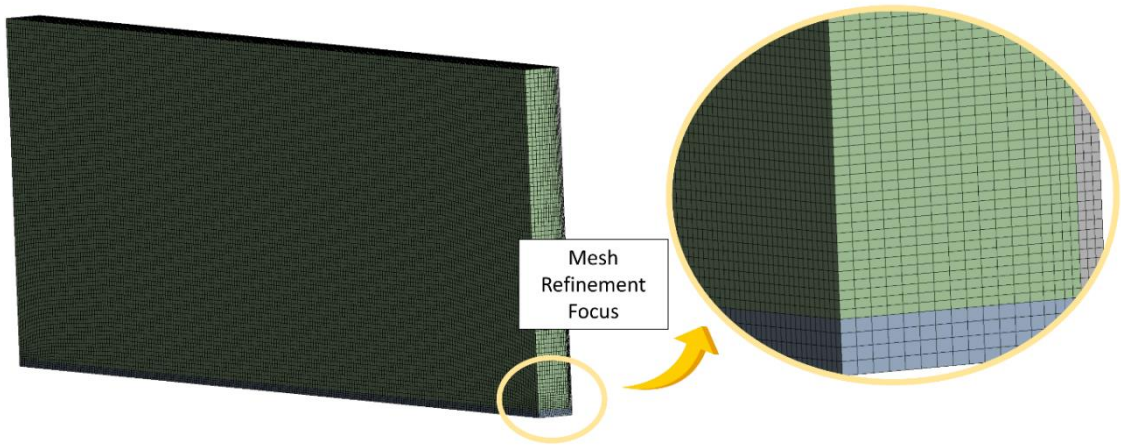

Fig. 35. Modelled geometry for the validation of the cell-graphite assembly.

Table 13. Material properties used in the validation processes. Graphite values come from Panasonic PGS sheet while cell equivalent properties were provided by Ricardo plc.

Material	Density [kg/m3]	Thermal conductivity [W/m K] inplane - thruplane	Specific Heat [J/kg K]
Cell	3720	46-0.7	1726
Graphite	1716	350-10	810
SS	7800	14.4-14.4	502

In Fig. 35 is evident that care has been taken to maintain three elements along the minimum thickness of the different bodies. Mesh statistics are 312,732 elements, with maximum skewness of 0.14 (<0.95) and minimum orthogonal quality of 0.88 (>0.15). Finally, the maximum aspect ratio of the cells was 12.58 (<35). From these parameters, and the mesh independency study shown in Fig. 36, the computational mesh quality was deemed acceptable.

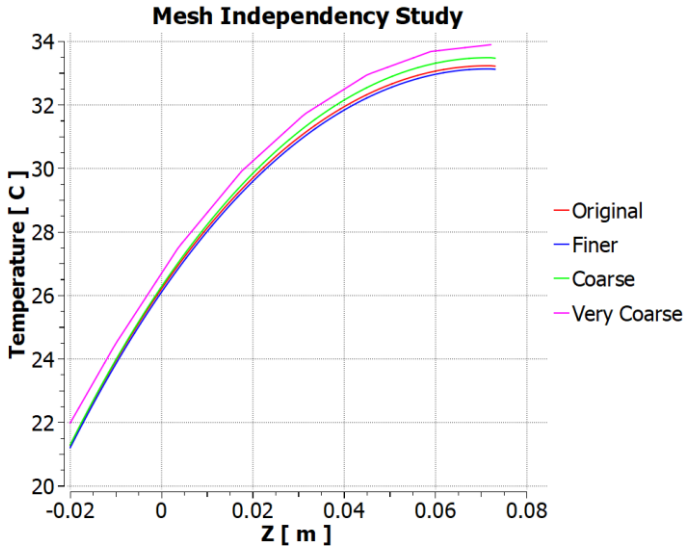

Fig. 36. Mesh Independency study results – temperature evolution on the z axis, (Coarse 165888 elements, Original 223600 elements, Finer 312732 elements).

The boundary condition applied in the FVM simulations is free convection to the top of the cell and graphite ($h_c = 10\, W/m^2K$). To replicate the heat generation rate of the cell, a volumetric heat generation value has been set dividing the total heat generated from the cell by its volume. This heat is mainly directed to the LHP evaporator wall, which is fixed at a constant temperature of 20°C. Since the aim of these simulations is only to validate the cell-graphite assembly thermal network, this assumption is considered acceptable. Temperature in the cell will increase until thermal equilibrium is reached, which is when the heat flux coming inside the LHP evaporator wall equals the total generated heat from the cell (minus the small losses due free convection).

The thermal network has been implemented in Octave v6.1.0, with the same physical properties and boundary conditions of the FVM model. Similarly, the value T_{wall} in equation (54) and (57) has been kept constant at 20°C and the simulation has been let running until steady state condition were reached. The value q_i has been set as a third of the total heat generated value imposed on the FVM simulation. Two heat generation rates for the cell were considered, low heat rate (5 W) and high heat rate (50W). Following, the comparison between the two simulations is presented, by first showing the FVM results in Fig. 37 and then the result from the transient thermal network.

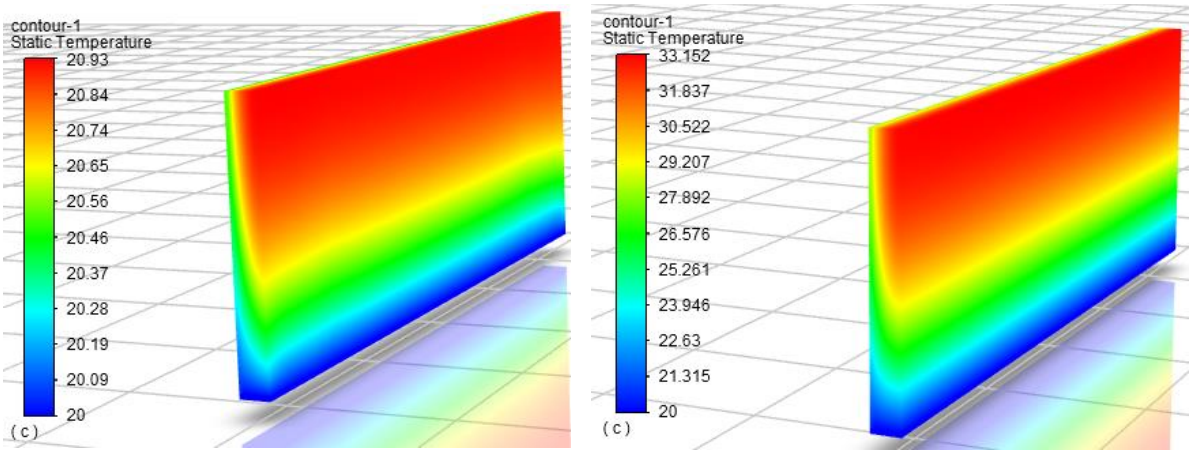

a) 5 W b) 50 W

Fig. 37. Fluent FVM results for the validation of the cell-graphite assembly thermal network with two cell heat generation rates conditions: a) 5W and b) 50W.

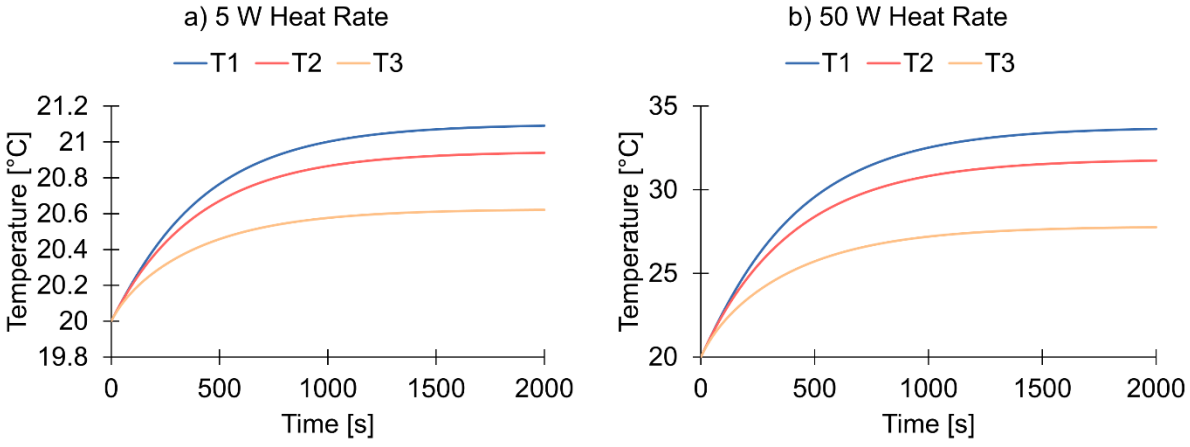

Fig. 38. Results of the cell-graphite assembly thermal network under 5 W (a) and 50 W (b) for validation purposes, where $T1, T2, T3$ are the temperatures of the cells nodes.

Table 14. Validation between thermal network and FVM simulations comparison results. For the FVM, the maximum temperature showed in the colormap was taken; for the LPM simulations, $T1$ was taken.

Case	T_{FEA} [°C]	T_{net}[°C]	ΔT [°C]
5 W	20.93	20.73	0.16
50 W	33.15	33.64	0.49

The comparison results in Table 14 show an excellent match in the maximum temperature calculated by the two models, giving enough confidence to move forward with the numerical activities. Hence, the next step is to merge the two lumped parameter models created so far, namely the one describing the thermo-fluid dynamic behaviour of the LHP and the one describing the temperature evolution of the cell-graphite assembly.

4.6. Unified Lumped Parameter Model

4.6.1. Unification of the two LPMs

In this section the code used to simulate the TMS proposed in this work will be introduced. It is composed by the two LPMs already presented in the previous sections, with small adaptations to the case in object. In more detail, the LPM model describing the heat generation and temperature distribution of the cell-graphite assembly is linked with the LPM describing the thermo-fluid dynamic behaviour of the LHP.

The way the two models are linked is by the external heat rate received by the LHP ($\dot{Q}_{ext}$ in Fig. 28), which is the heat rate released by the cell. This amount differs from the heat generated by the cell (from equations 49 and 50) as, due to the large mass of the cell and to the strongly transient behaviour of the heat generation rate in a cell subjected to a driving cycle, the thermal inertia effects in the cell itself play a major role. Therefore, the heat input inside the LHP is the resultant of the difference between the heat generated by the cell and the heat stored in the material of cell and graphite sheet.

Comparing the two thermal networks in Fig. 28 and Fig. 34, it is evident that the only common node is the evaporator wall (T_{wall}), connecting the two systems. Combining the two thermal networks, the overall thermal network in Fig. 39 is obtained. The ODE system that needs to be solved the proposed network is provided below Fig. 39.

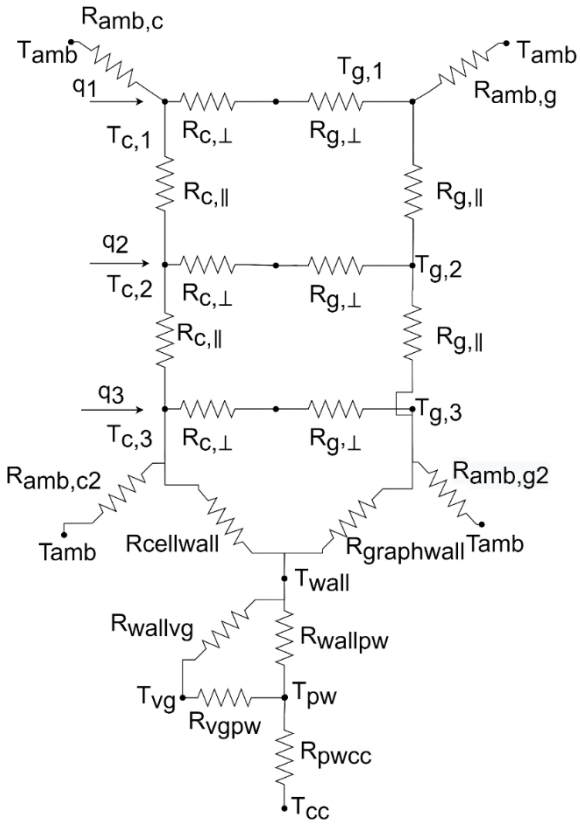

Fig. 39. Unified thermal network of the proposed TMS comprising of the cell-graphite assembly on top of a LHP.

$$m_{vg}c_{p,v}\frac{dT_{vg}}{dt} = \frac{T_{pw}-T_{vg}}{R_{vgpw}} + \frac{T_{wall}-T_{vg}}{R_{wallvg}} + \dot{m}c_{p,v}\left(T_{sat}-T_{vg}\right) \tag{66}$$

$$m_{pw}c_{pw}\frac{dT_{pw}}{dt} = \frac{T_{vg}-T_{pw}}{R_{vgpw}} + \frac{T_{wall}-T_{pw}}{R_{wallpw}} + \frac{T_{cc}-T_{\mathrm{pw}}}{R_{pwcc}} - \dot{Q}_{leak} \tag{67}$$

$$m_{wall}c_{pwall}\frac{dT_{wall}}{dt} = \frac{T_{vg}-T_{wall}}{R_{wallvg}} + \frac{T_{pw}-T_{wall}}{R_{wallpw}} + \dot{Q}_{ext} \tag{68}$$

$$m_{cc}c_{p,cc}\frac{dT_{cc}}{dt} = \dot{m}c_p(T_{\mathrm{cc}}-T_1) + \dot{Q}_{leak} + \frac{T_{amb}-T_{cc}}{R_{amb,cc}} + \frac{T_{pw}-T_{cc}}{R_{pwcc}} \tag{69}$$

$$m_c c_{p,c}\frac{dT_{c,1}}{dt} = q_1 + \frac{T_{amb}-T_{c,1}}{R_{amb,c}+R_{c,\parallel}} + \frac{T_{g,1}-T_{c,1}}{R_{g,\perp}+R_{c,\perp}} + \frac{T_{c,2}-T_{c,1}}{R_{c,\parallel}} \tag{70}$$

$$m_c c_{p,c}\frac{dT_{c,2}}{dt} = q_2 + \frac{T_{c,1}-T_{c,2}}{R_{c,\parallel}} + \frac{T_{g,2}-T_{c,2}}{R_{g,\perp}+R_{c,\perp}} + \frac{T_{c,3}-T_{c,2}}{R_{c,\parallel}} \tag{71}$$

$$m_c c_{p,c}\frac{dT_{c,3}}{dt} = q_3 + \frac{T_{c2}-T_{c,3}}{R_{c,\parallel}} + \frac{T_{g\,3}-T_{c,3}}{R_{g,\perp}+R_{c,\perp}} + \frac{T_{wall}-T_{c,3}}{R_{cellwall}} + \frac{T_{amb}-T_{c,3}}{R_{c,\parallel}+R_{amb,c2}} \tag{72}$$

$$m_g c_{p,g} \frac{dT_{g,1}}{dt} = \frac{T_{amb} - T_{g,1}}{R_{amb,g} + R_{g,\parallel}} + \frac{T_{c,1} - T_{g,1}}{R_{g,\perp} + R_{c,\perp}} + \frac{T_{g,2} - T_{g,1}}{R_{g,\parallel}} \quad (73)$$

$$m_g c_{p,g} \frac{dT_{g,2}}{dt} = \frac{T_{g,1} - T_{g,2}}{R_{g,\parallel}} + \frac{T_{c,2} - T_{g,2}}{R_{g,\perp} + R_{c,\perp}} + \frac{T_{g,3} - T_{g,2}}{R_{g,\parallel}} \quad (74)$$

$$m_g c_{p,g} \frac{dT_{g,3}}{dt} = \frac{T_{g,2} - T_{g,3}}{R_{g,\parallel}} + \frac{T_{c,3} - T_{g,3}}{R_{g,\perp} + R_{c,\perp}} + \frac{T_{wall} - T_{g,3}}{R_{graphwall}} + \frac{T_{amb} - T_{g,3}}{R_{g,\parallel} + R_{amb,g2}} \quad (75)$$

where the same notations and nomenclature of the previous two LPM are maintained. To account for the evaporator wall both on the LHP thermal network side and on the cell-graphite assembly side, the resistances $R_{cellwall}$, $R_{graphwall}$, R_{wallpw}, R_{vowall} are using half the thickness of the evaporator wall t_{ev}.

The heat rate input of the LHP is hence formulated as follows:

$$\dot{Q}_{ext} = \left(\frac{T_{graph,3} - T_{wall}}{R_{graphwall}} + \frac{T_{c,3} - T_{wall}}{R_{cellwall}} \right) n_{module} \quad (76)$$

where n_{module} is the number of cells that compose the module that the LHP is in thermal contact with.

In the following section, the liquid cooling system used as a benchmark to evaluate the feasibility of the novel LHP TMS system is introduced.

4.6.2. Liquid Coldplate TMS from Ricardo plc.

In order to evaluate the effectiveness of the use of the LHP TMS proposed in this work, a comparison with a standard liquid cooling system is conducted. This was the foundation of the feasibility study, motivating or discouraging the next experimental step of validating the model.

The liquid TMS has been developed by the industrial collaborator Ricardo plc which foresees aluminium side plates to transfer heat from the side surface of the cell to a liquid cold plate placed at the bottom of the module (similarly to the LHP), as presented in Fig. 40. This cold plate is part of a liquid cooling loop connected to a heat exchanger and a pump, running ethylene glycol at a constant temperature of 20°C.

This cooling system has been modelled with a 3D LPM that was then implemented in MATLAB R2020a Simulink. Following the LPM methodology, every cell in the module is represented by one cell model such as the one presented in Fig. 40b, consisting of 3 nodes, one for the plate itself and one for the bottom and top surface. The heat is conducted both through and across the plane. It is assumed that the plate covers the entire xy-area of the cell and that there is no contact resistance between the plate and the cell. The heat is generated in the center

of the cell and conducted in x, y and z direction. The resistances in Fig. 40b have the same formulation of the conduction thermal resistances of Table 12.

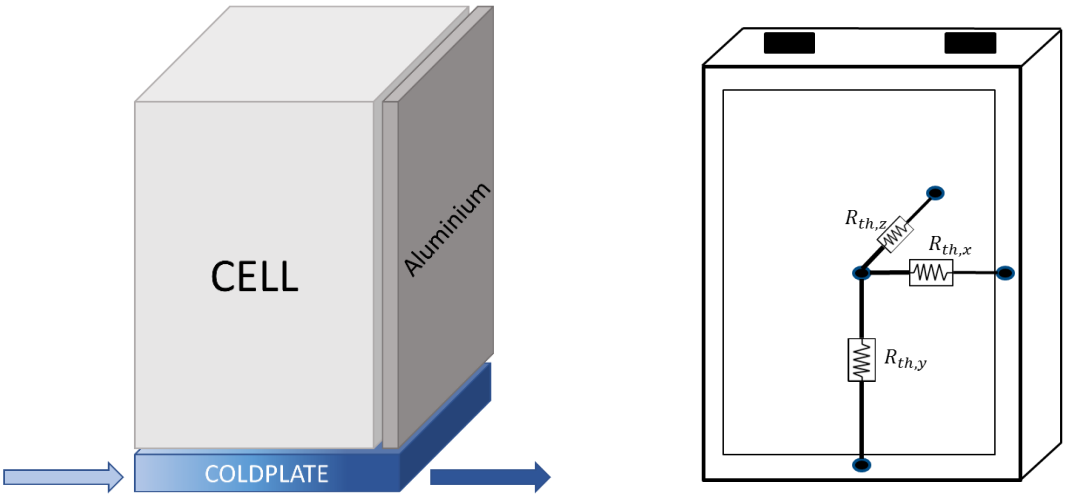

(a) (b)

Fig. 40. Liquid Coldplate design schematic (a) and primsatic cell thermal network (b) (adapted from industrial collaborator Ricardo.

This model accounts for both the temperature rise over time of the cooling fluid and the spatial temperature difference from cell to cell. The fluid flows through the channels inside the cold plate and cools the cell indirectly by cooling the cold plate. The side plate is solid without cooling channels inside. It is connected to the cold plate on the bottom of the plate. The heat from the cell is conducted along the z axis into the side plate and along the y-axis into the cold plate. Also, in the side plate the heat is conducted along the y-axis into the cold plate.

The heat conduction through the cell is modelled based on the Cauer-Model where the cell heat transfer is represented through an individual layer of semiconductor module (Fig. 41).

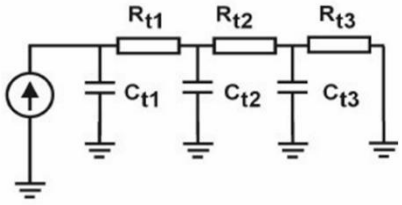

Fig. 41. Cauer-Model electric resistance circuit [343].

To reduce computation time, it is assumed that the coolant is independent from the location in the pack and has the same temperature at every cell. The temperature of the coolant therefore changes only with time. The procedure is reported as follows:

$$\dot{T}_{cool} = \frac{\sum \dot{Q}_{cell}}{\dot{m}_{cool} \cdot c_p} \tag{77}$$

$$\dot{Q}_{conv} = (T_{Plate} - T_{c,eff}) \cdot HTC \cdot A_{cel} \quad (78)$$

$$T_{c,eff} = \frac{T_{c,out,i} + T_{c,in,i}}{2} \quad (79)$$

As shown in equation (78), the transferred heat rate between the cooling plate and the coolant $\dot{Q}_{conv}$ is determined by the Temperature of the plate T_{plate}, the effective coolant temperature $T_{c,eff}$, the HTC and the cross-section area of the cell A_{cell}. The cell generated heat rate $\dot{Q}_{cell}$ increases the coolant temperature by $\dot{T}_{cool}$ (77).

The simulated pack has 4 modules of 105 cells each, for a total of 420 cells. Table 15 shows the data of the simulated cell/pack. In the LHP TMS case, 8 LHPs are used, one every 50 cells. Ambient temperature is kept fixed at 20°C.

Table 15 - Prismatic cells data specifications for LPM models.

Parameter	Value	Units
Thickness	10	mm
Height	96	mm
Width	280	mm
Thermal Conductivity inplane	46	W/m·K
Thermal Conductivity thruplane	0.7	W/m·K
Density	3720	kg/m^3
Mass Heat Capacity	1726	J/kg·K
Capacity	65	Ah

Following, a comparison between the two cooling systems is presented for two different driving cycles, a worldwide accepted standardised one (WLTP) and a custom made fast charge cycle one.

4.7. Preliminary Modelling Results

Driving cycles are sets of data showing the speed of a vehicle over time. They are mostly used to test and compare the performances of different vehicles on the base of fuel consumption, pollutant and CO_2 emissions and energy consumption values of alternative powertrains.

Since the New European Driving Cycle (NEDC), designed in the 80s, has become outdated, the European Union has developed a new test, called the Worldwide Harmonised Light Vehicle Test Procedure (WLTP), launched in September 2019. With respect to its predecessor, this driving cycle has more dynamic and realistic velocity profiles, with quicker accelerations and shorter brakes (comparison presented in Fig. 42). It represents a 30 min drive over 23.25 km, with average velocity of 46.5 km/h and top speed of 131.3 km/h. The WLTP driving cycle is

divided into four parts with different average speeds: low, medium, high and extra high. Each part contains a variety of driving phases, stops, acceleration and braking phases.

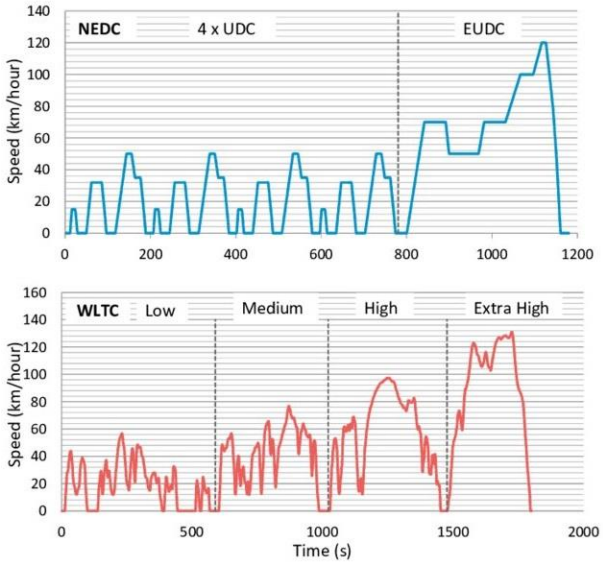

Fig. 42. Comparison of the NEDC (top) and WLTP (bottom) driving cycles [344].

The WLTP driving cycle is a cycle mainly used to test and evaluate CO_2 and other pollutant emissions and fuel consumption. However, it does not stress the vehicle for long periods (i.e. it lasts 30 min in total), not resulting in a significant depletion of the charge, neither it includes a section for fast charge. Since nowadays fast charging and its thermal management are some of the main focus and challenges regarding EVs, a custom-made driving cycle is created, divided in three steps: highway driving until depletion of the charge, ultra-fast charge from 0% to 80% SOC and finally another identical highway driving section till depletion of the charge, hence why from this point forward will be called HFCH driving cycle (Highway - Fast Charge – Highway).

The fast charge is stopped at 80% as this is the automotive standard practice to avoid damage to the battery cells [345]. In fact, charging towards higher SOC usually requires low currents to avoid overcharging processes that can lead to lithium plating, gas generation and damage. Moreover, low currents balance the counter effects of the rising impedance at high SOC, such as polarisation and energy losses, excessive temperatures. Hence the standard fast charge protocol is with Constant Current followed by Constant Voltage (CC-CV). In this method, the battery charges at constant current until the voltage reaches the predetermined cut-off limit, and then it charges at the same constant voltage until the current drops to some pre-determined minimum value. The CV section inefficiently doubles the total charging time, reason why EV manuals suggest to fast charge up to 80% only.

In Table 16 a breakdown of the C-Rates used in this driving cycle is presented. The C-Rate is defined as the charging/discharging current to/from the battery divided by its capacity, which is the theoretical current maximum current that can be draw from the battery in one hour (i.e. 1 C-Rate means total depletion of the battery in one hour, 0.5 C-Rate in two hours and 4 C-Rate in 15 minutes). Table 16 shows that two cooldown sections of 1 minute each have been introduced to mimic a real-life scenario where before and after charge the driver will have to detach the socket and re-enter and re-start the car. It is worth to point out that this HFCH cycle is more demanding than the current state of the art, where maximum fast charge C-Rate is still fixed at 3C. The corresponding heat generation rate of the cell is given in Fig. 43.

Table 16. Highway - Fast Charge – Highway (HFCH) driving cycle C-Rates and SOC.

C-rate	Duration (minutes)	Final SOC
-1	48	20%
0	1	0%
4	3	40%
3.75	3	59%
3.5	3	77%
2.5	1	81%
0	1	0%
-1	48	20%

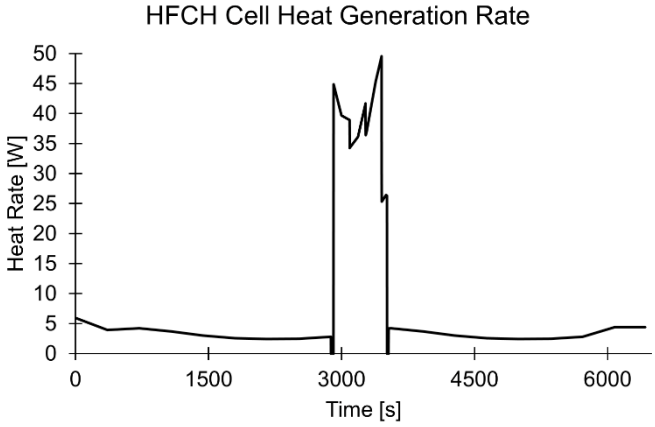

Fig. 43. Single cell heat generation rate during the HFCH driving cycle.

Fig. 43 shows that during highway driving the cell heat generation rate remains around a contained 5 W value, while spiking up to 50 W during fast charge. This is due to the much higher current provided during charging with respect to discharging, and since the thermal power goes with the square power of the current, the significant increase is explained. The strongly irregular variations of the heat rate generation profile are due to its strong dependency from charge rate, temperature and DOD, combined with the fact that the C-rate is changing

frequently, introducing strong transient phenomena [346]. For the pack, the peak is 22.7kW with an average heat rate release of 3 kW. This is sensibly more thermally demanding than the WLTP driving cycle.

The LHP simulated in this case comes from an optimized geometry of a cylindrical LHP used in another work done by the Authors on thermal management for electric vehicle [208], which was deemed appropriate as a starting point for the feasibility study of this idea. Its data characteristics are reported in Table 17. The chosen LHP working fluid is distilled water.

Table 17 - LHP geometrical data specifications for the WLTP simulations.

		Value	Units
Condenser	$r_{i,cond}$	3	mm
(Stainless Steel)	$r_{e,cond}$	4	mm
	L_{cond}	40	cm
Liquid Line	$r_{i,ll}$	3	mm
(Stainless Steel)	$r_{e,ll}$	4	mm
	z_{ll}	20	cm
	L_{ll}	45	cm
Vapour Line	$r_{i,vl}$	3	mm
(Stainless Steel)	$r_{e,vl}$	4	mm
	z_{vl}	20	cm
	L_{vl}	45	cm
Wick	r_{pw}	20	mm
(Nickel)	L_{pw}	15	cm
	r_{vg}	1	mm
	n_{vg}	10	-
	α	60%	
	$\bar{r}_{por}$	1.2	µm
Evaporator	t_{ev}	2	mm
(Stainless Steel)	$r_{bay,i}$	3	mm
	$r_{bay,e}$	4	mm
	L_{bay}	75	mm
Compensation Chamber	L_{cc}	20	mm
(Stainless Steel)	r_{cc}	6	mm
Total Mass LHP	1.5	kg	

Fig. 44 presents the temperature evolution of the three cell nodes. It shows that during highway driving, the temperature increase is moderate. During fast charging, the cell temperature is greatly influenced by the increase in heat rate from the cell, providing a noticeable and abrupt increase. It is observable that the slope of the temperature trend is steeper during the first bit of fast charging, corresponding to 4C C-rate, for then showing a smoother angle going forward. These are further indication that the built numerical model for the cell-

graphite assembly works properly and it is able to describe reactively the transient response of such system, as it will also be shown in Chapter 5 during the comparison with the experimental measurements.

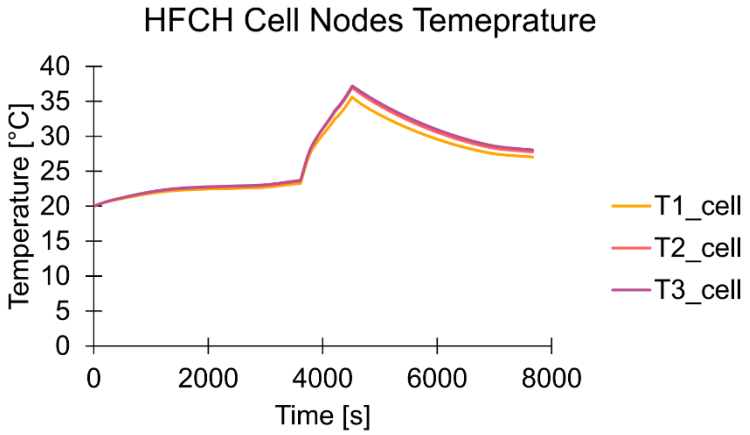

Fig. 44. Temperature evolution of the cell nodes during a HFCH driving cycle.

To understand the behaviour of the LHP, Fig. 45 shows the evolution of the wick pressure during operation. The section coincident with the motorway driving sees a small increase in pressure, due to the sensible heat heating up the fluid but not enough to onset boiling. During fast charge instead, a small overshoot happens building up the required pressure for boiling, followed by a pressure decrease meaning that start-up has happened. The small overshoot captured by the model is produced by the fluid trying to reach the saturation temperature at the vapour grooves node, before starting to travel the loop. Once the fluid travels the loop, it will also encounter the pressure load losses, hence explained the following undershoot. This condition was set in the code to represents the sudden pressure built up prior to start-up, which can be attributed to the formation to a large bubble, quickly escaping the primary wick domain, leaving a large gap which is then filled by colder liquid, hence explained the sizeable pressure drop.

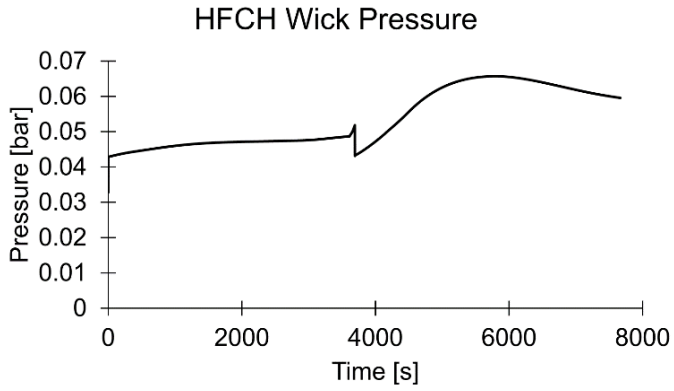

Fig. 45. Wick pressure variation during a HFCH driving cycle.

Looking at the comparison over the average cell temperatures for the two TMS solutions during the HFCH driving cycle presented in Fig. 46, it shows that not only the solution proposed in this work is feasible, but also it can provide great benefit in terms of maximum temperature reduction during ultra-fast charging. The LHP based TMS provides a peak temperature of 36.6°C during fast charge, contributing to a 3.3°C reduction against the maximum temperature of 39.8°C reached with the liquid cold plate TMS. Moreover, the TMS proposed in this work allows for a faster temperature reduction after fast charging, with the two solutions exhibiting 6.6°C of difference at the end of the driving cycle.

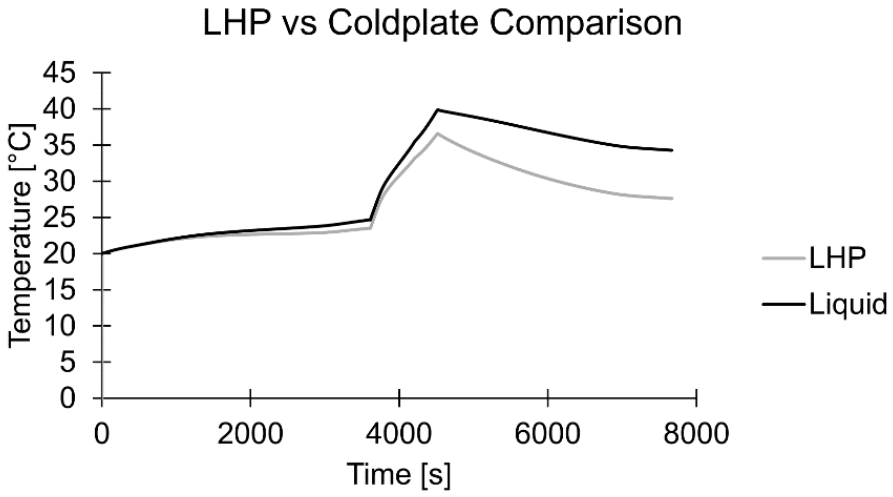

Fig. 46. Performance comparison between LHP and liquid cold plate TMS. The graph plots the average cell temperature during the HFCH driving cycle.

4.8.Parasitic Savings Potential

One of the most appealing benefits of the use of the LHP lies in the passive nature of this device. Thanks to the absence of the need for an external source of motion for the fluid, a pump is needed only to circulate the refrigerant for the heat exchanger used to cool down the condenser of the LHP. In the liquid cooling loop used as comparison, the pump needs to provide a pressure gradient sufficient for the fluid to travel the entirety of the battery pack length. This will adversely affect the all-electric range of the vehicle.

The HEX considered in these simulations has the same geometry that the one that will be described in the next Chapter, where the experimental validation campaign will be discussed. In that case, a tube in tube HEX was chosen for its manufacturing simplicity, allowing it to be made in-house at the laboratories in the Advanced Engineering Centre (AEC). Its specifications are reported in Table 18.

Table 18 - Specifications of HEX used in the simulations.

	Value	Units
Type	Tube in Tube	-
Material	Copper	-
Length	55	cm
Inner Diameter LHP Condenser Pipe	4.4	mm
Outer Diameter LHP Condenser Pipe	6	mm
Inner Diameter External HEX Pipe	7.7	mm
Total Mass	0.28	kg

In order to gauge the benefit of using a passive two-phase device on the power consumption, the mass flow rate at the heat exchanger side was calculated. In the LPM, a section implementing the ε-NTU method was added, as described in Appendix. Thanks to this, it was possible to plot the trend of the mass flow rate required to the heat exchanger to ensure full condensation and no subcooling at the end of the condenser for all the LHPs (Fig. 47).

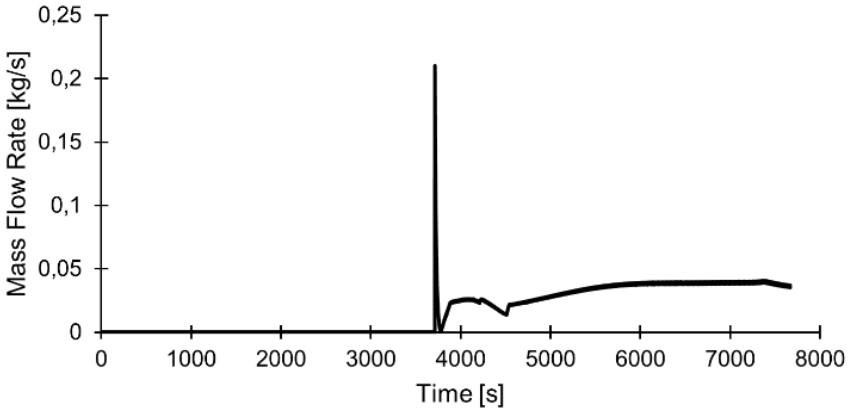

Fig. 47. Mass Flow Rate required to the HEX to ensure full condensation during the HFCH driving cycle. It is interesting to note how the HEX mass flow rate prior to start-up is null.

From the information provided by the industrial collaborator Ricardo, the volumetric flow rate for the cold plate liquid TMS amounts to be 20 l/min. Knowing that the mass flow rate is the product of the volumetric flow rate for the density of the fluid, for ethylene glycol ($\rho = 1110\ kg/m^3$) this gives $\dot{m}$ of 0.37 kg/s. From Fig. 47, it is evident how substantial this difference in mass flow rate is. Unfortunately, no information on the pump power or head are provided for the cooling loop, hence it is not possible to compare the power consumption of the two thermal management systems. However, considering the relationship between mass flow rate and pump power, it is reasonable to assume that the reduction of one order of magnitude in mass flow rate will reflect in a similar reduction of the parasitic power required

by the pump. The pressure load losses will also be reduced due to the minor length that the coolant has to travel.

Looking at the mass budget, considering 8 LHPs and same HEXs plus the added graphite sheets weight, the total added mass of the proposed TMS is 35.4 kg. The breakdown of the mass budget is presented in Table 19. Considering that the total mass for the cells amounts to 420 kg, the added mass for the TMS is the 8% only.

Table 19 - Total mass breakdown of the proposed TMS considering a battery pack composed by 420 cells.

Part	Mass [kg]	Total [kg]	Comments
LHP	1.5	14.4	Total mass for the 8 LHPs connected to 8 HEXs
HEX	0.3		
Graphite Sheet	0.05	21	Total mass of the graphite sheets
TMS		35.4	Total added mass for the TMS proposed herein
Prismatic Cell	1	420	Total battery pack mass made by cells only

In conclusion, the simulations presented in this section have shown the potential benefit of a TMS based on LHPs and graphite sheets in comparison to a more conventional TMS. Evidently, the proposed solution seems to perform sensibly better in terms of temperature reduction, over a variety of cases including fast charging, compared to the standard liquid cold plate approach. In addition, there are clear indications of potential benefits in terms of parasitic power savings.

4.9. Conclusions

In this Chapter, the steps to model the thermal behaviour the proposed TMS were detailed. Thanks to the described LPM, it was possible to simulate the behaviour of the novel TMS proposed in this work, which envisages the use of LHPs and graphite sheets, on a battery module consisting of prismatic cells. Two validation procedures for the two separate parts of the LPM (LHP and cell-graphite assembly, respectively) were successfully carried out, giving enough confidence to use the unified model to study the feasibility of the idea. Simulations results showed clear potential for this TMS to satisfy two of the three requirements for battery thermal management (the third requirement is covered by an assumption on the mathematical model). Moreover, when compared to a standard liquid cooling method, the LHP TMS provided better results in terms of temperature reduction, allowing for a favourable ΔT of 3.3°C during fast charging. Due to the passive nature of the LHP, significant power savings can be obtained by adopting this technology, as shown by the reduction in required mass flow rate at

the chiller side. An experimental investigation by means of a laboratory demonstrator, is carried out in Chapter 5, to confirm these findings.

Chapter 5 - Experimental Validation and Investigation

5.1. Introduction

Following on the numerical feasibility study, an experimental demonstrator was designed to validate the numerical model. The investigation had two aims: firstly, to verify the applicability of a LHP to cool down a battery module under varying heat generation rate loads; secondly, to validate the numerical LPM code presented in Chapter 4.

It was not the purpose of this investigation to go in depth in the fluid-dynamic performance of the LHP technology, for both budget reasons and because it is a topic already discussed in many scientific works in literature. Some preliminary considerations are due, to explain the research direction undertaken in this experimental campaign: firstly, that in order to build the wick for an LHP evaporator, a sintering process in a vacuum furnace under nitrogen shielding atmosphere is needed. The University of Brighton does not own such equipment, hence alternative solutions were sought. Secondly, the selection of the material used for the experiment is limited to the machining tools and expertise available at the university laboratories. This last point shows the benefit of a working numerical model, as validating the model with standard common materials allows to extend the investigation to materials that would been otherwise prohibitive to test experimentally.

The structure of this Chapter will describe first the experiment design selection, moving on detailing the experimental apparatus and the selection of the equipment for the manufacturing/assembly process description. Secondly, the validation procedure with ethanol and water is presented. Concluding, a comparison (with the validate code) between the proposed TMS and the liquid cold plate TMS is conducted.

5.2. Experimental Design

Following what was introduced in Chapter 4 regarding the chosen design, the proposed experiment is focussing on a 3-cell module. Graphite sheets are sandwiched between the cells and a LHP is placed at the bottom of the module, to transfer heat from the cells to a tube in tube HEX. The latter is cooled by a thermal bath running with distilled water. It was chosen to take non-intrusive temperature measurements, due to the above-mentioned limitations. This did not impede to thermally characterize the experiment and to validate the model.

In Fig. 48, a schematic of the experimental set up is presented. It shows how the three-cell module is placed on top of the LHP evaporator; the condenser of the LHP is cooled by a liquid cooling loop hooked to a programmable thermal bath running DI water; the heaters are powered by a programmable 30V power supply, allowing to replicate transient driving cycles. In the following sections, the different subsystem design and the assembly procedure are discussed.

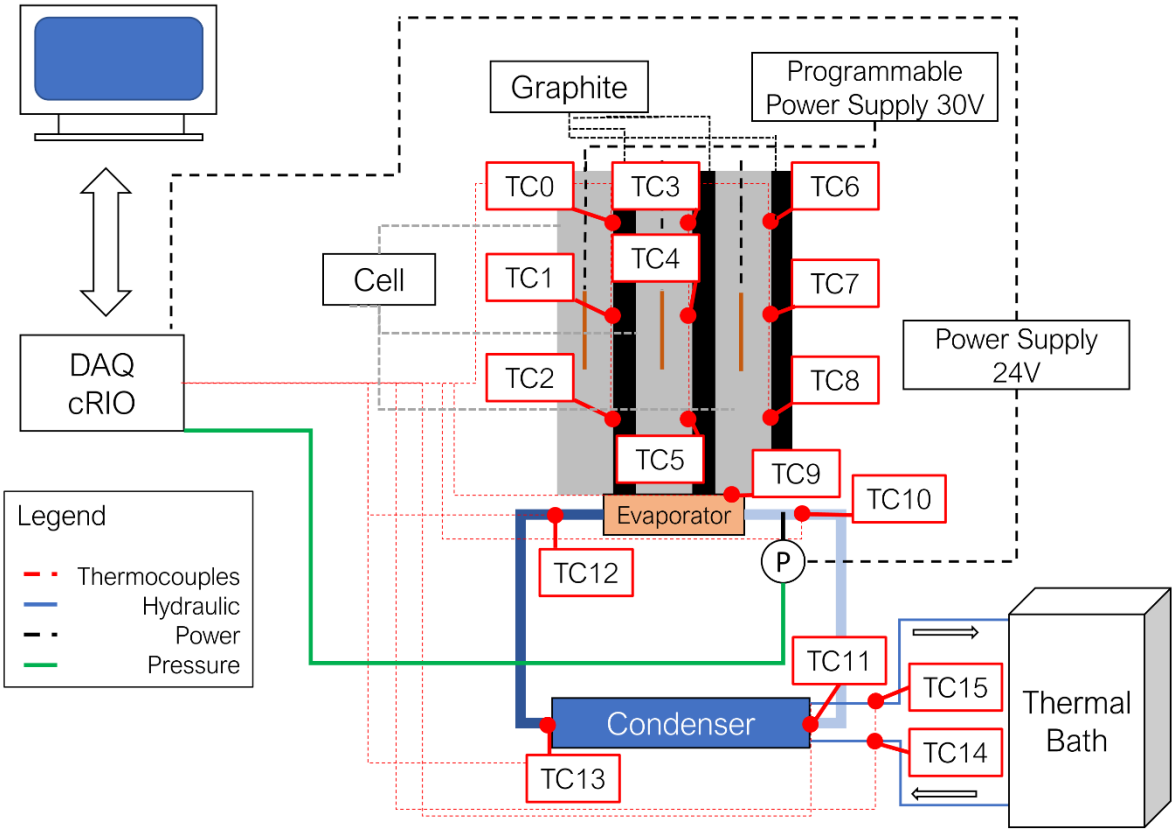

Fig. 48. Schematic of the experimental set up with details of thermocouples positioning and numbering, as well as instrumentation utilized. The grey and black rectangles are representing the battery cells and graphite sheets, respectively.

5.2.1. Battery Module

Usually, prohibitively expensive equipment is used to study the thermal behaviour of a battery cell, such as the equipment reported in [347], due to the normally high standard of precision required in terms of voltage and current measured. But considering the safety risks that testing a battery poses, as thermally stressing a battery can lead to unpredictable and unwanted fire/explosion scenarios, in this work the battery module is composed by cells dummy models, where an aluminium block with the same dimension of the cell is used to replicate the cell thermal behaviour. The selected procedure has been extensively used in literature [130,136,168,222,227,229,234,240] and as such it is deemed an acceptable practice. This will not affect the validation of the numerical model, as the same material data will be used in the simulations, proving once again the strength of the lumped parameter method approach.

Graphite sheets are sandwiched between the plates. In order to allow for temperature measurements, thermocouples (TCs) are used to measure the temperature at the cell-graphite interface. Three thermocouples per cell are used, to replicate the three nodes present in the LPM model. To replicate the heat generation mechanism of the cells, one heating element per cell is used. Polyimide flexible heaters are chosen due to their low thickness and high-power density. The aluminium plates are cut in half to ease the insertion of the heaters. In Fig. 49 the CAD design of the battery module is presented. Following, the steps taken for the assembly of such system are detailed.

Fig. 49. CAD Drawing of cell-graphite module assembly with thermocouples, fixing and heating wires.

For the creation of the cell dummy model, six aluminium 5083-O plates (Aluminium Warehouse, UK) are used. The thickness of these plates is half the thickness of the simulated

cell, as, given the length of the cell, it was deemed less challenging from the manufacturing point of view to clamp together the two halves over the heating elements.

Often referred to as N8, Aluminium 5083 is an aluminium alloy with magnesium, manganese and chromium, known for good performance in extreme environments. It is highly resistant to attack by both seawater and industrial chemical environments. Alloy 5083 also retains its strength after welding. It has the highest strength of the non-heat treatable alloys but is not recommended for use in temperatures higher than 65°C. Table 20 presents the material properties and dimensions of the aluminium plates and graphite sheets. As reported in the table, graphite sheets thickness is less than a millimetre, a fact that combined with graphite low density increases the energy density in the pack.

Table 20. Dimension and physical properties of aluminium 5083 plates [348] and graphite sheets (RS PRO) used for cell dummy model.

Parameter	Aluminium	Graphite	Units
Thickness	10	0.8	mm
Height	96	96	mm
Width	280	240	mm
Thermal Conductivity ∥	109	350	W/m·K
Thermal Conductivity ⊥	109	10	W/m·K
Density	2670	1300-1500	kg/m^3
Mass Heat Capacity	900	810	J/kg·K

The six plates had to be machined to allow space for the thermocouples, heaters and bolts. In order to have a perfect thermal contact between the two halves of the plate, no parts should protrude from the surface, hence appropriate slots and grooves are to be made. Firstly, the grooves for the thermocouples, 3 for each cell, are made. To measure the temperature in the central part of the cell, T-Type thermocouples (RS PRO) with a SS probe of 3 mm diameter and 150 mm length are used. Thus, three appropriate grooves are milled[3] on one face of the Al plates. T-type thermocouples are made by a copper and constantan junction, providing a level of accuracy of ±0.5°C. It was chosen to use a probe to prevent unnecessary electrical noise from contact with the surroundings, given the proximity of the heating elements. Hence these two choices guarantee a very precise temperature measurement, which will be the value that the LPM results have to match. A 3 mm diameter probe is chosen as, due to the non-negligible length to mill on the surface of the plates to create the TC slots (150mm) in relation to the

[3] Milling is the process of machining using rotary cutters to remove material by advancing a cutter into a work piece.

diameter of the cutting tool, lower tool diameter would break. Fig. 50a shows an image of the plates being milled and Fig. 50b shows the end product.

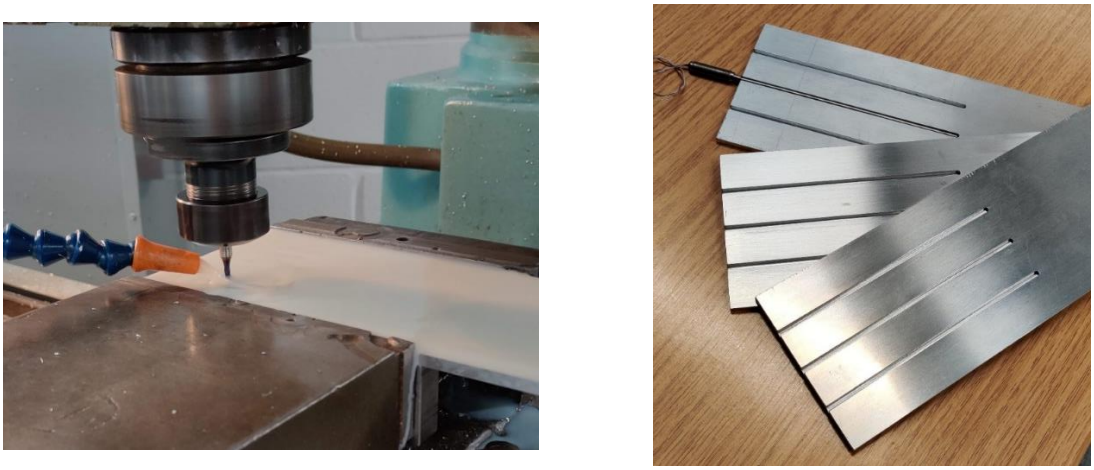

a) b)

Fig. 50. Milling process of the aluminium plates: a) detail of the operation and b) end product (aluminium plates with grooves to house the thermocouple probes).

Flexible polyimide (or *Kapton*) heaters were used (Omega KHLVA-105, 28 V, power density 10 W/in^2), providing up to 50 W of heat rate each. Characterized by ultra-low thickness (0.2 mm) everywhere apart from a protruding silicon patch (1.5 mm) used to protect the wires connection, highlighted in Fig. 51. Slots need to be made on the surface of the aluminium plates to allocate the silicon patch and the leading wires. Due to the precision required, CNC machining was used. The end product is shown in Fig. 52.

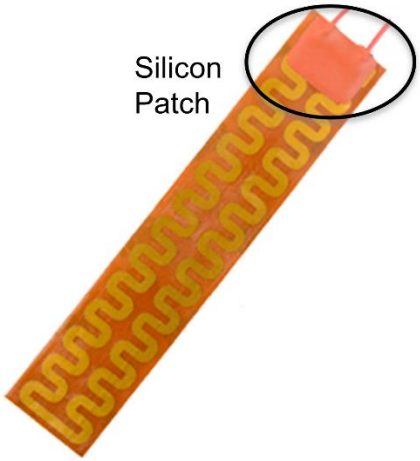

Fig. 51. OMEGA flexible Kapton heaters KHLVA-105 with silicon patch highlighted.

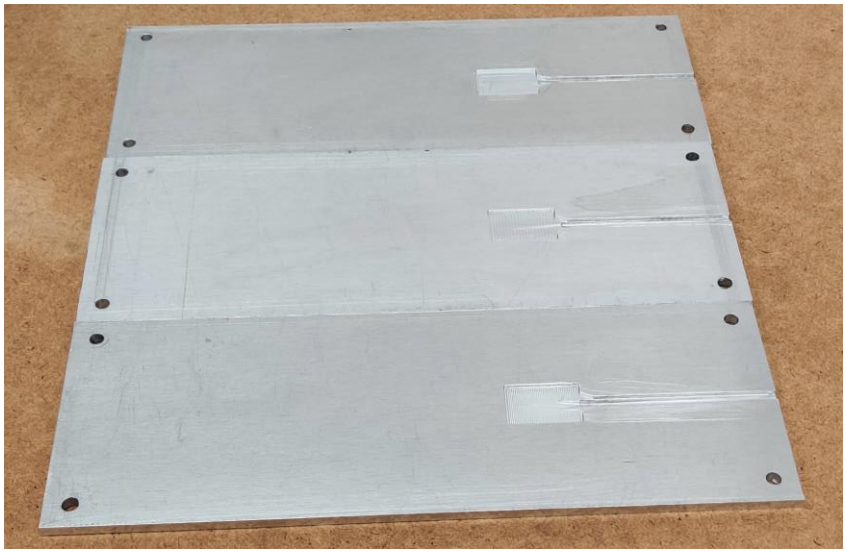

Fig. 52. Slots for flexible heaters created on the three Al plates.

Subsequently thermal paste (RS PRO, silicon-aluminium oxide grease, 5 W/m K thermal conductivity) has been applied to the plates with the twofold function of holding in place the flexible heater but also to improve the thermal contact between the heater and the plate. In fact, the rugosity of the materials adversely affects the heat transfer between two bodies, as the small air gaps entrapped at the interface act as thermal insulation. The role of the thermal paste is to fill these gaps and thus create a uniform smooth contact surface. Fig. 53 show the plate once the Kapton flexible heaters are applied.

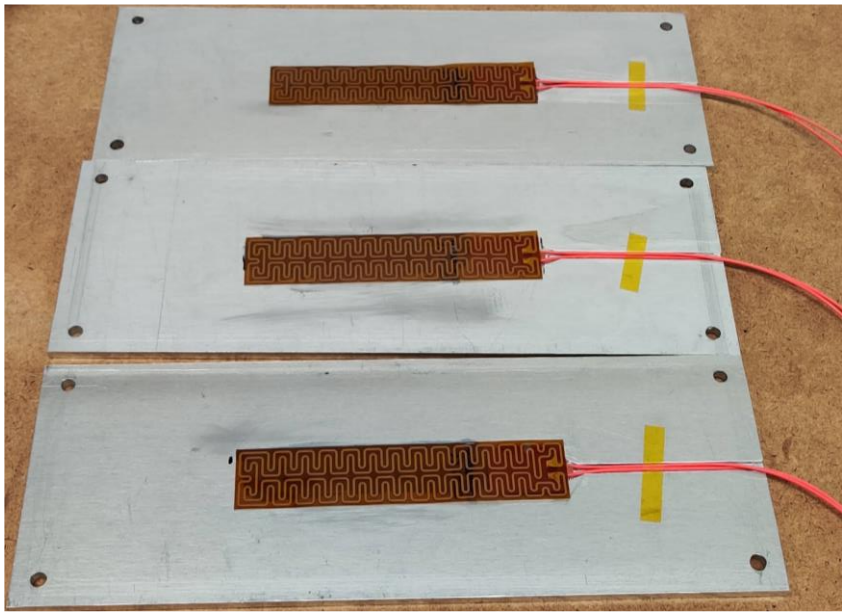

Fig. 53. Al plates with applied Kapton heaters thanks to machining of the plate and thermal paste application.

The thermocouples, after calibration, can be fixed to the aluminium plates using Kapton tape and thermal paste, as shown in Fig. 54. Thermal paste has been applied to the tip of the TC probe only, as that is the only active portion of the probe. In such a way, it is ensured that the TC is measuring the temperature of the interface between the two materials (aluminium and graphite).

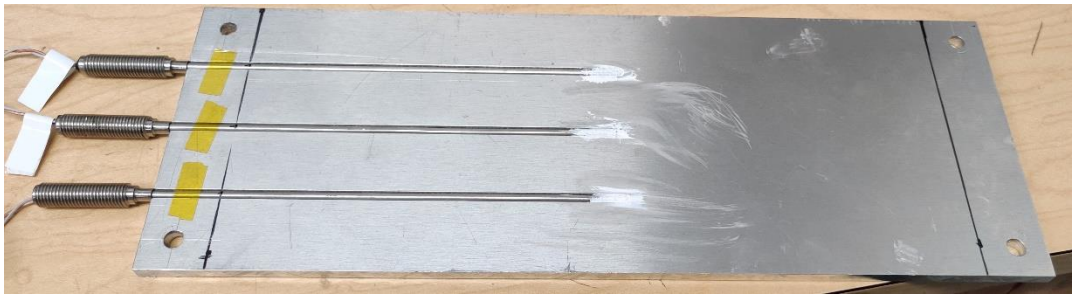

Fig. 54. Fixing of the thermocouples on the aluminium plates. Black lines identify the area that will be covered by the graphite sheets.

At this point, the graphite sheets can be applied to the aluminium plates. Table 20 presents the most important physical properties and dimensions. Due to their default factory dimensions being different from the cell dimension, they had to be cut and adapted to the cell side surface. Space is left to allow to use bolts as a fixing method. Fig. 55 shows the three half-cells completed with thermocouples and graphite.

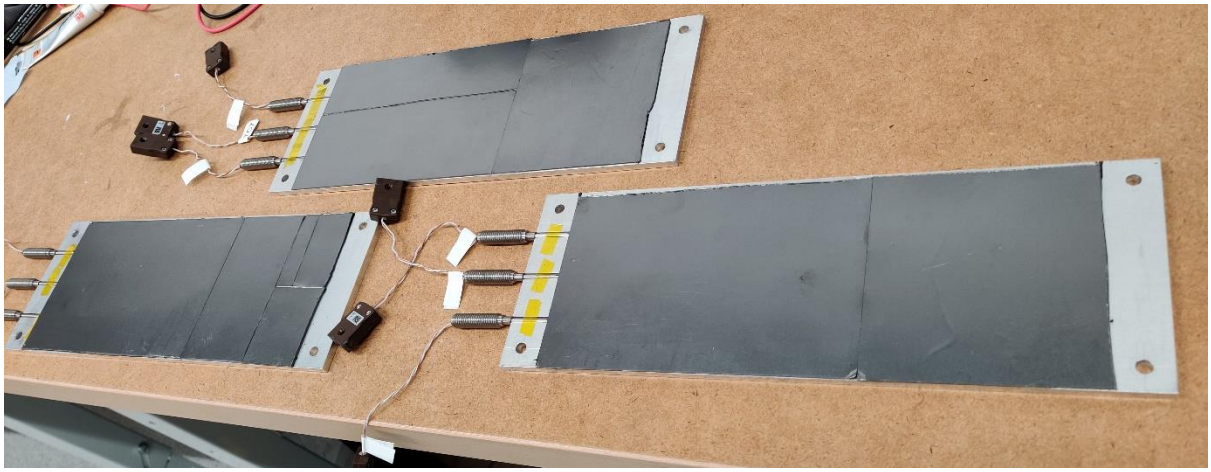

Fig. 55. Assembly of thermocouples and graphite completed for the three cell halves.

Finally, the two halves composing each dummy cell are completed and the module can be assembled. Fig. 56 presents front, top and isometric views of the assembled battery module, respectively.

a)

b)

c)

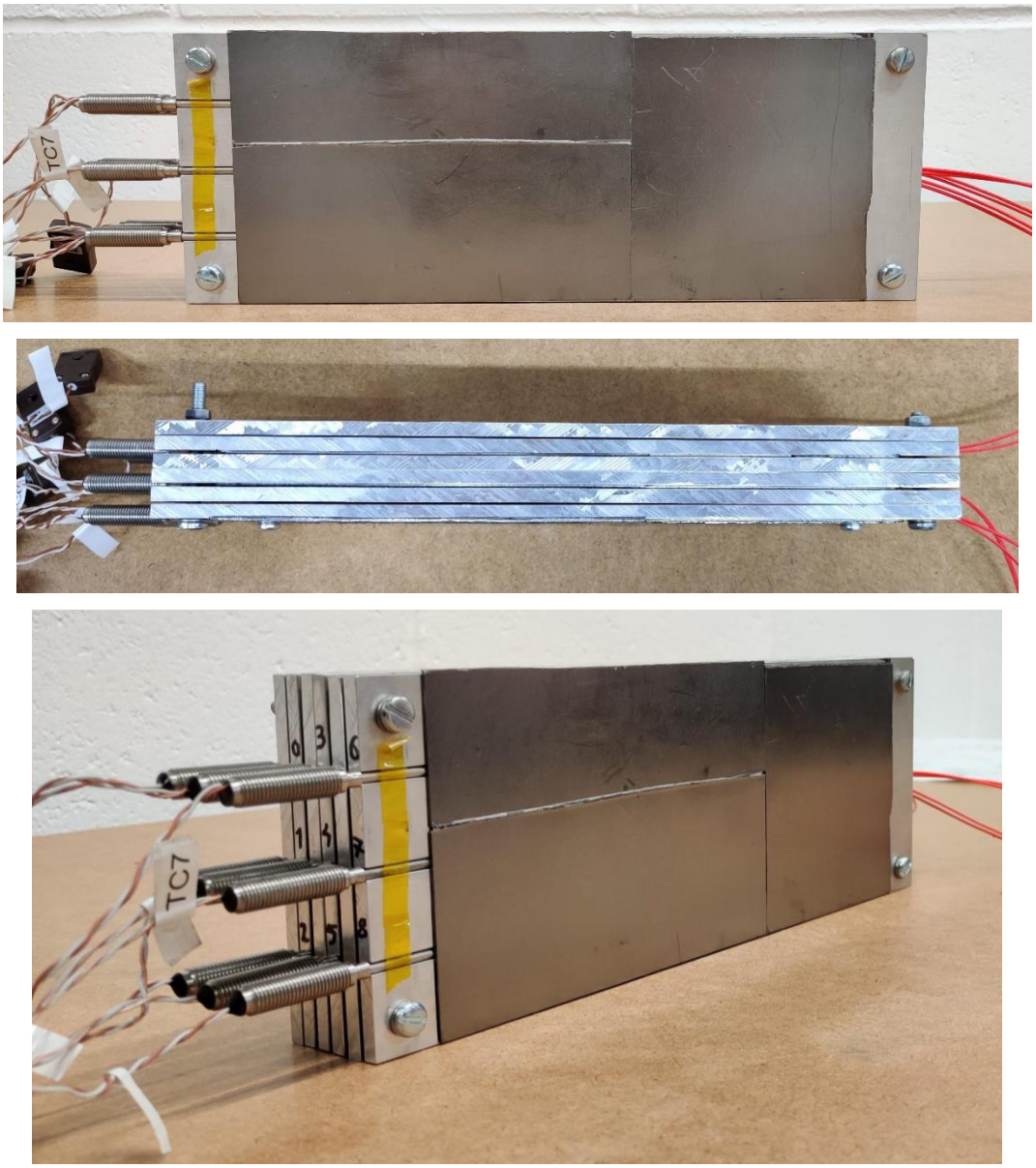

Fig. 56. Assembled battery dummy cell module: a) front view; b) top view; c) isometric view.

5.2.2. Thermal Bath

The function of the thermal bath is to provide constant temperature liquid to the tube-in-tube HEX, that is used to remove the excess heat at the condenser of the LHP. The chosen thermal bath is Fisherbrand™ Isotemp 5150 R28 (cooling capacity 500W, temperature range -28°C to +150°C). The working fluid is distilled water.

5.2.3. Tube in Tube Heat Exchanger

The selected design for the condenser heat exchanger is the tube in tube HEX, chosen for its construction simplicity. For the real EV application, a more compact HEX is preferred.

A tube in tube HEX, or tubular HEX, consists in two tubes mounted concentrically creating annular spaces for fluids to flow in a counter current fashion. In this case, two copper pipes have been welded together at the edges, to close the gap due to their different diameter; vertical inserts have been welded on the outer tube to connect it to the cooling loop (Fig. 57). The LHP working fluid in the inner tube of the condenser, while the HEX working fluid flows in the outer large tube. Table 21 summarises the main geometrical characteristics of the tube-in-tube HEX, that resulted via the ε-NTU method designed to dissipate the maximum heat rate released by the three cells during the HFCH driving cycle (150 W), using water at 20°C and considering the fixed requirement of the maximum mass flow rate of the thermal bath pump.

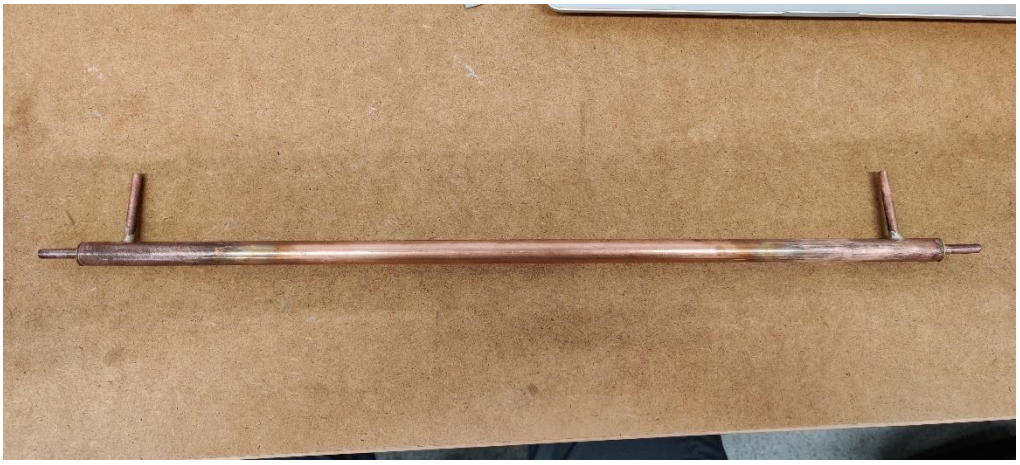

Fig. 57. Tube in tube condenser.

Table 21 - Geometrical parameters of tube in tube HEX.

	Value [mm]
Length LHP Tube	600
Length HEX Tube	550
Distance between Inserts	510
Inner Tube OD/ID	6 / 4.4
Outer Tube OD/ID	15 / 11

5.2.4. Loop Heat Pipe with Thercon Evaporator

The tested LHP uses a flat evaporator obtained from the Russian company Thercon (Fig. 58), co-founded by one of the inventors of the LHP, Yury F. Maydanik. Both the evaporator wall and its wick are made in copper. In the labs of the Advanced Engineering Centre (AEC), the fluidic lines, filling line, condenser were added and instrumented to complete the LHP. The geometry details can be found in Table 22.

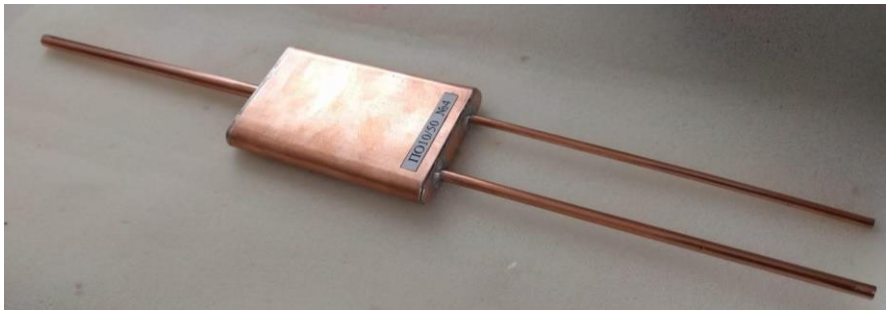

Fig. 58. LHP Flat evaporator from Thercon.

Table 22 - Geometry of the LHP using the Thercon evaporator (all parts are made in copper).

Part		Value	Units
Condenser	ID/OD	4.4/6	mm
	Length	580	mm
Liquid Line	ID/OD	4.4/6	mm
	Length	390	mm
	Elevation	0	cm
Vapour Line	ID/OD	4.4/6	mm
	Length	400	mm
	Elevation	0	cm
Wick	Thickness	8	mm
	Width	45	mm
	Length	50.5	mm
	Porosity	45%	
	Pore Size	7.3	µm
Vapour Grooves	Radius	1.5	mm
	N	9	-
	Length	43	mm
Evaporator Shell	Thickness	1	mm
	Width	50	mm
	Length	84	mm
Compensation Chamber	Thickness	8	mm
	Width	50.5	mm
	Length	24	mm

The choice of relying on an external supplier for the provision of the LHP evaporator was motivated from the constraints that manufacturing an evaporator poses. In fact, in order to create the sintered material which constitutes the wick, a sintering process in a vacuum furnace under nitrogen shielding atmosphere is needed. The wick needs then to be brazed to the evaporator wall. The AEC does not host of such facilities, nor the technical experience and knowledge for such operation, hence seeking an already made product was deemed more advantageous than seeking the realization of the single steps elsewhere.

Nevertheless, obtaining only the evaporator instead of a fully closed LHP allowed for a customisation of the fluidic lines and condenser lengths and diameter, as well as it allowed to test different working fluids. On the other hand, the choice of the evaporator footprint was limited to the availability from the manufacturer. As a result, the exchange surface area is much smaller than the bottom surface of the three-cell module. In fact, the available active heating zone of the LHP evaporator is 2080 mm^2 whereas the module footprint is 9072 mm^2, giving a coverage of roughly 23%. This is expected to negatively affect the cooling performance of the system.

Nevertheless, the purpose of this experimental campaign is the validation of the numerical code described in Chapter 4. Once this is objective is reached, the real values for geometry and physical properties of different batteries will be used to evaluate with confidence this novel application.

To join the different parts of piping of the LHP, stainless steel fittings from Swagelok were used, providing satisfactory design flexibility and a good resistance to vacuum conditions.

In order to carry out the procedure of vacuuming and filling, a valve is needed. This is a crucial component of the LHP as it is the major responsible of maintaining the vacuum conditions. In fact, as introduced in Chapter 3, a two-phase passive device requires vacuum to work properly and to prevent the generation of Non-Condensable Gases (NCG). The valve used in the present experiment is a micrometric valve (Upchurch Scientific P-447) (Fig. 59). In Fig. 60 the final assembled LHP is presented.

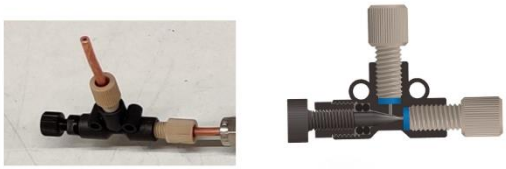

Fig. 59. Upchurch Scientific® Micro metering valve P-447 fitted on the filling line (left) and section view (right). This valve can reduce outgoing flow as low as 3.5 µL/min.

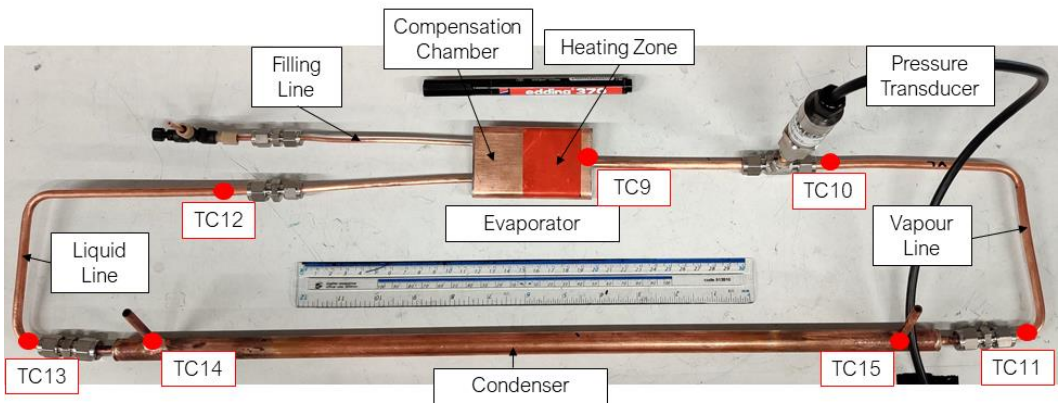

Fig. 60. Final LHP layout. 30cm ruler and marking pen for scale and LHP Thermocouples Position.

5.2.5. Data Logging and Instrumentation

The measuring devices used in the experimental campaign of the present investigation are the following:

- 9 T-type TC (RS Pro, SS probes 150x3mm) used to measure the temperature of the dummy cells.
- 1 mass flow meter (McMillan S-111, accuracy ±1.0%, range 0.5-5l/min) to measure the flow rate of the cooling liquid originating from the thermal bath.
- 1 pressure transducer (Omega PXM319, 0-7 bar range, 0.25% FS BSL accuracy) fitted directly in the LHP (at the inlet of the vapour line) to measure its fluid pressure.
- 6 T-type thermocouples used to measure the temperature of as many points on the LHP.
- 1 National Instruments cRIO datalogger.

A 5-points calibration procedure is carried out for the T-type thermocouples with a thermal bath (HAAKE C50P with Phoenix II Controller), over a temperature range from 10°C to 65°C. After this calibration procedure, the expected error in the temperature measurements can be assumed to be ±0.5°C, in compliance with the T-Type TC standard. Regarding the mass flow rate meter and the pressure transducer, they were both pre-calibrated and accompanied by a a 5-point traceable factory calibration certificate. On the LHP, the thermocouples are fixed on the external surface of the copper pipes, to avoid making holes and hence to minimise the sources of leakage. Fig. 48 and Fig. 60 shows the position of the thermocouples on the LHP.

On the data logging side, NI LabVIEW 2015 is used, allowing to simultaneously monitor all the temperature measurements as well as the mass flow rate and pressure measurements. Moreover, a function has been added to the logging architecture to control the current fed to the programmable power supply (TENMA 72-2710, 30V, 5 A). In this way, ad hoc power cycles could be created to mimic complex real-life applications. Fig. 61 shows a snapshot of the front panel of the LabVIEW architecture.

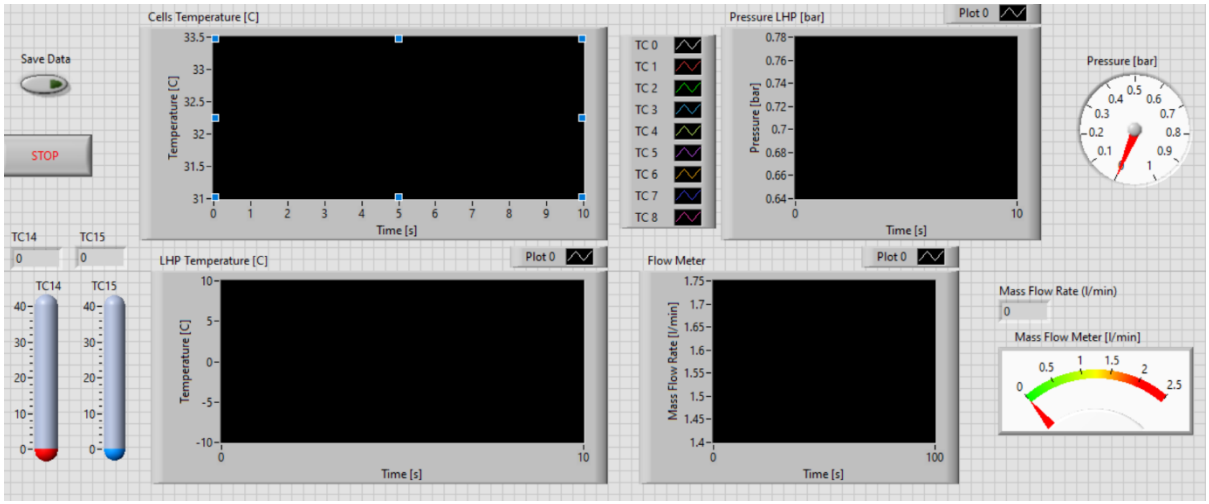

Fig. 61. LabVIEW bespoke front panel interface for the proposed experiments.

5.2.6. Leak Testing, Vacuuming and Filling Operations

As mentioned, vacuum conditions are of paramount importance for correct operation in a two-phase passive device such as the LHP. Vacuum inside the pipe needs to be kept for an appropriate amount of time, allowing to complete several tests in comparable conditions. In order for this to happen, the system must have no leakages. Therefore, the LHP was tested using a VS MD15 helium mass spectrometer leak detector from Agilent Technologies.

The Mass Spectrometer Leak Detector is a complete system for the localization and measurement of leaks inside of a device. This instrument uses a tracer gas, helium in this case, which fills up the device connected to the detector or alternatively it can be sprayed on the joints by means of an external Helium tank. Helium leaks in the tested product and then to the detector where its partial pressure is measured and displayed on a screen.

The principle of leak detector is based on a sector field mass spectrometer. Helium atoms are ionized in vacuum and then accelerated using added voltage and further separated in the magnetic field. The ion current is converted into electric current which is accelerated and displayed on the screen using leak detection units. The measured current is in direct proportion to helium concentration and therefore equal to the measured leak. By gently spraying Helium gas on the external surface of the joints, one can also have an indication of the location of the leakages. Fig. 62 shows the LHP subjected to leak testing.

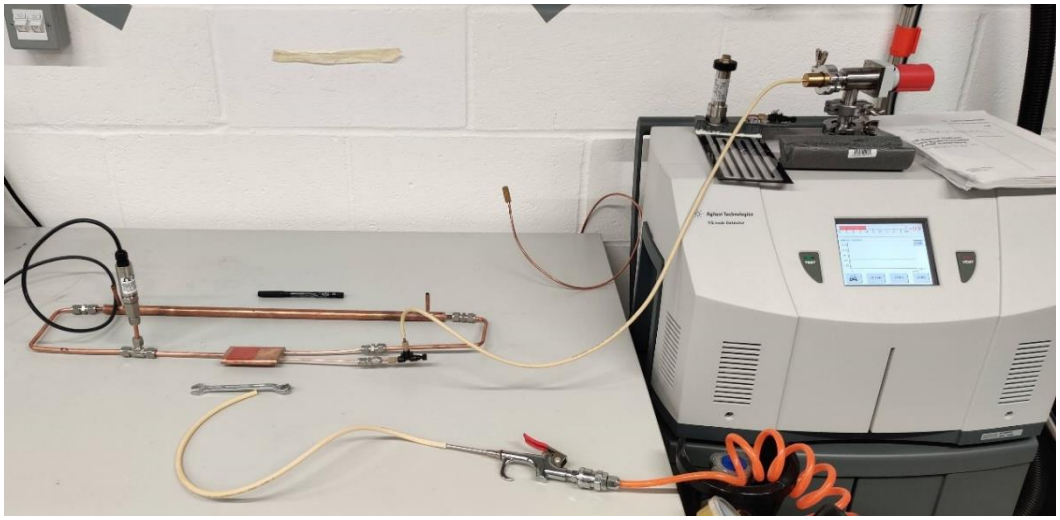

Fig. 62. LHP under leak testing with the Agilent Technologies VS MD15 helium mass spectrometer leak detector.

Acceptable gas tight leak rates are less than 10^{-7} mbar/l·s and acceptable vacuum leak rates are between 10^{-9} and 10^{-10} mbar/l·s. The measured leak rate of the LHP was $4.6 \cdot 10^{-10}$ mbar/l·s, which was considered satisfactory.

After ensuring that the LHP is free of leakages, it was evacuated by means of a two-stage vacuum pump system comprising of a volumetric scroll pump (Boc Edwards XDS35i) and a turbomolecular pump (Boc Edwards EXT255Hi), in order to reach satisfactory level of vacuum. Fig. 63 shows the LHP connected to the pump system. The vacuum level obtained with this system was $1.9 \cdot 10^{-5}$ mbar.

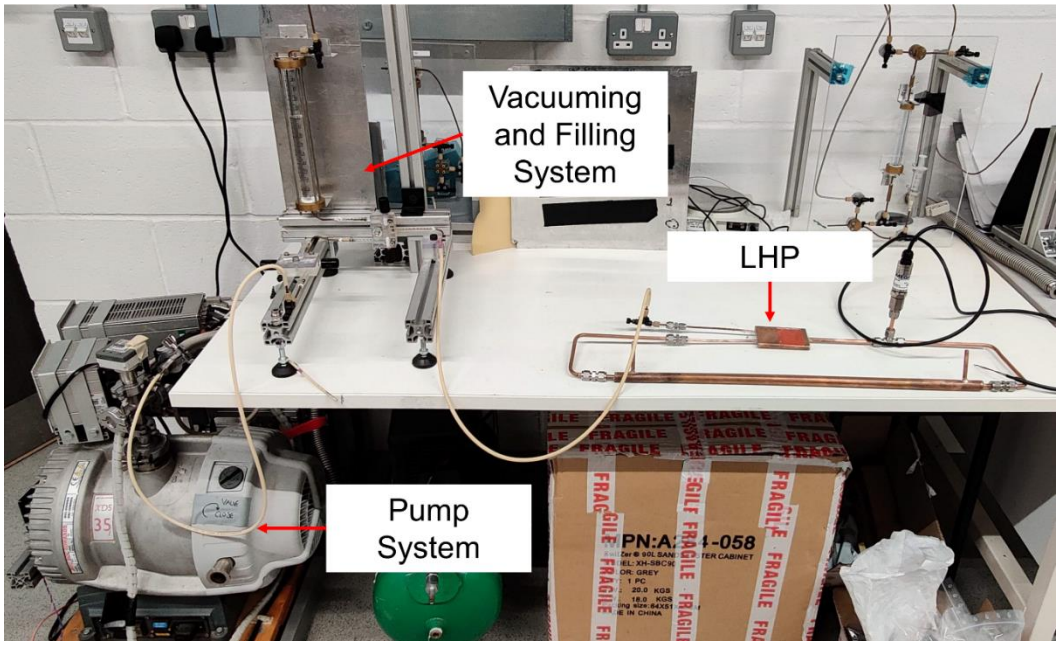

Fig. 63. LHP connected to the filling and vacuuming system and to the scroll-turbomolecular pump system.

The last step to make the LHP operational is the filling process. A bespoke filling rig was created, as shown at the top of Fig. 63, consisting of a set of valves and a graduated cylinder. This rig can be used for vacuuming as well as filling a device and to degas the working fluid. The degasification process is another paramount step of the preparation of a passive two-phase system, in fact it is needed to get rid of all the NCG and impurities that may be present in the working fluid. In this case, vacuum is created inside the cylinder containing the fluid, hence boiling is instigated. This will cause a separation from the species that are different from the fluid, which will float with the vapour at the top of the cylinder. Here, they can be sucked out from the volumetric pump and vented out to the atmosphere.

The quantity of working fluid (i.e. filling ratio) is also a factor that affects the performance of the LHP. As introduced in Chapter 3, literature suggests that, despite the fact that a general best filling ratio does not exist and every design has its own optimum filling ratio, the sweet spots usually lie between 50-60%. Hence in this case, 60% filling ratio was chosen. To fill the LHP, one should exploit the fact that fluids travel towards areas with lower pressure. Connecting the evacuated LHP to the cylinder containing the degassed working fluid, one just needs to open the valve and the fluid would simply flow into the LHP. During this procedure, the mass of the fluid entering the device was monitored to obtain the correct filling ratio.

Fig. 64 shows the final experimental set up during testing, which results are presented in the following section.

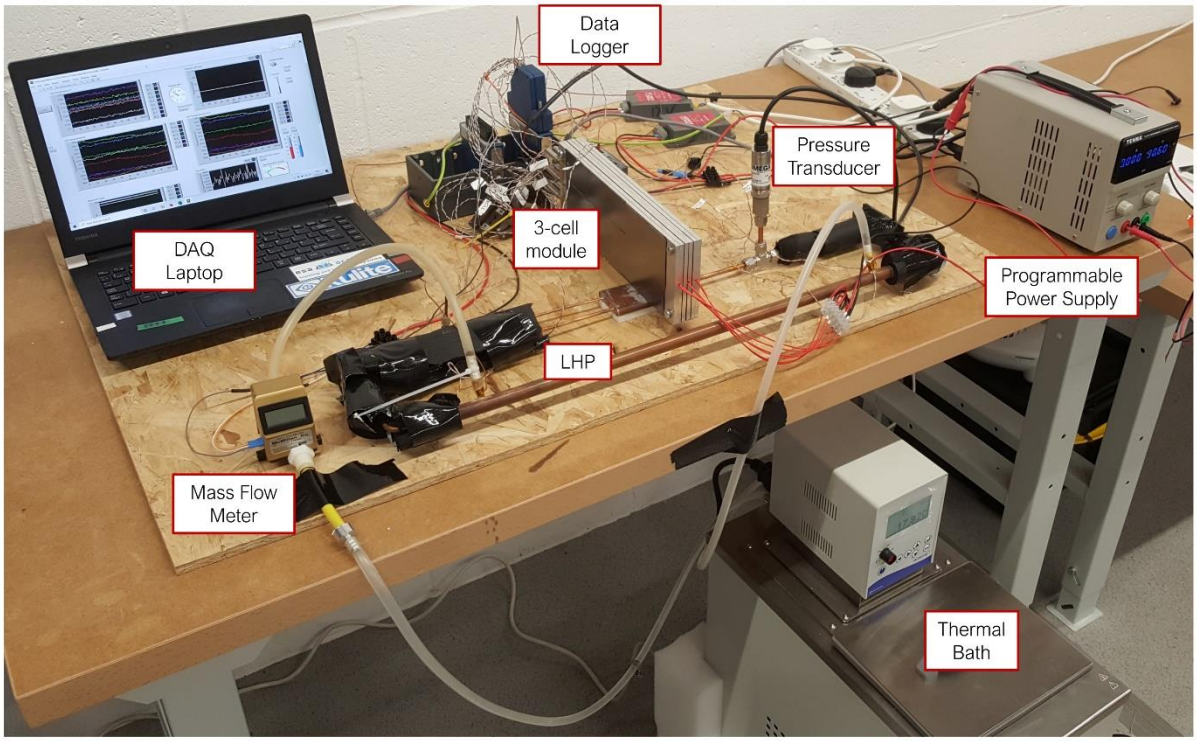

Fig. 64. Full experimental set up with annotation.

5.3. Preliminary Tests Results

5.3.1. Loop Heat Pipe Only Tests

Before investigating the effect of the LHP on the battery module, it is important to get to know the operation of this particular LHP that was created at the laboratories of the AEC. An experimental campaign involving the test on the LHP only, under different heat loads was initially carried out. The purpose of this experimental campaign was twofold: firstly, to gain confidence in the operation of this LHP, in order to better understand its effect on the cooling of the battery dummy model; secondly, to validate the part of the numerical model related to the LHP.

Two fluids have been tested, namely ethanol and water. The applied heat load ranged from 20W to a maximum of 150 W with water. Water was chosen for its ubiquity and its favourable properties such as high surface tension and thermal conductivity. Ethanol was chosen as a good compromise for its sub-zero freezing temperature and lower boiling point than water (78°C). Moreover, ethanol has a lower latent heat of vaporisation which can help in reaching a faster start-up. On the other hand, ethanol has lower values of thermal conductivity and higher saturation pressure with respect to water at the same temperature, with the latter point being an important consideration when it comes to flat plate evaporators. Table 23 presents the most important physical properties of the two fluids, evaluated at ambient conditions.

Table 23 - Water and Ethanol main physical properties comparison (evaluated at 25°C and 1 atm).

Fluid	Water	Ethanol
Density [kg/m]	998	804
Viscosity [mPa·s]	1.002	1.186
Thermal Conductivity [W/m·K]	0.598	0.169
Latent Heat [J/kg]	2453862	945123
Specific Heat [J/kg·K]	4177	3023
Surface Tension [N/m]	0.0727	0.0220
Saturation Pressure [bar]	0.023	0.062
Freezing Point [°C]	4	-114
Boiling Point [°C]	100	78

5.3.1.1. Water-LHP Tests

Fig. 66 shows the results of the first test where the water filled LHP has been subjected to 100 W of heat load. Heat is applied thanks to two heating cartridges (Rotfil 36 V, 120 W, 6.5x100 mm) inserted into an Aluminum block (Fig. 65).

Fig. 65. Rotfil heating cartridge 36 V, 120 W, 6.5x100 mm. Pen for scale.

In this case, the start-up is almost immediate, with the rise of the vapour line temperature (TC10) happening 50 seconds after the application of power to the evaporator. Following that, both pressure and temperatures of evaporator and vapour (TC9, TC10 and TC11) keep on increasing until steady state conditions are reached, after more than 10 minutes. Average evaporator wall temperature at steady state is 54.8°C, leading to a thermal resistance of 0.34 °C/W. It is interesting to notice how the temperatures for the condenser side (TC14 and TC15) are not noticeably increasing throughout, indicating that the condenser has been designed correctly.

The peak in pressure happening around is a phenomenon originating after the shutdown of the heating source (1000 s). The Author's opinion is that the boiling phenomena is transitioning from fully nucleate boiling to partial nucleate boiling, due to the lower heat flux, and here the fluid does not possess enough energy to break the liquid-vapour interface into forming several small dimension bubbles. Thus, yet a bigger bubble originates and expands with the remaining heat flux perceived by the evaporator due to the thermal inertia of the aluminium block, until it reaches a point when the bubbles break up and causes an abrupt decrease in temperature and pressure (especially evident by the trend of TC11).

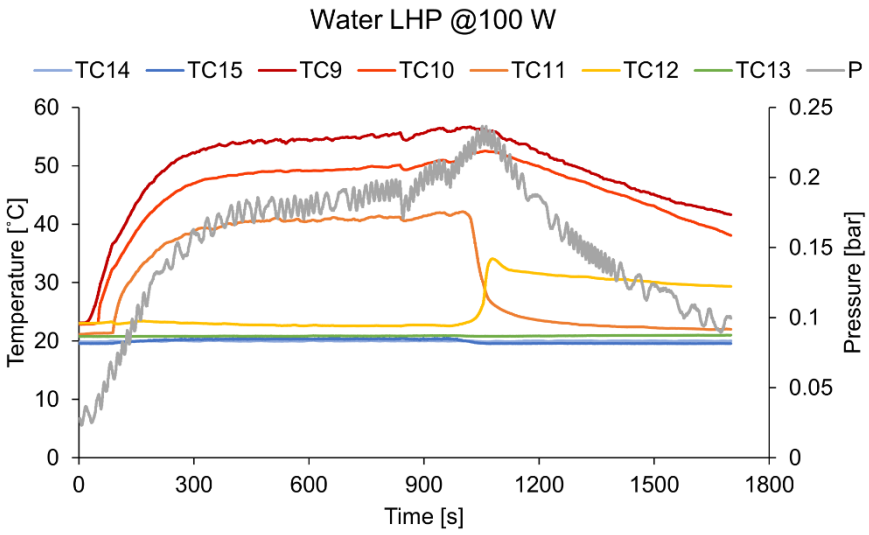

Fig. 66. LHP test results with water as working fluid and 100W heat load (TC position ref can be found in Fig. 58). Power was cut off at 1000 seconds.

With water, one can appreciate the influence and the importance of the difference between the operative pressure of the LHP with the saturation pressure of the fluid at the respective temperature. In fact, in time, the delta between the actual pressure inside the LHP (monitored daily) and the water saturation pressure have grown (Fig. 67). It is evident how the pressure has increased substantially at the beginning of operation, then it started to settle. To verify the effect on the LHP performance, the test of Fig. 66 was repeated after 3 weeks, and the comparison of the results is presented in Fig. 68. After 3 weeks, the discrepancy has reached a value, around 25 mbar, which is comparable to the saturation pressure at that temperature. This increase may be attributed to some leaks that have not being picked up from the leak detector, or to some natural creating of gassing happening in the internal surface of the copper pipes, copper evaporator or the pressure transducer.

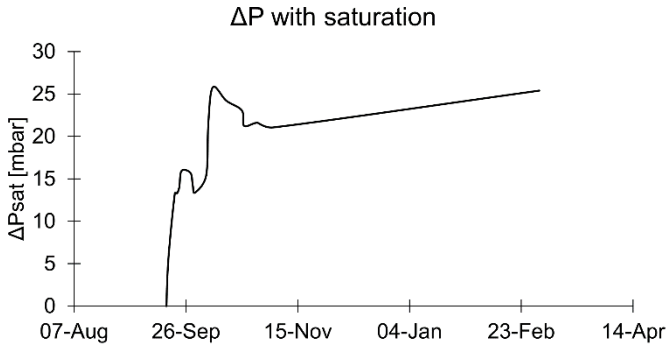

Fig. 67. Daily monitoring of the increase in the difference bewteen operating and saturation pressue for the water filled LHP. The measurements span across 2020 and 2021.

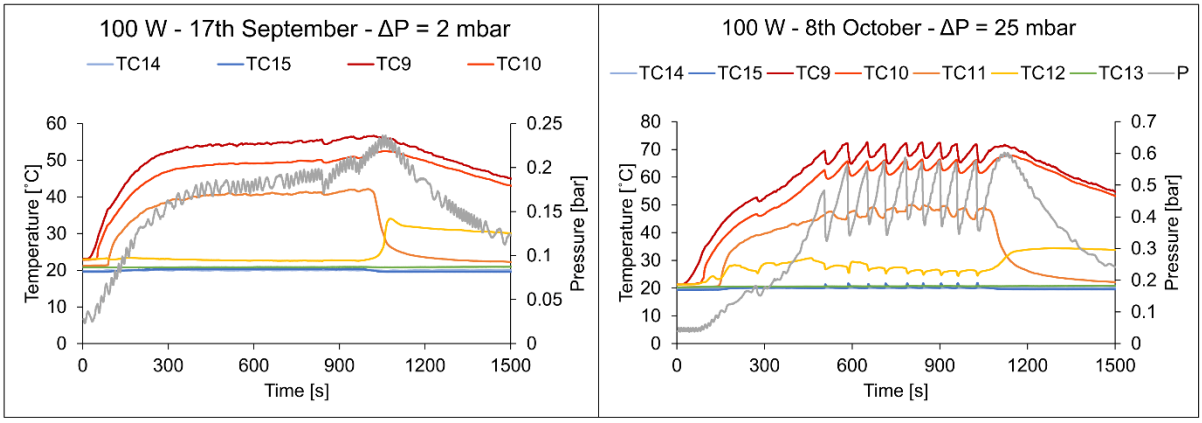

Fig. 68. Effect of NCG on water LHP performance: comparison of same tests undertaken 3 weeks after each other (100 W heat load).

The most evident effect of the NCG is the effect on the operative pressure, as the pressure inside the LHP is doubled in the 8th Oct test, with respect to the previous test. Consequently, temperature increased as well, with the evaporator temperature averaging 69.6°C, showing an

increase of 15°C from three weeks before. Another major difference lies in the behaviour of the fluid, as the smooth operation of the 17th of September is replaced by a strong pulsating oscillation.

5.3.1.2. Ethanol-LHP Test

With the ethanol charged LHP, both steady state tests and ramp tests were performed. But before starting the discussion of these results, it is important to point out that these tests were performed during hot days and the temperature in the labs for that week hovered between 26°C and 28°C, therefore the results could have been affected by this condition.

Fig. 69 shows the trend of the LHP temperatures during a steady state test with 70 W. It is evident that the start-up happens around 250 seconds, with a sudden increase in pressure accompanied by the increase of the temperature of the vapour line (TC10) and the decrease of the temperature in the liquid line (TC12), indicating that refreshed condensed liquid is coming back to the evaporator. The LHP takes a bit more than 15 minutes to reach steady state, with the wall temperature (TC9) stabilizing on 54°C. The thermal resistance here is 0.44 °C/K. The shut-off behaviour is clear, as in this case the power was turned off at 1411 seconds, but the LHP keeps working for an extra 5 minutes, until 1700 seconds, where a sudden drop of the pressure, followed by an analogue drop of the vapour lines temperatures (TC10 and TC11) denotes the extinguishing of the boiling conditions and thus the loop operations.

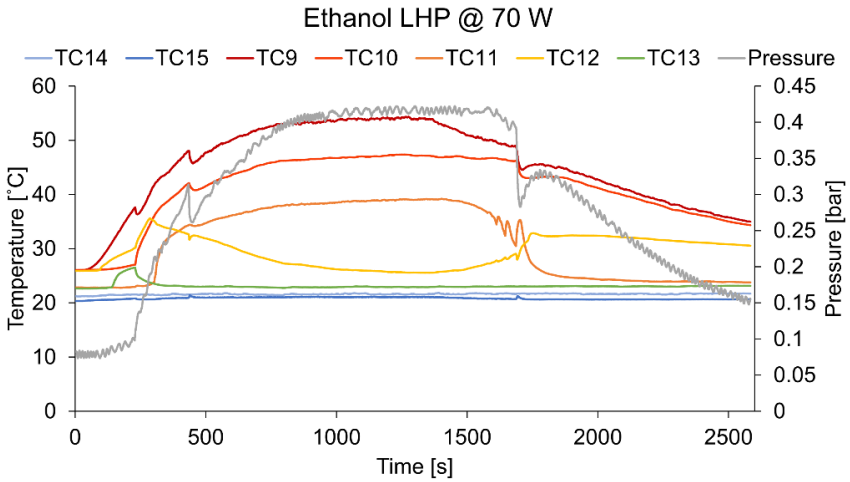

Fig. 69. Results of 70 W steady state test of the LHP with ethanol as working fluid. The power was cut off at 1411 seconds.

The ethanol LHP results of the test with 100W are presented in Fig. 70. As expected, the start-up happened even quicker and smoother than the previous, lower power case. In this test, the device struggled to reach quickly steady state, showing a pressure increase even after 28 minutes, however the temperature of the wall (TC9) shows a quasi-state trend over the last

minutes preceding power shut-off, which was set at 1700 seconds. Hence it was possible to obtain the information about the thermal resistance, calculated at 0.45 °C/K with a wall temperature of 68 °C.

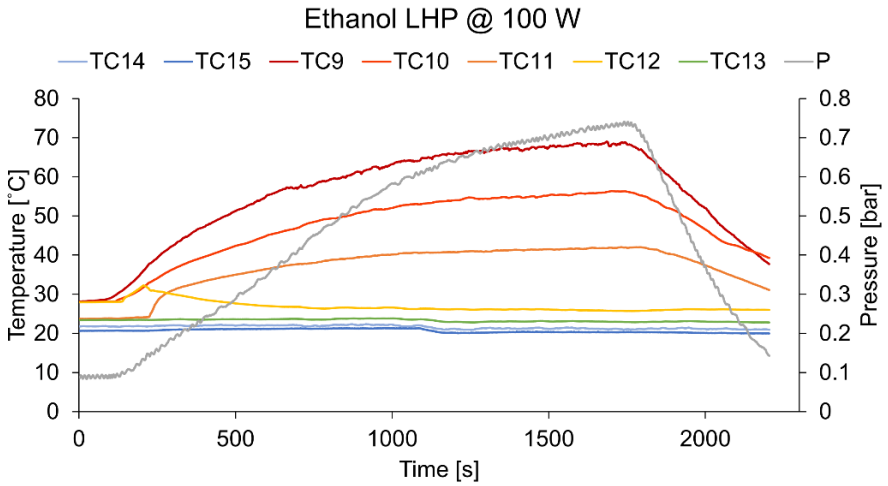

Fig. 70. Results of 100 W steady state test of the LHP with ethanol as working fluid. The power was cut off at 1700 seconds.

Ramp tests were carried out changing the temperature at the condenser, to investigate the reactivity of the LHP to different heat load. In Fig. 71 a ramp test from 20 to 100W in steps of 20W is presented, while the condenser temperature was set to 20°C. In Fig. 72 the same ramp was performed with the difference that the condenser temperature was set at 5°C, however, being the thermal bath hoses not insulated, the actual measured temperature of the water flow coming in the condenser was 7°C. In Table 24 and Table 25, the temperature values of evaporator wall together with the computed thermal resistance are given.

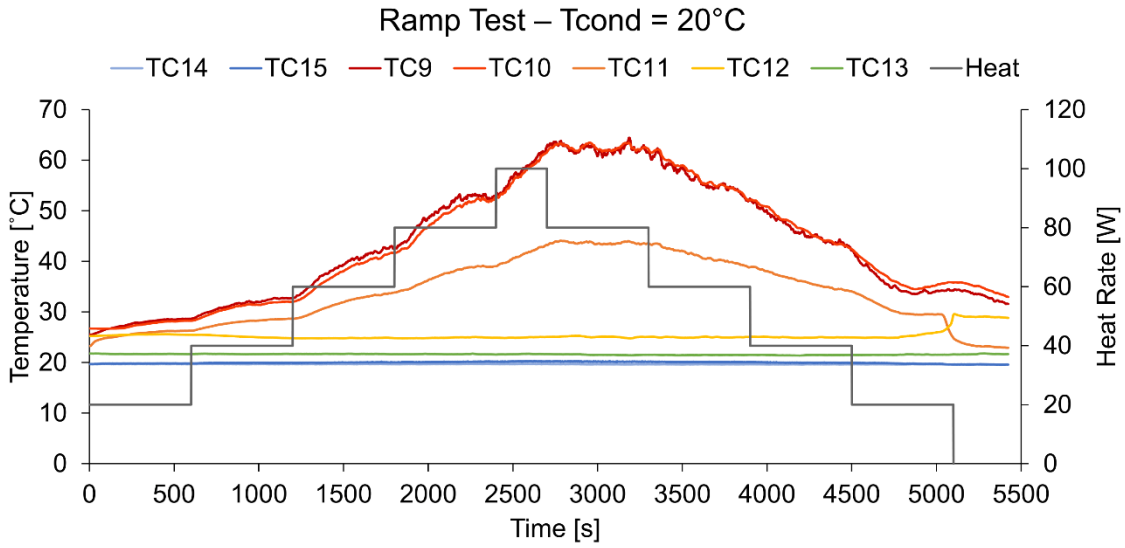

Fig. 71. Ethanol LHP ramp test from 20 to 100W in steps of 20W. Condenser temperature set at 20°C.

Table 24 – Wall temperatures and thermal Resistance of the 20 to 100 W ramp @20°C at the condenser.

Power ↑ [W]	TC9 [°C]	R [°C/W]	Power ↓ [W]	TC9 [°C]	R [°C/W]	ΔTC9 [°C]
20	28.6	0.35	20	34.5	0.63	5.6
40	32.7	0.27	40	43.4	0.55	10.7
60	42.5	0.35	60	53.2	0.53	10.8
80	52.8	0.39	80	62.1	0.51	9.3

In the test displayed in Fig. 71, each power level was kept for 10 minutes, allowing for the LHP to reach steady state at all power levels, showing the reactivity and flexibility of operation of this device. It is important to say that the 100W power level was maintained for less time than the others in order to prevent the pressure from overcoming the safety levels, hence why steady state was not reached and data not reported in Table 24. That level of power could not be sustained by the LHP as the internal pressure was dangerously going above 1.2 bar, which is the limitation of this copper thin-walled flat evaporator. Bringing the device to higher pressure, would generate the risk of ruining the wick/wall sealing, which would create a pressure short-circuit as the vapour goes towards both compensation chamber and vapour line, nullifying the pumping action of the capillary wick. Changing the envelope material to a sturdier metal (i.e., Stainless-Steel) or increasing the thickness of the wall would allow for much higher heat loads.

A form of hysteresis was noticed (introduced them in Chapter 3), as the LHP temperatures on the downward ramp are sensibly higher (e.g., 5-10°C increase at the same heat rate level). In addition, the downward temperature trends do not follow the step-down trend of the heat load, instead they decrease at a quasi-steady rate, most likely because of the thermal inertia of the 100 W heat load case still to be dissipated.

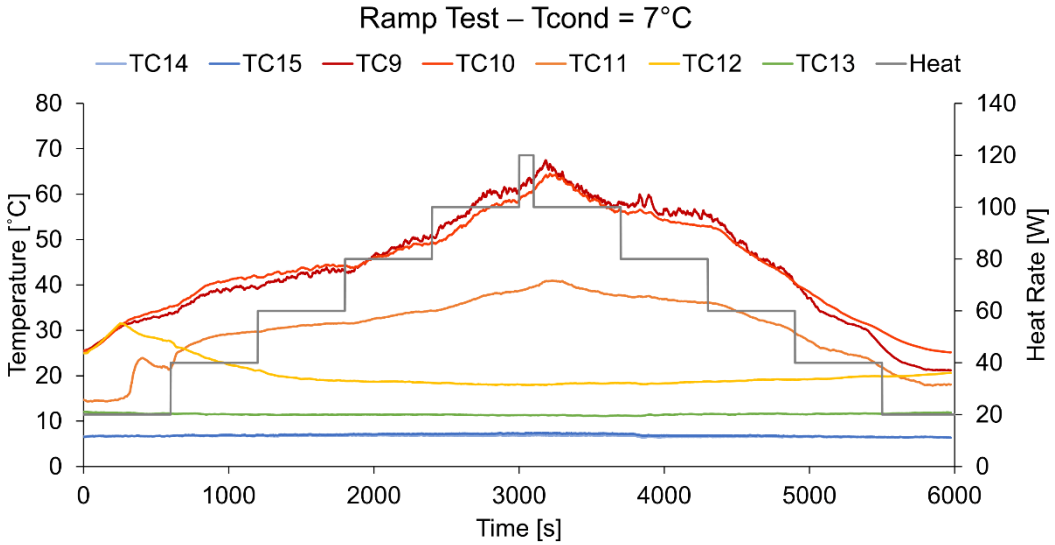

Fig. 72. Ethanol LHP ramp test from 20 to 120W (20W steps). Condenser effective temperature 7°C.

Table 25 – Wall temperatures and thermal Resistance of the 20 to 120 W ramp @5°C at the condenser.

Power ↑ [W]	TC9 [°C]	R [°C/W]	Power ↓ [W]	TC9 [°C]	R [°C/W]	ΔTC9 [°C]
20	33.5	1.09	20	21.2	0.47	-12.3
40	39.4	0.70	40	28.2	0.41	-11.2
60	43.2	0.53	60	42.4	0.51	-0.8
80	50.3	0.48	80	55.6	0.55	5.4
100	60.8	0.50	100	57.7	0.47	-3.1

The lower heat sink temperature allowed for an overall lower operative LHP, that allowed to reach steady state also at 100 W without getting to the 1.2 bar threshold. This was instead reached with 120W power level, hence why that power level was maintained for so little time. Temperature variations similar to the previous hysteresis cases were observed, with the minor difference that during the 60W downward power case, no steady state was reached.

5.3.2. System Level Tests

After understanding the behaviour of the LHP under known loads, the overall system has been tested. The dummy battery module was place transversally over the evaporator, to ensure that the contact was only in the heating zone, i.e., where the wick is. In fact, if heat is applied to both the wick and the compensation chamber (such would be the case of the longitudinally placed module) the LHP will not start as vapour will generate from the compensation chamber first and flow in the liquid line towards the condenser, since the compensation chamber is an empty container, it has low thermal inertia. This will create an adverse pressure gradient that the wick will not be able to overcome, therefore preventing the start-up of the LHP.

The system level tests involved the LHP with both fluids respectively. However, as shown in Fig. 73 the water-filled LHP was not able to start during the system level test. One can notice at around 1700 seconds, an instance of boiling appears, followed a few minutes after by another one. Nevertheless, the working fluid does not seem to be able to onset a steady boiling process, stuttering like an engine with not enough gas, with temperatures showing an increasing trend. The power was cut off shortly after the 90°C threshold to not damage the heaters. The Author believes that the reason for this behaviour is the low exchange surface between the evaporator and the battery module, where from one side (battery side) it is not enough to remove heat from the cells, and from the other side (LHP side) it is not enough to transfer enough heat to the fluid.

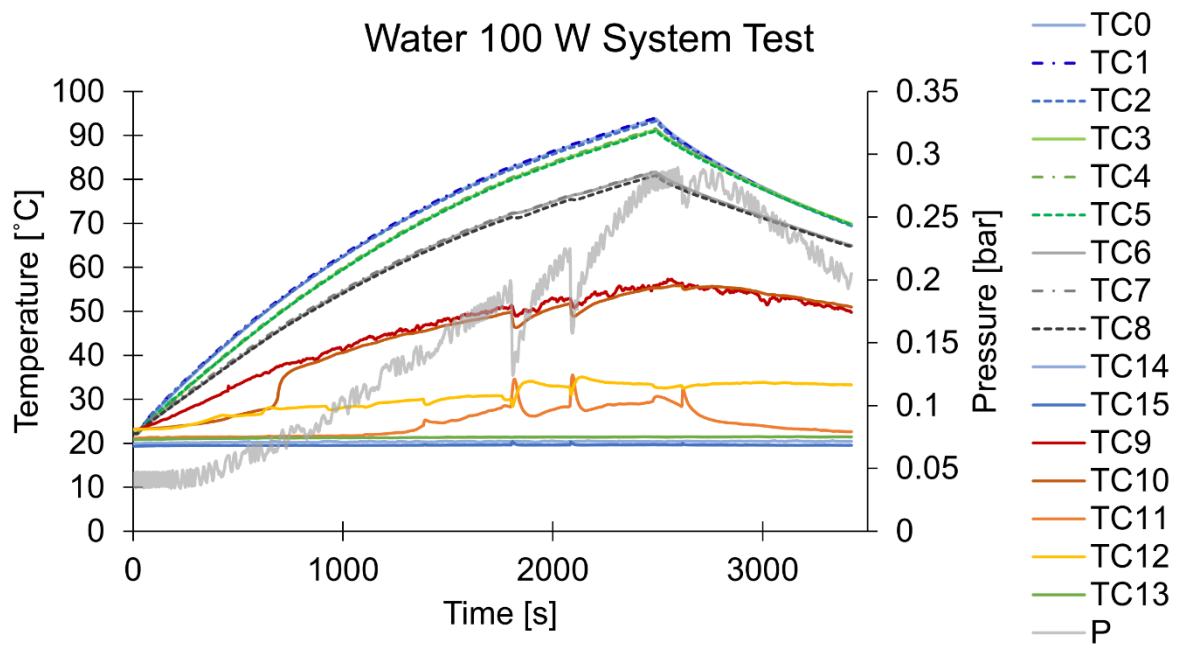

Fig. 73. System level test with water-filled LHP and 100 W power load.

On the other hand, with ethanol, given its lower latent heat and boiling point, the low exchange surface area did not prevent the start-up, it only delayed it. In fact, as we can see from Fig. 74 and Fig. 75, under a total heat load applied to the battery module of 70 W and 150 W respectively, the LHP starts up shortly before the 2000 seconds and 1500 seconds marks, indicated by the sudden increases in pressure and vapour line temperature (TC10) and decrease of the liquid condensate temperature (TC12 and TC13).

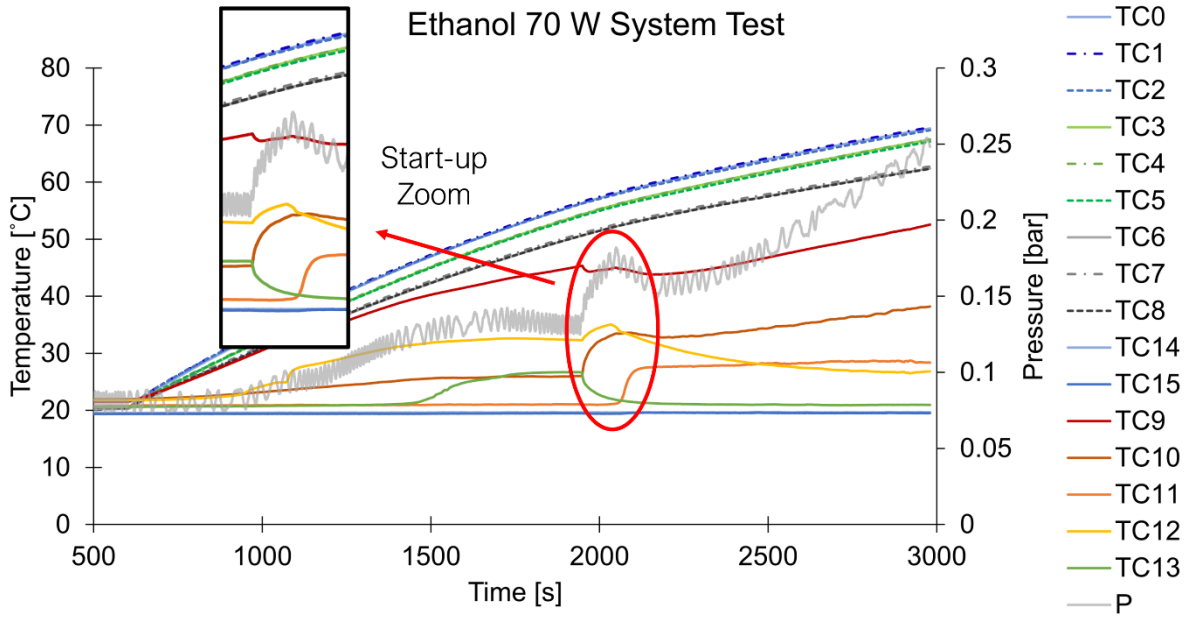

Fig. 74. System level test with ethanol-filled LHP and 70 W power load.

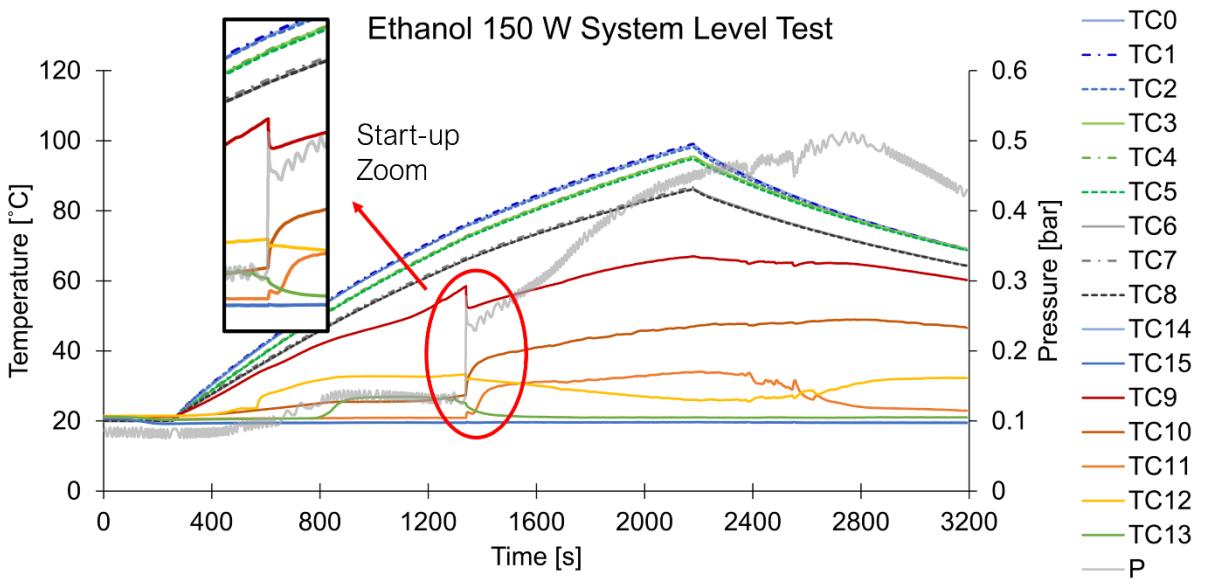

Fig. 75. System level test with ethanol-filled LHP and 150 W power load.

One can notice how the slope of the cell temperature increase changes and slightly flattens down after the activation of the LHP, to signify its effect. However, due to the unfavourable mismatch in terms of exchange area between the battery module and the LHP, the amount of heat removed by the LHP is not enough to stop the temperature increase of the module.

5.4. Numerical Validation

This numerical validation is describing a complex thermo-fluidic phenomenon by means of a one-dimensional lumped parameter model. Due to the number of limitations of this methodology, despite its many advantages, results are regarded as satisfactory if errors are below the 10% and 5°C threshold.

5.4.1. Validation of cell-graphite assembly code

The validation process consisted in three separate steps. Here, the first step regarding the validation of the model for the cell-graphite assembly is presented.

The purpose of this validation process is to verify the accuracy of the numerical model describing the cell-graphite assembly only, without considering the part of the model describing the LHP. Thus, the dummy battery module was left suspended from the workbench surface, supported by two small wooden pegs only.

To adapt the numerical model to the case in object, small modifications were necessary. In fact, being the module not insulated, heat losses to the ambient by free convection had to be

introduced to the sides of the cells. Moreover, being the model suspended, free convection boundary condition was added to the bottom of the module as well.

In the experiment, the lab ambient temperature was 23°C and the module was heated with the total power of 150 W until reaching 100°C, and then let to cool down for 25 minutes. Fig. 76 shows the comparison between the average temperature evolution of the first cell (the one with thermocouples TC0, TC1, TC2) and the average temperature predicted by the model. The maximum discrepancy at the top of the curve is of 2.4°C, while at the end of the cooling off period the error is 0.7°C. Considering the accuracy of these results and the fact that the experimental trend is also matched in time, the thermal network describing the cell-graphite assembly, and its relevant code, are deemed to be working properly.

Satisfied with the results presented in Fig. 76, the next section will move on and address the validation of the LHP part.

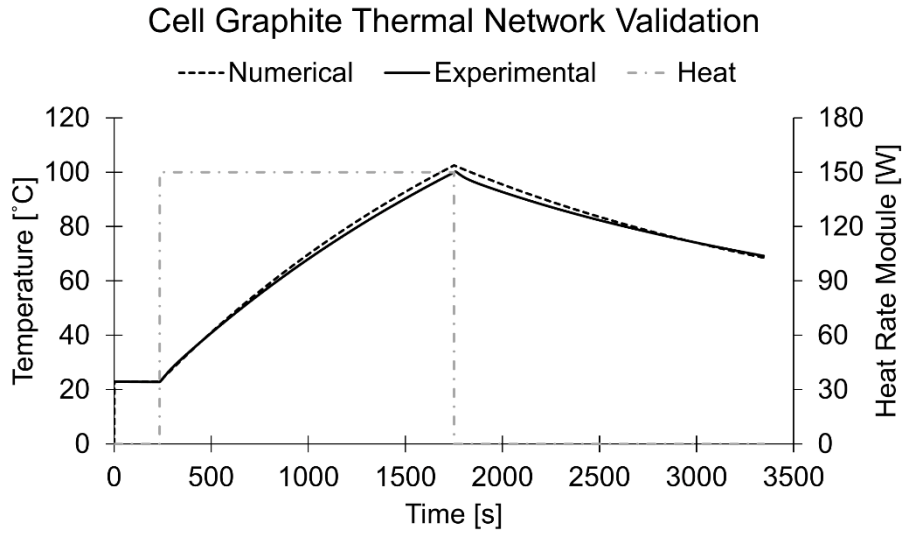

Fig. 76. Validation of the cell-graphite assembly: trends of the average nodes temperature of the first cell (TC0, TC1, TC2) in the experiment and the average nodes temperature resulting from the simulation.

5.4.2. Validation of LHP code

Here the second step of the validation process is presented, discussing the results of the code relative to the LHP only.

The validation of LHP code happens over three steps, aiming to:

1. replicate the data provided for the manufacturer using water as working fluid, with power from 40W to 900W;
2. replicate the results obtained in-house with the water-filled LHP;

3. replicate the results obtained in-house with the ethanol-filled LHP;

It is to be expected that the discrepancy between the numerical and experimental results will be higher in the first case as there are some unknown in the design such as the filling ratio and the fluidic lines' exact lengths.

Starting with the step 1, the graph in Fig. 77 presents the comparison of the data provided by the Thercon LHP against the numerical prediction of the proposed LPM, by means of highlighting the difference in temperature of the wall and vapour grooves, as well as the percentage difference in the thermal resistance, which was calculated as follow:

$$R = \frac{T_{wall} - T_{cool}}{\dot{Q}} \tag{79}$$

where T_{cool} is 20°C. The full numerical results are presented in Appendix A.

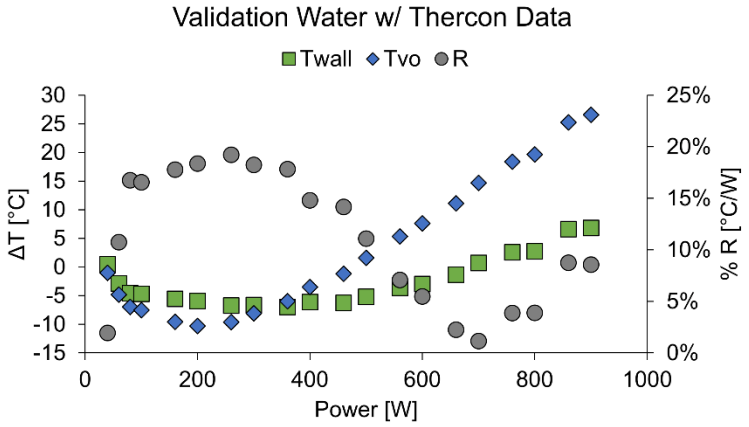

Fig. 77. Validation of the water filled LHP using the data provided from the utilised evaporator manufacturer. The Resistance is calculated using a condenser temperature of 20°C. The y axis shows the ΔT between Thercon experimental data and the numerical prediction obtained in this PhD thesis.

The average errors in the prediction of the wall temperature and vapour grooves showed in Fig. 77 are 4.5°C and 9.9°C, respectively, while the percentage error of the thermal resistance prediction is 10.9%. The error in the vapour grooves prediction increases after the power of 660W, suggesting that the code underestimates the phenomena happening at high powers, most likely linked to having superheated vapour at the inlet of the condenser (which is not considered in the present model). Nonetheless, the vapour temperature prediction at medium to low power, as well as the thermal resistance and wall temperature prediction in all power levels, are below the selected threshold. Considering again the effect of incomplete data, these results are considered successful.

Moving to the comparison with in-house results (step 2), Table 26 shows the results of the prediction of the steady state temperature of the water-filled LHP under a heat load of 100W.

Table 26 - Validation of the water-filled LHP by using the in-house produced data. The applied power was 100W.

	T_{wall} [°C]	T_{vo} [°C]	T_{ll} [°C]	T_{cond}[°C]	$R\left[\frac{°C}{W}\right]$
Model	54.51	51.25	20.98	20.14	0.345
InHouse Tests	54.80	49.45	22.62	20.87	0.348
ΔT	0.29	-1.80	1.64	0.72	0.84%

From Table 26 it is evident that in this case the discrepancy is minimal across the different nodes of the LHP (less than 2°C). Moreover, the thermal resistance percentage error is less than 1% (where R has been calculated by using T_{cond} instead of T_{cool} in equation (79)). This concludes the validation of the water-filled LHP.

For the last step of the LHP validation process, experimental data of the ethanol LHP are numerically replicated. Fig. 78 presents the error between the data obtained through both steady and ramped input power tests, with two different conditions at the condenser, i.e. thermal bath temperature set at 20°C and 5°C (full data are provided in Appendix B). The average discrepancy between the numerical and experimental data is very low, with temperature predictions errors for the 4 selected nodes within a ±5°C window, respectively 2.8°C for T_{wall}, 3.3°C for T_{vo}, 4.2°C for T_{ll} and 4.7°C for T_{cond}. Moreover, the average percentage error on the thermal resistance prediction is 8.8%, lower than the 10% threshold which is assumed acceptable considering the complexity of the modelled two-phase device.

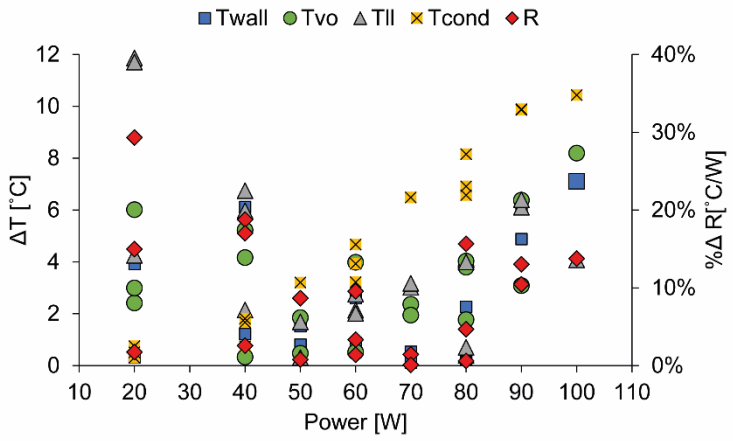

Fig. 78. Results from both steady state and ramp test for the validation of the ethanol LHP. The results, grouped by power levels, are showing the ΔT and % error on the thermal resistance R, between the experimental measurements and numerical prediction.

The numerical code proposed in this work is therefore able to reproduce, with satisfactory accuracy, the temperatures in various critical locations of the proposed heat transfer device.

The temperature prediction is accurate for all four of the considered nodes, namely the evaporator wall, vapour line, condenser and the liquid line, confirming the robustness of the designed thermal network and the accuracy of the lumped parameter approach. Accurate results are obtained for two different working fluids (water and ethanol), showing that the proposed model can be applied to extend the investigation to different fluids without the need of new experiments, which can be valuable in the case of fluids which are expensive, potentially harmful or even requiring non-standard testing conditions.

Concluding, this validation procedure on the LHP code was accomplished with excellent results (i.e., with errors below the selected thresholds of ±5°C and 10% error). The LHP numerical code proposed in this work is now able to reproduce, with satisfactory accuracy, the temperature of more than one node (such was the case of the previous validation presented in Chapter 4).

5.4.3. System Level Validation

For the system level validation, only the data obtained with experimental measurements with the LHP running with ethanol are used in the comparison with the numerical predictions, as it has shown better start-up behaviour. More specifically, the aim is to reproduce the data obtained with the steady power input simulations of 70 W, 150 W respectively, and with the system subjected to the HFCH driving cycle.

5.4.3.1. 70 W Test

Table 27 and Fig. 79 present the results of the validation procedure over the 70 W case, i.e. the error in temperature prediction over various nodes of the model (cells and LHP) as well as the comparison of the trends of the average cell temperature over time. The latter being estimated as the difference between the experimental and numerical average temperature of the three considered cell nodes. As already explained previously, since the lumped parameter methodology carries some intrinsic limitations due to its main assumptions, the obtained 3°C average discrepancy is considered a satisfactory result. Moreover, Table 27 shows that the prediction of the vapour temperature of the LHP is very close to the experimental measurement and for the condenser outlet there is a corresponding error of 4.6°C, which is below the acceptable threshold.

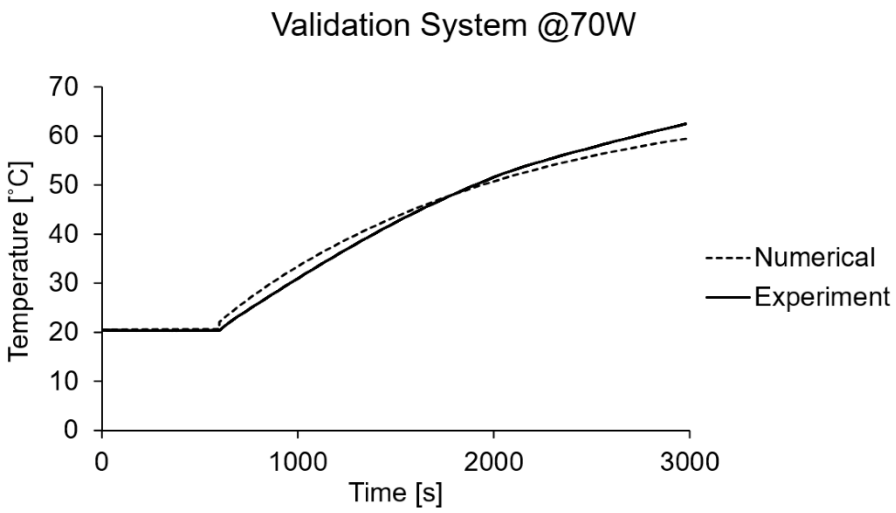

Fig. 79. System validation with total heat load of 70 W (ethanol as working fluid). Temperatures shown are the average of the three nodes. In the experimental case, the middle cell of the module is considered.

Table 27 - Error in temperature prediction for the system level validation with total heat load of 70W. All temperatures are shown in [°C].

	T_{wall}	T_{vo}	T_{cond}	$T_{cell,1}$	$T_{cell,2}$	$T_{cell,3}$
Experiment	52.6	38.2	21.0	62.4	62.8	62.3
Numerical	39.6	38.5	25.5	59.7	59.5	59.1
Δ	13.0	-0.3	-4.6	2.7	3.2	3.2
	Average ΔT_{cell}			3.0		

Looking at the trends of Fig. 79, a slight divergence is observed throughout the entire duration, starting with a slight overprediction and ending up with a slight underprediction. However, it is accepted, considering that this happens during a long duration event (30 mins) and considering the overall assumptions and simplifications of the model. The discrepancy in T_{wall} is due most likely to the position of the thermocouple during the test; however, being the vapour temperature quite close, it indicates that the LHP part of the code also works properly.

5.4.3.2. 150 W Test

In the case where the cells were subjected to a 150 W power input, the discrepancies between the experimental and the modelling results are similar to the 70 W case, as depicted in Fig. 80 and Table 28. The test was conducted by heating up the cells with 150 W for 30 minutes and then recording data with power switched off for subsequent 20 minutes. The temperature set for the thermal bath was 20°C. In this case the average temperature discrepancy between the experiment and the model for the three nodes of the cell is 2.4°C, thus consistent with the results of the validation for the 70W case.

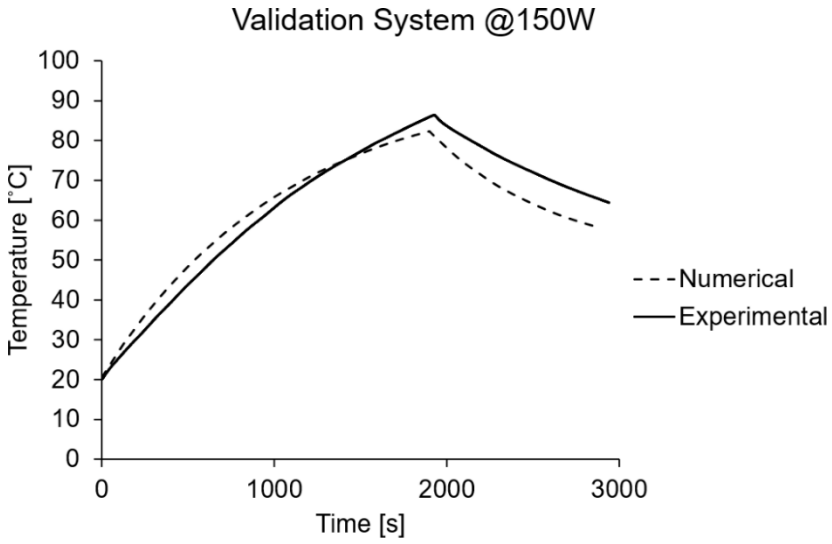

Fig. 80. System validation with total heat load of 150 W (ethanol as working fluid). Temperatures shown are the average of the three nodes. In the experimental case, the middle cell of the module is considered.

Table 28 - Error in temperature prediction for the system level validation with total heat load of 150W. All shown temperatures refers to the moment the power was turned off, and they are shown in [°C].

	T_{wall}	T_{vo}	T_{cond}	$T_{cell,1}$	$T_{cell,2}$	$T_{cell,3}$
Experiment	67.0	49.0	27.0	86.3	86.8	86.1
Numerical	50.5	46.4	39.6	84.8	84.2	83.0
Δ	16.5	0.9	-12.7	1.5	2.6	3.1
	Average ΔT_{cell}			2.4		

5.4.3.3. HFCH Driving Cycle Test

Finally, the last part of the system validation involved reproducing the results of the custom-made HFCH driving cycle test, described in Chapter 4. The test results are shown in Fig. 81, where the positions of thermocouples are depicted in Fig. 48 and Fig. 60. To help the reader's understanding of the graph in Fig. 81, an additional image showing the thermocouple and cell nomenclature is given in Fig. 82. Firstly, one can notice that the cell temperature is above the threshold required by the pack requirement for optimum and acceptable performance, as maximum temperature in the third cell is 53.3°C. This is due to the abovementioned mismatch in available surface between the battery module and the heating zone of the LHP evaporator, as the latter was bound by the manufacturer availability. However, maximum temperature in cell 1 is 59°C, so still below the upper safety limit of the requirement at the pack level.

Furthermore, it is interesting to notice how the cell temperature trends do not follow the sharp variations of the heat generation rate profile, due to the massive thermal inertia of the cells; behaviour that was already captured by the LPM numerical predictions.

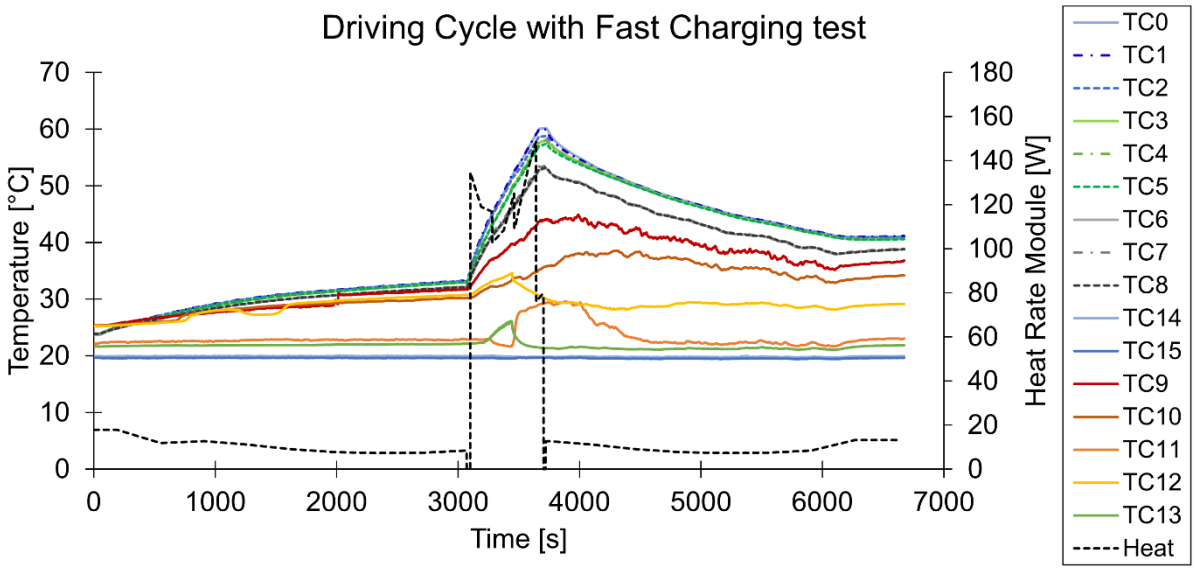

Fig. 81. Experiment results of the whole system subjected to the HFCH Driving cycle; the LHP is running with ethanol.

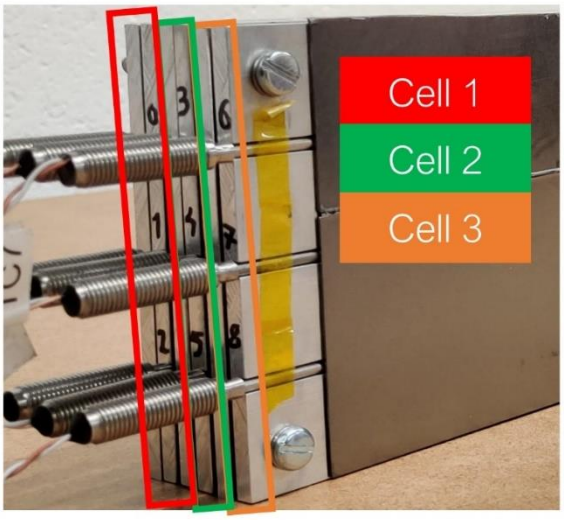

Fig. 82. Cell nomenclature and detail of thermocouples numbering and positioning.

The average temperature spread (i.e., maximum temperature difference over a single cell) over the three cells is 0.7°C, which is below the threshold of 3-5°C set by the cell requirement. Furthermore, the difference between the temperature of cell 2 (TC3,4,5) and the cell 3 (TC6,7,8) is 4.5°C, whereas the temperature difference between the cell 2 cell and the cell 1 (TC0,1,2) is 1.8°C. This difference is due to cell 1 being without the graphite sheet, which was a design choice to investigate the effect of graphite on the side cells of the modules. It shows that in both cases, with respect to the middle cell, the proposed design respects the module thermal requirement as well (i.e., ΔT between the cell to be less than 5°C). Moreover, it shows that having graphite on both side of the cell reduces the maximum temperature at the end of

fast charge by 1.8°C, compared to having graphite only on one side and free convection on the other (ΔT between cell 1 and cell 2).

The graph in Fig. 83 shows the comparison between experimental and numerical results of cell 2 and cell 3. For clarity purposes, the graph shows only the average temperature of the three thermocouple measurements as well as the average value of the three nodes for the numerical side. To produce these results, the code was run twice, changing the boundary conditions for the sides of the cell accordingly: for cell 2, since it is in the middle of two graphite sheets, half of its exchanged heat goes into one sheet and the other half in the other sheet, due to symmetry; for the cell 3, free convection on one side of the graphite was added. Hence it was chosen to make the cell dialoguing with one graphite sheet only receiving the whole exchanged heat (it makes no difference for LPMs) and the other side of the cell is subjected to insulated boundary conditions. Fig. 83 shows that there is a good agreement between experimental and numerical data, even with a complex driving cycle.

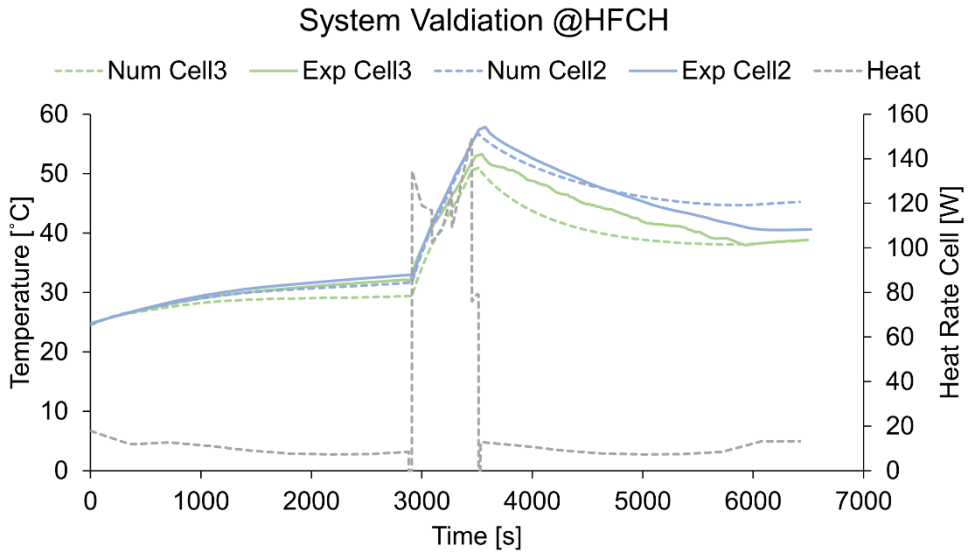

Fig. 83. System Validation with ethanol as working fluid during the HFCH driving cycle: comparison between experimental and numerical results for cell 2 and 3. Temperatures shown are the average of the three nodes. Cell 1 boundary conditions were not reproduced in the LPM, as matching two different sets of boundary conditions was deemed sufficient.

The difference between the experimental temperature and the numerical prediction is of 1.2°C for cell 2 and 2.3°C for cell 1, as shown in the data breakdown of Table 29. The discrepancy between prediction and experimental data grows towards the end of the driving cycle, in the case of cell 2, reaching a value of 4.6°C, whereas for cell 3 the prediction aligns with the experimental data, showing an error of 0.1°C. Furthermore, both experimental and numerical results show how the temperature spread across the cell is maintained below 1°C,

which is well below the requirement at the cell level (T<3-5°C), meaning the graphite sheets could be a promising choice.

Table 29. Results of the system validation on the HFCH driving cycle for cell 2 and 3.

	Numerical [°C]	Experimental [°C]	ΔT [°C]
Cell 2 T_{max}	56.7	57.9	1.2
Cell 3 T_{max}	51.0	53.3	2.3
Cell 2 T_{final}	45.3	40.6	4.6
Cell 3 final T_{final}	38.7	38.8	0.1
ΔT across cell 2	0.6	1.0	0.4
ΔT across cell 3	0.5	0.9	0.4

Another interesting development of this validation campaign is presented in Fig. 84, where the numerical and experimental results for the vapour and condenser outlet temperature are compared. It can be noted how the trends for the vapour temperature are closely matched until 5000 seconds, when the experimental temperature decreases by 4°C whereas in the numerical results the decrease is by 0.5°C only. However, it is interesting to observe how the outlet condenser temperature, in the numerical results, until 3500 seconds, has the same value of the vapour line temperature, meaning that the condensation process is not completed, and the condenser is not able to generate any subcooled liquid. After 3500 seconds, subcooled liquid starts to exit the condenser, indicating that the mass flow rate generated by the evaporator and the vapour temperature are high enough to ensure a full condensation process. Looking at the experimental trend of the condenser outlet temperature, this exhibits an increase (due to the conduction along the copper pipe) followed by a sudden drop which coincides with the start-up of the LHP, signifying the passage of the newly formed liquid making its way back to the evaporator. These results indicated that, although the LHP start-up cannot be precisely predicted, as it is a phenomenon that depends on unknown initial conditions (the arrangement of the working fluid inside the device), this code can give an indication as to when this might happen, based on the cooling capacity of the condenser.

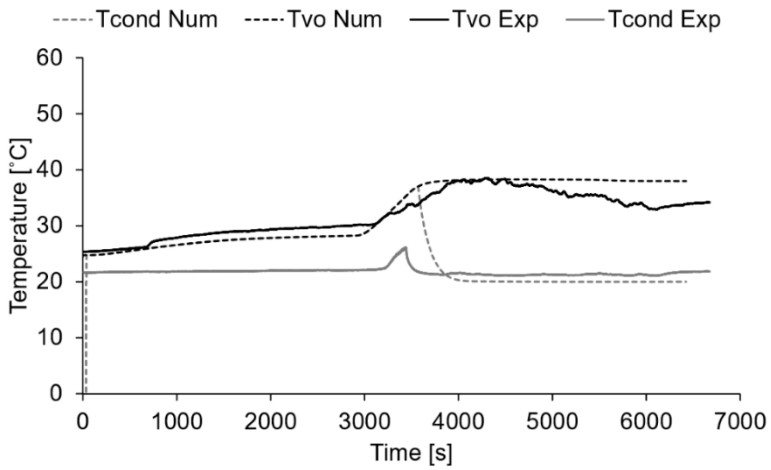

Fig. 84. Comparison between numerical and experimental results for the temperature of vapour exiting the evaporator and fluid exiting the condenser during the HFCH driving cycle test.

Considering all the above validation steps, it can be safely said that the proposed LPM model predictions are reliable and the model itself can be safely used as design tool for the proposed as well as other similar designs of TMS for EV battery cooling. This allows the utilisation of this tool for real applications.

5.5. Comparison of LHP vs Cold Plate TMS

One of the main reasons for the development and validation of the LPM tool proposed in this work, was for its application to compare the performance of the proposed novel LHP based design with the performances of a standard liquid cold plate based cooling system. The model describing the latter was developed and validated by the engineers of the industrial collaborator, Ricardo plc, and was described in Chapter 4.

For this comparison to be effective, in the LPM model proposed herein, the physical properties of the real cell detailed in Chapter 4 were used. Moreover, the footprint size of the evaporator heating zone was set to match the bottom footprint of the three-cell module, whilst maintaining all the other dimensions unaltered. This operation has the twofold purpose of maximizing the heat transfer between module and LHP and to maintain a comparable geometry to the one of the liquid cold plate. The two TMS solutions were evaluated over the HFCH driving cycle. All boundary conditions have been kept the same as the ones used in the simulations previously presented in this thesis. The chosen working fluids are ethanol for the LHP and ethylene glycol for the cold plate.

Fig. 85 presents the results of this comparison in terms of average temperature of the three cell nodes, in both cases. From these results it is evident that the LHP solution performs well

in terms of temperature reduction during the fast charging section, keeping the maximum cell temperature 3.6°C degree lower than the maximum temperature reached in the liquid cold plate case. In fact, the TMS proposed in this work is able to respect the temperature requirement at pack level, having a maximum temperature of 31.5°C, against the maximum temperature of the liquid cold plate of 35.1°C. Moreover, the LHP TMS allows for a faster temperature reduction after fast charging, with the two solutions exhibiting 3.9°C of difference at the end of the driving cycle. In addition, the simulation results showed that the graphite addition helps to respect the cell requirement as well, with the ΔT across the cell being 2°C.

One of the most appealing benefits of using LHPs lies in the passive nature of these devices. In fact, thanks to the absence of a need for an external source of motion for the fluid, a pump is needed to circulate the refrigerant only for the heat exchanger used to cool down the condenser of the LHP. In the liquid cooling loop used as comparison, the pump needs to provide a pressure gradient sufficient for the fluid to travel through the entire battery pack length. This will adversely affect the all-electric range of the vehicle.

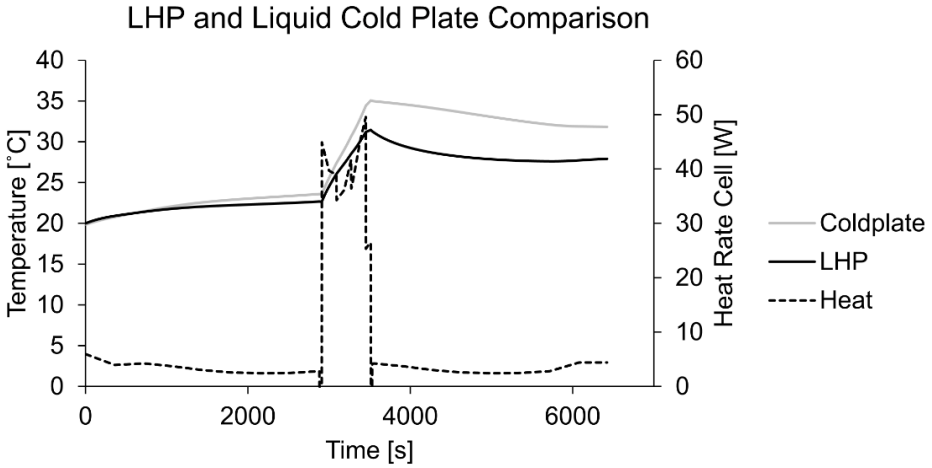

Fig. 85. Comparison between LHP and Liquid Cold Plate TMS during a HFCH driving cycle. This graph shows the average temperature of the three nodes in both cases.

The biggest intrinsic benefit of having a validated LPM is that it makes it possible to evaluate the effect of design changes on the actual performances without the need to test them experimentally. In the next Chapter, several numerical simulations on design aspects that are significant for the implementation of the proposed design in the automotive sector.

5.6. Conclusions

This Chapter describes in detail the experimental apparatus built to effectively study the feasibility of this new TMS design. A 3-cell module was machined and assembled with graphite

sheets sandwiched between the cells. Following, it was instrumented with temperature sensors and power heaters. This module was then linked to the proposed cooling medium, which is a copper/copper flat plate LHP (externally sourced). The condenser of the LHP was embedded in a tube in tube heat exchanger, connected to a thermal bath. The LHP was finally instrumented with temperature and pressure measurements. To verify the feasibility of this solution and to compare it against a standard liquid cold plate solution, the presented experimental demonstrator was used to validate the LPM. From the overall analysis and discussion of the results the following worth mentioning conclusions can be drawn:

- The experimental campaign resulted in a satisfactory validation over two different working fluids (ethanol and water), on every part of the LPM.
- The maximum ΔT between experimental and simulation data for the cell-graphite assembly was 2.4°C.
- The reproduction of the in-house experimental data with the LHP-only LPM gave excellent results, with the average percentage error for the thermal resistance always lower than 10%, and the discrepancy in the temperature prediction always falling inside a ±5°C window.
- The validation procedure for the whole system resulted in an average cell temperature discrepancy between experiment and numerical results of 3°C in the 70W heat load case, 2.4°C in the 150W heat load case and around 2°C for the HFCH driving cycle case.
- The proposed TMS respected the requirements at cell level (ΔT over a cell of 0.7°C) and at module level (ΔT between cells of 4.5°C and 1.8 °C).
- The proposed TMS was compared to a standard active liquid cold plate TMS, and resulted being able to reduce the maximum temperature after fast charge (during the HFCH driving cycle) by 3.6°C.
- For the requirements at pack level, the proposed TMS respected the upper safety limit, with maximum temperature of 59°C for cell 1 and just above the acceptable limit for cell 3 with 53.3°C, due to the limit in the available active zone of the evaporator.

Concluding, a novel design for an efficient TMS in EVs is proposed and the competitiveness of this has been successfully verified owing to a LPM validated with in-house experiments. Future developments presented in the next Chapter, will be a series of further analysis targeted to improve application of this technology following the automotive industry requirements.

Chapter 6 - Automotive-Tailored Investigations

6.1. Introduction

The automotive industry is one of the most fast-evolving and demanding industries worldwide. OEMs need to adapt to new technologies coming from other fields as well as regulations set by governments worldwide. Striking example of this is the UK ban on the sale of conventional ICE powered cars and vans that was put forward by 10 years, from 2040 to 2030 [24].

Moreover, many factors need to be considered when putting a vehicle on the market, or even when thinking to adapt a previous line of vehicles, such is the case shifting from ICE powered vehicle to EV. In fact, the whole structure of the car, for how we know it, will have to stay the same, both for easiness of integration and to avoid rethinking factories and production lines. Another important factor is that the car needs to feel the same to the costumer/passenger. Other complications are rising from the increased costs in the EV power unit and energy storage compared to conventional petrol cars, hence automotive manufacturers have to find cost-cutting strategies to compensate this, especially after the global sale slump (17% less vehicle sales worldwide [349]) that affected the automotive world due to the Covid-19 pandemic. Finally, not only newly designed EVs have to fulfil the above-mentioned requirements, and the performance requirement which have been previously introduced in this work (comfortable all-electric range, fast charging times and low cost of ownership), but also they have to respect high safety and environmental standards. For example, following regulation No 517/2014 of the European Parliament in 2014, the use of refrigerants with GWP higher than 150 is forbidden.

This Chapter contains a series of simulation and experimental results aiming to enhance the appeal to automotive industry of the new TMS proposed in this work. Most of these investigations were carried out numerically, showing once again the advantages of having an experimentally validated numerical code.

Firstly, an investigation on the number of LHP evaporators needed to cool down a 12-cell module (this was identified together with the industrial collaborator as the number better representing an actual application) and the effect of using a different geometry than the one used in the experimental demonstrator presented in Chapter 5, was carried out. This was motivated by the need of improve on the mismatch between the module footprint and the active heating zone of the LHP evaporator.

Secondly, the effect of the evaporator thickness was investigated. In fact, in order to accommodate the battery pack above the underbody of the vehicle, its height is of primary importance, to the point that millimetric reductions in height are sought to allow for maximum space in the cabin. Hence, simulations were made to see the minimum thickness of the evaporator that would still perform adequately in terms of cell temperature reduction.

Thirdly, following the automotive interest in lighter components, the effect of having one graphite sheet every two battery cells was evaluated.

Following, a new experimental campaign was carried out, where Novec™ 649, a novel heat transfer fluid from 3M™, was used as working fluid for the LHP. This fluid possesses some outstanding safety and environmental features, which is why it was chosen for experimental investigation. Results will show the comparison between this new fluid and ethanol, being the latter an already well-established working fluid in heat pipes.

Extending the range of comparisons with the proposed LHP based TMS, simulations were run to compare LHP, cold plate and free convection based TMS. The comparison was carried out over several heat generation profiles, including a real journey case study based on the Nissan Leaf.

Concluding, a parametric analysis was performed, whose object was to understand the effect of different LHP manufacturing materials and working fluid on the cells' temperature.

6.2. Number of Evaporators for 12-cell Module

From Chapter 5, it was evident that despite experimental results being satisfactory, the mismatch between the active heating zone of the LHP evaporator and the footprint of the module was detrimental to the thermal performance. This section investigates the effect of reducing that mismatch.

6.2.1. Effect of shape of evaporators

The number of cells in the module was fixed to 12, following specification from the industrial collaborator as this is the most common used module setup for prismatic cells. Secondly, it was

decided to vary the number of flat plate evaporators applied to the module, in order to understand how the coverage of the module footprint affects the maximum temperature reduction. The geometry of the evaporators is the same as the one used in the experimental demonstrator, to have maximum confidence in the simulation results. Each flat plate evaporator is connected to its own LHP, having the same dimension as the one used in the experimental demonstrator in the lab and cooled down in the same way (tube in tube condenser with coolant at 20°C). The tests are considered at an ambient temperature of 20°C.

At this point is worth to remind the reader that the temperature range for optimum performance and operational life is between 25°C and 40°C [7], but a larger interval of 20°C to 50°C is accepted for good performance [8], while a maximum safety limit of 60°C is established under normal operation [9].

In Fig. 86, the four considered cases are presented, where #2,4,6,10 evaporators are considered, respectively. In these representations, the fluidic lines are removed for clarity. Given the reduced length of the evaporator, it was necessary to mirror the number of evaporators on each half of the module footprint.

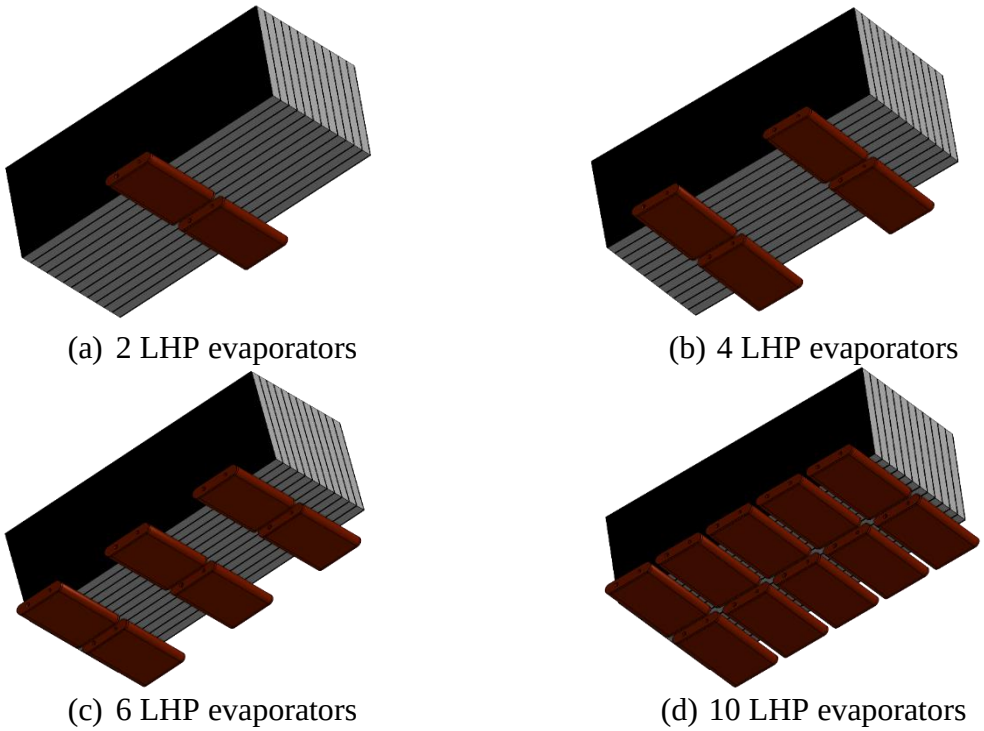

(a) 2 LHP evaporators (b) 4 LHP evaporators

(c) 6 LHP evaporators (d) 10 LHP evaporators

Fig. 86. The four cases considered for the investigation on the number of evaporators: a) 2 LHP evaporators; b) 4 LHP evaporators; c) 6 LHP evaporators and d) 10 LHP evaporators.

Considering that the module footprint surface is 35,896 mm^2 and the LHP active heating zone is 2,240 mm^2, the four cases in Fig. 86 cover respectively the 12% in the 2LHP case, the

25% in the 4LHP case, the 37% in the 6LHP case and 62% in 10 LHP case of the module footprint.

Firstly, the thermal behaviour of these four cases was evaluated over the same HFCH driving bespoke driving cycle, which was utilized in the previous Chapters. Following, to avoid the risk of being biased by using only one heat rate generation profile (the HFCH), new additional situations of fast charge were simulated, with C-rates ranging from 1 to 5, aiming to charge the cells from 20% to 80% SOC. Results are presented in Fig. 87.

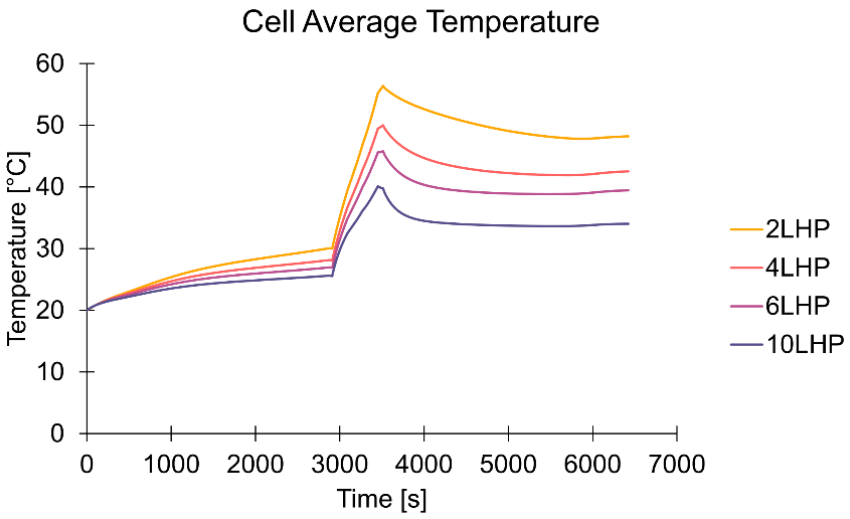

Fig. 87. Average cells temperature evolution during HFCH driving cycle for the different number of evaporators.

From Fig. 87, it is evident how the maximum cells temperature increases with the decrease of the number of evaporators. In fact, maximum temperature was 56.4°C for 2LHP, 50°C for 4LHP, 45.8°C for 6LHP and 40.1°C for 10LHP. Hence, the design using only 2LHP cannot cope with the fast charge section utilized in the HFCH driving cycle, and as such is not able to allow for good or acceptable performance and longevity of the battery pack. Nonetheless, none of the considered cases resulted in temperatures higher than the 60°C safety threshold, despite the extremely challenging charge rate the cells are subjected to. It is worth remembering that, at the moment of writing, the highest C-rate in the market is 3C, that can be accepted only by the Porsche Taycan [292], while the HFCH driving cycle comprehends charge rates up to 4C, in order to stay inside the 10 minutes duration window. So, this solution would still represent, even in the 2LHP case, a potential challenge to the state of the art in TMS.

It is possible to appreciate the reason why the temperatures are increasing with the decrease of the number of the evaporator by looking at Fig. 88. The heat rate absorbed/received by the single LHP goes from a maximum of 80W for the 2LHP case to a minimum of 38W in the

10LHP case. However, this does not mean that the 2LHP case will not be able to dissipate 160W of heat rate, but only that in the 10 minutes of fast charge, it does not reach steady state and that, in comparison with the 10LHP case, its dT/dt is higher, hence the steeper slope of the temperature curve.

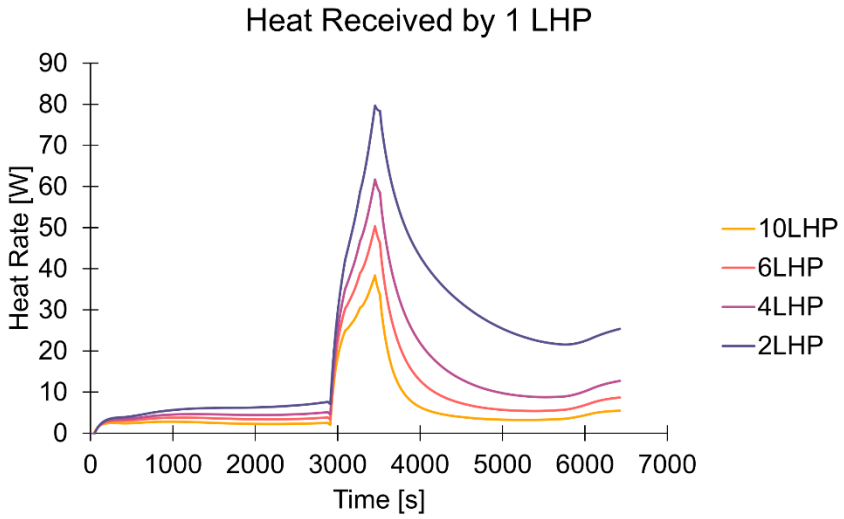

Fig. 88. Heat rate received by a single LHP whilst applied to the 12-cell module, during the HFCH driving cycle simulations.

So far, the only evaporator geometry tested has been the geometry used in the experimental demonstrator. To get a better understanding of the effect of a different geometry, a new evaporator shape was designed, with a wick of the same length of the width of the battery module (Fig. 89). The same proportions between length of the wick and compensation of the Thercon evaporator were maintained. The vapour grooves width was also adapted to avoid having prohibitive load losses (e.g. too thin and long grooves would hinder the fluid motion straight out of the evaporator). The geometrical properties are listed in Table 30.

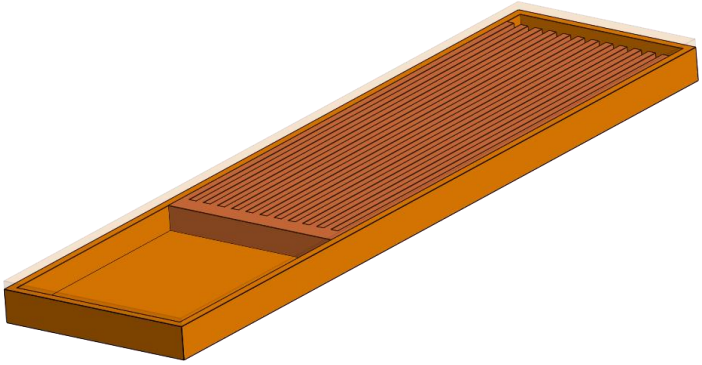

Fig. 89. Alternative wick geometry with longer wick, hence longer active heating zone. The length of the wick matches the width of the 12-c module.

Table 30. Geometry of the alternative longer evaporator.

Part		Value	Units
Wick	Thickness	6	mm
	Width	46	mm
	Length	125	mm
	Porosity	45%	
	Pore Size	7.3	µm
Vapour Grooves	Radius	2	mm
	N	11	-
	Length	120	mm
Evaporator Shell	Thickness	2	mm
	Width	50	mm
	Length	190	mm
Compensation Chamber	Thickness	6	mm
	Width	46	mm
	Length	56	mm

To compare the thermal performance of this alternative evaporator to the one used in the previous investigation, three configurations were considered, with 1, 2 and 3 evaporators respectively, as presented in Fig. 90. With the longer wick, hence with larger active heating zone, these evaporators allow for larger coverage percentages of the module footprint. In fact, this alternative LHP has an active heating zone of 6,250 mm^2, giving a coverage of 17.4% in the Fig. 90a case, 34,8% in the Fig. 90b case and 52,2% in the Fig. 90c case.

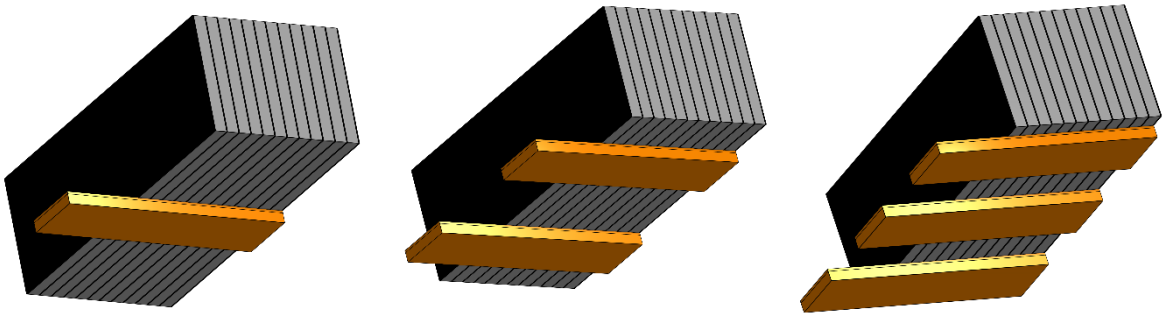

(a) (b) (c)

Fig. 90. Setups used in the investigation on the alternative longer LHP evaporators: a) 1 LHP; b) 2 LHPs and c) 3 LHPs.

Results presented in Fig. 91, showing the average cells temperature, do not present variation in terms of trends. However, there are differences in the maximum temperature in the different cases. In fact, as also shown in the summary Table 31, with the original evaporator geometry the maximum temperatures are clearly lower. Comparing %coverages, the 2evap case with the alternative evaporator is similar to the 6evap with the Thercon evaporator (35%

vs 36%, respectively), however the maximum cells temperature reached with the longer evaporator is 6.2 °C higher.

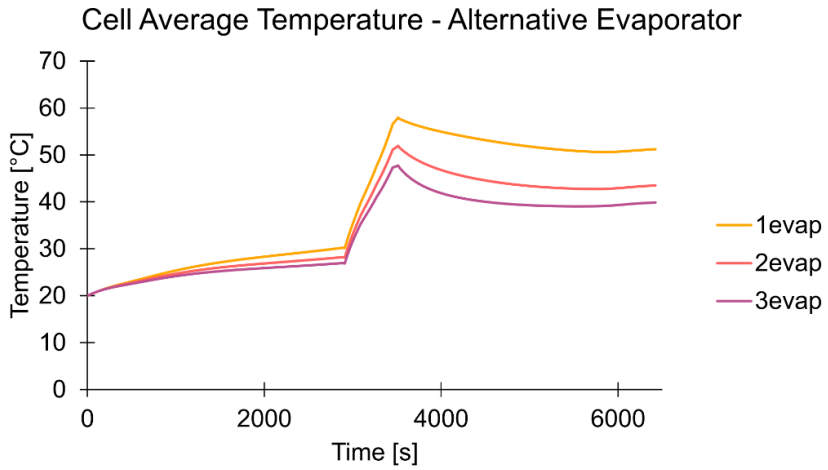

Fig. 91. Average cells temperature trend in the three different cases with the alternative longer evaporators.

Table 31. Summary table showing the comparison between the two considered geometries for the flat evaporator. Maximum temperature results are provided alongside the percentage coverage of the module footprint, to highlight the relationship between thermal performance.

	Alternative Evaporator			Thercon Evaporator			
	1evap	2evap	3evap	2evap	4evap	6evap	10evap
% Footprint Coverage	17.4%	34.8%	52.2%	12.5%	25%	36.4%	62.4%
Max Temperature	57.9 °C	51.9 °C	47.7 °C	56.3 °C	50 °C	45.7 °C	40.1 °C

There are two possible reasons as to why the longer evaporator is outperformed by the one used in the experimental demonstrator. Firstly, looking at the heat rate received by a single LHP depicted in Fig. 92, it is evident (and intuitive) that the heat received by a single LHP in this second case is much higher. A second reason is the actual design of the longer evaporator, that with its longer vapour grooves loses efficiency compared to the smaller Thercon evaporator. It is safe to presume that the larger evaporator would outperform the Thercon evaporator at higher levels of power.

Concluding the analysis on the evaporator shape, a few remarks can be made. It is evident that the size of the evaporator needs to be carefully designed, in order to maximise its efficiency. The longer evaporator, alternative to the one used in the experimental demonstrator, results in a sensible increase in maximum temperature at comparable coverage of the module footprint. This may be attributed to the higher power level seen by a single LHP, as shown in

Fig. 92. On the other hand, a larger evaporator would mean a lower number of LHPs to cover a single module, reducing the amount of piping comprising the whole TMS, which would be a clear benefit especially considering the condenser interface. Further research needs to be done in order to advise on an optimum design for this module geometry.

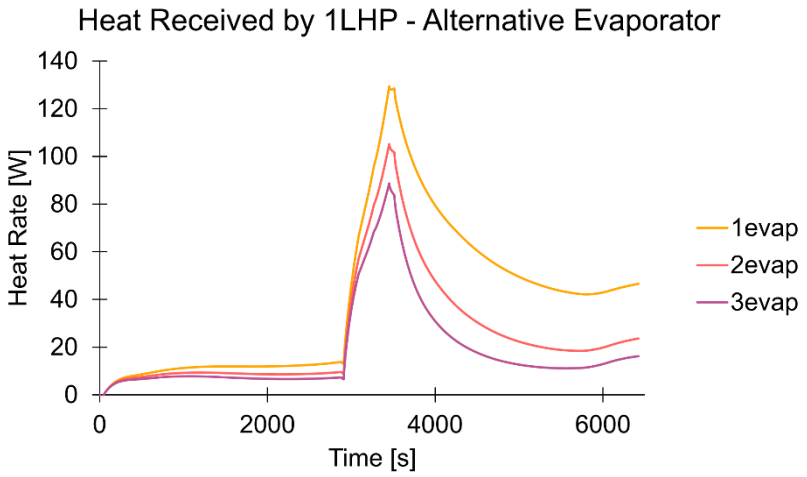

Fig. 92. Heat rate received by a single LHP in the three different cases for the longer evaporator.

6.2.2. Effect of Number of Evaporators

Second part of this investigation aims to further improve the understanding of the effect of the number of evaporators on the maximum cells' temperature. In addition, the bias of evaluating every case so far on the same driving cycle is removed thanks to the investigation of different C-rates, aiming to charge the cells from 20% to 80% SOC. The considered C-rates are from 1 to 5 C-rate, hence going beyond the current state of the art (3C), and their heat rate profiles are presented in Fig. 93. Again, one can notice how the heat rate generation profiles are not constant, justifying again the need of a transient code to simulate these boundary conditions.

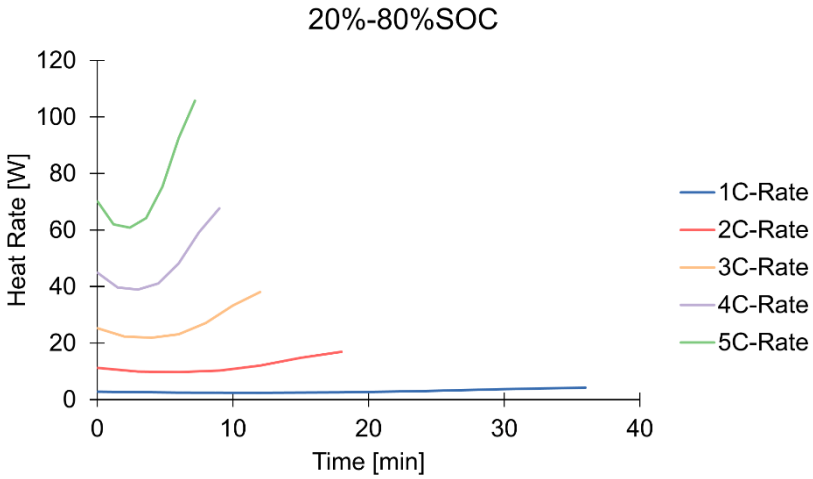

Fig. 93. Heat generation rates during different fast charge cycles.

In addition, the same fast charge boundary conditions were applied to the cold plate code, to have another evaluation of the comparison of the two TMS. It is worth remembering that the cold plate has the same footprint of the module, hence this investigation provides a further indication on how the LHP two-phase technology compares against the standard liquid single phase one. Results are presented in Fig. 94 and Table 32.

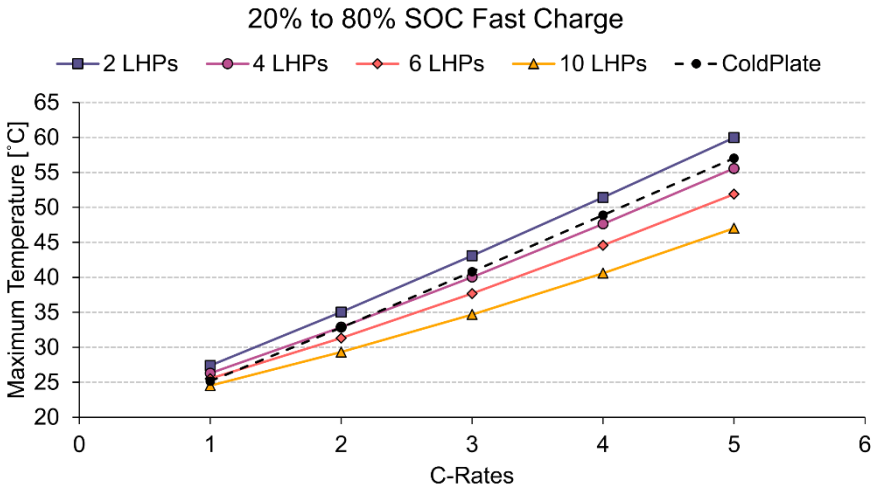

Fig. 94. Maximum cells temperature results when module was cooled down with different number of LHP evaporator and subjected to different fast charge C-rates.

Table 32. Maximum cells temperature results and fast charge times when module was subjected to different fast charge C-rates and different number of applied LHP evaporators.

	Fast Charge	Maximum Temperature [°C]				
	Time [min]	2 LHPs	4 LHPs	6 LHPs	10 LHPs	Cold plate
1C	36	27.4	26.3	25.5	24.5	25.2
2C	18	35.0	32.9	31.3	29.3	32.8
3C	12	43.1	40.0	37.7	34.7	40.8
4C	9	51.4	47.6	44.6	40.6	48.9
5C	7	60.0	55.6	51.9	47.0	57.0

From the results presented in Fig. 94 and Table 32 it is evident that, as expected, the maximum cell temperature increases with the increase of the C-rate. Moreover, the slope of the curve gets steeper with the decrease of the number of evaporators. It is very interesting to note that the 10 LHPs case, although perhaps of difficult implementation, can contain the maximum temperature below the 50°C even at an incredibly demanding condition such as 5C charge rate. Furthermore, at 4C charge rate (hence still charge time in less than 10 minutes), the maximum cell temperature for the 10 LHP case is inside the optimum operative range of 25-40°C, which would provide a massive change to the state of the art. At this C-rate, also the 6LHPs design provides maximum temperature lower than 50°C, which still would allow for good

performance and operational life, as would the 4 LHPs case. Looking at the state of the art at 3C (hence charge time in only 12 minutes) both 4LHP and 6LHP cases provide a maximum temperature inside the optimum range cited above, thus giving a bit of flexibility regarding the design consideration.

The LHP system once again shows clear potential to outperform the standard liquid cold plate technology, since the LHP design gives lower temperatures than the cold plate design from the 4 LHPs case onwards. Only the 2 LHPs case is worst performing, given the very small surface coverage of the battery module.

This investigation has proven the outstanding heat transfer capability of the LHP and graphite TMS concept proposed in this thesis, which could enable a clear-cut improvement in fast charge times for commercial EVs.

6.3. Evaporator Thickness

One of the most complicated challenges offered by the EV revolution is to adapt the vehicle to a new powertrain and energy storage solution without perturbing the experience that passengers are used to, in terms of performance of the car, appearance and comfort. As such, the space inside the cabin should be kept the same as on standard ICE powered vehicles even with the addition of the battery pack above the underbody of the vehicle. Considering that the battery cells themselves cannot be acted on or modified in shape, the remaining auxiliary components/system must be carefully designed in order to minimize their height/thickness. As a result, OEMs are racing to provide solutions able to shave millimetres to the total height of the battery pack system.

With this in mind, a numerical investigation was carried out to find out the minimum thickness of the LHP evaporator that would ensure acceptable thermal performance. It is important to point out that this was purely a thermal and fluid dynamic assessment only, and that structural problems were not considered but they must be going forward, also being mindful of problems arisen in the construction of large dimension vapour chambers [212].

6.3.1. Effect on Pressure Drop

A lower thickness of the evaporator means lower thickness of the porous structure (the wick), which carries along some hydrodynamic implications. In fact, changing the thickness of the wick affects its cross-surface area, hence its related pressure drop. The pressure drop in a porous media is defined by Darcy's Law [350], here expressed as a function of the mass flow rate instead of the fluid average velocity:

$$\Delta P = \frac{\dot{m}\mu}{\rho}\frac{1}{k_w}\frac{L}{A} \tag{80}$$

where ΔP is the pressure drop [Pa] across the wick, $\dot{m}$ is the mass flow rate [kg/s], μ is the dynamic viscosity [Pa·s], ρ is the mass density [kg/s], L is the length of the wick travelled across by the fluid, A is the cross-surface of the wick and k_w is the permeability coefficient [m^2]. The permeability coefficient was estimated via the Carman-Kozeny relationship for sintered structures [351]:

$$k_w = \frac{\bar{r}^2\varepsilon^2}{37{,}5(1-\varepsilon)^2} \tag{81}$$

where $\bar{r}$ is the medium pore size radius [m] and ε is the porosity of the wick.

The relationships in (80) and (81) were implemented in the numerical code in the pressure balance equation, in order to check that the pressure provided by capillarity (Laplace-Young Equation) would always be greater or equal than the sum of the load losses:

$$\Delta P = \frac{\dot{m}\mu}{\rho}\frac{1}{k_w}\frac{L}{A} + \Delta P_{loop} < \Delta P_{cap} = \frac{2\sigma cos\theta}{\bar{r}} \tag{82}$$

where ΔP_{loop} are the distributed and concentrated load losses given by the passage of a fluid flow in a pipe and ΔP_{cap} is the pressure gradient imparted by the capillarity following the Laplace-Young equation.

6.3.2. Effect on Dry-out

However, pressure drop is not the only way that the wick thickness affects the thermo-fluidic behaviour of the LHP, in fact a smaller wick means less amount of fluid inside the wick and the compensation chamber. Nonetheless, the heat applied to the evaporator is the same so the mass flow rate exiting the evaporator is the same, since it depends on the heat level and latent heat of vaporisation of the working fluid. Does this increase the chances of dry-out? To reply to this question, a different approach on the fluid velocity was implemented in the model which is following detailed, starting from the graphical schematic of Fig. 95.

Considering that the LHP is a closed system, hence there is no addition or subtraction of mass flow rate, once the mass flow rate exiting the evaporator is calculated, the velocity of the vapour in the vapour line is calculated. Since the model calculates the fluid properties in every node of the system, the mass density is always known, hence the fluid velocity is always known ($\dot{m} = \rho v A$). Knowing the geometry of the system, the time that the fluid takes to travel through the vapour is calculated. A similar consideration can be done for the condenser (and the liquid line), as the vapour quality is calculated in every node of the condenser, hence the two-phase

density is estimated. This allows to calculate the total time needed for the fluid to perform one full loop of the LHP Δt_{fluid}. In order not to have dry-out, the total mass of fluid entrapped in the evaporator needs to be greater than the mass of fluid leaving the evaporator in the time interval Δt_{fluid}. Wick thickness is involved in the fluid mass calculation in the evaporator. This procedure is graphically displayed in Fig. 95.

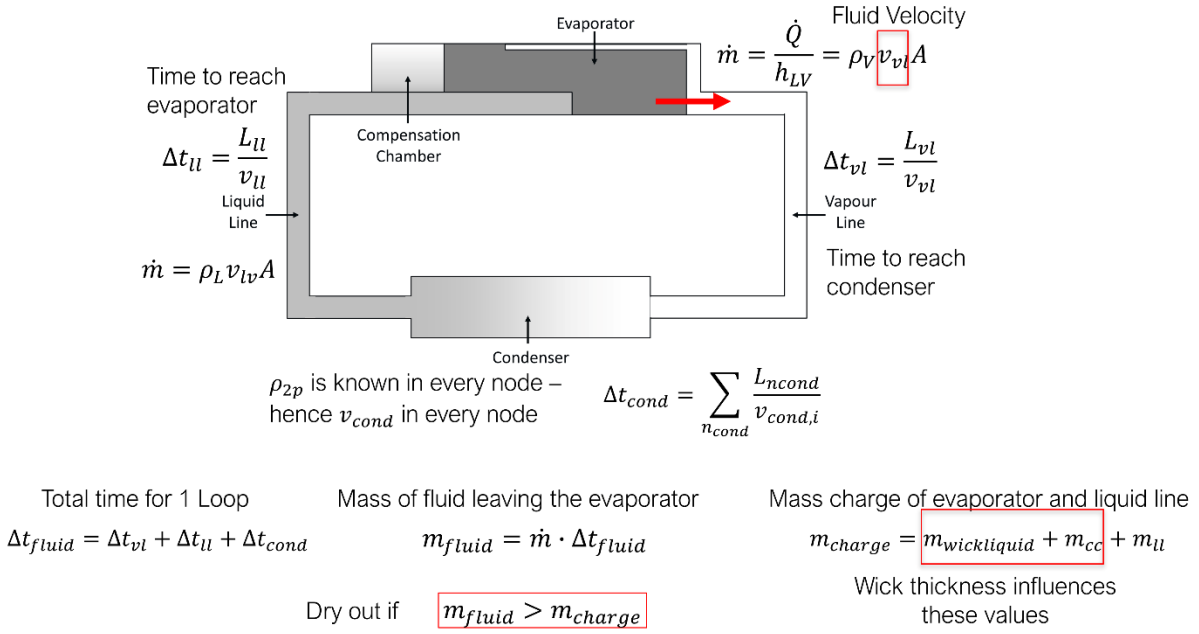

Fig. 95. Schematic of the code modifications to include the evaluation of possible dry-out scenarios induced by low thickness evaporators. The velocity is calculated in every node, so together with the geometry one can obtain the time it takes for the fluid to complete the loop. If this is greater than the time it takes to evaporate the fluid charge in the evaporator, then dry-out occurs.

6.3.3. Results

Simulations were carried out to appreciate the effect of the reduced thickness of the evaporator. It was chosen to perform them on the configuration with 10 LHPs evaporator applied to the 12-cell module subjected to the bespoke HFCH driving cycle already used in this work.

The results presented in Fig. 96 show the average cell temperature in three different cases: with a wick thickness of 8 mm (starting geometry); wick thickness 2mm and then 1mm. In the case of 1mm thick wick, the vapour grooves (originally with square section with side of 1.5mm) had to be obviously modified to 0.5mm, and this would affect adversely the pressure drops inside the grooves and the thermal performance, as there is less vapour removal capability hence less heat removal capability.

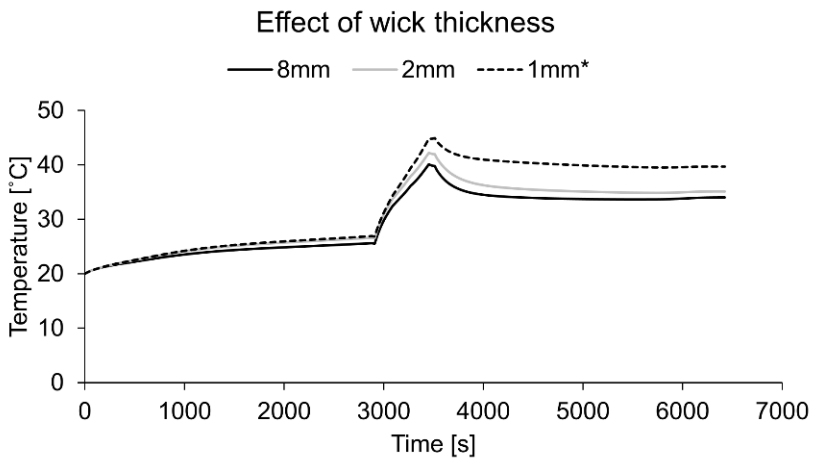

Fig. 96. Cell average temperature when module is cooled down with LHPs with different wick thickness: 8mm, 2mm and 1mm. The asterisk on the 1mm case stands as a reminder that the vapour grooves are smaller than in the other two cases.

Fig. 96 shows that there is perhaps less difference than expected when it comes to maximum temperature difference between the cases, with the 2mm case providing an increase of 2.1°C, which is still sizeable but worth considering in a cost-benefit trade-off. The 1mm case instead, shows a maximum temperature of 44.9°C, which is 4.8°C higher than the original 8mm case. This is probably due to the smaller vapour grooves surface.

More simulations were carried out to evaluate the likelihood of a dry-out event, when reducing the thickness of the wick. Two cases where considered, with liquid line full of liquid or with only vapour, hence changing the m_{charge} value shown in Fig. 95. During the experimental campaign it was noticed that the thermal history of the device (hence the liquid vapour distribution) influences the start-up behaviour, as also described in Chapter 3. Table 33 presents the results on this investigation, showing that a full liquid line would guarantee correct functioning (during the HFCH driving cycle) down to 4 mm thick wick, whereas considering only the fluid charge in the evaporator only, only the 8mm case would work, with dry-out arising from 7mm downwards.

Table 33. Simulated Dry-out behaviour depending on the starting filling condition of the liquid line

Thickness [mm]	Liquid Line Full	Liquid Line Empty
8	No dry out	No dry out
7	No dry out	Dry Out Risk
6	No dry out	Dry Out Risk
5	No dry out	Dry Out Risk
4	No dry out	Dry Out Risk
3	Dry Out Risk	Dry Out Risk
2	Dry Out Risk	Dry Out Risk

Nevertheless, to estimate such behaviour with a LPM can only provide indications, but not certainties because liquid is not only in the compensation chamber and the wick, but also scattered along the rest of the loop - a routine to consider the condensation after shut-down, to understand where it takes place, would be beneficial in this case. Moreover, it is really complicated with a LPM to analyse the inside of the evaporator, specifically the interface between compensation chamber and wick, in order to calculate the amount of fluid exchanged between the two nodes. This should be better modelled with advanced CFD technique such as a conjugate heat transfer model [352], as it is a better suited technique for small scale phenomena and will give a clearer indication on the possibility of dry-out.

6.4. Mass Savings by Reducing Number of Graphite Sheets

Weight is a crucial parameter in many engineering applications, and it is no different in the automotive sector. Moving from ICEs powered vehicles to EVs results in a sensible weight increase due to the increase in weight of the energy storage unit (fuel tank vs battery pack). The battery cells have small room to work on in terms of weight, as the energy density is more important in that case. In fact, the energy density (amount of energy stored in a given space per unit volume) is an even more important concept than weight when it comes to battery packs. Therefore, this section investigates one of the strategies sought in this work to increase the energy density of the battery pack, that is to explore the effect of using a graphite sheet every two cells, not for each cell as it is in the original design studied in the previous Chapters.

To consider the increased thermal stress on the graphite sheet, a modification to the thermal network was made, as shown in Fig. 97, which reflected in a change to the system of ODEs solving the problem in the numerical code, presented below.

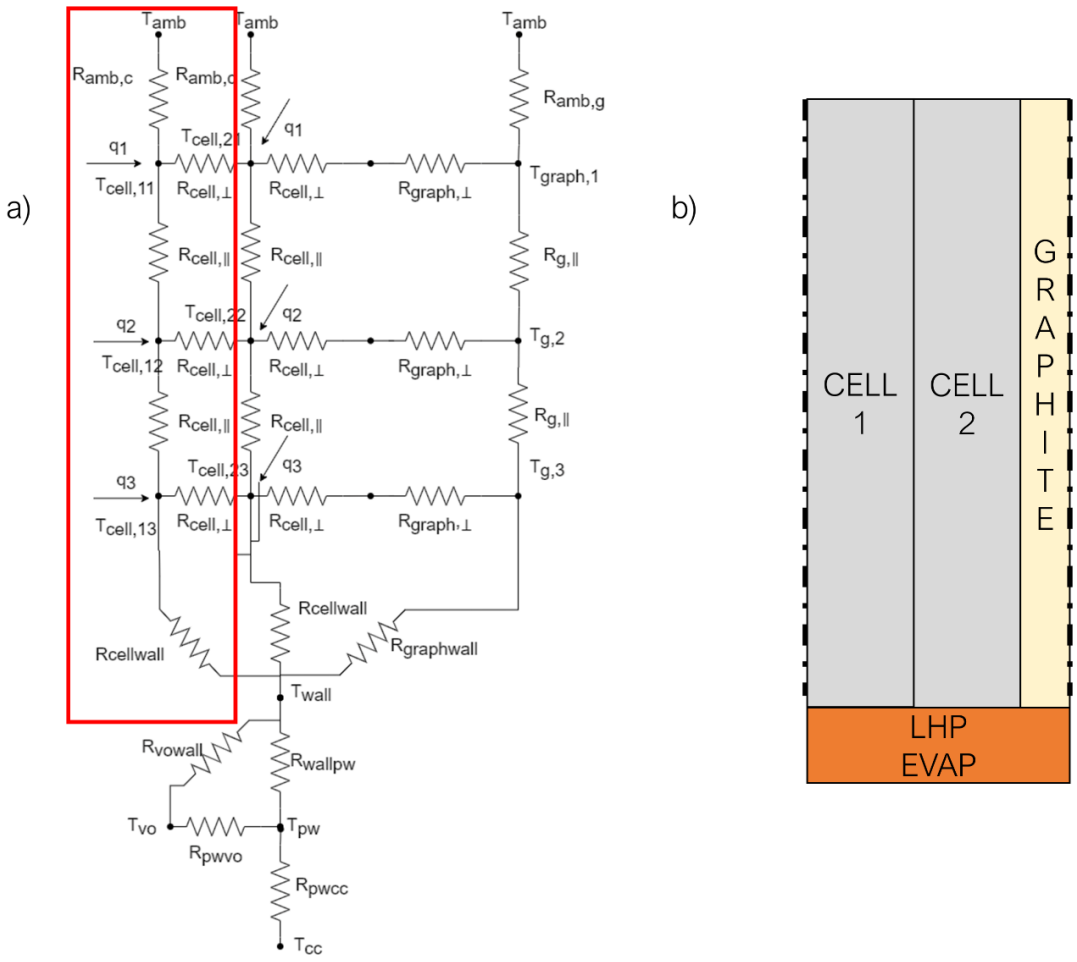

Fig. 97. a) Modified thermal network to account for the extra cell in the configuration with reduced number of graphite sheets (addition highlighted in red) and b) schematic for displaying purposes. Please note that dimensions and proportions are not to scale and not representative of the actual experiment.

Cell 1

$$m_c c_{p,c} \frac{dT_{c11}}{dt} = q + \frac{T_{amb} - T_{c1}}{R_{amb,c}} + \frac{T_{c21} - T_{c11}}{R_{c,\perp}} + \frac{T_{c12} - T_{c11}}{R_{c,\parallel}} \quad (83)$$

$$m_c c_{p,c} \frac{dT_{c12}}{dt} = q + \frac{T_{c11} - T_{c12}}{R_{c,\parallel}} + \frac{T_{c13} - T_{c12}}{R_{c,\parallel}} + \frac{T_{c22} - T_{c12}}{R_{c,\perp}} \quad (84)$$

$$m_c c_{p,c} \frac{dT_{c13}}{dt} = q + \frac{T_{12} - T_{13}}{R_{c,\parallel}} + \frac{T_{c23} - T_{c13}}{R_{c,\perp}} + \frac{T_{wall} - T_{c11}}{R_{eLHP} + R_{c,wall} + R_{c,\parallel}} \quad (85)$$

Cell 2

$$m_c c_{p,c} \frac{dT_{c21}}{dt} = q + \frac{T_{c11} - T_{c21}}{R_{c,\perp}} + \frac{T_{g1} - T_{c21}}{R_{g,\perp} + R_{c,\perp}} + \frac{T_{amb} - T_{c21}}{R_{amb,c}} + \frac{T_{c22} - T_{c21}}{R_{c,\parallel}} \quad (86)$$

$$m_c c_{p,c} \frac{dT_{c22}}{dt} = q + \frac{T_{c12} - T_{c22}}{R_{c,\perp}} + \frac{T_{g2} - T_{c22}}{R_{g,\perp} + R_{c,\perp}} + \frac{T_{c23} - T_{c22}}{R_{c,\parallel}} + \frac{T_{c21} - T_{c22}}{R_{c,\parallel}} \quad (87)$$

$$m_c c_{p,c} \frac{dT_{c23}}{dt} = q + \frac{T_{c13} - T_{c23}}{R_{c,\perp}} + \frac{T_{g3} - T_{c22}}{R_{g,\perp} + R_{c,\perp}} + \frac{T_{c22} - T_{c22}}{R_{c,\parallel}} + \frac{T_{wall} - T_{c23}}{R_{eLHP} + R_{c,wall} + R_{c,\parallel}} \quad (88)$$

Graphite

$$m_g c_{p,g} \frac{dT_{g,1}}{dt} = \frac{T_{amb} - T_{g,1}}{R_{amb,g} + R_{g,\parallel}} + \frac{T_{c,21} - T_{g,1}}{R_{g,\perp} + R_{c,\perp}} + \frac{T_{g,2} - T_{g,1}}{R_{g,\parallel}} \quad (89)$$

$$m_g c_{p,g} \frac{dT_{g,2}}{dt} = \frac{T_{g,1} - T_{g,2}}{R_{g,\parallel}} + \frac{T_{c,22} - T_{g,2}}{R_{g,\perp} + R_{c,\perp}} + \frac{T_{g,3} - T_{g,2}}{R_{g,\parallel}} \quad (90)$$

$$m_g c_{p,g} \frac{dT_{g,3}}{dt} = \frac{T_{g,2} - T_{g,3}}{R_{g,\parallel}} + \frac{T_{c,32} - T_{g,3}}{R_{g,\perp} + R_{c,\perp}} + \frac{T_{wall} - T_{g,3}}{R_{eLHP} + R_{g,wall} + R_{g,\parallel}} + \frac{T_{amb} - T_{g,3}}{R_{g,\parallel} + R_{amb,g3}} \quad (91)$$

LHP Evaporator

$$m_{vo} c_{p,v} \frac{dT_{vo}}{dt} = \frac{T_{pw} - T_{vo}}{R_{pwvo}} + \frac{T_{wall} - T_{vo}}{R_{vowall}} + \dot{m} c_{p,v} (T_{sat} - T_{vo}) \quad (92)$$

$$m_{pw} c_{pw} \frac{dT_{pw}}{dt} = \frac{T_{vo} - T_{pw}}{R_{pwvo}} + \frac{T_{wall} - T_{pw}}{R_{wallpw}} + \frac{T_{cc} - T_{\mathrm{pw}}}{R_{pw2}} - \dot{Q}_{leak} \quad (93)$$

$$m_{wall} c_{pwall} \frac{dT_{wall}}{dt} = \frac{T_{vo} - T_{wall}}{R_{vowall}} + \frac{T_{pw} - T_{wall}}{R_{wallpw}} + \dot{Q}_{ext} \quad (94)$$

$$m_{cc} c_{p,cc} \frac{dT_{cc}}{dt} = \dot{m} c_p (T_{\mathrm{cc}} - T_1) + \dot{Q}_{leak} + \frac{T_{amb} - T_{cc}}{R_{amb,cc}} + \frac{T_{pw} - T_{cc}}{R_{pwcc}} \quad (95)$$

$$\dot{Q}_{ext} = \frac{T_{graph,3} - T_{wall}}{R_{eLHP} + R_{g,wall} + R_{g,\parallel}} + \frac{T_{c,23} - T_{wall}}{R_{eLHP} + R_{c,wall} + R_{c,\parallel}} + \frac{T_{c,13} - T_{wall}}{R_{eLHP} + R_{c,wall} + R_{c,\parallel}} \quad (96)$$

The effect of the removal of one graphite sheet every two cells was evaluated with simulations on two configurations, namely the ones with 2 and 10 LHP evaporators applied to the module. To enhance consistency with previous work, it was chosen to keep the same boundary conditions of the investigation detailed in Section 2.2, hence the considered thermal stresses were the ones of fast charge, from 20% to 80% SOC, with different charge currents, from 1C to 5C. Following the results are presented in Fig. 98, Fig. 99 and Table 34 in terms of maximum average cell temperature for each C-rates.

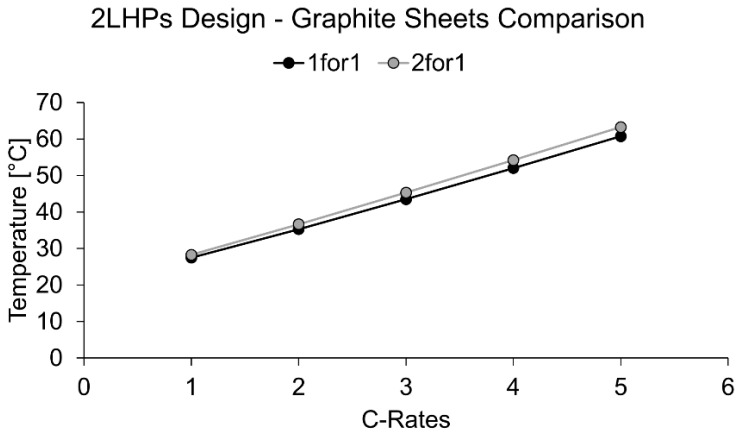

Fig. 98. Cell average temperature at varying C-rate when module is cooled by a 2LHP system – comparison of using one graphite sheet for every cell or every two cells.

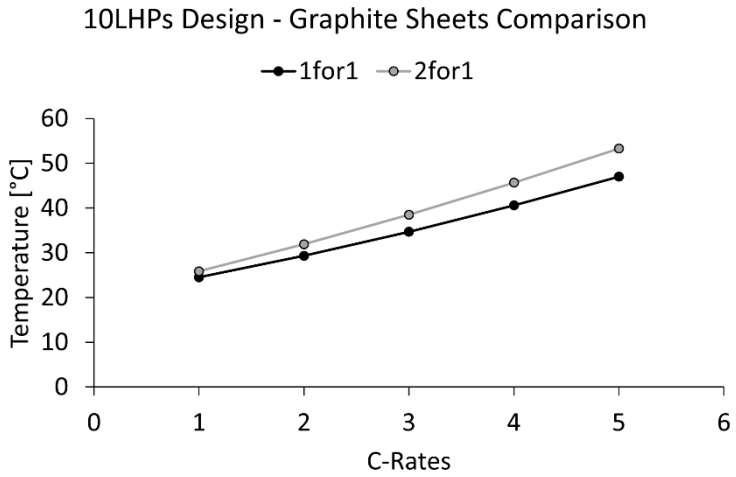

Fig. 99. Cell average temperature at varying C-rate when module is cooled by a 10LHP system – comparison of using one graphite sheet for every cell or every two cells.

Table 34. Cell maximum temperature variation imparted by the 2for1 graphite scenario, after fast charge for the 2 and 10 LHP cases. All temperatures are expressed in °C. 1for1 refers to the original design presented in the rest of the document and 2for1 for the alternative design with fewer graphite sheets.

C-rates	2LHP			10LHP		
	1for1	2for1	Δ	1for1	2for1	Δ
1C	27.5	28.3	-0.8	24.5	25.9	-1.3
2C	35.3	36.7	-1.4	29.3	31.9	-2.6
3C	43.5	45.3	-1.8	34.7	38.5	-3.8
4C	52.0	54.2	-2.2	40.6	45.7	-5.1
5C	60.7	63.3	-2.5	47.0	53.3	-6.3

From the results in Table 34 and the graphs of Fig. 98 and Fig. 99, it is evident that removing a graphite sheet has an incremental effect on the maximum cell temperature. However, this effect is more prominent in the 10LHP case, with maximum ΔT of 6.3°C with respect of the maximum ΔT of 2.5°C of the 2LHP case. On the other hand, it was already shown how the 10LHP case is able to contain the maximum temperature in a much more efficient way than the others, hence a detriment in its performance will result in a larger effect on the temperatures than in the 2LHP case, where the performance is not as good in the first place. Nevertheless, in the 10LHP case, even in the 2for1 graphite case, the maximum temperature with 3C fast charge (state of the art) stays lower than the 40°C optimum threshold.

From the mass savings point of view, a single graphite sheets weights 0.046 kg, hence the mass savings in using the 2for1 strategy on a 12-cell module are $0.046 \cdot 6 = 0.28$ kg. Considering for example a battery pack with 420 cells, it gives a mass saving of 9.66 kg, which is significant.

6.5. System Level Parametric Analysis on Working Fluids and Material

Exploring the avenues to improve the applicability and appeal of the proposed TMS design to the automotive industry, a parametric analysis was carried out, having as factors the working fluids and the manufacturing materials for the LHP applied to the 12-cell module.

These manufacturing materials were copper, aluminium, stainless steel and nickel (the last one for the wick only). The rationale behind the choice for these materials is that they are widely used as LHP manufacturing materials. While copper gives the best thermal performance, the other materials can each bring their own improvements: stainless steel gives a slightly lower weight and considerably more mechanical strength (7x) at the price of a much lower thermal conductivity; aluminium is three times lighter and cheaper than copper [353] and still provides good mechanical and thermal properties. Nickel was selected as typical material by choice for the wick, as it allows to reduce the heat leakage. Table 35 shows the physical properties of the chosen materials. The combinations were six, considering LHP entirely made (evaporator case, wick and piping) by the three main materials (copper, aluminium and stainless steel), each compared to their alternative where the wick was made in nickel.

Table 35. Physical properties of the chosen manufacturing materials for the parametric analysis.

Material	Density [kg/m]	Thermal Conductivity [W/m K]	Specific Heat [J/kg K]
SS	7800	14	502
Aluminium	2700	205	900
Nickel	8908	88	400
Copper	8960	385	390

The working fluids were chosen looking at two families. One family is the one of the standard working fluids used in two-phase applications such as LHPs and the other is a group of heat transfer fluids selected because they possess one of more of these qualities: freezing point below 0°C and favourable environmental properties such as low ODP and GWP < 150 (as the regulation No 517/2014 of the European Parliament in 2014 forbids the use of refrigerants with GWP higher than 150). They will be referred as low-GWP working fluids herein. The full list along with their properties is reported in Table 36.

The parametric analysis was carried out on the whole system (cell+LHP) cycling all the working fluids for all the materials combinations, for a total of 54 simulation cases. Each case was studied when the cells were subjected to a cycle of 3C fast charge, followed by 30 min of

discharging at 1C (Fig. 100). Since it represents a good balanced solution between performance and applicability, the 6LHPs design was selected as baseline.

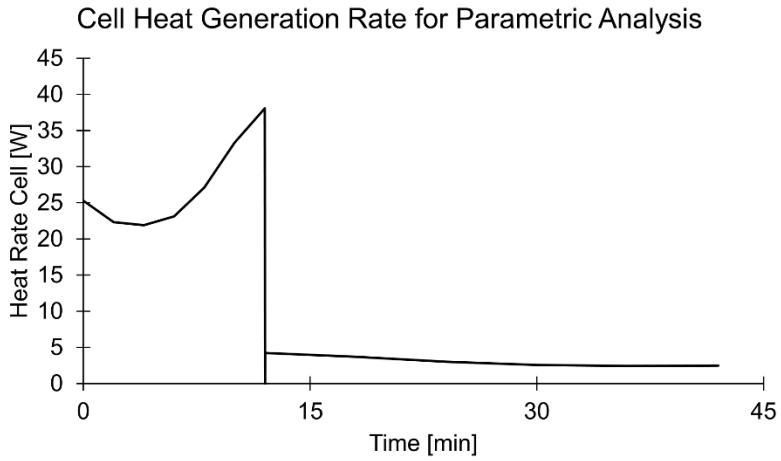

Fig. 100. Cell heat rate generation profile during a 3C fast charge cycle followed by 30 min of driving at 1C.

Given the heat rate profile, the parameters of interest of the parametric analysis are the maximum temperature, at the end of the fast charge section, and the final temperature, in order to better capture the contribution of the different working fluid or material. Results are presented in Table 37 and Table 38. The last row and column of the two tables are showing the effect of the fluid and material, respectively, by showing their average effect on the temperature.

It is important to point out that Aluminum evacuated two-phase heat exchangers are not compatible with water, due to a chemical reaction that breaks the hydroxide O-H bond and releases hydrogen as non-condensable gas. This then interferes with the vapour phase, preventing long term operation [354].

Results show that the minimum temperature is obtained in the water Cu/Cu case, as expected since it is the most common fluid/material combination in the heat pipe world.

Table 36. Physical properties of the working fluids selected for the Parametric Analysis. All values are estimated at 20°C.

Fluid	CAS Number	Density [kg/m]	Viscosity [mPa·s]	Thermal Conductivity [W/m K]	Latent Heat [J/kg]	Specific Heat [J/kg K]	Surface Tension [N/m]	Saturation Pressure [bar]	Freezing Point [°C]	Boiling Point [°C]	ODP	GWP
Water	7732-18-5	998	1.00	0.598	2453080	4184	0.073	0.024	4	100		
Methanol	67-56-1	794	0.57	0.201	1268980	3471	0.023	0.123	-98	65		
Ethanol	64-17-5	790	1.18	0.169	944826	3023	0.022	0.063	-114	78		
Acetone	67-64-1	792	0.32	0.163	550478	2050	0.024	0.238	-95	56		
R1233zd(e)	102687-65-0	1274	0.50	0.076	194338	1235	0.014	1.088	-107	18	0	1
Novec649	756-13-8	1600	0.64	0.06	96157	1103	0.011	0.400	-108	49	0	1
FlutecPP2	355-02-2	1799	1.94	0.070	100796	945	0.015	0.107	-37	76	0	100
Freon225	422-56-0	1561	0.61	0.064	161029	1026	0.016	0.296	-96	52	0	127
R1234ze	29118-24-9	1179	0.21	0.076	170479	1370	0.009	4.301	-156	-19	0	7

Table 37. Parametric Analysis results: maximum temperature at the end of fast charging. All temperatures are shown in [°C]. The colour scale helped identifying the highest temperature, indicated with reddish colour shades. The last column and row correspond to the average temperatures calculated on the same fluid and material, respectively.

Maximum Temperature	Al/Al	Al/Ni	Cu/Cu	Cu/Ni	SS/Ni	SS/SS	**Fluid Average**
Acetone	39.6	39.6	37.1	38.9	39.5	43.4	39.7
Ethanol	40.6	40.1	37.7	39.2	39.9	43.4	40.2
FlutecPP2	42.1	42.0	40.1	41.4	41.9	44.5	42.0
Freon225	42.7	42.2	40.4	41.5	42.0	44.5	42.2
Methanol	39.8	39.5	36.9	38.7	39.3	43.2	39.6
Novec649	42.9	42.5	40.6	41.7	42.3	44.6	42.4
R1233zd(e)	43.5	42.8	41.0	41.9	42.4	44.6	42.7
R1234ze	42.5	42.0	40.1	41.2	41.7	44.3	42.0
Water			33.8	36.9	37.2	42.3	37.6
Material Average	41.7	41.3	38.6	40.2	40.7	43.9	

Table 38. Parametric Analysis results: temperature at the end of the 30 min driving section. All temperatures are shown in [°C]. The colour scale helped identifying the highest temperature, indicated with reddish colour shades. The last column and row correspond to the average temperatures calculated on the same fluid and material, respectively.

Final Temperature	Al/Al	Al/Ni	Cu/Cu	Cu/Ni	SS/Ni	SS/SS	**Fluid Average**
Acetone	32.7	32.2	31.0	31.3	31.7	37.0	32.6
Ethanol	35.2	34.4	33.0	33.4	33.8	38.3	34.7
FlutecPP2	31.9	33.0	32.2	33.1	33.5	39.4	33.9
Freon225	33.7	34.7	33.8	34.7	35.0	40.3	35.4
Methanol	34.5	33.2	31.7	32.1	32.5	37.4	33.6
Novec649	33.5	34.5	33.5	34.5	34.9	40.2	35.2
R1233zd(e)	36.4	37.0	36.1	36.8	37.2	41.7	37.5
R1234ze	34.0	34.9	34.0	34.8	35.2	40.3	35.5
Water			26.3	26.8	27.0	33.0	28.3
Material Average	34.0	34.2	32.4	33.0	33.4	38.6	

However, water high freezing temperature is impractical for automotive application, as it would force to keep some sort of heating element on to prevent freezing in cold environments. In fact, given the peculiar tendency of water of expanding during solidification, it may damage the wick structure and therefore making the LHP inoperative.

The low-GWP working fluids are giving higher temperature than the standard working fluids for two-phase applications, also to no surprise. Amongst them, R1233zd(e) is the less effective one to contain the temperature increase. Whereas amongst the classic working fluids, methanol and acetone provide the best performances.

Looking at the influence of the wick material on the temperatures, from Table 38 is evident that it does not provide much difference at the final temperature. It does instead on the maximum temperature as shown in Table 37, specifically it seems to influence the most when there is a greater gradient between the thermal conductivities of the materials. For example, in the aluminium case, the temperature difference is negligible (-0.2°C), while in the copper and stainless-steel case there is a temperature increase in the first case (+1.5°C) and decrease in the second (-3.2°C). Nickel has medium thermal conductivity between aluminium and stainless steel, and as such it provides a good trade-off between promoting boiling and limiting heat leakage inside the evaporator.

Looking at the manufacturing material case, the stainless steel is the worst performing, but it allows for higher internal vapour pressure due to its higher tensile strength. Interestingly, the swapping a SS wick for a Nickel one improves greatly the thermal performance and makes it comparable with the Aluminum case.

In order to provide a visual representation of how the choice of the working fluid could affect the trends, Fig. 101 presents the cell average temperatures resulted from the parametric analysis on the working fluid in the Al/Al case. During the 1C driving phase, the cells cooled with the low-GWP working fluids seems to present a faster tendency to decrease in temperature than if cooled with the other fluids. In fact, looking at the graph in Fig. 101 in conjunction with Table 37 and Table 38, and disregarding water results (since they represent so clearly the best performance), the best three fluids in terms of maximum temperature are acetone (39.6°C), methanol (39.8°C) and ethanol (40.6°C). On the other hand, the best three fluids in terms of final temperature are FlutecPP2 (31.9°C), acetone (32.7°C) and Novec649 (33.7°C). In average, the low-GWP working fluids present a ΔT reduction between maximum and final temperatures of 8.8°C while the standard fluids have a ΔT reduction of 5.9°C. Probably this is attributed to the lower values of specific heat and latent heat (Table 36) of the low-GWP heat transfer fluids, which allow for a faster reaction to the lower heat input coming from the cells to the LHP during the 1C phase.

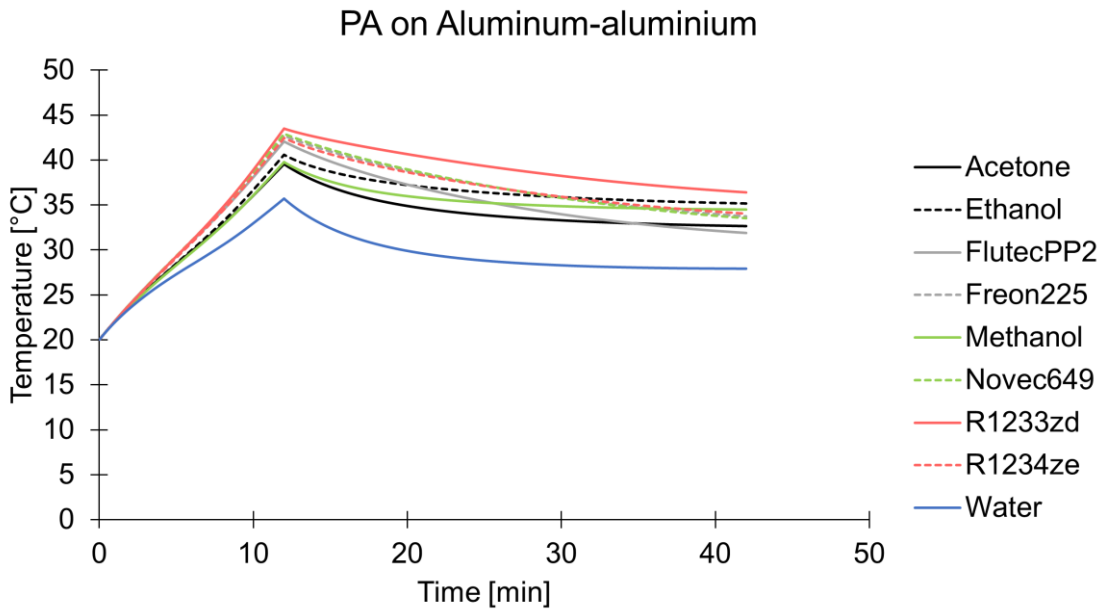

Fig. 101. Average cell temperature trends when cooled down by an Al/Al LHP running with different working fluids.

Looking at the rest of the fluid properties (Table 36), a few remarks can be made:

- The combination of having lower boiling point, latent heat of vaporisation and specific heat perhaps should onset a faster start-up with the low-GWP working fluids, as it will take less power to reach boiling conditions.
- Water has a considerably greater value of latent heat, specific heat and thermal conductivity than the other working fluids, hence it leads to much lower temperatures. However, it also means that start-up will onset at higher levels of applied power, limiting its flexibility.
- The low-GWP working fluids have higher saturation pressures, imposing some restraints to the design as particular care should be taken to the thickness of the evaporator shell or its material selection.
- Best working fluids in terms of boiling point are Novec649 (49°C), Freon225 (52°C) and acetone (56°C), as it would allow to keep the cell temperature in the intended temperature range, following the pack requirement.

The take home message of this parametric analysis is that even if the working fluid selection influences the operation of the LHP, this will affect also the cell temperature, with temperature variations between 2°C and 4°C (up to 8°C for water). The working fluid selection will be a trade-off between many factors, from safety and environmental (toxicity, flammability, GWP and OPD values), to freezing point (water) and thermal performance. Regarding the materials,

Table 37 shows that not using copper increases the maximum temperature by ~2°C, which perhaps is a good investment to save a third of the mass (in case of the aluminium LHP) or to gain 7 times more mechanical strength (yield stress for copper is 70 MPa while for Stainless Steel 302 is 502 MPa).

Ultimately, the numerical model proposed in this work has shown to provide useful insight on effect of materials and working fluids, which makes it an effective design tool for automotive applications.

6.6. Comparison with Free Convection

This section deals with comparing the performance of the LHP-based TMS design introduced in this thesis with the performance of a free convection TMS, one of the most common TMS design for EV. Free (or natural) convection happens when there is no forced velocity of the fluid, but when a body force acts on a fluid subjected to density gradients. The density gradient is due to a temperature gradient and the body force is due to the gravitational field [296].

Free convection is the TMS of choice for the Nissan Leaf, for many years the most sold EV worldwide. For most non-demanding application, free convection works fine, however it is the interest of this study to verify what happens at high level of fast charging and, most importantly, during the immediately following driving period.

6.6.1. Modifications to the LPM

Simply, a free convection TMS is when the module is enclosed in a volume, with a fixed air gap between it and the volume walls. The module structure of 12 prismatic cell was maintained, and the cells are of the same geometry adopted so far. To model this new TMS, modifications were applied to the LPM utilized. Particularly, in order to reproduce the transient situation and the “long”-term effect (reproducing a several minutes long event), the increase in temperature of the air entrapped inside the battery module was also considered. Fig. 102 displays the schematic of the control volume considered around the 12-cell module. As first conservative approximation, a 5 cm uniform gap was considered between the cells and the envelope of the module, which was assumed to be at a fixed temperature of 20°C throughout.

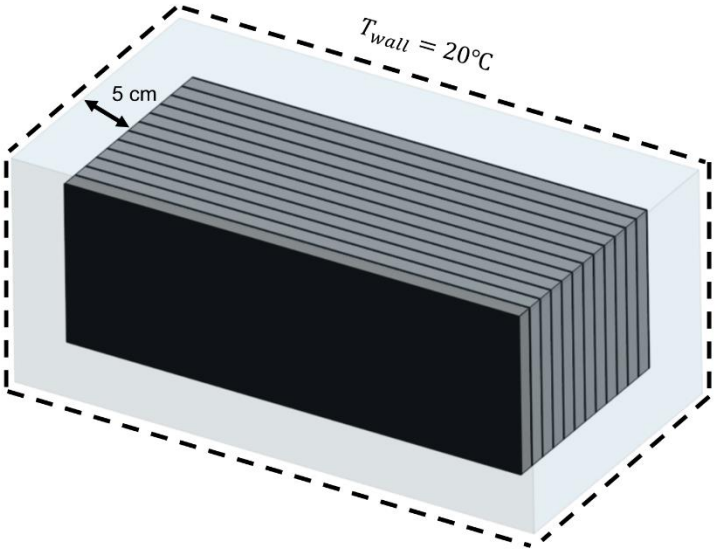

Fig. 102. Schematic of control volume used in the free convection numerical simulations.

From the numerical point of view, the same strategy of considering a single middle cell was maintained, exchanging heat to the adjacent graphite sheets from the side and with the air from front, top and bottom sides. Hence, a new equation was added to the solving ODE system:

$$m_{air}c_{p,air}\frac{dT_{air}}{dt} = \frac{T_{c,1} - T_{air}}{R_{amb,top,c}} + \frac{T_{g,1} - T_{air}}{R_{amb,top,g}} + \frac{T_{c,2} - T_{air}}{R_{amb,side,c}} + \frac{T_{g,2} - T_{air}}{R_{amb,side,g}} + \frac{T_{cw} - T_{air}}{R_{aircw}} \quad (97)$$

where m_{air} is the mass of the entrapped air, where the volume is considered (and hence the gap between module and containment wall), the suffixes c and g indicate the cell and graphite, respectively, while the suffixes *1* and *2* indicate the top and middle node, which are used for the top and side convection, respectively; T_{air} is the air temperature; $R_{amb,top,i}$ and $R_{amb,side,i}$ are the thermal resistances associated to the top and side free convection. Finally, T_{cw} is the temperature of the containment wall of the module, which is kept fixed at 20°C, and air exchanges heat with it through the thermal resistance R_{aircw}. Each one of the right-hand terms of equations (97) was added to the ODE solving the corresponding node.

Many thermal resistances are needed because three different empirical correlations were used for the Nusselt number to better describe the problem, presented in Table 39. In fact, for a vertical plate heated relative to an ambient fluid (equation (98)), since the plate is aligned with the gravitational vector, the buoyancy force acts exclusively to induce fluid motion in the upward direction. However, if the plate is not aligned with gravity, the buoyancy force has a normal component, as well as parallel, to the plate surface. If the plate is horizontal, the buoyancy force is exclusively normal to the surface (equation (99)), typically meaning that there will be a reduction in free convection heat transfer. Equation (100) consists in the

empirical correlation to describe free convection of a vertical cavity, to represent the heat transfer from the containment wall to the cells.

Table 39. Empirical correlations used for describe the free convection around the 12cell module [355].

Side of the cell – Vertical plate	$Nu_{side} = 0.68 + \frac{0.67Ra^{1/4}}{\left[1 + \left(\frac{0.492}{Pr}\right)^{\frac{9}{16}}\right]^{4/9}}$	(98)
Top of the cell – Horizontal Plate	$Nu_{top} = \begin{cases} 0.54Ra^{1/4} \text{ for } 10^3 < Ra < 10^7 \\ 0.15Ra^{1/3} \text{ for } 10^7 < Ra < 10^{11} \\ 1 \quad for \quad Ra < 10^3 \end{cases}$	(99)
For the containment wall – vertical cavity	$Nu_{cw} = 0.22\left(\frac{Pr}{0.2 + Pr}Ra\right)^{0.28}\left(\frac{H}{L}\right)^{-1/4}$	(100)

In Table 39, $Ra = \frac{g\beta(T_{cw} - T_{air})l^3}{\nu\alpha}$ is the Rayleigh number, where g is gravity, β is the expansion coefficient, l is the characteristic length, which it the length subjected to gravity, ν is the kinematic viscosity and α is the thermal diffusivity. The Prandtl number has already been defined in this document (Chapter 4, section 4.3). For equation (100), L is the thickness of the air volume, or the distance between the two plates at different temperature, thus the cells and the confinement wall, and H is the height. The Nusselt numbers in Table 39 are used to calculate the free convection heat transfer coefficient featured in the relative thermal resistances.

6.6.2. Free Convection Numerical Results

As mentioned above, particular interest of this study is to see how a free convection TMS copes with high fast charge C-rates and with the following driving scenario, i.e., is it able to return the temperature to optimum values after fast charge? To answer this question, the heat generation rate profiles applied to the cells comprise of a fast charge section (with C-rates from 1C to 5C), followed by 30 minutes of driving (discharging) at 1C. It is worth pointing out that for this reason the driving cycles will last 30 minutes longer than the durations listed in Table 32 and shown in Fig. 93, and their trends will look like the one presented in Fig. 100. For clarity, the legend adopted on the figures of this section distinguishes the different curves only by the fast charge section of the driving cycle.

The results showed in Fig. 103 confirm the expectations about the potentiality of free convection, that is whilst continuous operation is maintained, this TMS will not bring about a

decrease in temperature, only a contained increase at low demanding conditions. However, it is worth pointing out that discharge at 1C is still a quite demanding condition.

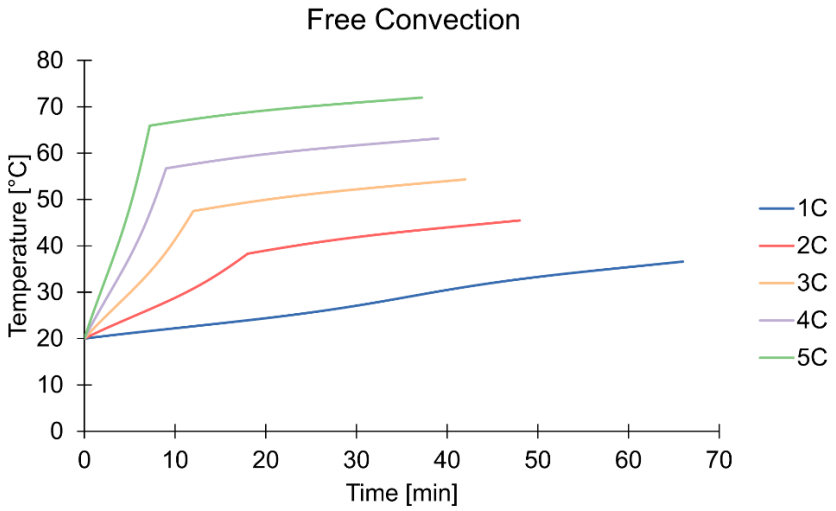

(a)

	T_{FC} [°C]	T_{max} [°C]
1C	29.1	36.6
2C	38.3	45.5
3C	47.5	54.3
4C	56.7	63.2
5C	64.1	72.0

(b)

Fig. 103. Cell average temperature trends (a) and final temperature values (b) subjected to fast charge at different C-rates and discharge at 1C when cooled with free convection. The timings shown on the x-axis are obtained by adding the duration of the related fast charge cycle plus the 30 minutes of 1C discharge.

From Fig. 103a, it is evident how the temperature is ever-increasing on each case studied, with only the slope changing, following the heat generation rate magnitude. In the table in Fig. 103b, the temperatures at the end of the fast charging section as well as the final temperature are presented. Interestingly, the temperature after the 2C fast charge, that would still reduce the charge time under 20 minutes, is below the optimum threshold of 40°C. However, it then keeps on increasing for the following half an hour up to 45.5°C. Similar behaviour is found in the other C-rate cases.

6.6.3. Comparison with other TMS

The other TMS considered herein are the liquid cold plate already introduced in Chapter 4, which numerical code was provided by the industrial collaborator Ricardo plc, and the novel LHP-based design featured in this work. For the comparison to have sense, the same C-rates were applied to the module cells.

Results for the liquid cold plate TMS are presented in Fig. 104, in which is evident how, with respect to the free convection case, not only the maximum temperature at the end of fast charging is contained, but also the temperature consistently decreases in the 1C discharge section. It is worth reminding the reader that ethylene glycol runs in the liquid cold plate at

20°C from the HVAC system of the vehicle. Fig. 104 shows the temperatures keep on decreasing asymptotically towards that threshold.

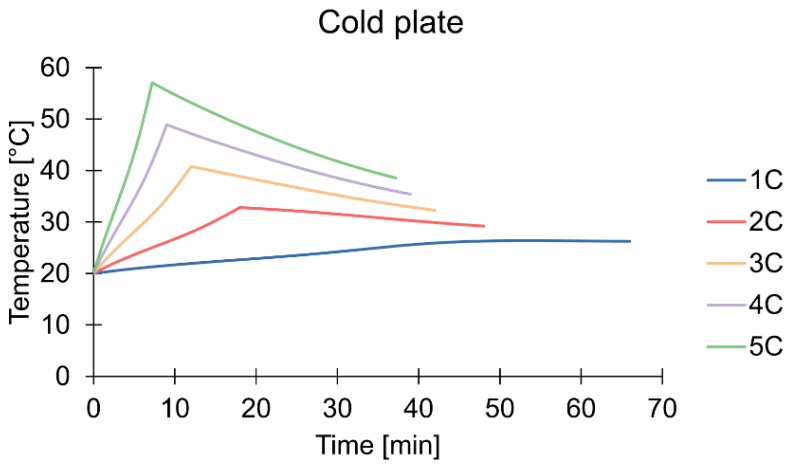

Fig. 104. Average cell temperature when subjected to different fast charge C-rates and cooled by the liquid cold plate TMS.

In Fig. 105 instead, the results of the temperature trends for the average cell temperature under different C-rates cooled by LHPs are presented. To confirm with the previous parametric analysis, the 6 LHP evaporators configuration was selected. Fig. 105 shows that the design allows for an excellent containment of the maximum temperature during fast charge and for a subsequent temperature reduction in the 1C driving phase. In more detail, a sharp decrease can be seen right after the end of the fast charging section (identifiable by the different peaks on the temperature trends), followed by a flattening of the trends towards a quasi-steady state condition.

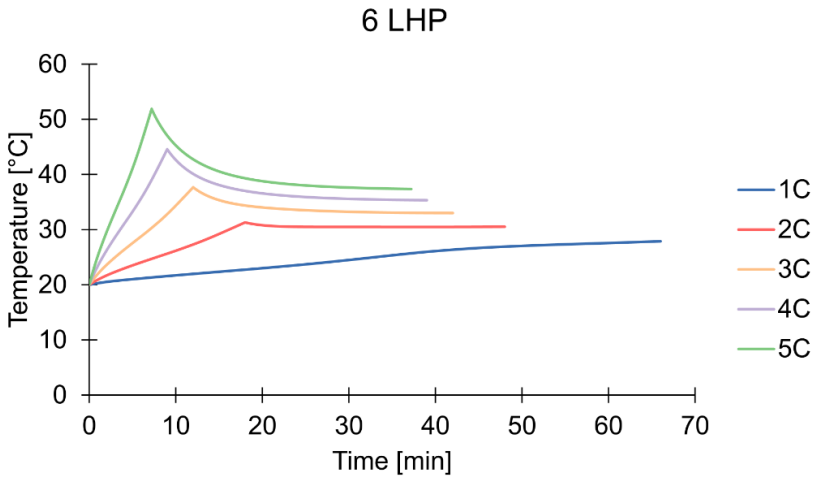

Fig. 105. Average cell temperature when subjected to different fast charge C-rates and cooled by 6 LHP evaporators.

Comparing the three TMS, Fig. 103a, Fig. 104 and Fig. 105 show the trends differences between free convection, liquid cold plate and LHP respectively, which have been already discussed. Looking at the numerical values, Fig. 106 and Fig. 107 provide a graphical representation of the comparison between the different TMS in terms of maximum temperature after fast charge and after driving for 30 min at 1C, respectively. Firstly, the difference between free convection and the other TMS becomes evident from 2C and up, while at 1C free convection performs in line with the other options, even outperforming the 2LHP scenario by 2.5°C. This is mostly due to the LHPs not experiencing start-up at low powers. While free convection and liquid cold plate present a relatively uniform straight-line trend, the LHP TMS shows a slope change between 1C and 2C, identifying that the boiling process has taken place. However, the average difference between free convection and the LHP, as provided in Table 40, is always quite significative.

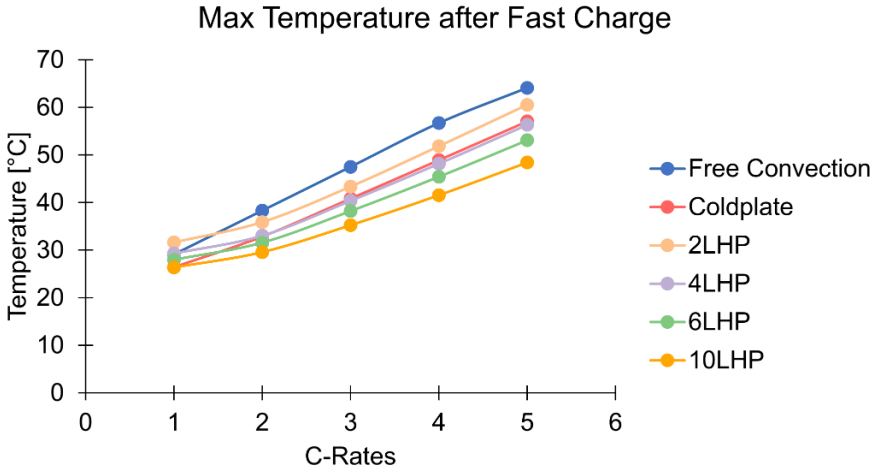

Fig. 106. Comparison between maximum cell average temperatures at the end of fast charging with different C-rates, with the application of different TMS.

The differences between the systems become even more evident when comparing the final temperatures (Fig. 107), where there is an ever-widening gap between the free convection trend and the ones of the other TMS, identifying thus the biggest distinction between the TMS operations.

Comparing instead the cold plate versus the LHP designs, both graphs show that from C-rates from 2C to 5C, the 4LHP, 6LHP and 10LHP designs perform better in terms of maximum temperature during fast charge, while at 1C the cold plate is better performing, for the reasons above mentioned. Whereas, looking at the final temperatures, the comparison is a bit closer, with the cold plate giving the same temperature than the 6LHPs design at 4C, and giving lower

temperatures at lower C-rates. The complete numerical results of the investigation are presented in Table 40.

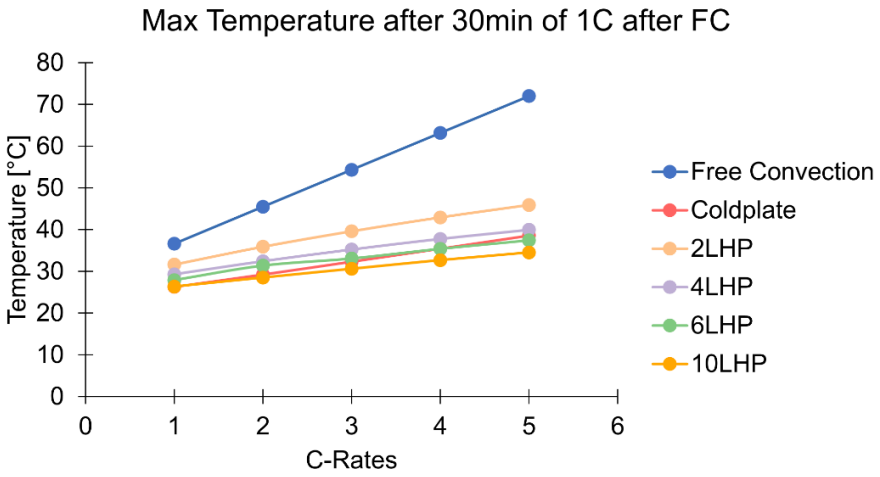

Fig. 107. Comparison between final cell average temperatures at the end of the different tests, after the 30 minutes of 1C discharge, with the application of different TMS.

Table 40. Temperature results of the comparison between different TMS when applied to a battery module subjected to the different fast charge scenarios, followed by 30 mins of 1C discharge. All temperatures are measured in [°C]. T_{max} is the temperature at the end of the fast charge section and T_{final} is the temperature at the end of the cycle.

		1C	2C	3C	4C	5C	Average
Free Convection	T_{max}	29.1	38.3	47.5	56.7	64.1	
	T_{final}	36.6	45.5	54.3	63.2	72.0	
Coldplate	T_{max}	26.4	32.8	40.8	48.9	57.1	
	T_{final}	26.3	29.2	32.3	35.4	38.6	
	Δmax	2.7	5.5	6.7	7.8	7.0	5.9
	$\Delta final$	10.3	16.3	22.0	27.8	33.4	22.0
2LHP	T_{max}	31.6	35.9	43.3	51.8	60.5	
	T_{final}	31.6	35.9	39.6	42.9	45.9	
	Δmax	-2.5	2.4	4.2	4.9	3.6	2.5
	$\Delta final$	5.0	9.6	14.8	20.3	26.1	15.1
4LHP	T_{max}	29.3	33.0	40.4	48.2	56.3	
	T_{final}	29.3	32.4	35.2	37.8	40.0	
	Δmax	-0.2	5.3	7.1	8.5	7.8	5.7
	$\Delta final$	7.3	13.1	19.1	25.4	32.0	19.4
6LHP	T_{max}	27.9	31.6	38.2	45.4	53.1	
	T_{final}	27.9	31.4	33.1	35.4	37.4	
	Δmax	1.2	6.7	9.3	11.3	11.0	7.9
	$\Delta final$	8.7	14.1	21.3	27.8	34.6	21.3
10LHP	T_{max}	26.4	29.6	35.2	41.5	48.4	
	T_{final}	26.4	28.5	30.6	32.7	34.5	
	Δmax	2.7	8.7	12.3	15.2	15.7	10.9
	$\Delta final$	10.2	17.0	23.7	30.5	37.5	23.8

From Table 40, the gain of the LHP-based TMS and the cold plate TMS on the free convection TMS is clear in terms of both maximum and final temperature, with average ΔT as high as 10.9°C and 23.8°C for maximum and final temperature, respectively.

6.6.4. Example on London – Liverpool Journey

As a final investigation to compare the potentialities of the TMS so far introduced, the Author devised a hypothetical journey from London to Liverpool, to be performed with a BEV, comprising a single stop to charge the batteries. The aim is to compare the performance of TMS on a real case scenario and how the TMS can affect the actual journey.

The vehicle selected was the Nissan Leaf 2021 standard version, as it has a free convection TMS. This vehicle has a 40kWh battery pack, and assuming an average speed of 55 mph (88.5 km/h) and ambient temperature of 20°C, it will have an all-electric range of 140 miles (225 km) [356]. As depicted in Fig. 108, the drive is 224 miles long, so a stop to charge the batteries is needed. Three stints are foreseen: the first one S1, using 80% of the range and bringing the battery SOC from 100% to 20%, travelling for 112 miles (80% of 140 miles). Following, a stop to charge the battery is performed (S2), to bring the SOC back up to 80%. For the standard Nissan Leaf that takes around 40 minutes [357]. Finally, for the last stint S3, the remaining 112 miles are travelled, and the battery charge will be depleted fully. The total journey time (assuming no breaks) is 4 hours and 40 minutes.

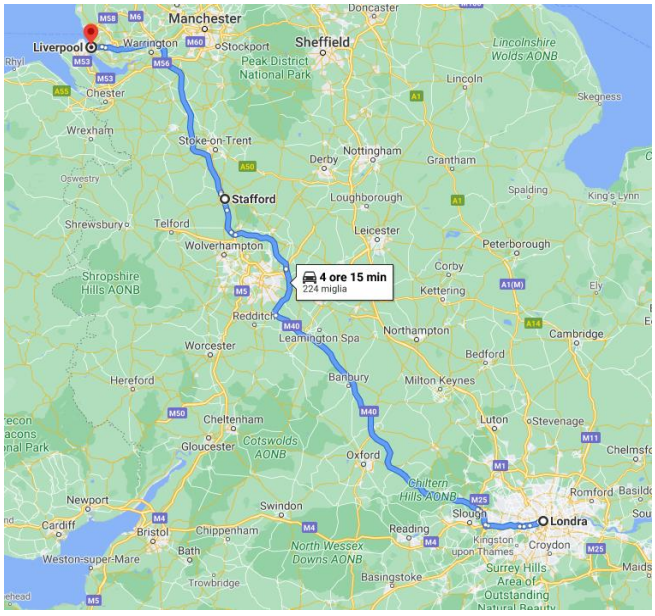

Fig. 108. London-Liverpool itinerary (source: Google Maps©).

Table 41 gives the breakdown of the C-rates of each stint. The C-rates were calculated considered the inverse of the full time to fully deplete of the charge. The resulting cell heat

generation rates associated to the driving cycle just described is presented in Fig. 109. It is evident that this is a less demanding scenario that the ones considered so far in this work.

Table 41. C-rates breakdown of the London-Liverpool drive cycle.

Stint	Time [h]	C-rate
S1	2.55	0.39
S2 - FC	1.1	0.91
S3	2.55	0.39

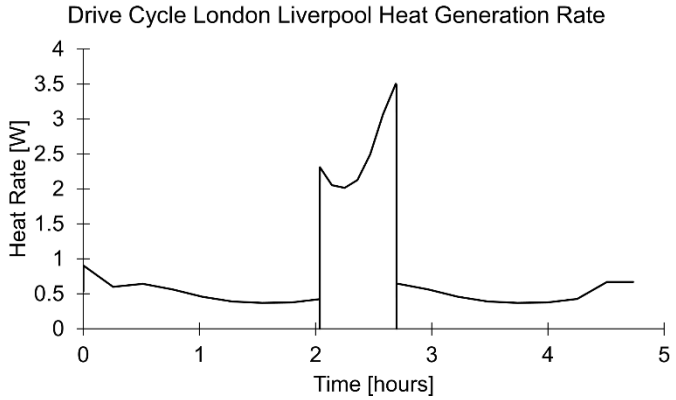

Fig. 109. Cell heat generation rate associated to the London-Liverpool driving cycle.

The results in terms of cell average temperature, when different TMS are applied to the 12cell module, are presented in Fig. 110. Free convection TMS temperature never actually surpasses the optimum threshold of 40°C, yet temperature keeps on increasing considerably after the charge. Due to the low power involved (Fig. 109), the LHPs do not start up properly, hence why the LHP TMS has been outperformed by the liquid cold plate, which in this case results the best solution. However, with the exception of free convection, the remaining 5 technical solutions are able to maintain the temperature below 30°C throughout the whole event.

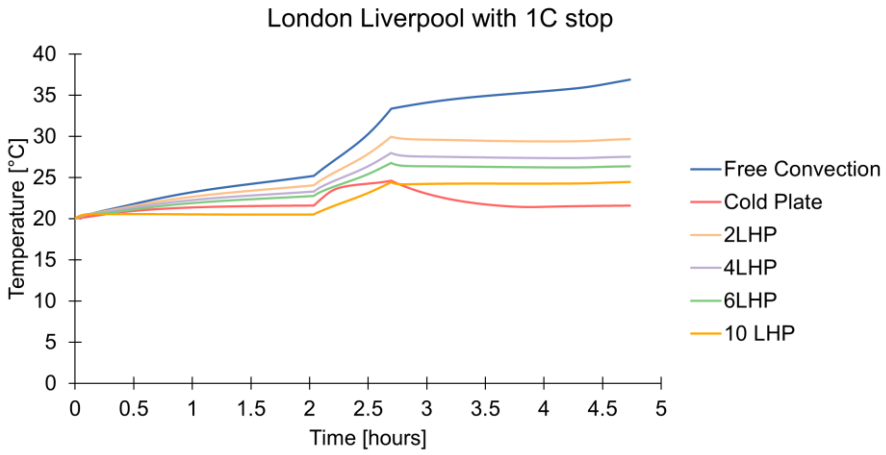

Fig. 110. Cell average temperature during the London Liverpool journey when the different TMS are applied to the module.

Second part of London-Liverpool study foresees speeding up the charge to a 3C fast charge, able then to charge the battery from 20% to 80% in 12 minutes. The profile of the heat rate released by a single cell changed to the one presented in Fig. 111, where the increase compared to the previous 1C fast charge case is evident (i.e., a 10 times higher peak than in the previous case).

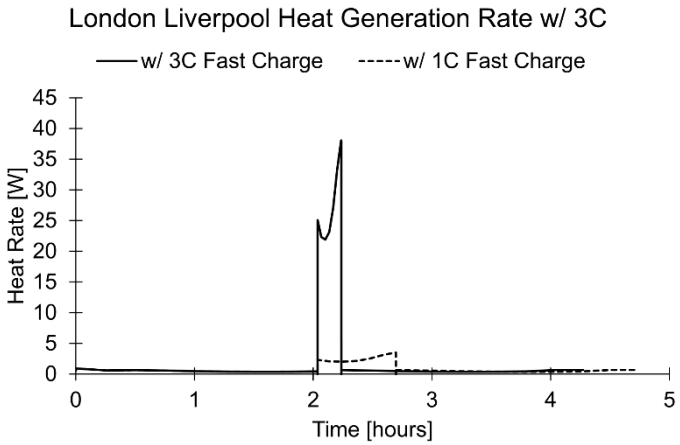

Fig. 111. Cell heat generation rate associated to the London-Liverpool driving cycle with 3C fast charge. In dashed line the heat generation rate of the previous test with 1C fast charge is compared.

The increased heat release associated to a fast charge rate is reflected in the much higher cell average temperatures displayed in Fig. 112. However, the increase is more contained in the LHPs and cold plate cases, whereas cells temperature when cooled via free convection raise above the acceptable threshold of 50°C, but more importantly it does not decrease during the second stint, making this technology unsuitable to guarantee good performance and operational life of the battery cells for 3C levels of fast charge.

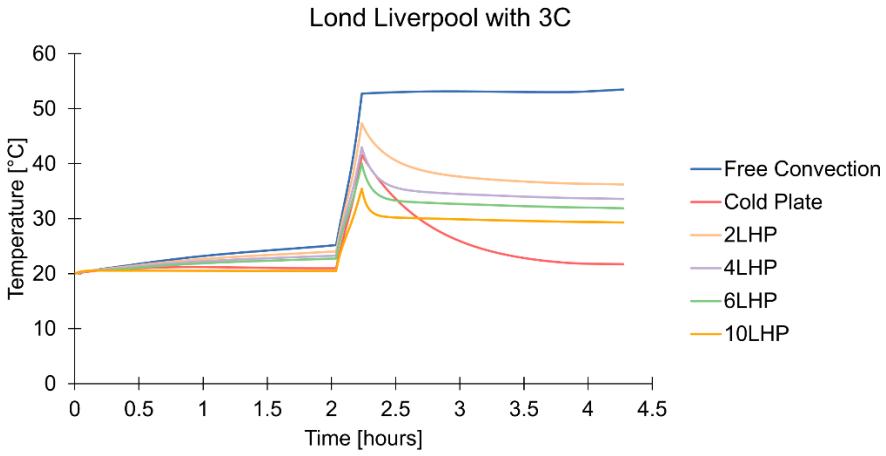

Fig. 112. Cell average temperature during the London-Liverpool journey when the different TMS are applied to the module (3C Fast charge case).

On the other hand, LHPs and cold plate TMS are able to contain the temperature overshoot during fast charge and reduce the temperature during the second stint. As shown in Table 42, 6LHPs and 10 LHP are performing better than the cold plate in terms of maximum temperature, with the 4LHP and 2LHP giving a maximum temperature higher than the optimum threshold of 40°C but still below the acceptable one of 50°C. Moreover, the cold plate provides a final cell temperature outside the optimum temperature range of 25°C-40°C.

Table 42. Maximum and final cell average temperature during the London-Liverpool journey with 3C fast charge, depending on the different TMS applied to the module.

	T_{max}[°C]	T_{final}[°C]
Cold Plate	41.6	21.7
Free Convection	53.5	53.5
2LHP	47.3	36.2
4LHP	43.0	33.6
6LHP	40.0	31.9
10 LHP	35.5	29.3

Concluding, swapping the free convection TMS with the 6 or 10 LHP design would allow to save 28 minutes on the journey (~10% of the time), whilst maintaining the cell temperature inside the optimum range for performance and operative range.

6.7. Experimental Analysis on Alternative Fluid: Novec™ 649

The temperature requirements at the pack, module and cell levels are not the only requirements for the TMS. Safety, environmental impact and temperature range are three crucial aspects OEMs are pressured to consider when selecting the working fluid for a battery TMS. With this in mind, the last part of this work involves the use of the heat transfer fluid Novec™ 649, developed by 3M™, in the LHP-based TMS herein proposed. The aim of this investigation was to experimentally compare the performance of this novel fluid against the performance of an already well-established working fluid in the sector of passive two-phase devices such as ethanol. Finally, the performances of the proposed TMS with Novec™ 649 are evaluated over a series of fast charge cycles.

6.7.1. Novec™ 649 Selection Rationale

The working fluid selection is of paramount important not only for the performance of the TMS, but also to ensure safety of the system and passengers, as well as not to present a threat

to the environment. As such, Novec™ 649 was chosen as working fluid because of the following characteristic:

- It is non-toxic, so it will not harm passengers in case of leakages and presents advantages for production as not requiring precautions for handling.
- It is non-flammable, as the TMS should not add any risk of incrementing a failure, not only in cases of leaks, but also in disruptive cases (such as accidents, crashes).
- It is inert and dielectric, so in case of leakage and contact with the battery cells, the working fluid will not cause short-circuit.
- It has a GWP value of 1 and ODP of 0, which are unparalleled values compared to other refrigerants and heat transfer fluids used in the automotive sector. Moreover, regulation No 517/2014 of the European Parliament prevents the use of refrigerants with GWP higher than 150.
- It has a low freezing point at -108°C, allowing it to be used in cold climates without damage risk to the LHP.
- Its boiling point at 49°C is lower than other standards working fluid used in two-phase passive devices, which is makes it more suitable to keep the cell temperature in the desired range.

Table 43 compares standard working fluids used in LHPs and EV thermal management systems, highlighting the reason why the Author believe that Novec™ 649 is an excellent candidate for the application.

Table 43. How Novec™ 649 compares against other standard LHP and automotive working fluids.

Fluid	Boiling Point [°C]	Freezing Point [°C]	Application	Cons compared to Novec™ 649
Novec™ 649	49	-108	This work	
Water	100	0	EV [195,358]; LHP [321]	Freezing at 0°C with expansion that can break wick and piping of LHP; electrical conductor
Ethanol	78	-114	LHP [359]	Toxic and flammable
Ammonia	-33	-77	LHP [360]	High Vapour Pressure (10 bar@25°C); toxic and flammable
Acetone	56	-95	LHP [361]	Toxic and flammable
R134a	-26	-103	EV [362]	High GWP of 1430; low boiling point (<20°C)
Novec™ 7000	34	-123	EV [15,196]	High GWP of 420
Ethylene Glycol	197	-13	EV [127,129]	Toxic and flammable
R1234yf	-30	-150	EV [363]	Mildly flammable per ASTM E-681-04;

	boiling point too low (<20°C)

As mentioned in the Introduction, this work carries out a comparison between the results obtained using ethanol and Novec™ 649, together with an assessment of the performance of the proposed TMS design running Novec™ 649 over different C-rates. Finally, to the Authors' best knowledge, this is the first case in which Novec™ 649 is used as working fluid for a LHP.

6.7.2. Experimental Comparison between Novec™ 649 and Ethanol

Ethanol was chosen as benchmark fluid since it already proved to be a well-performing working fluid both in LHP standalone applications as well as LHP applied to EV. The comparison was carried out over the bespoke HFCH driving cycle, already introduced in this work. The experimental apparatus is the same one described in Chapter 5, and to remind the reader of the thermocouple positions, the general schematic is given again in Fig. 113.

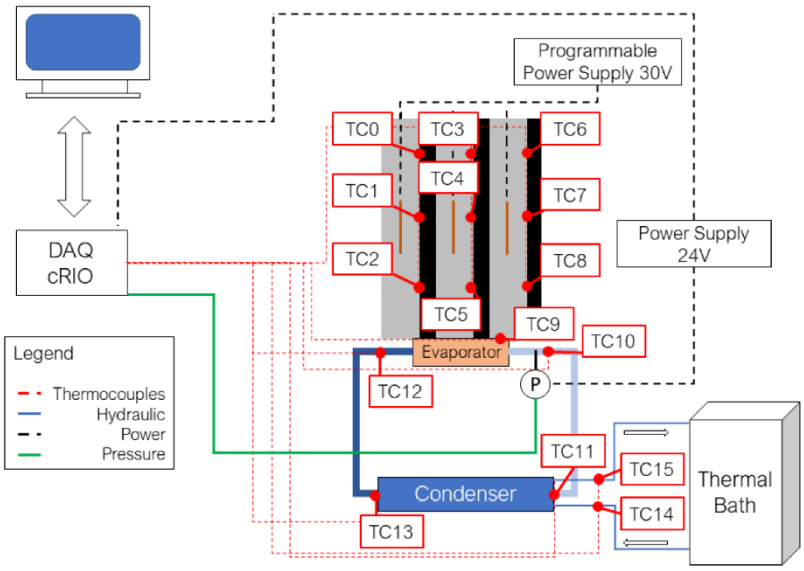

Fig. 113. General schematic of the experimental apparatus used, with details of the thermocouple positioning.

In Fig. 114, the general results with ethanol as working fluid are presented. Firstly, one can notice that the cell temperature is above the threshold required by the pack requirement, as maximum temperatures in the middle and side cells of the module are 57°C and 53°C for the ethanol case. This is due to the mismatch in available surface between the battery module and the heating zone of the LHP evaporator, as the latter was bound by the manufacturer availability. As shown in Chapter 5, it has been proven that if the heating zone of the LHP evaporator has a size close to the battery module footprint, the maximum temperature drops considerably below 40°C.

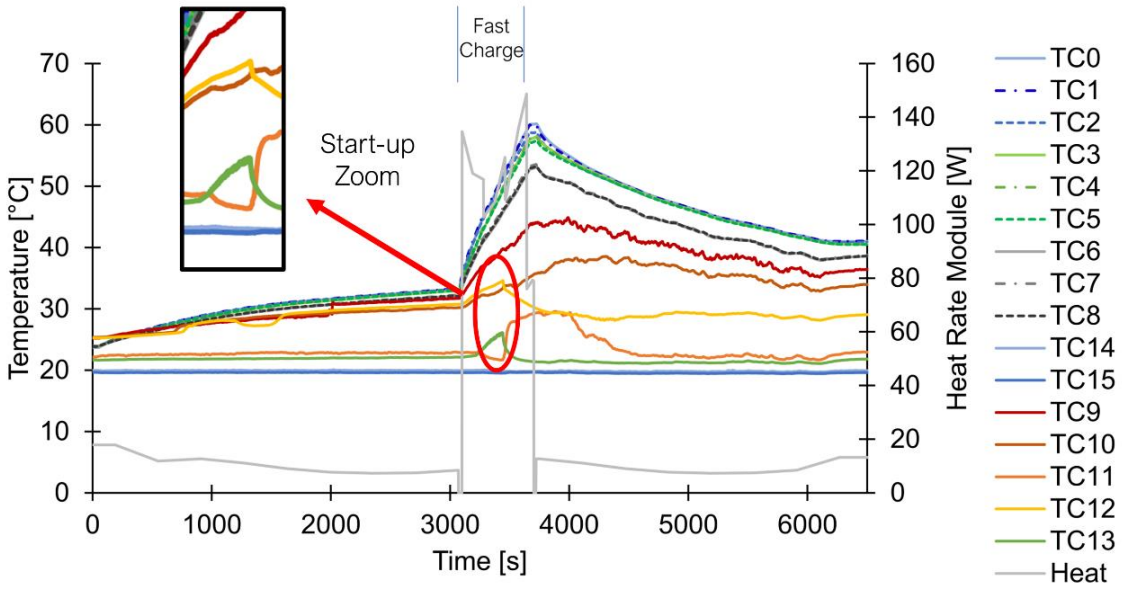

Fig. 114. Test results during a HFCH driving cycle using Ethanol as working fluid.

Looking at the LHP behaviour in the ethanol case in Fig. 114, one can notice that the onset of the predominant boiling condition typical of the LHP, the so-called start-up, happened well into the fast charging section around 3500 seconds, as shown by the sudden increase of the temperature at the inlet of the condenser (orange line – TC11) and the decrease of the temperature at the outlet of the condenser (green line – TC13) and at the end of the liquid line back into the evaporator (yellow line – TC12). These temperature trends mean that the vapour has reached the condenser to reject the heat (increase of orange line), and condensation happens creating cooler subcooled liquid that exit the condenser (green line) and reaches the evaporator by the end of the liquid line (yellow line).

However, the start-up took place halfway through the fast charging period, which is not optimal. In fact, the comparison shown in Fig. 115 between heat rate generated by the module and heat rate received by the LHP (obtained from the simulations in [271]), shows a great difference due to heat being stored as heat capacity in the cell material, as results of the strongly transient nature of the driving cycle. The actual system that receives the heat input is massive with respect to the LHP evaporator and therefore the transient heat capacity terms in the ODE equations store most of the heat during such a fast, aggressive phenomenon like the fast charging. To reduce this component, one can think of reducing the mass of the cell or its specific heat. This was outside the scope of the present work, as the actual battery was given as a boundary condition and could not be modified.

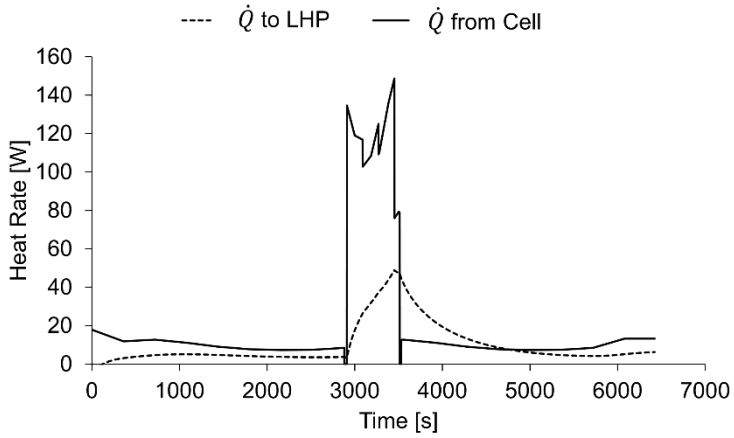

Fig. 115. Comparison between heat rates generated by the module and received by the LHP during the HFCH driving cycle.

A design where the LHP starts sooner or at lower power levels would be beneficial. With this in mind, Fig. 116 presents the results of the test carried out with Novec™ 649 as working fluid. The sudden increase of the temperature of the condenser inlet (orange line – TC11) denotes that the start-up is happening as soon as the fast charge section is initiated, which is a clear improvement from the ethanol case. This behaviour was expected since Novec™ 649 has lower boiling point, latent heat of vaporisation and mass specific heat with respect to ethanol (Table 44).

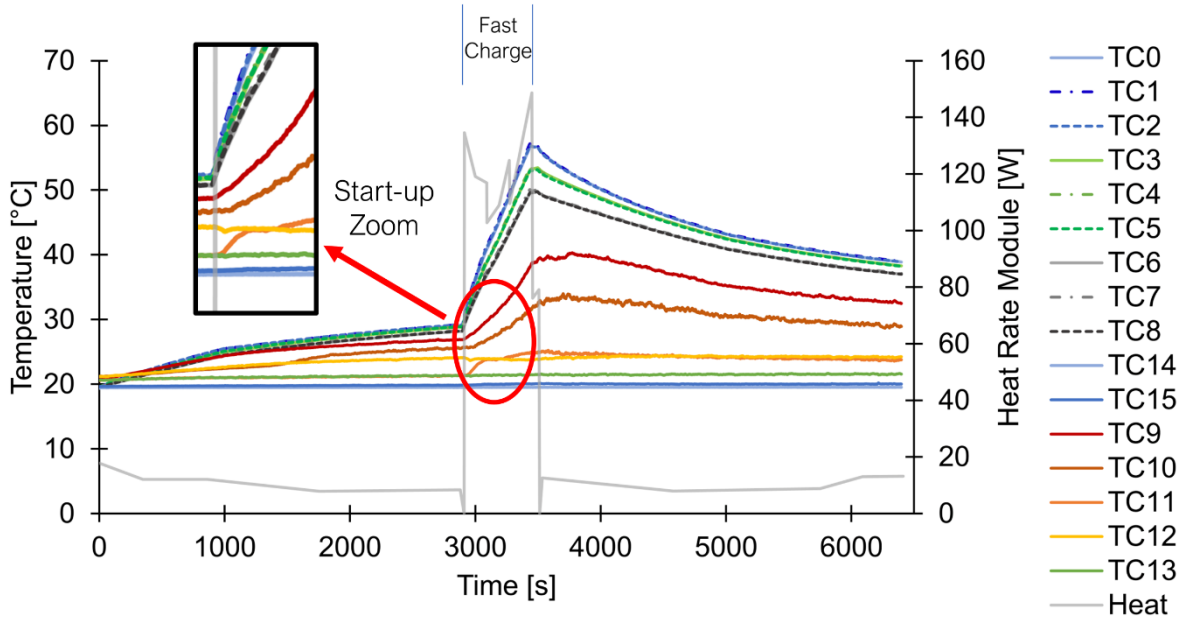

Fig. 116. Test results during a HFCH driving cycle using Novec™ 649 as working fluid.

Looking at the difference between the two fluids, their main physical properties are presented in Table 44. Considering the lower boiling point, the significantly lower latent heat

of vaporisation and specific heat one can expect that the LHP start-up while running with Novec™ 649 would happen at lower temperatures and heat inputs than with ethanol.

Table 44. Key physical properties of ethanol and Novec™ 649. All properties are evaluated at 20°C.

	Ethanol	Novec™ 649
Boiling Point [°C]	78	49
Freezing Point [°C]	-114	-108
Density [kg/m]	804	1600
Viscosity [mPa·s]	1.19	0.64
Thermal Conductivity [W/m·K]	0.17	0.06
Latent Heat of Vaporisation [kJ/kg]	945	88
Specific Heat [J/kg·K]	3023	1103
Surface Tension [N/m]	0.022	0.011
Saturation Pressure [bar]	0.062	0.400

Fig. 117 presents a comparison between the average cell temperature obtained using the two working fluids in the LHP-based TMS. The two tests were performed in different lab temperatures (20°C for the Novec™ 649 test and 25°C for the ethanol test), so to effectively compare the two cases, the temperature is expressed as ΔT from the ambient temperature. Results show that the two fluids performed in a similar fashion, with maximum temperature at the end of fast charging being only different by 0.7°C in the two cases. Ethanol looks slightly better in reducing the temperature in the final highway driving section, giving a final temperature 2.2°C lower than the other fluids. The take home message of the comparison graph of Fig. 117 is that using Novec™ 649 provides a non-flammable, environmentally friendly and non-toxic alternative to ethanol, without a significant decrease in thermal performance.

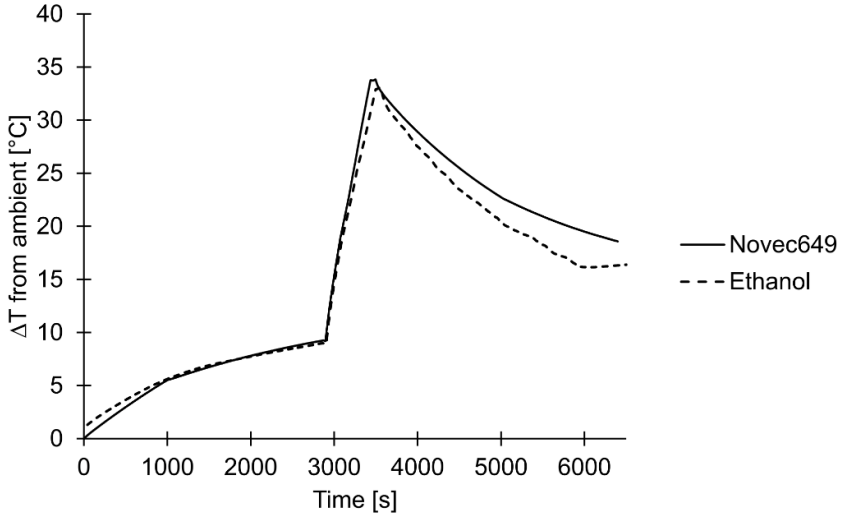

Fig. 117. Average cell temperature comparison over the HFCH obtained using the LHP with Novec™ 649 or ethanol as working fluids.

6.7.3. Assessment of TMS with Novec™ 649 during different C-rates

The previous section showed that there was no significant difference in maximum temperature reduction between the two fluids investigated. Therefore, there is enough confidence to proceed the investigation on Novec™ 649 as working fluid. This section presents a study assessing the potential for using this design as an effective way to contain the temperature during fast charge. The tests have been carried out supplying the cells with power equivalent to fast charge cycle with three different C-rates, namely 1C, 2C and 3C, from 20% to 80% SOC, as this is the standard practice due to safety limitations [292]. Fig. 118 shows the power profile of the modules depending on the C-rate. Thus, as shown in Table 45 these fast charging profiles lasts for 36 minutes for 1C-rate, 18 minutes for 2C-rate and 12 minutes for 3C-rate.

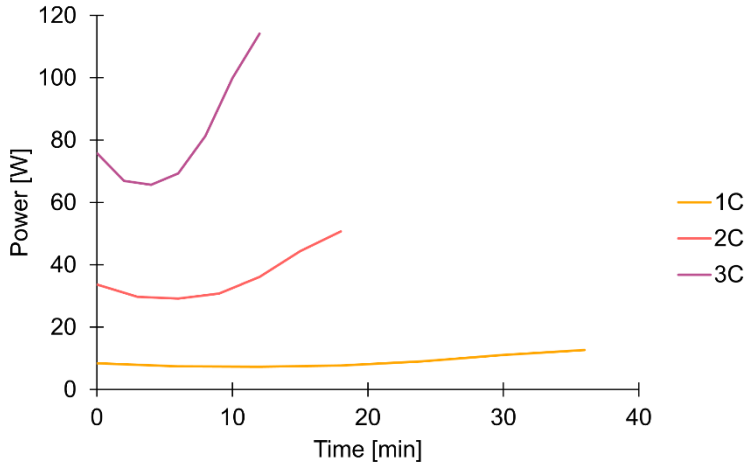

Fig. 118. Power vs time (in minutes) profiles of the different C-rates use in this investigation. These figures refer to a 20% to 80% SOC charge.

Table 45. Duration and average heat generation rate of single cell and module, considering a fast charge from 20% to 80% depending on the different C-rates.

C-rate	Charge Times 20-80% SOC	Heat Rate Cell [W]	Heat Rate 3Cell Module [W]
1C	36 min	3	9
2C	18 min	12	36
3C	12 min	27	81

The current state of the art is represented by the Porsche Taycan, which provides a maximum charging rate of 3C, whereas for the remaining of EVs the charge rate is limited to 1-1.5C [292]; therefore, it was deemed appropriate to test the solution presented in this work against the state-of-the-art condition. All the below reported tests were carried out at ambient temperature of 20°C.

Fig. 119 shows the temperature and pressure trends when the cells are subjected to a 1C charge profile, hence an average total heat rate generated by the module of 9 W. As shown by the temperature of the LHP nodes, no start-up is taking place, indicating in this case the heat provided to the evaporator is not sufficient. However, the maximum temperature of the cells is 28.4°C (as also provided in Table 46) so this condition remains within the optimal operating temperature range of the cell.

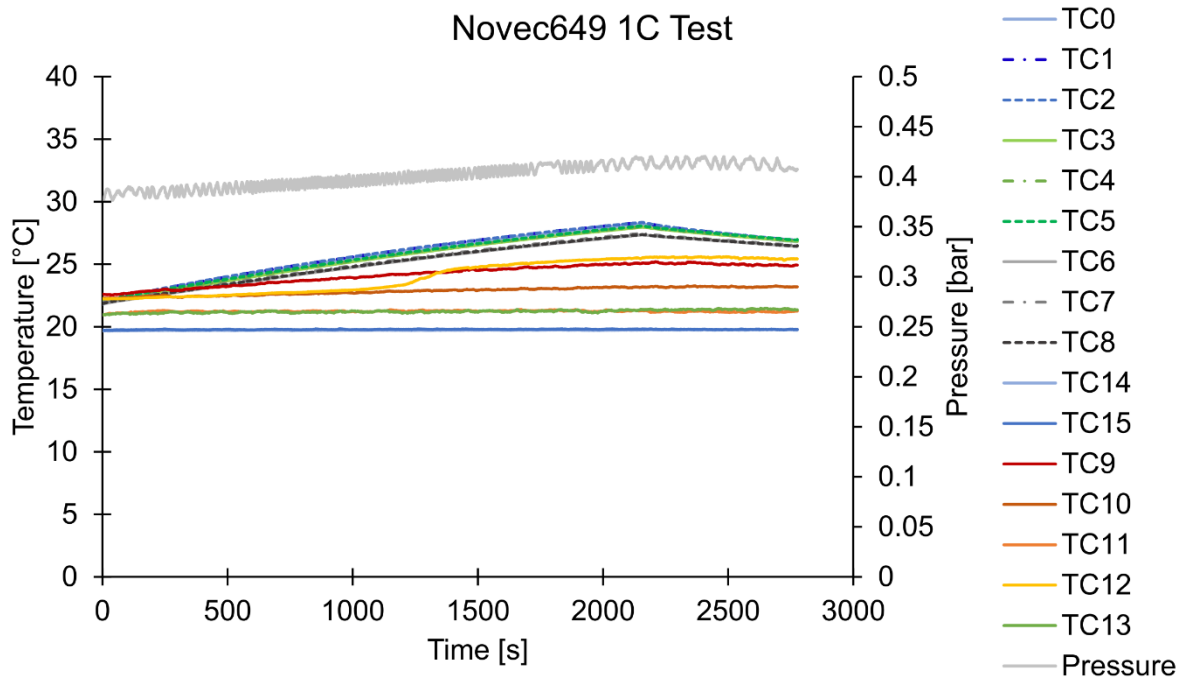

Fig. 119. Novec™ 649 fast charging test results with 1C. Heaters were turned off after 36 min (~ 2100 seconds, end of the 1C charging), hence the cell temperatures decrease.

On the other hand, during the fast charge test at 2C condition, shown in Fig. 120, the LHP start-up takes place as indicated by the increase in temperature of the vapour line inlet (TC10) followed by the increase in the condenser inlet temperature (TC11). Due to the much higher heat generation rate that the cell is providing (4 times as much as the 1C case), the conditions are favourable to the onset of boiling and consequently for the fluid to circulate in a preferential direction. In fact, one can notice from Fig. 120 that the temperature of the outlet of the liquid line (TC12) is not increasing, rather it decreases following the increase of the condenser inlet, thus proving that the condensed liquid is flowing back to the evaporator. As proof that this behaviour is due to the start-up, Fig. 120 shows that when the heating power is turned off (at 1000 seconds ~ 18 minutes, end of the 2C fast charge), the trends of TC12 and TC10 are reversed.

During this test, maximum average temperature for the cell was 36.3°C degrees, while its state of charge would reach 80% in 18 minutes.

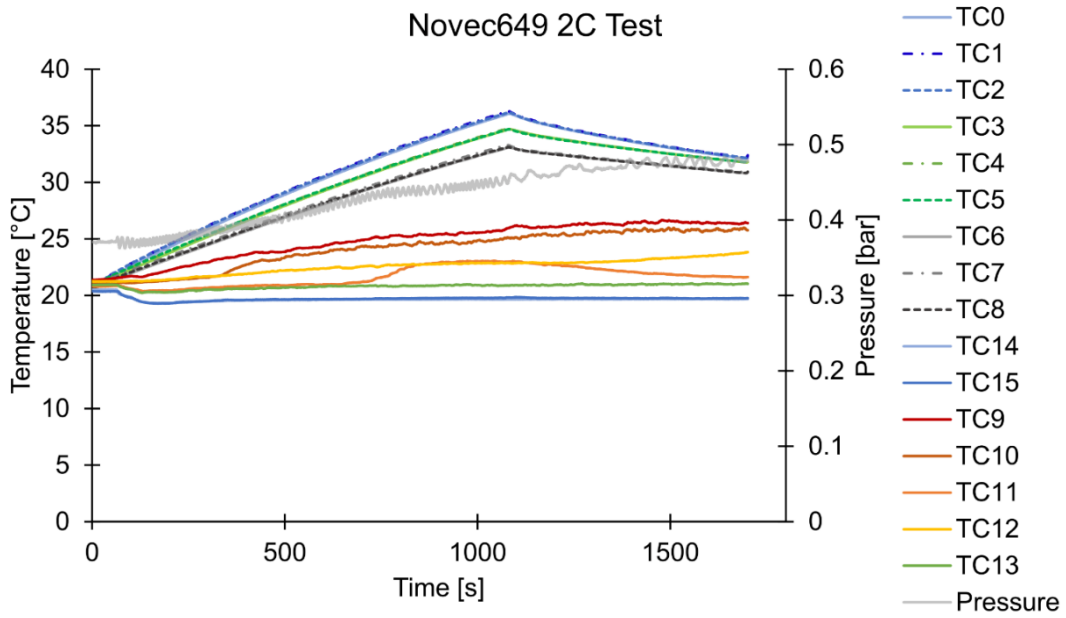

Fig. 120. Novec™ 649 Fast Charging test results with 2C.

Finally, the fast charge test with 3C is presented in Fig. 121. Following the increased cell heat generation rate, start-up happens sooner than in the other two cases. In this case the maximum average temperature of the cell was 46.4°C, at the end of a fast charge profile that would allow 80% of the SOC to be reached in only 12 minutes.

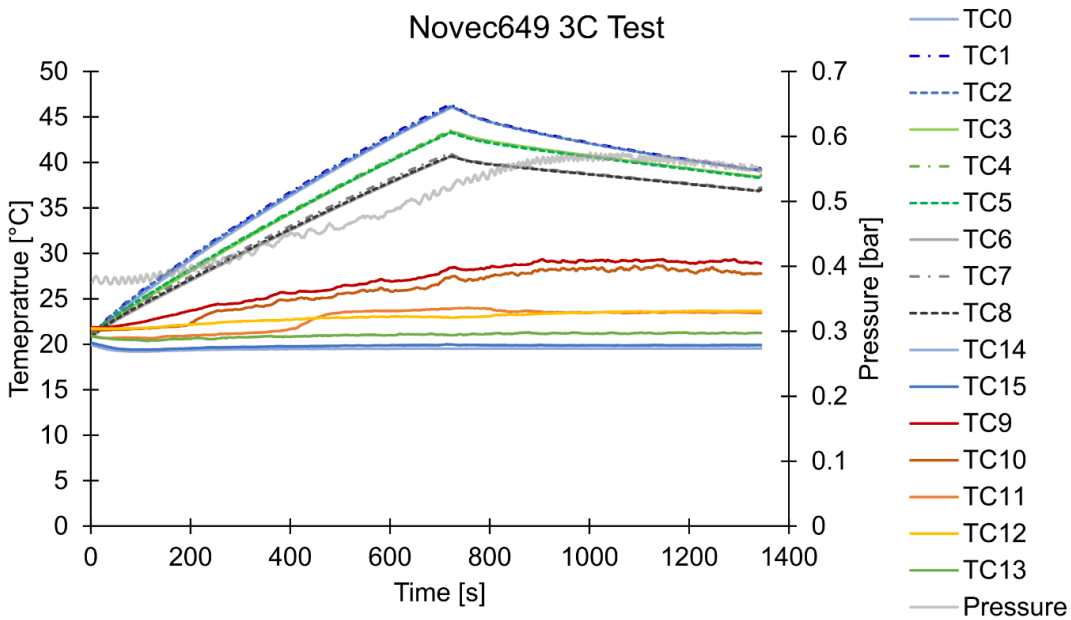

Fig. 121. Novec™ 649 Fast Charging test results with 3C.

Summarising, Fig. 122 shows the maximum temperature of each cell during the fast charge experiments. In addition, Table 46 shows the numerical predictions results. The maximum temperature during the 3C fast charge is above the optimal threshold of 40°C, but nonetheless it is below the safety threshold of 60°C, despite the LHP possessing a much smaller active heating zone than required. This indicates the potential of this design solution and motivates the need of further investigation by means of a bespoke larger prototype. Moreover, the temperature spread over the module is inside the requirement at the module level, as shown in Table 46.

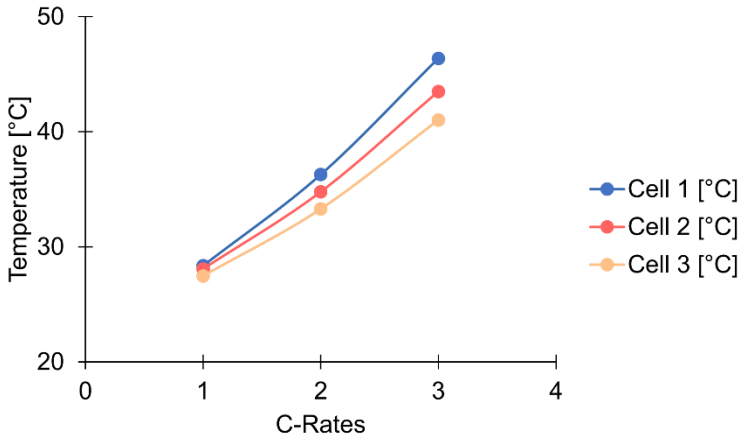

Fig. 122. Comparison of the maximum temperature reached by each cell during the fast charge experiments with Novec™ 649.

Table 46. Comparison of maximum cell temperatures during the fast charge tests, together with the temperature difference across the module.

	Cell 1 [°C]	Cell 2 [°C]	Cell 3 [°C]	ΔT [°C]
1C	28.4	28.1	27.5	0.9
2C	36.3	34.8	33.3	3.0
3C	46.4	43.5	41.0	5.4

These results prove that Novec™ 649 can be a valuable substitute to standard heat transfer fluids already employed in two-phase applications, and if applied to the proposed design with LHP and graphite sheets, battery temperature can be contained within acceptable levels even during aggressive state of the art fast charge scenarios (3C).

6.8. Conclusions

In this section, a series of investigations were performed to assess and improve the applicability of the proposed LHP-based TMS to the automotive sector, specifically targeting the EV world

and in particular a 12-cell module. The effect of several factors was examined, from the shape, number and thickness of the evaporators applied to the module, the number of graphite sheets. Moreover, an extensive parametric analysis on the working fluids and manufacturing materials of the LHP was carried out, exploring standard heat transfer fluids together with low-GWP heat transfer fluids chosen because of their environmental properties and freezing temperature. A comparison with free convection was then performed, over different fast charge cycles and a case study over a hypothetical journey from London to Liverpool with a Nissan Leaf 2021. Finally, an experimental investigation was performed assessing the potentiality of using an appealing new heat transfer fluid, Novec™ 649.

The concluding remarks that can be drawn are:

- The size of the evaporator active heating zone needs to be carefully considered, as larger does not always imply better performance.
- The design with 10 LHP evaporators applied to the module is able to keep the cell temperature below 50°C at 5C fast charge conditions; designs with 4LHP and 6LHP would still provide an improvement in state of the art, with fast charge in less than 10 minutes and temperature in the acceptable range.
- There is the potential to have very thin evaporator wicks (between 2mm and 4mm), without a dramatic increase of the maximum cell temperature. However, the actual feasibility of this idea needs to be further studied considering the stress-strain curve of the material and the complex fluid-dynamic linked to the dry-out phenomena.
- Using one graphite sheet every two cells allows to save 9.66 kg in a 420-cell battery pack (0.28 kg per module) at the expense of a maximum temperature increase during 3C fast charge of 1.8°C for the 2LHP case and 3.8°C for the 10LHP case.
- If the working fluid selection influences the operation of the LHP, this will also affect the cell temperature, with temperature variations between 2°C and 4°C (up to 8°C for water); the working fluid selection will be a trade-off between many factors, from safety and environmental, to freezing point (water) and thermal performance. Regarding the materials, not using copper increases the maximum temperature by ~2°C, but can allow to save a third of the mass and cost (in case of the aluminium LHP) or to gain 7 times more mechanical strength (in case of using SS).
- Free convection, compared to the LHP-based and cold plate TMS, can contain maximum cell temperature at low values of C-rates, but is not able to reduce the temperature once the vehicle returns to normal driving conditions.

- The LHP-based TMS and the cold plate TMS provided an improvement in terms of both maximum and final temperature with respect to the free convection TMS, with average ΔT as high as 10.9°C and 23.8°C, respectively.
- For the first time a LHP filled with Novec™ 649 as working fluid (a fluid that is non-flammable, non-toxic, with low freezing and boiling point and GDP = 1 and ODP = 0) is utilized and thermally characterized.
- Comparing the Novec™ 649 results with the same LHP filled with ethanol over the HFCH driving cycle, the cell temperatures at the end of fast charge differed by only 0.7°C.
- Quicker start-up was achieved while using Novec™ 649, as the lower boiling point and latent heat of vaporisation compared to ethanol, made the LHP start as soon as the fast charge was initiated.
- The proposed TMS, running Novec™ 649 was tested for different fast charge cycles, 1C, 2C and 3C, where the maximum temperatures were 28.4°C, 36.3°C and 46.4°C respectively; these results are below the safety threshold of 60°C and very close to the 25°C-40°C optimum window.
- Moreover, the temperature difference across the cells belonging to the module was 5.4°C at 3C fast charge, which in line with the thermal requirement at the module level.

Chapter 7 - Conclusions

The pressing problem of Global Warming has pushed governments worldwide to take actions into reducing GHG emissions, targeting the transportation sector as one of the main areas where to act, being one of the main sources of harmful pollutant emissions. In the most likelihood future, the only passenger vehicles allowed to travel the roads will be BEV or HEV, following governments regulations banning the sale of conventional ICE powered cars and vans. Despite all these efforts and the incredible growth in worldwide sales in the recent years, EV still are relegated to the 1% of the global fleet. Reasons can be found in the complaints made by customers about EV's elevated cost, limited all-electric range (triggering the range anxiety phenomenon) and long recharging time, to cite the most important ones. Motivated by the need of improving on these aspects, by increasing the all-electric range, decreasing maintenance requirements hence reducing operational costs, and finally decreasing the charging time, this thesis's purpose is to identify, develop and characterise an innovative Thermal Management System for EV battery modules.

An extensive literature review led to the understanding that none of the currently employed and/or studied TMS can solely cope with the stringent thermal requirements of Li-ion cells, and at the same time have low cost, low complexity and low effect on the all-electric range. Hence the suggestion that a hybrid TMS comprising of two different TMS could deal efficiently with the identified thermal requirements. These are: temperature gradient across the cell should not exceed 5°C (cell requirement); temperature between cells should be maintained between a 5°C difference (module requirement); overall temperature of the cells (pack requirement) belonging to the pack needs to be kept between 25°C and 40°C for optimum performance, 50°C for good acceptable performance and a final overall limit of 60°C is fixed for safety purposes.

The hybrid TMS innovative design proposed in this thesis comprises of a Loop Heat Pipe placed at the bottom of a prismatic cell module, which cells are sandwiched between graphite sheets. The LHP acts as main thermal vector, transferring passively the excess heat from the cells to a remote liquid chiller, already part of the HVAC system of the vehicle, hence reducing the complexity of the TMS. Graphite sheets have the twofold function of promoting heat transfer along the cell plane direction, while hindering it in the transverse direction, thanks to their anisotropic thermal conductivity properties. LHPs are reliable, low-maintenance, safe and not expensive systems already used in electronics, space and aeronautical applications. Since LHPs need no electrical power, they reduce the parasitic power consumption compared to forced air or liquid-based TMS. The design thus creates a perfect example of the hybridization of two technologies, as the LHP will save the parasitic power and extra components needed for the liquid loop, still achieving excellent thermal performance.

The feasibility of the proposed design was firstly studied via a Lumped Parameter Model, implemented in the open-source software Octave, describing the thermodynamic behaviour of the system. Two sub-thermal networks were firstly created, one dedicated to the cell-graphite assembly and one dedicated to the LHP evaporator. The cell-graphite LPM was validated via comparison with FVM results obtained with Ansys Fluent, where the same cases were simulated and the maximum discrepancy in the temperature results was 0.5°C. The LHP LPM was validated via comparison with literature available data, utilizing three different geometries and three different working fluids (ammonia, water and R134a), resulting in maximum discrepancy in the temperature results of 2.8°C. The two validated sub-models were then put together to form the unified LPM that describes the proposed TMS. Due to the separated validations procedures, there was enough confidence to run a comparison simulation between the LHP-based TMS and a standard liquid cold plate design. The latter was developed by the industrial collaborator Ricardo plc and runs ethylene glycol at fixed temperature of 20°C coming from the HVAC system of the vehicle. Preliminary results over a bespoke driving cycle including fast charging (HFCH driving cycle) showed that the LHP TMS provided better results, allowing for a favourable reduction ΔT of 3.3°C during fast charging.

Due to the promising results of this preliminary feasibility study, an experimental demonstrator of the proposed design was built, aiming to validate the numerical model. A 3-cell aluminium module was machined, assembled with graphite sheets sandwiched between the cells and instrumented with temperature sensors and power heaters. It was placed on top of a copper/copper flat plate LHP. The condenser of the LHP was embedded in a tube in tube heat

exchanger, connected to a thermal bath. The LHP was finally instrumented with temperature and pressure measurements. The experimental campaign resulted in a satisfactory validation over two different working fluids (ethanol and water), on every part of the LPM:

- The maximum ΔT between experimental and simulation data for the cell-graphite assembly was 2.4°C.
- The reproduction of the in-house experimental data with the LHP-only LPM gave excellent results, with the average percentage error for the thermal resistance always lower than 10%, and the discrepancy in the temperature prediction always falling inside the ±5°C window.
- The validation procedure for the whole system resulted in a maximum cell temperature discrepancy between experiment and numerical results of 3°C in a 70 W heat rate case, 2.4°C in a 150 W heat rate case and around 2°C for the HFCH driving cycle case.

The main findings obtained thanks to the experimental demonstrator and the validated LPM are presented in the next section.

7.1. Main Findings

Following, the main findings of the present PhD Thesis are presented as a comprehensive numbered list:

1) The performance of the proposed TMS was satisfactory, as it respected the requirements at cell level (ΔT over a cell of 0.7 °C) and at module level (ΔT between cells of 4.5°C and 1.8 °C); for the requirements at pack level, the proposed TMS respected the upper safety limit, with maximum temperature of 59°C for cell 1 and a bit above the acceptable limit for cell 3 with 53.3°C, due to the limit in the available active zone of the evaporator, highlighted in section 7.3.

2) The validated numerical model allowed to confidently verify what would be the thermal performance of the design if the LHP active zone had the same footprint of the module. Simulating over the bespoke HFCH driving cycle, results showed that the LHP TMS proposed in this work (with ethanol as working fluid) has the potential to be more efficient in reducing the maximum temperature compared to a standard liquid cold plate TMS (with ethylene glycol) achieving a peak temperature of 31.5°C, which constitutes a reduction of 3.6°C from the cold plate results. This result not only showed potential to satisfactory respect the pack requirement, but also it marked the success of the feasibility study of the novel idea proposed in this thesis.

Taking the investigation a step further than a feasibility study, a series of investigations were performed to assess and to improve the applicability of the proposed LHP-based TMS to the automotive sector, specifically targeting the EV world and in particular a 12-cell module. The effects of several factors were examined, and the worth mentioning remarks are presented as follows:

3) The number of LHP evaporators applied to the 12-cell module was varied, together with their geometry. Two shapes were considered, one equal to the one used in the experimental demonstrator and one able to cover the length of the module. The goal here was to study the effect of the coverage of the module footprint. It resulted that the size of the evaporator active zone needs to be carefully considered, as larger does not always imply better performance. Regarding the number of evaporators, cases with 2, 4, 6, and 10 LHP evaporators were simulated, resulting in the design with 10 LHP evaporators being able to keep the cell temperature below 50°C at 5C fast charge conditions, thus allowing fast charge in only 7 minutes. Designs with 4LHP and 6LHP would still provide an improvement in state of the art, with fast charge in less than 10 minutes and temperature in the acceptable range.

4) The thickness of the evaporator was also investigated, aiming to reduce as much as possible the encumbrance of the TMS to the battery pack, in order to leave more room for passengers in the cabin. Results showed the potential to have very thin evaporator wicks (between 2mm and 4mm), without a dramatic increase of the maximum cell temperature ($\Delta T < 7°C$). However, the actual feasibility of this idea needs to be further studied considering the stress-strain curve of the evaporator envelope material and the complex fluid-dynamic linked to the dry-out phenomena associated with having less fluid volume.

5) Aiming to reduce added mass and encumbrance and hence improve the energy density, a design where only one graphite per 2 cells was investigated. It allows to save 9.66 kg in a 420-cell battery pack (0.28 kg per module) at the expense of a temperature increase during 3C fast charge between 1.8°C - 3.8°C for the studied cases.

6) An extensive parametric analysis on the effect of LHP working fluids and manufacturing materials was carried out. Copper, aluminium and stainless steel were the considered materials, and standard heat transfer fluids (water, ethanol, methanol, acetone) together with low-GWP heat transfer fluids (R1233zd(e), Novec™ 649, FlutecPP2, Freon225, R1234ze) were also chosen because of their environmental properties and freezing temperature. Results showed how the LHP working fluid selection will affect the cell temperature, with temperature

variations between 2°C and 4°C (up to 8°C for water), thus the working fluid selection will be a trade-off between many factors, from safety and environmental, to freezing point (water) and thermal performance. Results showed that amongst the low-GWP working fluids, to worst performing was R1233zd(e), while the others offer comparable performances. The selection of the LHP of the manufacturing materials can bring about increase of ~2-4°C, but also significant mass reduction or strength improvement.

7) Intending to compare the proposed LHP-based TMS with another passive cooling solution, a comparison with free convection was then performed. Several fast charge cycles boundary conditions were considered and a case study over a hypothetical journey from London to Liverpool with a Nissan Leaf 2021 was conducted. The results showed that free convection, compared to the LHP-based and cold plate TMS, can contain maximum cell temperature at low values of C-rates, but is not able to reduce the temperature once the vehicle returns to normal driving conditions. During the London-Liverpool case study, the LHP-based TMS provided, at the end of the simulation, a temperature reduction of 23.8°C compared to free convection.

8) Finally, an experimental investigation was performed assessing the possibility of using an appealing new heat transfer fluid, 3M™ Novec™ 649, selected as working fluid because of outstanding properties like non-flammability, non-toxicity, low freezing and boiling point. More importantly, it possesses extremely low pollutant factors (GDP = 1 and ODP = 0). In fact, a gap in the current research was identified, as the focus is often on addressing the system thermal performance, without considering the implication of the thermal medium. This must not only provide suitable performances, but also it must not add any risks to both the passengers and the environment. The remarks of major significance are drawn:

- For the first time a LHP filled with Novec™ 649 as working fluid is utilized and thermally characterized.
- Comparing Novec™ 649 results with the same LHP filled with ethanol over the HFCH driving cycle, the cell temperatures at the end of fast charge differed by only 0.7°C, indicating that the safety and environmental benefits of using Novec™ 649 came with no detriment to the thermal performance.
- Quicker start-up was achieved while using Novec™ 649, as having lower boiling point and latent heat of vaporisation compared to ethanol, made the LHP start as soon as the fast charge was initiated.
- The proposed TMS, running with Novec™ 649 was tested for different fast charge cycles, 1C, 2C and 3C, obtaining maximum temperatures of 28.4°C, 36.3°C and 46.4°C

respectively; these results are below the safety threshold of 60°C and very close to the 25°C-40°C optimum window.

- The temperature difference across the cells belonging to the module was 5.4°C at 3C fast charge, which in line with the thermal requirement at the module level.

These thermal results are very promising, especially considering that, due to manufacturing limitations, the active heating area of the LHP evaporator was much smaller than the battery module footprint. Even pushing a demanding fast charge cycle in 12 minutes, the maximum cell temperature still was below 50°C.

7.2. Contributions to Knowledge

In conclusions, this thesis has presented the conception, design and production of an innovative Thermal Management System for Electric Vehicles that is able to cope with highly demanding thermal requirements, often improving on the performance of the current state of the art, in terms of temperature reduction. This was achieved with passive systems and equipment already present in the vehicle, hence without additional parasitic power consumption or the added complexity of more parts.

A design tool was obtained, thanks to a validated numerical model, able to evaluate the effect of several design aspects.

An additional step further was performed when, for the first time, Novec™ 649 was employed as LHP working fluid, providing benefits in terms of safety, temperature range and environmental impact, with no detriment to the thermal performance.

7.3. Limitations of the work

The limitations of the work were imposed by the impossibility of manufacturing the wick for the LHP evaporator at the laboratories of the Advanced Engineering Centre. Hence, the LHP was externally sourced and the shape availability was bound by the manufacturer production line. This brought about the inconvenience of having a mismatch between the LHP evaporator and the footprint of the battery module, where the active zone of the evaporator covered less than a quarter of the module footprint. As a result, the heat removed from the battery module was limited by the small heat transfer surface shared with the evaporator active zone. However, this fact did not affect the validation process, as it made no difference for the LPM, nor the feasibility study, since the geometry could be easily changed in the LPM to have matching surfaces or to increase the number of evaporators applied to the module.

7.4. Suggestions for future work

The Author suggests the following research activities to extend the research undergone in this PhD Thesis, and effectively bridging the gap between a feasibility study and the actual implementation in the automotive sector of the design produced in this work.

1. Design, building and characterisation of a large dimension flat plate LHP evaporator to be applied to a 12-cell battery cell module, as opposed to utilise several smaller LHP evaporators.
2. To obtain industry-led data on TMS employed in commercially available EVs (i.e., pumped liquid convection and forced air convection), in order to perform a comparison on power consumption, cost and weight.
3. Extending the investigation to different ambient temperatures, by means of a climatic chamber, to better understand the link between ambient temperature, cell temperature and LHP start-up.
4. Following the philosophy adopted in during this PhD Thesis of favouring the reduction of the parasitic power consumption, one should study the effect of thermal insulation applied to the module, combined with the capability of heat removal of the LHPs, particularly aiming to improve the efficiency of the heating side of the TMS.
5. This work has proven the possibility of using LHPs as thermal vector between remote zones of a vehicle. This concept should be studied further, considering using LHPs in the thermal network of the vehicle, favouring efficient heat transfer without parasitic power consumption and improving the waste heat recovery of the thermal network. Said zones include but are not limited to vehicle interior (seats, HVAC system), heat pump, electronics, drivetrain.

References

[1] Department for Business Energy & Industrial Stratagy, 2018 UK greenhouse gas emissions, Final figures, Natl. Stat. (2020) 40. https://assets.publishing.service.gov.uk/government/uploads/system/uploads/attachment_data/file/790626/2018-provisional-emissions-statistics-report.pdf.

[2] C.E. Sandy Thomas, Transportation options in a carbon-constrained world: Hybrids, plug-in hybrids, biofuels, fuel cell electric vehicles, and battery electric vehicles, Int. J. Hydrogen Energy. 34 (2009) 9279–9296. https://doi.org/10.1016/j.ijhydene.2009.09.058.

[3] P.H. Andersen, J.A. Mathews, M. Rask, Integrating private transport into renewable energy policy: The strategy of creating intelligent recharging grids for electric vehicles, Energy Policy. 37 (2009) 2481–2486. https://doi.org/10.1016/j.enpol.2009.03.032.

[4] International Energy Agency (IEA), Global EV Outlook 2021, 2021. https://doi.org/10.1787/d394399e-en.

[5] P. Ramadass, B. Haran, R. White, B.N. Popov, Capacity fade of Sony 18650 cells cycled at elevated temperatures, J. Power Sources. 112 (2003) 614–620. https://doi.org/10.1016/s0378-7753(02)00473-1.

[6] G. Nagasubramanian, Electrical characteristics of 18650 Li-ion cells at low temperatures, J. Appl. Electrochem. 31 (2001) 99–104. https://doi.org/https://doi.org/10.1023/A:1004113825283.

[7] J. Lin, X. Liu, S. Li, C. Zhang, S. Yang, A review on recent progress, challenges and perspective of battery thermal management system, Int. J. Heat Mass Transf. 167 (2021) 120834. https://doi.org/10.1016/j.ijheatmasstransfer.2020.120834.

[8] P. Qin, M. Liao, D. Zhang, Y. Liu, J. Sun, Q. Wang, Experimental and numerical study on a novel hybrid battery thermal management system integrated forced-air convection and phase change material, Energy Convers. Manag. 195 (2019) 1371–1381. https://doi.org/10.1016/j.enconman.2019.05.084.

[9] P.R. Tete, M.M. Gupta, S.S. Joshi, Developments in battery thermal management systems for electric vehicles: A technical review, J. Energy Storage. 35 (2021) 102255. https://doi.org/10.1016/j.est.2021.102255.

[10] S. Panchal, I. Dincer, M. Agelin-Chaab, R. Fraser, M. Fowler, Experimental and theoretical investigations of heat generation rates for a water cooled LiFePO4battery, Int. J. Heat Mass Transf. 101 (2016) 1093–1102. https://doi.org/10.1016/j.ijheatmasstransfer.2016.05.126.

[11] D. Chen, J. Jiang, G.H. Kim, C. Yang, A. Pesaran, Comparison of different cooling methods for lithium ion battery cells, Appl. Therm. Eng. 94 (2016) 846–854. https://doi.org/10.1016/j.applthermaleng.2015.10.015.

[12] M. Lu, X. Zhang, J. Ji, X. Xu, Y. Zhang, Research progress on power battery cooling technology for electric vehicles, J. Energy Storage. 27 (2020) 101155. https://doi.org/10.1016/j.est.2019.101155.

[13] G. Zhao, X. Wang, M. Negnevitsky, H. Zhang, A review of air-cooling battery thermal management systems for electric and hybrid electric vehicles, J. Power Sources. 501 (2021) 230001. https://doi.org/10.1016/j.jpowsour.2021.230001.

[14] L. Ianniciello, P.H. Biwolé, P. Achard, Electric vehicles batteries thermal management systems employing phase change materials, J. Power Sources. 378 (2018) 383–403. https://doi.org/10.1016/j.jpowsour.2017.12.071.
[15] R.W. Van Gils, D. Danilov, P.H.L. Notten, M.F.M. Speetjens, H. Nijmeijer, Battery thermal management by boiling heat-transfer, Energy Convers. Manag. 79 (2014) 9–17. https://doi.org/10.1016/j.enconman.2013.12.006.
[16] H. Hirano, T. Tajima, T. Hasegawa, T. Sekiguchi, M. Uchino, Boiling liquid battery cooling for electric vehicle, IEEE Transp. Electrif. Conf. Expo, ITEC Asia-Pacific 2014 - Conf. Proc. (2014) 1–4. https://doi.org/10.1109/ITEC-AP.2014.6940931.
[17] N.S.V. Studio, Climate Time Machine, (n.d.). https://climate.nasa.gov/interactives/climate-time-machine (accessed May 2, 2019).
[18] United States Global Change Research Program, Global Climate Change Impacts in the United States, 2009.
[19] P.-A. Dessandier, J. Knies, A. Plaza-Faverola, C. Labrousse, M. Renoult, G. Panieri, Ice-sheet melt drove methane emissions in the Arctic during the last two interglacials, Geology. 49 (2021) 799–803. https://doi.org/10.1130/G48580.1.
[20] Z. Rezvani, J. Jansson, J. Bodin, Advances in consumer electric vehicle adoption research: A review and research agenda, Transp. Res. Part D Transp. Environ. 34 (2015) 122–136. https://doi.org/10.1016/j.trd.2014.10.010.
[21] F.S. Boureima, M. Messagie, J. Matheys, V. Wynen, N. Sergeant, J. van Mierlo, M. de Vos, B. de Caevel, Comparative LCA of electric, hybrid, LPG and gasoline cars in Belgian context, World Electr. Veh. J. 3 (2009) 469–476.
[22] T.R. Hawkins, B. Singh, G. Majeau-Bettez, A.H. Strømman, Comparative Environmental Life Cycle Assessment of Conventional and Electric Vehicles, J. Ind. Ecol. 17 (2013) 53–64. https://doi.org/10.1111/j.1530-9290.2012.00532.x.
[23] UK Department for Transport, Air quality plan for nitrogen dioxide (NO2) in UK, (2017). https://doi.org/10.1056/NEJMc1503870.
[24] B. Johnson, Boris Johnson: Now is the time to plan our green recovery, Financ. Times. (2020) 6–9. https://www.ft.com/content/6c112691-fa2f-491a-85b2-b03fc2e38a30.
[25] G. Dong, R.E. Morgan, M.R. Heikal, Thermodynamic analysis and system design of a novel split cycle engine concept, Energy. 102 (2016) 576–585. https://doi.org/10.1016/j.energy.2016.02.102.
[26] M. Guarnieri, Looking back to electric cars, 3rd Reg. IEEE Hist. Electro - Technol. Conf. Orig. Electrotechnol. HISTELCON 2012 - Conf. Proc. (2012) 1–6. https://doi.org/10.1109/HISTELCON.2012.6487583.
[27] Y. Nishi, The development of lithium ion secondary batteries, Chem. Rec. 1 (2001) 406–413. https://doi.org/10.1002/tcr.1024.
[28] International Energy Agency (IEA), Global EV Outlook 2020, Paris, 2020. https://doi.org/10.1787/d394399e-en.
[29] L. Noel, G. Zarazua de Rubens, B.K. Sovacool, J. Kester, Fear and loathing of electric vehicles: The reactionary rhetoric of range anxiety, Energy Res. Soc. Sci. 48 (2019) 96–107. https://doi.org/10.1016/j.erss.2018.10.001.
[30] X. Shi, J. Pan, H. Wang, H. Cai, Battery Electric Vehicles: What is the Minimum Range Required?, Energy. 166 (2018) 352–358. https://doi.org/10.1016/j.energy.2018.10.056.
[31] W. Feng, M. Figliozzi, An economic and technological analysis of the key factors affecting the competitiveness of electric commercial vehicles: A case study from the USA market, Transp. Res. Part C Emerg. Technol. 26 (2013) 135–145. https://doi.org/10.1016/j.trc.2012.06.007.
[32] Zap-Map, EV Charging Stats 2021, (n.d.). https://www.zap-map.com/statistics/ (accessed July 20, 2021).
[33] Electric Vehicle Database, (n.d.). https://ev-database.org/ (accessed July 20, 2021).
[34] J.A. Sanguesa, V. Torres-Sanz, P. Garrido, F.J. Martinez, J.M. Marquez-Barja, A Review on Electric Vehicles: Technologies and Challenges, Smart Cities. 4 (2021) 372–404. https://doi.org/10.3390/smartcities4010022.
[35] A. Pruteanu, B.V. Florean, G.M. Moraru, R.C. Ciobanu, Development of a thermal simulation and testing model for a superior lithium-ion-polymer battery, Proc. Int. Conf. Optim. Electr.

Electron. Equipment, OPTIM. (2012) 947–952. https://doi.org/10.1109/OPTIM.2012.6231870.
[36] S. Arora, Selection of thermal management system for modular battery packs of electric vehicles: A review of existing and emerging technologies, J. Power Sources. 400 (2018) 621–640. https://doi.org/10.1016/j.jpowsour.2018.08.020.
[37] S. Ma, M. Jiang, P. Tao, C. Song, J. Wu, J. Wang, T. Deng, W. Shang, Temperature effect and thermal impact in lithium-ion batteries: A review, Prog. Nat. Sci. Mater. Int. 28 (2018) 653–666. https://doi.org/10.1016/j.pnsc.2018.11.002.
[38] C.-K. Huang, J.S. Sakamoto, J. Wolfenstine, S. Surampudi, The Limits of Low-Temperature Performance of Li-Ion Cells, J. Electrochem. Soc. 147 (2000) 2893. https://doi.org/10.1149/1.1393622.
[39] Y. Ji, C.Y. Wang, Heating strategies for Li-ion batteries operated from subzero temperatures, Electrochim. Acta. 107 (2013) 664–674. https://doi.org/10.1016/j.electacta.2013.03.147.
[40] J. Jaguemont, L. Boulon, Y. Dubé, A comprehensive review of lithium-ion batteries used in hybrid and electric vehicles at cold temperatures, Appl. Energy. 164 (2016) 99–114. https://doi.org/10.1016/j.apenergy.2015.11.034.
[41] E.. Polzin, I. Bloom, J.. Sohn, C. Motloch, B.. Cole, S.. Jones, T. Unkelhaeuser, R. Richardson, G.. Henriksen, V.. Battaglia, H.. Case, D. Ingersoll, An accelerated calendar and cycle life study of Li-ion cells, J. Power Sources. 101 (2002) 238–247. https://doi.org/10.1016/s0378-7753(01)00783-2.
[42] M. Kassem, J. Bernard, R. Revel, S. Pélissier, F. Duclaud, C. Delacourt, Calendar aging of a graphite/LiFePO 4 cell, J. Power Sources. 208 (2012) 296–305. https://doi.org/10.1016/j.jpowsour.2012.02.068.
[43] J. Shim, K.A. Striebel, Characterization of high-power lithium-ion cells during constant current cycling: Part I. Cycle performance and electrochemical diagnostics, J. Power Sources. 122 (2003) 188–194. https://doi.org/10.1016/S0378-7753(03)00351-3.
[44] M.C. Niculuţă, C. Veje, Analysis of the thermal behavior of a LiFePO4 battery cell, J. Phys. Conf. Ser. 395 (2012). https://doi.org/10.1088/1742-6596/395/1/012013.
[45] T.M. Bandhauer, S. Garimella, T.F. Fuller, A Critical Review of Thermal Issues in Lithium-Ion Batteries, J. Electrochem. Soc. 158 (2011) R1. https://doi.org/10.1149/1.3515880.
[46] X. Feng, M. Ouyang, X. Liu, L. Lu, Y. Xia, X. He, Thermal runaway mechanism of lithium ion battery for electric vehicles: A review, Energy Storage Mater. 10 (2018) 246–267. https://doi.org/10.1016/j.ensm.2017.05.013.
[47] Q. Wang, B. Jiang, B. Li, Y. Yan, A critical review of thermal management models and solutions of lithium-ion batteries for the development of pure electric vehicles, Renew. Sustain. Energy Rev. 64 (2016) 106–128. https://doi.org/10.1016/j.rser.2016.05.033.
[48] B. Smith, Chevrolet Volt Battery Incident Overview Report, 2012.
[49] J. Tübke, K. Pinkwart, C.E. Hendricks, D.A. Fuentevilla, H. Doering, V. Liebau, X. Feng, M. Ouyang, L. Lu, L. Hollmotz, J. Vogt, Li-Secondary Battery: Damage Control, in: Electrochem. Power Sources Fundam. Syst. Appl. Li-Battery Saf., Elsevier, 2019: pp. 507–629. https://doi.org/10.1016/B978-0-444-63777-2.00012-8.
[50] Q. Wang, P. Ping, X. Zhao, G. Chu, J. Sun, C. Chen, Thermal runaway caused fire and explosion of lithium ion battery, J. Power Sources. 208 (2012) 210–224. https://doi.org/10.1016/j.jpowsour.2012.02.038.
[51] V. Linja-aho, Hybrid and Electric Vehicle Fires in Finland 2015-2019, Int. Conf. Fires Veh. 2020. (2020).
[52] G.P. Beauregard, Report of investigation: Hybrids plus plug in hybrid electric vehicle, 2008.
[53] J. Cen, Z. Li, F. Jiang, Experimental investigation on using the electric vehicle air conditioning system for lithium-ion battery thermal management, Energy Sustain. Dev. 45 (2018) 88–95. https://doi.org/10.1016/j.esd.2018.05.005.
[54] G. Xia, L. Cao, G. Bi, A review on battery thermal management in electric vehicle application, J. Power Sources. 367 (2017) 90–105. https://doi.org/10.1016/j.jpowsour.2017.09.046.
[55] T. Yuksel, S. Litster, V. Viswanathan, J.J. Michalek, Plug-in hybrid electric vehicle LiFePO4battery life implications of thermal management, driving conditions, and regional climate, J. Power Sources. 338 (2017) 49–64. https://doi.org/10.1016/j.jpowsour.2016.10.104.
[56] A.A.H. Akinlabi, D. Solyali, Configuration, design, and optimization of air-cooled battery

thermal management system for electric vehicles: A review, Renew. Sustain. Energy Rev. 125 (2020) 109815. https://doi.org/10.1016/j.rser.2020.109815.
[57] A.A. Pesaran, Battery thermal models for hybrid vehicle simulations, J. Power Sources. 110 (2002) 377–382. https://doi.org/10.1097/01253086-199216010-00008.
[58] M. Zolot, A.A. Pesaran, M. Mihalic, Thermal Evaluation of Toyota Prius Battery Pack, SAE Int. (2002).
[59] P. Nelson, D. Dees, K. Amine, G. Henriksen, Modeling thermal management of lithium-ion PNGV batteries, J. Power Sources. 110 (2002) 349–356. https://doi.org/10.1016/S0378-7753(02)00197-0.
[60] D.Y. Jung, B.H. Lee, S.W. Kim, Development of battery management system for nickel-metal hydride batteries in electric vehicle applications, J. Power Sources. 109 (2002) 1–10. https://doi.org/10.1016/S0378-7753(02)00020-4.
[61] R. Sabbah, R. Kizilel, J.R. Selman, S. Al-Hallaj, Active (air-cooled) vs. passive (phase change material) thermal management of high power lithium-ion packs: Limitation of temperature rise and uniformity of temperature distribution, J. Power Sources. 182 (2008) 630–638. https://doi.org/10.1016/j.jpowsour.2008.03.082.
[62] M. Mousavi, S. Hoque, S. Rahnamayan, I. Dincer, G.F. Naterer, Optimal design of an air-cooling system for a Li-Ion battery pack in Electric Vehicles with a genetic algorithm, 2011 IEEE Congr. Evol. Comput. CEC 2011. (2011) 1848–1855. https://doi.org/10.1109/CEC.2011.5949840.
[63] H. Teng, Y. Ma, K. Yeow, M. Thelliez, An Analysis of a Lithium-ion Battery System with Indirect Air Cooling and Warm-Up, SAE Int. J. Passeng. Cars - Mech. Syst. 4 (2011) 2011-01–2249. https://doi.org/10.4271/2011-01-2249.
[64] R. Mahamud, C. Park, Reciprocating air flow for Li-ion battery thermal management to improve temperature uniformity, J. Power Sources. 196 (2011) 5685–5696. https://doi.org/10.1016/j.jpowsour.2011.02.076.
[65] I.L. Krüger, D. Limperich, G. Schmitz, Energy Consumption Of Battery Cooling In Hybrid Electric Vehicles, Int. Refrig. Air Cond. Conf. (2012).
[66] M.R. Giuliano, A.K. Prasad, S.G. Advani, Experimental study of an air-cooled thermal management system for high capacity lithium-titanate batteries, J. Power Sources. 216 (2012) 345–352. https://doi.org/10.1016/j.jpowsour.2012.05.074.
[67] X. Hu, S. Asgari, S. Lin, S. Stanton, W. Lian, A linear parameter-varying model for HEV/EV battery thermal modeling, 2012 IEEE Energy Convers. Congr. Expo. ECCE 2012. (2012) 1643–1649. https://doi.org/10.1109/ECCE.2012.6342616.
[68] G.. Karimi, X. Li, Thermal management of lithium-ion batteries for electric vehicles, Int. J. Energy Res. 37 (2013) 13–24. https://doi.org/10.1002/er.
[69] X.M. Xu, R. He, Research on the heat dissipation performance of battery pack based on forced air cooling, J. Power Sources. 240 (2013) 33–41. https://doi.org/10.1016/j.jpowsour.2013.03.004.
[70] H. Park, A design of air flow configuration for cooling lithium ion battery in hybrid electric vehicles, J. Power Sources. 239 (2013) 30–36. https://doi.org/10.1016/j.jpowsour.2013.03.102.
[71] Z. Li, J. Zhang, B. Wu, J. Huang, Z. Nie, Y. Sun, F. An, N. Wu, Examining temporal and spatial variations of internal temperature in large-format laminated battery with embedded thermocouples, J. Power Sources. 241 (2013) 536–553. https://doi.org/10.1016/j.jpowsour.2013.04.117.
[72] X. Li, F. He, L. Ma, Thermal management of cylindrical batteries investigated using wind tunnel testing and computational fluid dynamics simulation, J. Power Sources. 238 (2013) 395–402. https://doi.org/10.1016/j.jpowsour.2013.04.073.
[73] L. Fan, J.M. Khodadadi, A.A. Pesaran, A parametric study on thermal management of an air-cooled lithium-ion battery module for plug-in hybrid electric vehicles, J. Power Sources. 238 (2013) 301–312. https://doi.org/10.1016/j.jpowsour.2013.03.050.
[74] C. Zhu, X. Li, L. Song, L.X. School, Development of a theoretically based thermal model for lithium ion battery pack, J. Power Sources. 223 (2013) 155–164. https://doi.org/10.1016/j.jpowsour.2012.09.035.
[75] Y.S. Choi, D.M. Kang, Prediction of thermal behaviors of an air-cooled lithium-ion battery

system for hybrid electric vehicles, J. Power Sources. 270 (2014) 273–280. https://doi.org/10.1016/j.jpowsour.2014.07.120.
[76] P. Kritzer, H. Döring, B. Emermacher, Improved Safety for Automotive Lithium Batteries : An Innovative Approach to include an Emergency Cooling Element, Adv. Chem. Eng. Sci. (2014) 197–207. https://doi.org/10.4236/aces.2014.42023.
[77] T. Wang, K.J. Tseng, J. Zhao, Z. Wei, Thermal investigation of lithium-ion battery module with different cell arrangement structures and forced air-cooling strategies, Appl. Energy. 134 (2014) 229–238. https://doi.org/10.1016/j.apenergy.2014.08.013.
[78] H. Sun, R. Dixon, Development of cooling strategy for an air cooled lithium-ion battery pack, J. Power Sources. 272 (2014) 404–414. https://doi.org/10.1016/j.jpowsour.2014.08.107.
[79] B. Severino, F. Gana, R. Palma-Behnke, P.A. Estévez, W.R. Calderón-Muñoz, M.E. Orchard, J. Reyes, M. Cortés, Multi-objective optimal design of lithium-ion battery packs based on evolutionary algorithms, J. Power Sources. 267 (2014) 288–299. https://doi.org/10.1016/j.jpowsour.2014.05.088.
[80] F. He, X. Li, L. Ma, Combined experimental and numerical study of thermal management of battery module consisting of multiple Li-ion cells, Int. J. Heat Mass Transf. 72 (2014) 622–629. https://doi.org/10.1016/j.ijheatmasstransfer.2014.01.038.
[81] R. Liu, J. Chen, J. Xun, K. Jiao, Q. Du, Numerical investigation of thermal behaviors in lithium-ion battery stack discharge, Appl. Energy. 132 (2014) 288–297. https://doi.org/10.1016/j.apenergy.2014.07.024.
[82] N. Yang, X. Zhang, G. Li, D. Hua, Assessment of the forced air-cooling performance for cylindrical lithium-ion battery packs: A comparative analysis between aligned and staggered cell arrangements, Appl. Therm. Eng. 80 (2015) 55–65. https://doi.org/10.1016/j.applthermaleng.2015.01.049.
[83] T. Wang, K.J. Tseng, J. Zhao, Development of efficient air-cooling strategies for lithium-ion battery module based on empirical heat source model, Appl. Therm. Eng. 90 (2015) 521–529. https://doi.org/10.1016/j.applthermaleng.2015.07.033.
[84] F. He, H. Wang, L. Ma, Experimental demonstration of active thermal control of a battery module consisting of multiple Li-ion cells, Int. J. Heat Mass Transf. 91 (2015) 630–639. https://doi.org/10.1016/j.ijheatmasstransfer.2015.07.069.
[85] J. Zhao, Z. Rao, Y. Huo, X. Liu, Y. Li, Thermal management of cylindrical power battery module for extending the life of new energy electric vehicles, Appl. Therm. Eng. 85 (2015) 33–43. https://doi.org/10.1016/j.applthermaleng.2015.04.012.
[86] S.K. Mohammadian, Y. Zhang, Thermal management optimization of an air-cooled Li-ion battery module using pin-fin heat sinks for hybrid electric vehicles, J. Power Sources. 273 (2015) 431–439. https://doi.org/10.1016/j.jpowsour.2014.09.110.
[87] F. He, L. Ma, Thermal management of batteries employing active temperature control and reciprocating cooling flow, Int. J. Heat Mass Transf. 83 (2015) 164–172. https://doi.org/10.1016/j.ijheatmasstransfer.2014.11.079.
[88] Z. Ling, F. Wang, X. Fang, X. Gao, Z. Zhang, A hybrid thermal management system for lithium ion batteries combining phase change materials with forced-air cooling, Appl. Energy. 148 (2015) 403–409. https://doi.org/10.1016/j.apenergy.2015.03.080.
[89] H. Wang, F. He, L. Ma, Experimental and modeling study of controller-based thermal management of battery modules under dynamic loads, Int. J. Heat Mass Transf. 103 (2016) 154–164. https://doi.org/10.1016/j.ijheatmasstransfer.2016.07.041.
[90] W. Tong, K. Somasundaram, E. Birgersson, A.S. Mujumdar, C. Yap, Thermo-electrochemical model for forced convection air cooling of a lithium-ion battery module, Appl. Therm. Eng. 99 (2016) 672–682. https://doi.org/10.1016/j.applthermaleng.2016.01.050.
[91] L.H. Saw, Y. Ye, A.A.O. Tay, W.T. Chong, S.H. Kuan, M.C. Yew, Computational fluid dynamic and thermal analysis of Lithium-ion battery pack with air cooling, Appl. Energy. 177 (2016) 783–792. https://doi.org/10.1016/j.apenergy.2016.05.122.
[92] K. Chen, S. Wang, M. Song, L. Chen, Configuration optimization of battery pack in parallel air-cooled battery thermal management system using an optimization strategy, Appl. Therm. Eng. 123 (2017) 177–186. https://doi.org/10.1016/j.applthermaleng.2017.05.060.
[93] A. De Vita, A. Maheshwari, M. Destro, M. Santarelli, M. Carello, Transient thermal analysis of

a lithium-ion battery pack comparing different cooling solutions for automotive applications, Appl. Energy. 206 (2017) 101–112. https://doi.org/10.1016/j.apenergy.2017.08.184.

[94] K. Chen, S. Wang, M. Song, L. Chen, Structure optimization of parallel air-cooled battery thermal management system, Int. J. Heat Mass Transf. 111 (2017) 943–952. https://doi.org/10.1016/j.ijheatmasstransfer.2017.04.026.

[95] J. Xie, Z. Ge, M. Zang, S. Wang, Structural optimization of lithium-ion battery pack with forced air cooling system, Appl. Therm. Eng. 126 (2017) 583–593. https://doi.org/10.1016/j.applthermaleng.2017.07.143.

[96] W. Situ, G. Zhang, X. Li, X. Yang, C. Wei, M. Rao, Z. Wang, C. Wang, W. Wu, A thermal management system for rectangular LiFePO4battery module using novel double copper mesh-enhanced phase change material plates, Energy. 141 (2017) 613–623. https://doi.org/10.1016/j.energy.2017.09.083.

[97] S. Hong, X. Zhang, K. Chen, S. Wang, Design of flow configuration for parallel air-cooled battery thermal management system with secondary vent, Int. J. Heat Mass Transf. 116 (2018) 1204–1212. https://doi.org/10.1016/j.ijheatmasstransfer.2017.09.092.

[98] R.D. Jilte, R. Kumar, L. Ma, Thermal performance of a novel confined flow Li-ion battery module, Appl. Therm. Eng. 146 (2019) 1–11. https://doi.org/10.1016/j.applthermaleng.2018.09.099.

[99] H. Zhou, F. Zhou, L. Xu, J. Kong, QingxinYang, Thermal performance of cylindrical Lithium-ion battery thermal management system based on air distribution pipe, Int. J. Heat Mass Transf. 131 (2019) 984–998. https://doi.org/10.1016/j.ijheatmasstransfer.2018.11.116.

[100] T. Han, B. Khalighi, E.C. Yen, S. Kaushik, Li-ion battery pack thermal management: Liquid versus air cooling, J. Therm. Sci. Eng. Appl. 11 (2019). https://doi.org/10.1115/1.4041595.

[101] L. Cheng, A. Garg, A.K. Jishnu, L. Gao, Surrogate based multi-objective design optimization of lithium-ion battery air-cooled system in electric vehicles, J. Energy Storage. 31 (2020) 101645. https://doi.org/10.1016/j.est.2020.101645.

[102] K. Chen, Y. Chen, Y. She, M. Song, S. Wang, L. Chen, Construction of effective symmetrical air-cooled system for battery thermal management, Appl. Therm. Eng. 166 (2020) 114679. https://doi.org/10.1016/j.applthermaleng.2019.114679.

[103] Y. Wang, Y. Yu, Z. Jing, C. Wang, G. Zhou, W. Zhao, Thermal performance of lithium-ion batteries applying forced air cooling with an improved aluminium foam heat sink design, Int. J. Heat Mass Transf. 167 (2021). https://doi.org/10.1016/j.ijheatmasstransfer.2020.120827.

[104] F. Zhang, A. Lin, P. Wang, P. Liu, Optimization design of a parallel air-cooled battery thermal management system with spoilers, Appl. Therm. Eng. 182 (2021) 116062. https://doi.org/10.1016/j.applthermaleng.2020.116062.

[105] K. Kirad, M. Chaudhari, Design of cell spacing in lithium-ion battery module for improvement in cooling performance of the battery thermal management system, J. Power Sources. 481 (2021) 229016. https://doi.org/10.1016/j.jpowsour.2020.229016.

[106] J. Zhang, X. Wu, K. Chen, D. Zhou, M. Song, Experimental and numerical studies on an efficient transient heat transfer model for air-cooled battery thermal management systems, J. Power Sources. 490 (2021) 229539. https://doi.org/10.1016/j.jpowsour.2021.229539.

[107] H. Teng, K. Yeow, Design of Direct and Indirect Liquid Cooling Systems for High- Capacity, High-Power Lithium-Ion Battery Packs, SAE Int. J. Altern. Powertrains. 1 (2012) 2012-01–2017. https://doi.org/10.4271/2012-01-2017.

[108] L.H. Saw, A.A.O. Tay, L.W. Zhang, Thermal management of lithium-ion battery pack with liquid cooling, Annu. IEEE Semicond. Therm. Meas. Manag. Symp. 2015-April (2015) 298–302. https://doi.org/10.1109/SEMI-THERM.2015.7100176.

[109] X.H. Yang, S.C. Tan, J. Liu, Thermal management of Li-ion battery with liquid metal, Energy Convers. Manag. 117 (2016) 577–585. https://doi.org/10.1016/j.enconman.2016.03.054.

[110] D.R. Pendergast, E.P. Demauro, M. Fletcher, E. Stimson, J.C. Mollendorf, A rechargeable lithium-ion battery module for underwater use, J. Power Sources. 196 (2011) 793–800. https://doi.org/10.1016/j.jpowsour.2010.06.071.

[111] A. Jarrett, I.Y. Kim, Design optimization of electric vehicle battery cooling plates for thermal performance, J. Power Sources. 196 (2011) 10359–10368. https://doi.org/10.1016/j.jpowsour.2011.06.090.

[112] R. Parrish, K. Elankumaran, M. Gandhi, B. Nance, P. Meehan, D. Milburn, S. Siddiqui, A. Brenz, Voltec Battery Design and Manufacturing, SAE Int. (2011). https://doi.org/10.4271/2011-01-1360.
[113] J. Xun, R. Liu, K. Jiao, Numerical and analytical modeling of lithium ion battery thermal behaviors with different cooling designs, J. Power Sources. 233 (2013) 47–61. https://doi.org/10.1016/j.jpowsour.2013.01.095.
[114] L.W. Jin, P.S. Lee, X.X. Kong, Y. Fan, S.K. Chou, Ultra-thin minichannel LCP for EV battery thermal management, Appl. Energy. 113 (2014) 1786–1794. https://doi.org/10.1016/j.apenergy.2013.07.013.
[115] H.S. Hamut, I. Dincer, G.F. Naterer, Analysis and optimization of hybrid electric vehicle thermal management systems, J. Power Sources. 247 (2014) 643–654. https://doi.org/10.1007/978-3-319-07977-6_3.
[116] K. Chen, X. Li, Accurate determination of battery discharge characteristics - A comparison between two battery temperature control methods, J. Power Sources. 247 (2014) 961–966. https://doi.org/10.1016/j.jpowsour.2013.09.060.
[117] S.K. Mohammadian, Y.L. He, Y. Zhang, Internal cooling of a lithium-ion battery using electrolyte as coolant through microchannels embedded inside the electrodes, J. Power Sources. 293 (2015) 458–466. https://doi.org/10.1016/j.jpowsour.2015.05.055.
[118] Y. Huo, Z. Rao, The numerical investigation of nanofluid based cylinder battery thermal management using lattice Boltzmann method, Int. J. Heat Mass Transf. 91 (2015) 374–384. https://doi.org/10.1016/j.ijheatmasstransfer.2015.07.128.
[119] Y. Huo, Z. Rao, X. Liu, J. Zhao, Investigation of power battery thermal management by using mini-channel cold plate, Energy Convers. Manag. 89 (2015) 387–395. https://doi.org/10.1016/j.enconman.2014.10.015.
[120] S. Panchal, I. Dincer, M. Agelin-Chaab, R. Fraser, M. Fowler, Thermal modeling and validation of temperature distributions in a prismatic lithium-ion battery at different discharge rates and varying boundary conditions, Appl. Therm. Eng. 96 (2016) 190–199. https://doi.org/10.1016/j.applthermaleng.2015.11.019.
[121] S. Basu, K.S. Hariharan, S.M. Kolake, T. Song, D.K. Sohn, T. Yeo, Coupled electrochemical thermal modelling of a novel Li-ion battery pack thermal management system, Appl. Energy. 181 (2016) 1–13. https://doi.org/10.1016/j.apenergy.2016.08.049.
[122] S. Panchal, I. Dincer, M. Agelin-Chaab, R. Fraser, M. Fowler, Experimental and theoretical investigation of temperature distributions in a prismatic lithium-ion battery, Int. J. Therm. Sci. 99 (2016) 204–212. https://doi.org/10.1016/j.ijthermalsci.2015.08.016.
[123] J. Smith, M. Hinterberger, C. Schneider, J. Koehler, Energy savings and increased electric vehicle range through improved battery thermal management, Appl. Therm. Eng. 101 (2016) 647–656. https://doi.org/10.1016/j.applthermaleng.2015.12.034.
[124] C. Lan, J. Xu, Y. Qiao, Y. Ma, Thermal management for high power lithium-ion battery by minichannel aluminum tubes, Appl. Therm. Eng. 101 (2016) 284–292. https://doi.org/10.1016/j.applthermaleng.2016.02.070.
[125] Z. Qian, Y. Li, Z. Rao, Thermal performance of lithium-ion battery thermal management system by using mini-channel cooling, Energy Convers. Manag. 126 (2016) 622–631. https://doi.org/10.1016/j.enconman.2016.08.063.
[126] Z. Rao, Q. Wang, C. Huang, Investigation of the thermal performance of phase change material/mini-channel coupled battery thermal management system, Appl. Energy. 164 (2016) 659–669. https://doi.org/10.1016/j.apenergy.2015.12.021.
[127] T. Zhang, Q. Gao, G. Wang, Y. Gu, Y. Wang, W. Bao, D. Zhang, Investigation on the promotion of temperature uniformity for the designed battery pack with liquid flow in cooling process, Appl. Therm. Eng. 116 (2017) 655–662. https://doi.org/10.1016/j.applthermaleng.2017.01.069.
[128] Z. Rao, Z. Qian, Y. Kuang, Y. Li, Thermal performance of liquid cooling based thermal management system for cylindrical lithium-ion battery module with variable contact surface, Appl. Therm. Eng. 123 (2017) 1514–1522. https://doi.org/10.1016/j.applthermaleng.2017.06.059.
[129] J. Xu, C. Lan, Y. Qiao, Y. Ma, Prevent thermal runaway of lithium-ion batteries with minichannel cooling, Appl. Therm. Eng. 110 (2017) 883–890.

https://doi.org/10.1016/j.applthermaleng.2016.08.151.
[130] F. Bahiraei, A. Fartaj, G.A. Nazri, Electrochemical-thermal Modeling to Evaluate Active Thermal Management of a Lithium-ion Battery Module, Electrochim. Acta. 254 (2017) 59–71. https://doi.org/10.1016/j.electacta.2017.09.084.
[131] B. Mondal, C.F. Lopez, P.P. Mukherjee, Exploring the efficacy of nanofluids for lithium-ion battery thermal management, Int. J. Heat Mass Transf. 112 (2017) 779–794. https://doi.org/10.1016/j.ijheatmasstransfer.2017.04.130.
[132] L. Ramotar, G.L. Rohrauer, R. Filion, K. MacDonald, Experimental verification of a thermal equivalent circuit dynamic model on an extended range electric vehicle battery pack, J. Power Sources. 343 (2017) 383–394. https://doi.org/10.1016/j.jpowsour.2017.01.040.
[133] Z. Tian, W. Gan, X. Zhang, B. Gu, L. Yang, Investigation on an integrated thermal management system with battery cooling and motor waste heat recovery for electric vehicle, Appl. Therm. Eng. 136 (2018) 16–27. https://doi.org/10.1016/j.applthermaleng.2018.02.093.
[134] C. Zhao, W. Cao, T. Dong, F. Jiang, Thermal behavior study of discharging/charging cylindrical lithium-ion battery module cooled by channeled liquid flow, Int. J. Heat Mass Transf. 120 (2018) 751–762. https://doi.org/10.1016/j.ijheatmasstransfer.2017.12.083.
[135] E. Jiaqiang, D. Han, A. Qiu, H. Zhu, Y. Deng, J. Chen, X. Zhao, W. Zuo, H. Wang, J. Chen, Q. Peng, Orthogonal experimental design of liquid-cooling structure on the cooling effect of a liquid-cooled battery thermal management system, Appl. Therm. Eng. 132 (2018) 508–520. https://doi.org/10.1016/j.applthermaleng.2017.12.115.
[136] L.H. Saw, H.M. Poon, H.S. Thiam, Z. Cai, W.T. Chong, N.A. Pambudi, Y.J. King, Novel thermal management system using mist cooling for lithium-ion battery packs, Appl. Energy. 223 (2018) 146–158. https://doi.org/10.1016/j.apenergy.2018.04.042.
[137] G. Titov, M. Santacesaria, J. Winkler, M. Zima, A. Khawaja, J. Lustbader, M. Govindarajalu, S. Chowdhury, J. Rugh, L. Leitzel, Total Thermal Management of Battery Electric Vehicles (BEVs), SAE Tech. Pap. Ser. 1 (2018) 1–7. https://doi.org/10.4271/2018-37-0026.
[138] S. Park, D.S. Jang, D.C. Lee, S.H. Hong, Y. Kim, Simulation on cooling performance characteristics of a refrigerant-cooled active thermal management system for lithium ion batteries, Int. J. Heat Mass Transf. 135 (2019) 131–141. https://doi.org/10.1016/j.ijheatmasstransfer.2019.01.109.
[139] C. Zhao, A.C.M. Sousa, F. Jiang, Minimization of thermal non-uniformity in lithium-ion battery pack cooled by channeled liquid flow, Int. J. Heat Mass Transf. 129 (2019) 660–670. https://doi.org/10.1016/j.ijheatmasstransfer.2018.10.017.
[140] S. Panchal, M. Haji Akhoundzadehr, K. Raahemifar, M. Fowler, R. Fraser, Heat and mass transfer modeling and investigation of multiple LiFePO4/graphite batteries in a pack at low C-rates with water-cooling, Int. J. Heat Mass Transf. 135 (2019) 368–377. https://doi.org/10.1016/j.ijheatmasstransfer.2019.01.076.
[141] Y. Chung, M.S. Kim, Thermal analysis and pack level design of battery thermal management system with liquid cooling for electric vehicles, Energy Convers. Manag. 196 (2019) 105–116. https://doi.org/10.1016/j.enconman.2019.05.083.
[142] S.H. Hong, D.S. Jang, S. Park, S. Yun, Y. Kim, Thermal performance of direct two-phase refrigerant cooling for lithium-ion batteries in electric vehicles, Appl. Therm. Eng. 173 (2020) 115213. https://doi.org/10.1016/j.applthermaleng.2020.115213.
[143] M. Shen, Q. Gao, Structure design and effect analysis on refrigerant cooling enhancement of battery thermal management system for electric vehicles, J. Energy Storage. 32 (2020) 101940. https://doi.org/10.1016/j.est.2020.101940.
[144] S. Wiriyasart, C. Hommalee, S. Sirikasemsuk, R. Prurapark, P. Naphon, Thermal management system with nanofluids for electric vehicle battery cooling modules, Case Stud. Therm. Eng. 18 (2020) 100583. https://doi.org/10.1016/j.csite.2020.100583.
[145] K. Monika, C. Chakraborty, S. Roy, S. Dinda, S.A. Singh, S.P. Datta, An improved mini-channel based liquid cooling strategy of prismatic LiFePO4 batteries for electric or hybrid vehicles, J. Energy Storage. 35 (2021) 102301. https://doi.org/10.1016/j.est.2021.102301.
[146] M. Akbarzadeh, J. Jaguemont, T. Kalogiannis, D. Karimi, J. He, L. Jin, P. Xie, J. Van Mierlo, M. Berecibar, A novel liquid cooling plate concept for thermal management of lithium-ion batteries in electric vehicles, Energy Convers. Manag. 231 (2021) 113862.

https://doi.org/10.1016/j.enconman.2021.113862.
[147] X. Tang, Q. Guo, M. Li, C. Wei, Z. Pan, Y. Wang, Performance analysis on liquid-cooled battery thermal management for electric vehicles based on machine learning, J. Power Sources. 494 (2021) 229727. https://doi.org/10.1016/j.jpowsour.2021.229727.
[148] W.Q. Li, Z.G. Qu, Y.L. He, Y.B. Tao, Experimental study of a passive thermal management system for high-powered lithium ion batteries using porous metal foam saturated with phase change materials, J. Power Sources. 255 (2014) 9–15. https://doi.org/10.1016/j.jpowsour.2014.01.006.
[149] J. Jaguemont, N. Omar, P. Van den Bossche, J. Mierlo, Phase-change materials (PCM) for automotive applications: A review, Appl. Therm. Eng. 132 (2018) 308–320. https://doi.org/10.1016/j.applthermaleng.2017.12.097.
[150] X. Zhang, C. Liu, Z. Rao, Experimental investigation on thermal management performance of electric vehicle power battery using composite phase change material, J. Clean. Prod. 201 (2018) 916–924. https://doi.org/10.1016/j.jclepro.2018.08.076.
[151] A. Hussain, I.H. Abidi, C.Y. Tso, K.C. Chan, Z. Luo, C.Y.H. Chao, Thermal management of lithium ion batteries using graphene coated nickel foam saturated with phase change materials, Int. J. Therm. Sci. 124 (2018) 23–35. https://doi.org/10.1016/j.ijthermalsci.2017.09.019.
[152] S. Al-Hallaj, J.R. Selman, Thermal modeling of secondary lithium batteries for electric vehicle/hybrid electric vehicle applications, J. Power Sources. 110 (2002) 341–348. https://doi.org/10.1016/S0378-7753(02)00196-9.
[153] S.A. Khateeb, M.M. Farid, J.R. Selman, S. Al-Hallaj, Design and simulation of a lithium-ion battery with a phase change material thermal management system for an electric scooter, J. Power Sources. 128 (2004) 292–307. https://doi.org/10.1016/j.jpowsour.2003.09.070.
[154] S.A. Khateeb, S. Amiruddin, M. Farid, J.R. Selman, S. Al-Hallaj, Thermal management of Li-ion battery with phase change material for electric scooters: Experimental validation, J. Power Sources. 142 (2005) 345–353. https://doi.org/10.1016/j.jpowsour.2004.09.033.
[155] R. Kizilel, A. Lateef, R. Sabbah, M.M. Farid, J.R. Selman, S. Al-Hallaj, Passive control of temperature excursion and uniformity in high-energy Li-ion battery packs at high current and ambient temperature, J. Power Sources. 183 (2008) 370–375. https://doi.org/10.1016/j.jpowsour.2008.04.050.
[156] R. Kizilel, R. Sabbah, J.R. Selman, S. Al-Hallaj, An alternative cooling system to enhance the safety of Li-ion battery packs, J. Power Sources. 194 (2009) 1105–1112. https://doi.org/10.1016/j.jpowsour.2009.06.074.
[157] X. Duan, G.F. Naterer, Heat transfer in phase change materials for thermal management of electric vehicle battery modules, Int. J. Heat Mass Transf. 53 (2010) 5176–5182. https://doi.org/10.1016/j.ijheatmasstransfer.2010.07.044.
[158] Z. Rao, S. Wang, G. Zhang, Simulation and experiment of thermal energy management with phase change material for ageing LiFePO4 power battery, Energy Convers. Manag. 52 (2011) 3408–3414. https://doi.org/10.1016/j.enconman.2011.07.009.
[159] Z. Ling, J. Chen, X. Fang, Z. Zhang, T. Xu, X. Gao, S. Wang, Experimental and numerical investigation of the application of phase change materials in a simulative power batteries thermal management system, Appl. Energy. 121 (2014) 104–113. https://doi.org/10.1016/j.apenergy.2014.01.075.
[160] N. Javani, I. Dincer, G.F. Naterer, B.S. Yilbas, Heat transfer and thermal management with PCMs in a Li-ion battery cell for electric vehicles, Int. J. Heat Mass Transf. 72 (2014) 690–703. https://doi.org/10.1016/j.ijheatmasstransfer.2013.12.076.
[161] Z.G. Qu, W.Q. Li, W.Q. Tao, Numerical model of the passive thermal management system for high-power lithium ion battery by using porous metal foam saturated with phase change material, Int. J. Hydrogen Energy. 39 (2014) 3904–3913. https://doi.org/10.1016/j.ijhydene.2013.12.136.
[162] N. Javani, I. Dincer, G.F. Naterer, New latent heat storage system with nanoparticles for thermal management of electric vehicles, J. Power Sources. 268 (2014) 718–727. https://doi.org/10.1016/j.jpowsour.2014.06.107.
[163] Z. Wang, Z. Zhang, L. Jia, L. Yang, Paraffin and paraffin/aluminum foam composite phase change material heat storage experimental study based on thermal management of Li-ion battery,

Appl. Therm. Eng. 78 (2015) 428–436. https://doi.org/10.1016/j.applthermaleng.2015.01.009.
[164] B. Schweitzer, S. Wilke, S. Khateeb, S. Al-Hallaj, Experimental validation of a 0-D numerical model for phase change thermal management systems in lithium-ion batteries, J. Power Sources. 287 (2015) 211–219. https://doi.org/10.1016/j.jpowsour.2015.04.016.
[165] A. Greco, X. Jiang, D. Cao, An investigation of lithium-ion battery thermal management using paraffin/porous-graphite-matrix composite, J. Power Sources. 278 (2015) 50–68. https://doi.org/10.1016/j.jpowsour.2014.12.027.
[166] Z. Rao, Y. Huo, X. Liu, G. Zhang, Experimental investigation of battery thermal management system for electric vehicle based on paraffin/copper foam, J. Energy Inst. 88 (2015) 241–246. https://doi.org/10.1016/j.joei.2014.09.006.
[167] C. Lin, S. Xu, G. Chang, J. Liu, Experiment and simulation of a LiFePO4 battery pack with a passive thermal management system using composite phase change material and graphite sheets, J. Power Sources. 275 (2015) 742–749. https://doi.org/10.1016/j.jpowsour.2014.11.068.
[168] J.T. Zhao, Z.H. Rao, C.Z. Liu, Y.M. Li, Experiment study of oscillating heat pipe and phase change materials coupled for thermal energy storage and thermal management, Int. J. Heat Mass Transf. 99 (2016) 252–260. https://doi.org/10.1016/j.ijheatmasstransfer.2016.03.108.
[169] Q. Wang, Z. Rao, Y. Huo, S. Wang, Thermal performance of phase change material/oscillating heat pipe-based battery thermal management system, Int. J. Therm. Sci. 102 (2016) 9–16. https://doi.org/10.1016/j.ijthermalsci.2015.11.005.
[170] A. Hussain, C.Y. Tso, C.Y.H. Chao, Experimental investigation of a passive thermal management system for high-powered lithium ion batteries using nickel foam-paraffin composite, Energy. 115 (2016) 209–218. https://doi.org/10.1016/j.energy.2016.09.008.
[171] W. Wu, X. Yang, G. Zhang, X. Ke, Z. Wang, W. Situ, X. Li, J. Zhang, An experimental study of thermal management system using copper mesh-enhanced composite phase change materials for power battery pack, Energy. 113 (2016) 909–916. https://doi.org/10.1016/j.energy.2016.07.119.
[172] N.O. Moraga, J.P. Xamán, R.H. Araya, Cooling Li-ion batteries of racing solar car by using multiple phase change materials, Appl. Therm. Eng. 108 (2016) 1041–1054. https://doi.org/10.1016/j.applthermaleng.2016.07.183.
[173] G. Jiang, J. Huang, Y. Fu, M. Cao, M. Liu, Thermal optimization of composite phase change material/expanded graphite for Li-ion battery thermal management, Appl. Therm. Eng. 108 (2016) 1119–1125. https://doi.org/10.1016/j.applthermaleng.2016.07.197.
[174] J. Yan, Q. Wang, K. Li, J. Sun, Numerical study on the thermal performance of a composite board in battery thermal management system, Appl. Therm. Eng. 106 (2016) 131–140. https://doi.org/10.1016/j.applthermaleng.2016.05.187.
[175] W. Wu, W. Wu, S. Wang, Thermal optimization of composite PCM based large-format lithium-ion battery modules under extreme operating conditions, Energy Convers. Manag. 153 (2017) 22–33. https://doi.org/10.1016/j.enconman.2017.09.068.
[176] Z. Wang, H. Zhang, X. Xia, Experimental investigation on the thermal behavior of cylindrical battery with composite paraffin and fin structure, Int. J. Heat Mass Transf. 109 (2017) 958–970. https://doi.org/10.1016/j.ijheatmasstransfer.2017.02.057.
[177] B. Mortazavi, H. Yang, F. Mohebbi, G. Cuniberti, T. Rabczuk, Graphene or h-BN paraffin composite structures for the thermal management of Li-ion batteries: A multiscale investigation, Appl. Energy. 202 (2017) 323–334. https://doi.org/10.1016/j.apenergy.2017.05.175.
[178] J. Zhao, P. Lv, Z. Rao, Experimental study on the thermal management performance of phase change material coupled with heat pipe for cylindrical power battery pack, Exp. Therm. Fluid Sci. 82 (2017) 182–188. https://doi.org/10.1016/j.expthermflusci.2016.11.017.
[179] Q. Huang, X. Li, G. Zhang, J. Zhang, F. He, Y. Li, Experimental investigation of the thermal performance of heat pipe assisted phase change material for battery thermal management system, Appl. Therm. Eng. 141 (2018) 1092–1100. https://doi.org/10.1016/j.applthermaleng.2018.06.048.
[180] S. Arora, A. Kapoor, W. Shen, A novel thermal management system for improving discharge/charge performance of Li-ion battery packs under abuse, J. Power Sources. 378 (2018) 759–775. https://doi.org/10.1016/j.jpowsour.2017.12.030.
[181] Z. Ling, X. Wen, Z. Zhang, X. Fang, X. Gao, Thermal management performance of phase

change materials with different thermal conductivities for Li-ion battery packs operated at low temperatures, Energy. 144 (2018) 977–983. https://doi.org/10.1016/j.energy.2017.12.098.
[182] Y. Lv, G. Liu, G. Zhang, X. Yang, A novel thermal management structure using serpentine phase change material coupled with forced air convection for cylindrical battery modules, J. Power Sources. 468 (2020) 228398. https://doi.org/10.1016/j.jpowsour.2020.228398.
[183] S. Landini, R. Waser, A. Stamatiou, R. Ravotti, J. Worlitschek, T.S. O'Donovan, Passive cooling of Li-Ion cells with direct-metal-laser-sintered aluminium heat exchangers filled with phase change materials, Appl. Therm. Eng. 173 (2020) 115238. https://doi.org/10.1016/j.applthermaleng.2020.115238.
[184] X. Wu, Z. Zhu, H. Zhang, S. Xu, Y. Fang, Z. Yan, Structural optimization of light-weight battery module based on hybrid liquid cooling with high latent heat PCM, Int. J. Heat Mass Transf. 163 (2020) 120495. https://doi.org/10.1016/j.ijheatmasstransfer.2020.120495.
[185] F. Chen, R. Huang, C. Wang, X. Yu, H. Liu, Q. Wu, K. Qian, R. Bhagat, Air and PCM cooling for battery thermal management considering battery cycle life, Appl. Therm. Eng. 173 (2020) 115154. https://doi.org/10.1016/j.applthermaleng.2020.115154.
[186] M.M. Heyhat, S. Mousavi, M. Siavashi, Battery thermal management with thermal energy storage composites of PCM, metal foam, fin and nanoparticle, J. Energy Storage. 28 (2020) 101235. https://doi.org/10.1016/j.est.2020.101235.
[187] M. Safdari, R. Ahmadi, S. Sadeghzadeh, Numerical investigation on PCM encapsulation shape used in the passive-active battery thermal management, Energy. 193 (2020) 116840. https://doi.org/10.1016/j.energy.2019.116840.
[188] M. Suresh Patil, J.H. Seo, M.Y. Lee, A novel dielectric fluid immersion cooling technology for Li-ion battery thermal management, Energy Convers. Manag. 229 (2021) 113715. https://doi.org/10.1016/j.enconman.2020.113715.
[189] H. Liu, S. Ahmad, Y. Shi, J. Zhao, A parametric study of a hybrid battery thermal management system that couples PCM/copper foam composite with helical liquid channel cooling, Energy. 231 (2021) 120869. https://doi.org/10.1016/j.energy.2021.120869.
[190] S. Landini, W. Delgado-Diaz, R. Ravotti, R. Waser, A. Stamatiou, J. Worlitschek, T.S. O'Donovan, Effect of geometry and thermal mass of Direct-Metal-Laser-Sintered aluminium Heat Exchangers filled with phase change materials on Lithium-Ion cells' passive cooling, Appl. Therm. Eng. 195 (2021) 117151. https://doi.org/10.1016/j.applthermaleng.2021.117151.
[191] K. Vontas, M. Andredaki, A. Georgoulas, N. Miché, M. Marengo, The effect of surface wettability on flow boiling characteristics within microchannels, Int. J. Heat Mass Transf. 172 (2021) 121133. https://doi.org/10.1016/j.ijheatmasstransfer.2021.121133.
[192] R. Van Gils, M. Speetjens, H. Nijmeijer, Boiling Heat Transfer in Battery Electric Vehicles, Proc. EEVC. (2011) 1–12. http://purl.tue.nl/695476559315605.pdf.
[193] V.K. Dhir, BOILING HEAT TRANSFER, Annu. Rev. Fluid Mech. 30 (1998) 365–401.
[194] A.K. Thakur, R. Prabakaran, M.R. Elkadeem, S.W. Sharshir, M. Arıcı, C. Wang, W. Zhao, J.Y. Hwang, R. Saidur, A state of art review and future viewpoint on advance cooling techniques for Lithium–ion battery system of electric vehicles, J. Energy Storage. 32 (2020) 101771. https://doi.org/10.1016/j.est.2020.101771.
[195] Y. Ren, Z. Yu, G. Song, Thermal management of a Li-ion battery pack employing water evaporation, J. Power Sources. 360 (2017) 166–171. https://doi.org/10.1016/j.jpowsour.2017.05.116.
[196] Z. An, L. Jia, X. Li, Y. Ding, Experimental investigation on lithium-ion battery thermal management based on flow boiling in mini-channel, Appl. Therm. Eng. 117 (2017) 534–543. https://doi.org/10.1016/j.applthermaleng.2017.02.053.
[197] R. Zhao, S. Zhang, J. Gu, J. Liu, S. Carkner, E. Lanoue, An experimental study of lithium ion battery thermal management using flexible hydrogel films, J. Power Sources. 255 (2014) 29–36. https://doi.org/10.1016/j.jpowsour.2013.12.138.
[198] S. Zhang, R. Zhao, J. Liu, J. Gu, Investigation on a hydrogel based passive thermal management system for lithium ion batteries, Energy. 68 (2014) 854–861. https://doi.org/10.1016/j.energy.2014.03.012.
[199] R. Zhao, J. Liu, J. Gu, Simulation and experimental study on lithium ion battery short circuit, Appl. Energy. 173 (2016) 29–39. https://doi.org/10.1016/j.apenergy.2016.04.016.

[200] M. Al-Zareer, I. Dincer, M.A. Rosen, Novel thermal management system using boiling cooling for high-powered lithium-ion battery packs for hybrid electric vehicles, J. Power Sources. 363 (2017) 291–303. https://doi.org/10.1016/j.jpowsour.2017.07.067.
[201] M. Al-Zareer, I. Dincer, M.A. Rosen, A novel phase change based cooling system for prismatic lithium ion batteries, Int. J. Refrig. 86 (2018) 203–217. https://doi.org/10.1016/j.ijrefrig.2017.12.005.
[202] M. Al-Zareer, I. Dincer, M.A. Rosen, Development and analysis of a new tube based cylindrical battery cooling system with liquid to vapor phase change, Int. J. Refrig. 108 (2019) 163–173. https://doi.org/10.1016/j.ijrefrig.2019.08.027.
[203] Y.F. Wang, J.T. Wu, Thermal performance predictions for an HFE-7000 direct flow boiling cooled battery thermal management system for electric vehicles, Energy Convers. Manag. 207 (2020) 112569. https://doi.org/10.1016/j.enconman.2020.112569.
[204] R. Zhao, J. Liu, J. Gu, L. Zhai, F. Ma, Experimental study of a direct evaporative cooling approach for Li-ion battery thermal management, Int. J. Energy Res. 44 (2020) 6660–6673. https://doi.org/10.1002/er.5402.
[205] V.S. Devahdhanush, S. Lee, I. Mudawar, Consolidated theoretical/empirical predictive method for subcooled flow boiling in annuli with reference to thermal management of ultra-fast electric vehicle charging cables, Int. J. Heat Mass Transf. 175 (2021) 121224. https://doi.org/10.1016/j.ijheatmasstransfer.2021.121224.
[206] Y. Fang, W. Yang, D. Xu, L. Hu, L. Su, Y. Huang, Experimental investigation on flow boiling characteristics of R1233zd(E) in a parallel mini-channel heat sink for the application in battery thermal management, Int. J. Heat Mass Transf. 178 (2021) 121591. https://doi.org/10.1016/j.ijheatmasstransfer.2021.121591.
[207] W. Wu, S. Wang, W. Wu, K. Chen, S. Hong, Y. Lai, A critical review of battery thermal performance and liquid based battery thermal management, Energy Convers. Manag. 182 (2019) 262–281. https://doi.org/10.1016/j.enconman.2018.12.051.
[208] M. Bernagozzi, S. Charmer, A. Georgoulas, I. Malavasi, N. Michè, M. Marengo, Lumped parameter network simulation of a Loop Heat Pipe for energy management systems in full electric vehicles, Appl. Therm. Eng. 141 (2018) 617–629. https://doi.org/10.1016/j.applthermaleng.2018.06.013.
[209] M. Mameli, M. Marengo, S. Khandekar, Local heat transfer measurement and thermo-fluid characterization of a pulsating heat pipe, Int. J. Therm. Sci. 75 (2014) 140–152. https://doi.org/10.1016/j.ijthermalsci.2013.07.025.
[210] D. Mangini, M. Pozzoni, M. Mameli, L. Pietrasanta, M. Bernagozzi, D. Fioriti, N. Miché, L. Araneo, S. Filippeschi, M. Marengo, Infrared analysis and pressure measurements on a single loop pulsating heat pipe at different gravity levels, Jt. 19th IHPC 13th IHPS. (2018) 1–10.
[211] S. Khandekar, A.P. Gautam, P.K. Sharma, Multiple quasi-steady states in a closed loop pulsating heat pipe, Int. J. Therm. Sci. 48 (2009) 535–546. https://doi.org/10.1016/j.ijthermalsci.2008.04.004.
[212] C. Feng, M.J. Gibbons, M. Marengo, S. Chandra, A novel ultra-large flat plate heat pipe manufactured by thermal spray, Appl. Therm. Eng. 171 (2020) 115030. https://doi.org/10.1016/j.applthermaleng.2020.115030.
[213] M.R. Shaeri, D. Attinger, R.W. Bonner, Vapor chambers with hydrophobic and biphilic evaporators in moderate to high heat flux applications, Appl. Therm. Eng. 130 (2018) 83–92. https://doi.org/10.1016/j.applthermaleng.2017.11.051.
[214] M.S. Wu, K.H. Liu, Y.Y. Wang, C.C. Wan, Heat dissipation design for lithium-ion batteries, J. Power Sources. 109 (2002) 160–166. https://doi.org/10.1016/S0378-7753(02)00048-4.
[215] J.-C. Jang, S. Rhi, Battery Thermal Management System of Future Electric Vehicles with Loop Thermosyphon, US-Korea Conf. Sci. Technol. Entrep. 110 (2010) 2.
[216] Z. Rao, S. Wang, M. Wu, Z. Lin, F. Li, Experimental investigation on thermal management of electric vehicle battery with heat pipe, Energy Convers. Manag. 65 (2013) 92–97. https://doi.org/10.1016/j.enconman.2012.08.014.
[217] G. Burban, V. Ayel, A. Alexandre, P. Lagonotte, Y. Bertin, C. Romestant, Experimental investigation of a pulsating heat pipe for hybrid vehicle applications, in: Appl. Therm. Eng., 2013: pp. 94–103. https://doi.org/10.1016/j.applthermaleng.2012.05.037.

[218] A. Greco, D. Cao, X. Jiang, H. Yang, A theoretical and computational study of lithium-ion battery thermal management for electric vehicles using heat pipes, J. Power Sources. 257 (2014) 344–355. https://doi.org/10.1016/j.jpowsour.2014.02.004.
[219] Q. Wang, B. Jiang, Q.F. Xue, H.L. Sun, B. Li, H.M. Zou, Y.Y. Yan, Experimental investigation on EV battery cooling and heating by heat pipes, Appl. Therm. Eng. 88 (2014) 54–60. https://doi.org/10.1016/j.applthermaleng.2014.09.083.
[220] T.-H. Tran, S. Harmand, B. Sahut, Experimental investigation on heat pipe cooling for Hybrid Electric Vehicle and Electric Vehicle lithium-ion battery, J. Power Sources. 265 (2014) 262–272. https://doi.org/10.1016/j.jpowsour.2014.04.130.
[221] T.H. Tran, S. Harmand, B. Desmet, S. Filangi, Experimental investigation on the feasibility of heat pipe cooling for HEV/EV lithium-ion battery, Appl. Therm. Eng. 63 (2014) 551–558. https://doi.org/10.1016/j.applthermaleng.2013.11.048.
[222] Z. Rao, Y. Huo, X. Liu, Experimental study of an OHP-cooled thermal management system for electric vehicle power battery, Exp. Therm. Fluid Sci. 57 (2014) 20–26. https://doi.org/10.1016/j.expthermflusci.2014.03.017.
[223] R. Zhao, J. Gu, J. Liu, An experimental study of heat pipe thermal management system with wet cooling method for lithium ion batteries, J. Power Sources. 273 (2015) 1089–1097. https://doi.org/10.1016/j.jpowsour.2014.10.007.
[224] Y. Ye, L.H. Saw, Y. Shi, A.A.O. Tay, Numerical analyses on optimizing a heat pipe thermal management system for lithium-ion batteries during fast charging, Appl. Therm. Eng. 86 (2015) 281–291. https://doi.org/10.1016/j.applthermaleng.2015.04.066.
[225] V. Manno, S. Filippeschi, M. Mameli, C. Romestant, V. Ayel, Y. Bertin, THERMAL-HYDRAULIC CHARACTERIZATION OF A FLAT PLATE PULSATING HEAT PIPE FOR AUTOMOTIVE APPLICATIONS, Interfacial Phenom. Heat Transf. 3 (2015) 413–425. https://doi.org/10.1615/InterfacPhenomHeatTransfer.2016013273.
[226] S. Hong, X. Zhang, S. Wang, Z. Zhang, Experiment study on heat transfer capability of an innovative gravity assisted ultra-thin looped heat pipe, Int. J. Therm. Sci. 95 (2015) 106–114. https://doi.org/10.1016/j.ijthermalsci.2015.04.003.
[227] N. Putra, B. Ariantara, R.A. Pamungkas, Experimental investigation on performance of lithium-ion battery thermal management system using flat plate loop heat pipe for electric vehicle application, Appl. Therm. Eng. 99 (2016) 784–789. https://doi.org/10.1016/j.applthermaleng.2016.01.123.
[228] Y. Ye, Y. Shi, L.H. Saw, A.A.O. Tay, Performance assessment and optimization of a heat pipe thermal management system for fast charging lithium ion battery packs, Int. J. Heat Mass Transf. 92 (2016) 893–903. https://doi.org/10.1016/j.ijheatmasstransfer.2015.09.052.
[229] K. Shah, C. McKee, D. Chalise, A. Jain, Experimental and numerical investigation of core cooling of Li-ion cells using heat pipes, Energy. 113 (2016) 852–860. https://doi.org/10.1016/j.energy.2016.07.076.
[230] F. Liu, F. Lan, J. Chen, Dynamic thermal characteristics of heat pipe via segmented thermal resistance model for electric vehicle battery cooling, J. Power Sources. 321 (2016) 57–70. https://doi.org/10.1016/j.jpowsour.2016.04.108.
[231] H. Zou, W. Wang, G. Zhang, F. Qin, C. Tian, Y. Yan, Experimental investigation on an integrated thermal management system with heat pipe heat exchanger for electric vehicle, Energy Convers. Manag. 118 (2016) 88–95. https://doi.org/10.1016/j.enconman.2016.03.066.
[232] W. Yuan, Z. Yan, Z. Tan, W. Chen, Y. Tang, Heat-pipe-based thermal management and temperature characteristics of Li-ion batteries, Can. J. Chem. Eng. 94 (2016) 1901–1908. https://doi.org/10.1002/cjce.22566.
[233] D. Worwood, Q. Kellner, M. Wojtala, W.D. Widanage, R. McGlen, D. Greenwood, J. Marco, A new approach to the internal thermal management of cylindrical battery cells for automotive applications, J. Power Sources. 346 (2017) 151–166. https://doi.org/10.1016/j.jpowsour.2017.02.023.
[234] J. Liang, Y. Gan, Y. Li, Investigation on the thermal performance of a battery thermal management system using heat pipe under different ambient temperatures, Energy Convers. Manag. 155 (2018) 1–9. https://doi.org/10.1016/j.enconman.2017.10.063.
[235] J. Qu, C. Wang, X. Li, H. Wang, Heat transfer performance of flexible oscillating heat pipes for

electric/hybrid-electric vehicle battery thermal management, Appl. Therm. Eng. 135 (2018) 1–9. https://doi.org/10.1016/j.applthermaleng.2018.02.045.
[236] X. Ye, Y. Zhao, Z. Quan, Experimental study on heat dissipation for lithium-ion battery based on micro heat pipe array (MHPA), Appl. Therm. Eng. 130 (2018) 74–82. https://doi.org/10.1016/j.applthermaleng.2017.10.141.
[237] R.G. Chi, W.S. Chung, S.H. Rhi, Thermal characteristics of an oscillating heat pipe cooling system for electric vehicle Li-ion batteries, Energies. 11 (2018). https://doi.org/10.3390/en11030655.
[238] J. Smith, R. Singh, M. Hinterberger, M. Mochizuki, Battery thermal management system for electric vehicle using heat pipes, Int. J. Therm. Sci. 134 (2018) 517–529. https://doi.org/10.1016/j.ijthermalsci.2018.08.022.
[239] L. Feng, S. Zhou, Q. Zhao, K. Yan, Y. Li, Y. Wang, G. Wang, C. Luo, Experimental investigation of thermal and strain management for lithium-ion battery pack in heat pipe cooling, J. Energy Storage. 16 (2018) 84–92. https://doi.org/10.1016/j.est.2018.01.001.
[240] J. Gou, W. Liu, Feasibility study on a novel 3D vapor chamber used for Li-ion battery thermal management system of electric vehicle, Appl. Therm. Eng. 152 (2019) 362–369. https://doi.org/10.1016/j.applthermaleng.2019.02.034.
[241] J. Wang, Y. Gan, J. Liang, M. Tan, Y. Li, Sensitivity analysis of factors influencing a heat pipe-based thermal management system for a battery module with cylindrical cells, Appl. Therm. Eng. 151 (2019) 475–485. https://doi.org/10.1016/J.APPLTHERMALENG.2019.02.036.
[242] D. Dan, C. Yao, Y. Zhang, H. Zhang, Z. Zeng, X. Xu, Dynamic thermal behavior of micro heat pipe array-air cooling battery thermal management system based on thermal network model, Appl. Therm. Eng. 162 (2019) 114183. https://doi.org/10.1016/j.applthermaleng.2019.114183.
[243] J. Liang, Y. Gan, Y. Li, M. Tan, J. Wang, Thermal and electrochemical performance of a serially connected battery module using a heat pipe-based thermal management system under different coolant temperatures, Energy. 189 (2019) 116233. https://doi.org/10.1016/j.energy.2019.116233.
[244] Y. Liu, T. Jiang, Y. Zheng, J. Tian, Z. Ma, Multi-scale multi-field coupled analysis of power battery pack based on Heat Pipe Cooling, Processes. 7 (2019). https://doi.org/10.3390/pr7100696.
[245] R.G. Chi, S.H. Rhi, Oscillating heat pipe cooling system of electric vehicle's Li-ion batteries with direct contact bottom cooling mode, Energies. 12 (2019) 1–14. https://doi.org/10.3390/en12091698.
[246] J. Gou, W. Liu, Y. Luo, The thermal performance of a novel internal cooling method for the electric vehicle battery: An experimental study, Appl. Therm. Eng. 161 (2019) 114102. https://doi.org/10.1016/j.applthermaleng.2019.114102.
[247] A. Wei, J. Qu, H. Qiu, C. Wang, G. Cao, Heat transfer characteristics of plug-in oscillating heat pipe with binary-fluid mixtures for electric vehicle battery thermal management, Int. J. Heat Mass Transf. 135 (2019) 746–760. https://doi.org/10.1016/j.ijheatmasstransfer.2019.02.021.
[248] S. Deng, K. Li, C. Wu, P. Wang, M. Yu, B. Li, J. Zheng, Heat Pipe Thermal Management Based on High-Rate Discharge and Pulse Cycle Tests for Lithium-Ion Batteries, Energies. 12 (2019).
[249] N. Putra, A.F. Sandi, B. Ariantara, N. Abdullah, T.M. Indra Mahlia, Performance of beeswax phase change material (PCM) and heat pipe as passive battery cooling system for electric vehicles, Case Stud. Therm. Eng. 21 (2020) 100655. https://doi.org/10.1016/j.csite.2020.100655.
[250] H. Zhou, C. Dai, Y. Liu, X. Fu, Y. Du, Experimental investigation of battery thermal management and safety with heat pipe and immersion phase change liquid, J. Power Sources. 473 (2020) 228545. https://doi.org/10.1016/j.jpowsour.2020.228545.
[251] Y. Gan, J. Wang, J. Liang, Z. Huang, M. Hu, Development of thermal equivalent circuit model of heat pipe-based thermal management system for a battery module with cylindrical cells, Appl. Therm. Eng. 164 (2020) 114523. https://doi.org/10.1016/j.applthermaleng.2019.114523.
[252] W. Zhang, J. Qiu, X. Yin, D. Wang, A novel heat pipe assisted separation type battery thermal management system based on phase change material, Appl. Therm. Eng. 165 (2020) 114571. https://doi.org/10.1016/j.applthermaleng.2019.114571.
[253] H. Behi, D. Karimi, M. Behi, J. Jaguemont, M. Ghanbarpour, M. Behnia, M. Berecibar, J. Van

Mierlo, Thermal management analysis using heat pipe in the high current discharging of lithium-ion battery in electric vehicles, J. Energy Storage. 32 (2020) 101893. https://doi.org/10.1016/j.est.2020.101893.
[254] M. Bernagozzi, A. Georgoulas, N. Miché, C. Rouaud, M. Marengo, A Novel Loop Heat Pipe Based Cooling System for Battery Packs in Electric Vehicles, in: 2020 IEEE Transp. Electrif. Conf. Expo, IEEE, Chicago, IL, USA, 2020: pp. 251–256. https://doi.org/10.1109/ITEC48692.2020.9161607.
[255] X. Yuan, A. Tang, C. Shan, Z. Liu, J. Li, Experimental investigation on thermal performance of a battery liquid cooling structure coupled with heat pipe, J. Energy Storage. 32 (2020) 101984. https://doi.org/10.1016/j.est.2020.101984.
[256] H. Jouhara, N. Serey, N. Khordehgah, R. Bennett, S. Almahmoud, S.P. Lester, Investigation, development and experimental analyses of a heat pipe based battery thermal management system, Int. J. Thermofluids. 1–2 (2020) 100004. https://doi.org/10.1016/j.ijft.2019.100004.
[257] S. Lei, Y. Shi, G. Chen, Heat-pipe based spray-cooling thermal management system for lithium-ion battery: Experimental study and optimization, Int. J. Heat Mass Transf. 163 (2020) 120494. https://doi.org/10.1016/j.ijheatmasstransfer.2020.120494.
[258] M. Chen, J. Li, Nanofluid-based pulsating heat pipe for thermal management of lithium-ion batteries for electric vehicles, J. Energy Storage. 32 (2020) 101715. https://doi.org/10.1016/j.est.2020.101715.
[259] H. Behi, D. Karimi, M. Behi, M. Ghanbarpour, J. Jaguemont, M.A. Sokkeh, F.H. Gandoman, M. Berecibar, J. Van Mierlo, A new concept of thermal management system in Li-ion battery using air cooling and heat pipe for electric vehicles, Appl. Therm. Eng. 174 (2020) 115280. https://doi.org/10.1016/j.applthermaleng.2020.115280.
[260] C. Yao, D. Dan, Y. Zhang, Y. Wang, Y. Qian, Y. Yan, W. Zhuge, Thermal Performance of a Micro Heat Pipe Array for Battery Thermal Management Under Special Vehicle-Operating Conditions, Automot. Innov. 3 (2020) 317–327. https://doi.org/10.1007/s42154-020-00114-0.
[261] T. Wei, X. Xiaoming, D. Hua, G. Yaohua, L. Jicheng, W. Hongchao, Sensitivity Analysis of the Battery Thermal Management System with a Reciprocating Cooling Strategy Combined with a Flat Heat Pipe, ACS Omega. 5 (2020) 8258–8267. https://doi.org/10.1021/acsomega.0c00552.
[262] C. Zhang, Z. Xia, B. Wang, H. Gao, S. Chen, S. Zong, K. Luo, A Li-ion battery thermal management system combining a heat pipe and thermoelectric cooler, Energies. 13 (2020). https://doi.org/10.3390/en13040841.
[263] J. Huang, S. Shoai Naini, R. Miller, D. Rizzo, K. Sebeck, S. Shurin, J. Wagner, Development of a heat pipe–based battery thermal management system for hybrid electric vehicles, Proc. Inst. Mech. Eng. Part D J. Automob. Eng. 234 (2020) 1532–1543. https://doi.org/10.1177/0954407019899588.
[264] J. Kleiner, R. Singh, M. Schmid, L. Komsiyska, G. Elger, C. Endisch, Influence of heat pipe assisted terminal cooling on the thermal behavior of a large prismatic lithium-ion cell during fast charging in electric vehicles, Appl. Therm. Eng. 188 (2021) 116328. https://doi.org/10.1016/j.applthermaleng.2020.116328.
[265] Z. Liang, R. Wang, A.H. Malt, M. Souri, M.N. Esfahani, M. Jabbari, Systematic evaluation of a flat-heat-pipe-based thermal management: Cell-to-cell variations and battery ageing, Appl. Therm. Eng. 192 (2021) 116934. https://doi.org/10.1016/j.applthermaleng.2021.116934.
[266] M. Yao, Y. Gan, J. Liang, D. Dong, L. Ma, J. Liu, Q. Luo, Y. Li, Performance simulation of a heat pipe and refrigerant-based lithium-ion battery thermal management system coupled with electric vehicle air-conditioning, Appl. Therm. Eng. 191 (2021). https://doi.org/10.1016/j.applthermaleng.2021.116878.
[267] K. Chen, J. Hou, M. Song, S. Wang, W. Wu, Y. Zhang, Design of battery thermal management system based on phase change material and heat pipe, Appl. Therm. Eng. 188 (2021) 116665. https://doi.org/10.1016/j.applthermaleng.2021.116665.
[268] A. Alihosseini, M. Shafaee, Experimental study and numerical simulation of a Lithium-ion battery thermal management system using a heat pipe, J. Energy Storage. 39 (2021) 102616. https://doi.org/10.1016/j.est.2021.102616.
[269] S. Abbas, Z. Ramadan, C.W. Park, Thermal performance analysis of compact-type simulative battery module with paraffin as phase-change material and flat plate heat pipe, Int. J. Heat Mass

Transf. 173 (2021) 121269. https://doi.org/10.1016/j.ijheatmasstransfer.2021.121269.
[270] J. E, F. Yi, W. Li, B. Zhang, H. Zuo, K. Wei, J. Chen, H. Zhu, H. Zhu, Y. Deng, Effect analysis on heat dissipation performance enhancement of a lithium-ion-battery pack with heat pipe for central and southern regions in China, Energy. 226 (2021) 120336. https://doi.org/10.1016/j.energy.2021.120336.
[271] M. Bernagozzi, A. Georgoulas, N. Miché, C. Rouaud, M. Marengo, Novel battery thermal management system for electric vehicles with a loop heat pipe and graphite sheet inserts, Appl. Therm. Eng. 194 (2021). https://doi.org/10.1016/j.applthermaleng.2021.117061.
[272] Q.L. Yue, C.X. He, H.R. Jiang, M.C. Wu, T.S. Zhao, A hybrid battery thermal management system for electric vehicles under dynamic working conditions, Int. J. Heat Mass Transf. 164 (2021). https://doi.org/10.1016/j.ijheatmasstransfer.2020.120528.
[273] H. Behi, M. Behi, D. Karimi, J. Jaguemont, M. Ghanbarpour, M. Behnia, M. Berecibar, J. Van Mierlo, Heat pipe air-cooled thermal management system for lithium-ion batteries: High power applications, Appl. Therm. Eng. 183 (2021) 116240. https://doi.org/10.1016/j.applthermaleng.2020.116240.
[274] Y. Li, H. Guo, F. Qi, Z. Guo, M. Li, L. Bertling Tjernberg, Investigation on liquid cold plate thermal management system with heat pipes for LiFePO4 battery pack in electric vehicles, Appl. Therm. Eng. 185 (2021) 116382. https://doi.org/10.1016/j.applthermaleng.2020.116382.
[275] H. Mbulu, Y. Laoonual, S. Wongwises, Experimental study on the thermal performance of a battery thermal management system using heat pipes, Case Stud. Therm. Eng. 26 (2021) 101029. https://doi.org/10.1016/j.csite.2021.101029.
[276] L. Liang, Y. Zhao, Y. Diao, R. Ren, H. Jing, Inclined U-shaped flat microheat pipe array configuration for cooling and heating lithium-ion battery modules in electric vehicles, Energy. 235 (2021) 121433. https://doi.org/10.1016/j.energy.2021.121433.
[277] M. Panahi, H.R. Heydari, G. Karimi, Effects of micro heat pipe arrays on thermal management performance enhancement of cylindrical lithium-ion battery cells, Int. J. Energy Res. 45 (2021) 11245–11257. https://doi.org/10.1002/er.6604.
[278] H. Jouhara, B. Delpech, R. Bennett, A. Chauhan, N. Khordehgah, N. Serey, S.P. Lester, Heat Pipe Based Battery Thermal Management: Evaluating the potential of two novel battery pack integrations, Int. J. Thermofluids. 12 (2021) 100115. https://doi.org/10.1016/j.ijft.2021.100115.
[279] H. Behi, D. Karimi, F.H. Gandoman, M. Akbarzadeh, S. Khaleghi, T. Kalogiannis, M.S. Hosen, J. Jaguemont, J. Van Mierlo, M. Berecibar, PCM assisted heat pipe cooling system for the thermal management of an LTO cell for high-current profiles, Case Stud. Therm. Eng. 25 (2021) 100920. https://doi.org/10.1016/j.csite.2021.100920.
[280] D. Karimi, M.S. Hosen, H. Behi, S. Khaleghi, M. Akbarzadeh, J. Van Mierlo, M. Berecibar, A hybrid thermal management system for high power lithium-ion capacitors combining heat pipe with phase change materials, Heliyon. 7 (2021) e07773. https://doi.org/10.1016/j.heliyon.2021.e07773.
[281] M. Chen, J. Li, Experimental study on heating performance of pure electric vehicle power battery under low temperature environment, Int. J. Heat Mass Transf. 172 (2021) 121191. https://doi.org/10.1016/j.ijheatmasstransfer.2021.121191.
[282] M. Wafirulhadi, T. Trisnadewi, N. Putra, Thermal Management System Based on Phase Change Material (PCM) and Heat Pipe in Lithium-ion Electric Vehicle Batteries, J. Adv. Res. Exp. Fluid Mech. Heat Transf. 3 (2021) 26–35.
[283] W. Zhang, Z. Liang, W. Wu, G. Ling, R. Ma, Design and optimization of a hybrid battery thermal management system for electric vehicle based on surrogate model, Int. J. Heat Mass Transf. 174 (2021) 121318. https://doi.org/10.1016/j.ijheatmasstransfer.2021.121318.
[284] Z. Zhou, Y. Lv, J. Qu, Q. Sun, D. Grachev, Performance evaluation of hybrid oscillating heat pipe with carbon nanotube nanofluids for electric vehicle battery cooling, Appl. Therm. Eng. 196 (2021) 117300. https://doi.org/10.1016/j.applthermaleng.2021.117300.
[285] M. Bernagozzi, N. Miché, A. Georgoulas, C. Rouaud, M. Marengo, Performance of an Environmentally Friendly Alternative Fluid in a Loop Heat Pipe-Based Battery Thermal Management System, Energies. 14 (2021) 7738. https://doi.org/https://doi.org/10.3390/en14227738.
[286] X. Li, Z. Zhong, J. Luo, Z. Wang, W. Yuan, G. Zhang, C. Yang, C. Yang, Experimental

Investigation on a Thermoelectric Cooler for Thermal Management of a Lithium-Ion Battery Module, Int. J. Photoenergy. 2019 (2019). https://doi.org/10.1155/2019/3725364.
[287] C. Alaoui, Z.M. Salameh, A Novel Thermal Management for Electric and Hybrid Vehicles, IEEE Trans. Veh. Technol. 54 (2005) 468–476. https://doi.org/10.1201/9781420075359.
[288] Y. Lyu, A.R.M. Siddique, S.H. Majid, M. Biglarbegian, S.A. Gadsden, S. Mahmud, Electric vehicle battery thermal management system with thermoelectric cooling, Energy Reports. 5 (2019) 822–827. https://doi.org/10.1016/j.egyr.2019.06.016.
[289] I.S. Suh, H. Cho, M. Lee, Feasibility study on thermoelectric device to energy storage system of an electric vehicle, Energy. 76 (2014) 436–444. https://doi.org/10.1016/j.energy.2014.08.040.
[290] M. De Gennaro, E. Paffumi, G. Martini, U. Manfredi, H. Scholz, H. Lacher, H. Kuehnelt, D. Simic, Experimental Investigation of the Energy Efficiency of an Electric Vehicle in Different Driving Conditions, SAE Tech. Pap. (2014). https://doi.org/10.4271/2014-01-1817.
[291] Heat-Pump Cabin Heater, (n.d.). https://www.nissan-global.com/EN/TECHNOLOGY/OVERVIEW/heat_pump_cabin_heater.html (accessed July 22, 2021).
[292] A. Tomaszewska, Z. Chu, X. Feng, S. O'Kane, X. Liu, J. Chen, C. Ji, E. Endler, R. Li, L. Liu, Y. Li, S. Zheng, S. Vetterlein, M. Gao, J. Du, M. Parkes, M. Ouyang, M. Marinescu, G. Offer, B. Wu, Lithium-ion battery fast charging: A review, ETransportation. 1 (2019) 100011. https://doi.org/10.1016/j.etran.2019.100011.
[293] M.S. Kumar, S.T. Revankar, Development scheme and key technology of an electric vehicle: An overview, Renew. Sustain. Energy Rev. 70 (2017) 1266–1285. https://doi.org/10.1016/j.rser.2016.12.027.
[294] N. Putra, B. Ariantara, Electric motor thermal management system using L-shaped flat heat pipes, Appl. Therm. Eng. 126 (2017) 1156–1163. https://doi.org/10.1016/j.applthermaleng.2017.01.090.
[295] H. Chen, H. Mo, Z. Wan, S. Huang, X. Wang, H. Zhu, Thermal performance of a boiling and condensation enhanced heat transfer tube—stepped lattice finned tube, Appl. Therm. Eng. 173 (2020) 115227. https://doi.org/10.1016/j.applthermaleng.2020.115227.
[296] F.P. Incropera, D.P. DeWitt, T.L. Bergman, A.S. Lavine, Fundamentals of Heat and Mass Transfer, Sitxh Edit, John Wiley & Sons, 2007. https://doi.org/10.1109/TKDE.2004.30.
[297] Z. Rao, S. Wang, A review of power battery thermal energy management, Renew. Sustain. Energy Rev. 15 (2011) 4554–4571. https://doi.org/10.1016/j.rser.2011.07.096.
[298] J. Jaguemont, J. Van Mierlo, A comprehensive review of future thermal management systems for battery-electrified vehicles, J. Energy Storage. 31 (2020) 101551. https://doi.org/10.1016/j.est.2020.101551.
[299] Y.F. Maydanik, Loop heat pipes, Appl. Therm. Eng. 25 (2005) 635–657. https://doi.org/10.1016/j.applthermaleng.2004.07.010.
[300] A. Ambirajan, A. Adoni, J.S. Vaidya, A. a. Rajendran, D. Kumar, P. Dutta, Loop Heat Pipes: A Review of Fundamentals, Operation,and Design, Heat Transf. Eng. 33 (2012) 387–405. https://doi.org/10.1080/01457632.2012.614148.
[301] F. Pagnoni, V. Ayel, Y. Bertin, J. Coullox, M. Zebian, Loop Heat Pipe for thermal management of aircraft engine equipment, J. Thermophys. Heat Transf. 35 (2021). https://doi.org/https://doi.org/10.2514/1.T6049.
[302] T.T. Hoang, J. Ku, HEAT AND MASS TRANSFER IN LOOP HEAT PIPES, in: Proc. 2003 ASME Summer Heat Transf. Conf., 2003: pp. 1–9.
[303] J. Ku, Loop Heat Pipe Start-up Behaviors, in: 18th Work. Thermophys. Microgravity, El Segundo, California, 2014.
[304] J. Ku, Operating Characteristics of Loop Heat Pipes, in: 29 Th Int. Conf. Environ. Syst., Denver, 1999: p. 16. https://doi.org/10.4271/1999-01-2007.
[305] S. Launay, V. Sartre, J. Bonjour, Parametric analysis of loop heat pipe operation: a literature review, Int. J. Therm. Sci. 46 (2007) 621–636. https://doi.org/10.1016/j.ijthermalsci.2006.11.007.
[306] M. Smitka, Z. Kolková, P. Nemec, M. Malcho, Impact of the amount of working fluid in loop heat pipe to remove waste heat from electronic component, in: EPJ Web Conf., 2014: pp. 1–4. https://doi.org/10.1051/epjconf/20146702109.

[307] H. Zhang, G. Lin, T. Ding, W. Yao, X. Shao, R.G. Sudakov, Y.F. Maidanik, Investigation of startup behaviors of a loop heat pipe, J. Thermophys. Heat Transf. 19 (2005) 509–518. https://doi.org/10.2514/1.12008.
[308] J. Ku, Operating characteristics of loop heat pipes, SAE Trans. 108 (2007) 503–519. https://doi.org/10.4271/1999-01-2007.
[309] K. Cheung, Thermal Performance and Operational Characteristics of Loop Heat Pipe (NRL LHP), SAE Tech. Pap. (1998). https://doi.org/10.4271/981813.
[310] Sintered Wicks, (n.d.). https://www.1-act.com/resources/heat-pipe-resources/heat-pipe-wicks/sintered-wicks/ (accessed September 3, 2021).
[311] P. Grossa, A. a M. Oliveira, E. Bazzo, Theoretical and Experimental Study of CPL and LHP with Ceramic Wicks, in: 16th Int. Heat Pipe Conf., Lyon, France, 2012.
[312] Y. Zhang, J. Liu, L. Liu, H. Jiang, T. Luan, Numerical simulation and analysis of heat leakage reduction in loop heat pipe with carbon fiber capillary wick, Int. J. Therm. Sci. 146 (2019) 106100. https://doi.org/10.1016/j.ijthermalsci.2019.106100.
[313] S. Okutani, H. Nagano, S. Okazaki, H. Ogawa, H. Nagai, Operating Characteristics of Multiple Evaporators and Multiple Condensers Loop Heat Pipe with Polytetrafluoroethylene, J. Electron. Cool. Therm. Control. (2014) 22–32.
[314] S.C. Wu, T.J. Lee, W.J. Lin, Y.M. Chen, T.W. Gu, D. Wang, Y.M. Chen, Study of PTFE wick structure applied to loop heat pipe, Appl. Therm. Eng. 81 (2015) 51–57. https://doi.org/10.1016/j.applthermaleng.2015.01.048.
[315] D. Mishkinis, P. P, S. R, R. A, T. A, Tjiptahardja, Loop Heat Pipe working fluids for intermediate temperature range: from -40ºC to +125ºC, in: Int. Conf. Heat Pipes Sp. Appl., Moscow, Russia, 2009.
[316] J. He, G. Lin, L. Bai, J. Miao, H. Zhang, Effect of non-condensable gas on the operation of a loop heat pipe, Int. J. Heat Mass Transf. 70 (2014) 449–462. https://doi.org/10.1016/j.ijheatmasstransfer.2013.11.043.
[317] R. Singh, A. Akbarzadeh, M. Mochizuki, Operational characteristics of the miniature loop heat pipe with non-condensable gases, Int. J. Heat Mass Transf. 53 (2010) 3471–3482. https://doi.org/10.1016/j.ijheatmasstransfer.2010.04.008.
[318] O. Romberg, F. Bodendieck, J. Block, R. Nadalini, N. Schneider, NetLander thermal control, in: R.A. Harris (Ed.), Low-Cost Planet. Mission., 2003: pp. 459–465.
[319] T.D. Swanson, G.C. Birur, NASA thermal control technologies for robotic spacecraft, Appl. Therm. Eng. 23 (2003) 1055–1065. https://doi.org/10.1016/S1359-4311(03)00036-X.
[320] Q. Su, S. Chang, M. Song, Y. Zhao, C. Dang, An experimental study on the heat transfer performance of a loop heat pipe system with ethanol-water mixture as working fluid for aircraft anti-icing, Int. J. Heat Mass Transf. 139 (2019) 280–292. https://doi.org/10.1016/j.ijheatmasstransfer.2019.05.015.
[321] G. Zhou, J. Li, Z. Jia, Power-saving exploration for high-end ultra-slim laptop computers with miniature loop heat pipe cooling module, Appl. Energy. 239 (2019) 859–875. https://doi.org/10.1016/j.apenergy.2019.01.258.
[322] Y. Qu, S. Wang, Y. Tian, A review of thermal performance in multiple evaporators loop heat pipe, Appl. Therm. Eng. 143 (2018) 209–224. https://doi.org/10.1016/j.applthermaleng.2018.07.070.
[323] B. Xiao, W. Deng, Z. Ma, S. He, L. He, X. Li, F. Yuan, W. Liu, Z. Liu, Experimental investigation of loop heat pipe with a large squared evaporator for multi-heat sources cooling, Renew. Energy. 147 (2020) 239–248. https://doi.org/10.1016/j.renene.2019.08.142.
[324] Z. Wang, W. Yang, A review on loop heat pipe for use in solar water heating, Energy Build. 79 (2014) 143–154. https://doi.org/10.1016/j.enbuild.2014.04.051.
[325] M. Discacciati, P. Gervasio, A. Quarteroni, The Interface Control Domain Decomposition (ICDD) Method for Elliptic Problems, SIAM J. Control Optim. 51 (2013) 3434–3458. https://doi.org/10.1137/15M101854X.
[326] A.F. Robertson, D. Gross, An Electrical-Analog Method for Transient Heat-Flow Analysis, J. Res. Natl. Bur. Stand. (1934). 61 (1958) 105–115. https://doi.org/10.6028/jres.061.016.
[327] K.W. Oh, K. Lee, B. Ahn, E.P. Furlani, B. Ahn et al., Design of pressure-driven microfluidic networks using electric circuit analogy, Lab Chip. 12 (2012) 515–545.

https://doi.org/10.1039/C2LC20799K.
[328] I.E. Idel'chik, Handbook of hydraulic resistance (3rd edition), Washington. (1960) 517. https://doi.org/AEC-tr- 6630.
[329] J. Ku, Methods of Controlling the Loop Heat Pipe Operating Temperature, in: 38th Int. Conf. Environ. Syst. San Fr. Calif. June 29-July 2, 2008, 2008.
[330] Hill Philip G., Peterson Carl R., Mechanics and thermodynamics of propulsion (2nd revised and enlarged edition), 1992.
[331] G. Nema, S. Garimella, B.M. Fronk, Flow regime transitions during condensation in microchannels, Int. J. Refrig. 40 (2014) 227–240. https://doi.org/10.1016/j.ijrefrig.2013.11.018.
[332] J.C. Chato, Laminar Condensation Inside Horizontal and Inclined Tubes, ASHRAE J. 4 (1962) 52–60.
[333] M.M. Shah, An Improved and Extended General Correlation for Heat Transfer During Condensation, Hvac&R Res. 15 (2009) 37–41. https://doi.org/10.1080/10789669.2009.10390871.
[334] R. Sánta, The Analysis of Two-Phase Condensation Heat Transfer Models Based on the Comparison of the Boundary Condition, Acta Polytech. Hungarica. 9 (2012) 167–180.
[335] M.M. Awad, Y.S. Muzychka, Effective property models for homogeneous two-phase flows, Exp. Therm. Fluid Sci. 33 (2008) 106–113. https://doi.org/10.1016/j.expthermflusci.2008.07.006.
[336] E. Pouzet, J.L. Joly, V. Platel, J.Y. Grandpeix, C. Butto, Dynamic response of a capillary pumped loop subjected to various heat load transients, Int. J. Heat Mass Transf. 47 (2004) 2293–2316. https://doi.org/10.1016/j.ijheatmasstransfer.2003.11.003.
[337] T. Tharayil, L. Godson, V. Ravindran, S. Wongwises, Effect of filling ratio on the performance of a novel miniature loop heat pipe having different diameter transport lines, Appl. Therm. Eng. 106 (2016) 588–600. https://doi.org/10.1016/j.applthermaleng.2016.05.125.
[338] B.B. Chen, W. Liu, Z.C. Liu, H. Li, J.G. Yang, Experimental investigation of loop heat pipe with flat evaporator using biporous wick, Appl. Therm. Eng. 42 (2012) 34–40. https://doi.org/10.1016/j.applthermaleng.2012.03.006.
[339] D. Bernardi, E. Pawlikowski, J. Newman, General Energy Balance for Battery Systems., J. Electrochem. Soc. 132 (1985) 5–12. https://doi.org/10.1149/1.2113792.
[340] H. Fathabadi, A novel design including cooling media for Lithium-ion batteries pack used in hybrid and electric vehicles, J. Power Sources. (2014). https://doi.org/10.1016/j.jpowsour.2013.06.160.
[341] Rechargeable battery technologies: an electronic engineer's view point, Energy Storage Devices Electron. Syst. Recharg. Batter. Supercapacitors. (2015) 29–61. https://doi.org/10.1016/B978-0-12-407947-2.00002-X.
[342] H. Mu, R. Xiong, Modeling, Evaluation, and State Estimation for Batteries, Model. Dyn. Control Electrified Veh. (2018) 1–38. https://doi.org/10.1016/B978-0-12-812786-5.00001-X.
[343] Z. Zhou, P.M. Holland, P. Igic, Compact thermal model of a three-phase IGBT inverter power module, in: "2008 26th Int. Conf. Microelectron. Proceedings, MIEL 2008," 2008. https://doi.org/10.1109/ICMEL.2008.4559249.
[344] G. Fontaras, B. Ciuffo, N. Zacharof, S. Tsiakmakis, A. Marotta, J. Pavlovic, K. Anagnostopoulos, The difference between reported and real-world CO2 emissions: How much improvement can be expected by WLTP introduction?∗, Transp. Res. Procedia. 25 (2017) 3933–3943. https://doi.org/10.1016/j.trpro.2017.05.333.
[345] A.S. Mussa, M. Klett, M. Behm, G. Lindbergh, R.W. Lindström, Fast-charging to a partial state of charge in lithium-ion batteries: A comparative ageing study, J. Energy Storage. 13 (2017) 325–333. https://doi.org/10.1016/j.est.2017.07.004.
[346] S. Arora, A. Kapoor, Experimental study of heat generation rate during discharge of lifePO4 pouch cells of different nominal capacities and thickness, Batteries. 5 (2019). https://doi.org/10.3390/batteries5040070.
[347] I. Chroma ATE, Model 17011 Programmable Battery Charge/Discharge Test System, (n.d.). https://www.chromaus.com/product_17011_Battery_Charge_Discharge_Test_System.php (accessed April 23, 2020).
[348] ASM International Handbook Committee, ASM Handbook Vol. 2: Properties and selection--

nonferrous alloys and special-purpose materials, 2001. https://doi.org/10.1016/S0026-0576(03)90166-8.
[349] Industries in 2021 : a slow , painful recovery, 2021.
[350] D. Jafari, W.W. Wits, B.J. Geurts, Metal 3D-printed wick structures for heat pipe application: Capillary performance analysis, Appl. Therm. Eng. 143 (2018) 403–414. https://doi.org/10.1016/j.applthermaleng.2018.07.111.
[351] B. Siedel, V. Sartre, F. Lefèvre, Numerical investigation of the thermohydraulic behaviour of a complete loop heat pipe, Appl. Therm. Eng. 61 (2013) 541–553. https://doi.org/10.1016/j.applthermaleng.2013.08.017.
[352] A. Georgoulas, M. Andredaki, M. Marengo, An enhanced VOF method coupled with heat transfer and phase change to characterise bubble detachment in saturated pool boiling, Energies. 10 (2017). https://doi.org/10.3390/en10030272.
[353] Goran Djukanovic, Copper vs. Aluminium – substitution slows but continues, (n.d.). https://aluminiuminsider.com/copper-vs-aluminium-substitution-slows-but-continues/.
[354] K. Xie, Y. Ji, C. Yu, M. Wu, H. Yi, Experimental investigation on an aluminum oscillating heat pipe charged with water, Appl. Therm. Eng. 162 (2019) 114182. https://doi.org/10.1016/j.applthermaleng.2019.114182.
[355] F.P. Incropera, D.P. DeWitt, Fundamentals of Heat and Mass Transfer, Water. 6th (2007) 997. http://www.osti.gov/energycitations/product.biblio.jsp?osti_id=6008324.
[356] How Far Can I Drive?, (n.d.). https://www.nissan.co.uk/vehicles/new-vehicles/leaf/range-charging.html (accessed July 19, 2021).
[357] Nissan Leaf, (n.d.). https://ev-database.org/car/1106/Nissan-Leaf (accessed July 19, 2021).
[358] S. Panchal, R. Khasow, I. Dincer, M. Agelin-Chaab, R. Fraser, M. Fowler, Thermal design and simulation of mini-channel cold plate for water cooled large sized prismatic lithium-ion battery, Appl. Therm. Eng. 122 (2017) 80–90. https://doi.org/10.1016/j.applthermaleng.2017.05.010.
[359] Y.F. Maydanik, M.A. Chernysheva, V.G. Pastukhov, Review: Loop heat pipes with flat evaporators, Appl. Therm. Eng. 67 (2014) 294–307. https://doi.org/10.1016/j.applthermaleng.2014.03.041.
[360] L. Bai, J. Fu, G. Lin, C. Zhou, D. Wen, Quiet power-free cooling system enabled by loop heat pipe, Appl. Therm. Eng. 155 (2019) 14–23. https://doi.org/10.1016/j.applthermaleng.2019.03.147.
[361] V. V. Vlassov, R.R. Riehl, Mathematical model of a loop heat pipe with cylindrical evaporator and integrated reservoir, Appl. Therm. Eng. 28 (2008) 942–954. https://doi.org/10.1016/j.applthermaleng.2007.07.016.
[362] T.M. Bandhauer, S. Garimella, Passive, internal thermal management system for batteries using microscale liquid-vapor phase change, Appl. Therm. Eng. 61 (2013) 756–769. https://doi.org/10.1016/j.applthermaleng.2013.08.004.
[363] L. Chang, J. Wang, X. Wang, Y. Chen, Z. Zhang, X. Feng, The solutions to electric vehicle air conditioning systems: A review, Renew. Sustain. Energy Rev. 91 (2018) 443–463. https://doi.org/10.1016/j.rser.2018.04.005.

Appendices

Appendix A – ε-NTU Method

First, there is the need to calculate the heat that needs to be removed from the condenser at every time step, which is equal to the difference in enthalpy of the working fluid:

$$\dot{Q}_{cond} = \dot{m}(h_l - h_v) \tag{1}$$

This is the heat that will need to be matched by the HEX in order to obtain full condensation at the end of the condenser. Hence the assumption made here is that the mass flow rate for the HEX gets updated at every time step to achieve full condensation and no subcooling.

Second, the HEX internal convection heat transfer coefficient needs to be calculated. Assuming that the HEX working fluid (ethylene glycol, in this case) stays always in liquid state, allows to use the Dittus-Boelter correlation:

$$\begin{gathered} Re_{HEX} > 10000 \\ 0.7 < Pr_{HEX} < 160 \\ L_{HEX} > 20 r_{HEX} \\ h_{c,e} = 0.023 \left(Re_{HEX}^{4/5}\right)\left(Pr_{HEX}^{1/3}\right)\left(\frac{k_{l,HEX}}{2r_{HEX}}\right) \end{gathered} \tag{2}$$

For the condenser internal convection heat transfer coefficient $h_{c,i}$, the correlation for annular and stratified flow detailed in the previous sections are used. At this point, knowing both heat transfer coefficient, the overall heat transfer coefficient UA is calculated:

$$\frac{1}{UA} = \frac{1}{h_{c,i}A_{c,i}} + \frac{R_{fouling}}{A_{c,i}} + \frac{log\left(\frac{r_{c,e}}{r_{c,i}}\right)}{2\pi k_{c,i} L_{c,i}} + \frac{R_{fouling}}{A_{HEX}} + \frac{1}{h_{c,e}A_{HEX}} \tag{3}$$

where $R_{fouling}$ is a fouling (i.e. accumulation of working fluid residuals on the inner surface of heat exchanger that ruins the performance) coefficient for refrigerants; on the right term of

eq. (42) there are considered both the internal and external heat transfer phenomena for convection as well as the fouling effect and the conduction thought the condenser pipe wall.

Last thing needed for the number of transfer unit (NTU) is to calculate the minimum thermal capacity C_{min}. Remembering that the specific heat during phase change is infinite:

$$\begin{cases} C_{HEX} = \dot{m}_{HEX}\, c_{p,HEX} \\ C_{cond} = \dot{m}\, c_{p,cond} = \infty \end{cases} \xrightarrow{yields} C_{min} = C_{HEX} \tag{4}$$

hence, following the method leads to:

$$\begin{gathered} NTU = \frac{UA}{C_{min}} \\ \varepsilon = 1 - e^{-NTU} \\ \dot{Q}_{max} = C_{min}\left(T_{c,in} - T_{HEX,in}\right) \\ \dot{Q}_{HEX} = \varepsilon \dot{Q}_{max} \\ T_{HEX,out} = T_{HEX,in} + \frac{\dot{Q}_{HEX}}{C_{cold}} \end{gathered} \tag{5}$$

If $\dot{Q}_{HEX} \neq \dot{Q}_{cond}$, that means that full condensation is not reached or subcooling condition have arisen. Thus, in order to avoid that, a subroutine changes the m_{HEX} until the absolute difference between the heat exchanged from the HEX (eq. 44) and the condenser (eq. 40) is less than 0.1W.

Appendix B – LHP Validation with water (Comparison with Thercon Data)

Table 47 - Validation of the water-filled LHP by using the data provided from Thercon. Resistance is calculated by using a condenser temperaBture of 20°C.

	Numerical Model				Thercon Tests			Δ		
Power [W]	T_{wall} [°C]	T_{vo} [°C]	$R\ \left[\frac{°C}{W}\right]$		T_{wall} [°C]	T_{vo} [°C]	$R\ \left[\frac{°C}{W}\right]$	T_{wall} [°C]	T_{vo} [°C]	$R\ \left[\frac{°C}{W}\right]$
40	45.9	44.6	0.647		46.4	43.6	0.660	0.5	-1.0	1.9%
60	49.4	47.5	0.490		46.6	42.6	0.443	-2.9	-4.8	10.7%
80	51.7	49.1	0.397		47.2	42.2	0.340	-4.6	-7.0	16.8%
100	52.9	49.7	0.329		48.3	42.1	0.283	-4.7	-7.5	16.6%
160	56.9	51.7	0.231		51.3	42.1	0.196	-5.6	-9.6	17.8%
200	58.4	51.8	0.192		52.4	41.5	0.162	-6.0	-10.3	18.4%
260	61.8	53.3	0.161		55.1	43.7	0.135	-6.7	-9.6	19.2%
300	63.1	53.3	0.144		56.5	45.2	0.122	-6.7	-8.1	18.2%
360	66.1	54.4	0.128		59.2	48.4	0.109	-7.0	-6.0	17.8%
400	67.3	54.3	0.118		61.2	50.8	0.103	-6.1	-3.5	14.8%
460	70.5	55.5	0.110		64.2	54.3	0.096	-6.3	-1.2	14.2%
500	72.2	55.9	0.104		67.0	57.5	0.094	-5.2	1.6	11.1%
560	75.1	56.8	0.098		71.5	62.1	0.092	-3.6	5.3	7.1%
600	77.2	57.6	0.095		74.2	65.2	0.090	-3.0	7.6	5.5%

660	80.5	58.9	0.092		79.1	70.0	0.090	-1.3	11.1	2.3%
700	81.2	58.3	0.087		81.9	73.0	0.088	0.7	14.7	1.2%
760	84.0	59.1	0.084		86.6	77.5	0.088	2.6	18.4	3.9%
800	87.7	61.5	0.085		90.4	81.2	0.088	2.7	19.7	3.9%
860	89.1	60.9	0.080		95.7	86.1	0.088	6.6	25.2	8.7%
900	92.8	63.3	0.081		99.57	89.88	0.088	6.8	26.6	8.6%
					Average Discrepancy			4.5	9.9	10.9%

Appendix C – LHP Validation with Ethanol

Table 48 - Results from both steady state and ramp test for the validation of the ethanol LHP. T_{bath} refers to the temperature set for the thermal bath.

			Model					Experiments					Δ				
Test Type	Power [W]	T_{bath} [°C]	T_{wall} [°C]	T_{vo} [°C]	T_{ll} [°C]	T_{cond} [°C]	R [$°C/W$]	T_{wall} [°C]	T_{vo} [°C]	T_{ll} [°C]	T_{cond} [°C]	R [$°C/W$]	T_{wall} [°C]	T_{vo} [°C]	T_{ll} [°C]	T_{cond} [°C]	R [$°C/W$]
Steady State	50	20	47.8	46.0	25.0	24.8	0.54	46.3	44.2	24.7	21.6	0.49	1.5	1.8	0.3	3.2	8.7%
	70	20	52.8	50.3	27.8	28.0	0.45	52.9	48.0	24.8	21.6	0.45	0.1	2.4	3.0	6.5	1.4%
	90	20	57.0	53.8	31.0	31.6	0.40	63.0	60.2	24.9	21.7	0.46	6.0	6.4	6.1	9.9	13.0%
Steady State	20	5	32.9	32.3	16.0	11.2	1.10	33.3	34.7	27.9	11.7	1.08	0.3	2.4	11.9	0.5	1.7%
	40	5	40.5	39.1	14.7	12.2	0.74	41.7	39.4	21.5	11.4	0.76	1.2	0.3	6.7	0.7	2.6%
	60	5	45.8	43.7	16.2	14.6	0.58	43.2	44.2	18.9	11.4	0.53	2.6	0.5	2.7	3.2	9.5%
	80	5	50.0	47.2	18.9	18.0	0.49	50.3	49.0	18.5	11.5	0.48	0.2	1.8	0.4	6.6	0.6%
	100	5	53.7	50.2	22.1	21.7	0.43	60.8	58.4	18.1	11.3	0.50	7.1	8.2	4.1	10.4	13.7%
Ramp	20	5	29.3	28.7	16.2	11.4	0.92	33.3	34.7	27.9	11.7	1.08	3.9	6.0	11.7	0.3	15.0%
	40	5	35.6	34.2	15.5	13.1	0.61	41.7	39.4	21.5	11.4	0.76	6.1	5.2	6.0	1.7	18.7%
	60	5	42.3	40.3	16.8	15.4	0.52	43.2	44.2	18.9	11.4	0.53	0.9	4.0	2.1	3.9	1.4%
	80	5	48.0	45.2	19.2	18.4	0.46	50.3	49.0	18.5	11.5	0.48	2.3	3.8	0.7	6.9	4.6%
Ramp	50	20	45.4	43.7	26.4	24.8	0.49	46.3	44.2	24.7	21.6	0.49	0.8	0.5	1.7	3.2	0.8%
	70	20	52.3	49.9	27.9	28.0	0.45	52.9	48.0	24.8	21.6	0.45	0.5	1.9	3.2	6.5	0.1%
	90	20	56.9	53.8	31.0	31.6	0.40	61.8	56.9	24.6	21.7	0.45	4.9	3.1	6.4	9.9	10.4%
Ramp	20	20	32.3	31.6	29.8	22.4	0.49	29.3	28.7	25.5	21.7	0.38	3.0	3.0	4.2	0.7	29.3%
	40	20	39.7	38.4	27.0	23.5	0.41	35.6	34.2	24.9	21.7	0.35	4.2	4.2	2.1	1.8	17.0%
	60	20	46.3	44.2	26.9	26.3	0.33	42.3	40.3	24.9	21.7	0.34	4.0	4.0	2.0	4.7	3.3%
	80	20	52.0	49.3	28.9	29.8	0.28	48.0	45.2	24.9	21.6	0.33	4.0	4.0	4.0	8.2	15.6%
Average Discrepancy													2.8	3.3	4.2	4.7	8.8%

Thank you for reading.